博士論文

A Study on Auroral-Zone Thermospheric Temperatures and Winds Using Fabry-Perot Doppler Imaging Observations at Syowa Station, Antarctica

（南極昭和基地におけるファブリーペロードップラーイメージング観測によるオーロラ帯の熱圏温度と風に関する研究）

中島英彰

平成4年

A Study on Auroral-Zone Thermospheric Temperatures and Winds Using Fabry-Perot Doppler Imaging Observations at Syowa Station, Antarctica

（南極昭和基地におけるファブリーペロードップラーイメージング観測によるオーロラ帯の熱圏温度と風に関する研究）

Hideaki Nakajima
中島英彰

Upper Atmosphere and Space Research Laboratory, Tohoku University

Thesis Presented for the Degree of Doctor of Science, Tohoku University

December, 1992

Abstract

A new–type of optical instrument, called a 'Fabry-Perot Doppler Imaging System', has been developed to obtain two-dimensional distributions of thermospheric winds and temperatures from measurements of the Doppler shift and width of aurora and/or airglow emission lines of OI 557.7 nm and OI 630.0 nm over a wide field of view (165°). Observations of thermospheric winds and temperatures have been carried out at Syowa Station, Antarctica for a period of one austral winter in 1990. The observations were made on 46 clear nights from April 1, 1990 to September 20, 1990 covering various auroral conditions, and 900,000 Doppler image data of OI 557.7 nm and OI 630.0 nm emission lines as well as the stabilized He–Ne laser calibration data were stored in 17 optical disks. An analog image data stored in the optical disk were digitized and converted to 640 × 480 × 2-bytes digital image data and were subjected to image processings. After removing distortions in these images which may arise from aberration of electric lens in the detector employing a interpolation method of two-dimensional spline function, Doppler temperatures and wind velocities were derived. A frequency stabilized He–Ne laser was used for calibration of the instrument. It become possible to obtain the thermospheric winds and temperatures with an unprecedented high temporal resolution of 3 minutes as a result of data analysis. The thermospheric temperatures in F-region were observed to increase by 200–500 K associated with an auroral breakup event occurred at 21:38 UT, September 11, 1990. The line-of-sight wind velocities were observed to change by 400–600 m/s in a time period as short as ∼10 m/s. In addition, occurrence of periodic variations of winds at most positions on an image with a period of 10–20 min after the auroral breakup event is observed. At around 22:57 UT, September 13, 1990, distinct decrease in westward wind velocities by more than 500 m/s within 6 to 9 min were observed at every position in the east–west sectors including the inner and the outer fringe positions. These variations occurred just before the time of auroral

breakup event. It is suggested that neutral particles were forced by the ion drag due to the eastward auroral electrojet current occurred at that time. At the same time, the existence of strong vertical flow is suggested.

When the results on thermospheric dynamics described in this thesis are combined with a variety of space-borne data, we can expect to achieve more clear and comprehensive understanding on physics of the thermosphere.

Acknowledgments

I wish to express my heavy gratitude for the guidance and encouragement received from Prof. H.Fukunishi throughout the course of this work. I also wish to extend my deep appreciation to Dr. S.Okano for his useful advice and guidance to complete this thesis. Special thanks are due to Mr. T.Abe for his valuable help in constructing the instrument. I would also like to acknowledge Mr. Y.Niihara for his helpful assistance in dealing with the FPDIS data, Mr. M.Okabayashi for making Tables by TEX, Mr. I.Okubo for providing star calibration programs, and all members of the Upper Atmosphere and Space Research Laboratory for helpful assistance and encouragement. I am very grateful to Prof. H.Oya, Prof. T.Saito, and Dr. A.Morioka for their valuable advice.

I extent my sincere appreciation to Dr. T.Ono of National Institute of Polar Research for his valuable help in the preparation and the execution of observations at Syowa Station, Antarctica and for his helpful advice. I would also like to express my appreciation to Prof. T.Hirasawa of National Institute of Polar Research for his valuable advice and support, to Prof. Y.Naito, the leader of the 31-st wintering party of Japanese Antarctic Research Expedition, for his kind suggestions and help during my stay in the Antarctica, and to all members of the World Data Center-C2 for Aurora in NIPR for their kind supports in dealing with the FPDIS data during my stay in NIPR. Thanks are due to all members of the 31-st wintering party of Japanese Antarctic Research Expedition for their warmhearted encouragement and support during my stay in the Antarctica.

I am much indebted to Mr. K.Shiokawa of the Solar Terrestrial Environment Laboratory, Nagoya University for his assistance in the FPDIS data analysis.

Finally, I want to express my hearty gratitude to Mr. M.Taguchi—my great friend, and to Mrs. H.Nakajima—my wife, who continuously encouraged me to complete this work, especially

when the author is in the Antarctica.

The data analysis of the FPDIS was partly supported by the ARSAD system in the WDC-C2 for Aurora in National Institute of Polar Research.

Contents

List of Figures

List of Tables

Chapter 1

INTRODUCTION

1.1 The Earth's Thermosphere

The upper atmosphere of the Earth is conventionally divided into several regions on the basis of the vertical temperature profile as shown in Figure 1.1. The thermosphere is defined as the region above the mesopause ($\sim$ 80–90 km) where the neutral gas temperature increases towards an asymptotic value (the exospheric temperature) in the isothermal regime which is controlled by the thermal balance between the absorption of solar UV and EUV radiation by atmospheric constituents and the downward molecular conduction of heat as well as the radiative cooling. The solar UV and EUV radiation is not only a major heat source of the thermosphere, but it also ionizes a fraction of neutral species to form the ionosphere in the same altitude region. Hence, the thermosphere contains the ionospheric E- and F-regions. The upper boundary of the thermosphere is conventionally defined as the exobase ($\sim$ 500–600 km), above where the thin atmosphere becomes collisionless.

The temperature in the thermosphere increases with height. It increases from a value as low as $\sim$180 K at the mesopause to the exospheric value as high as 1000–2000 K which largely varies in response to solar activity [*Crowley*, 1991]. Such high temperatures are due to absorption

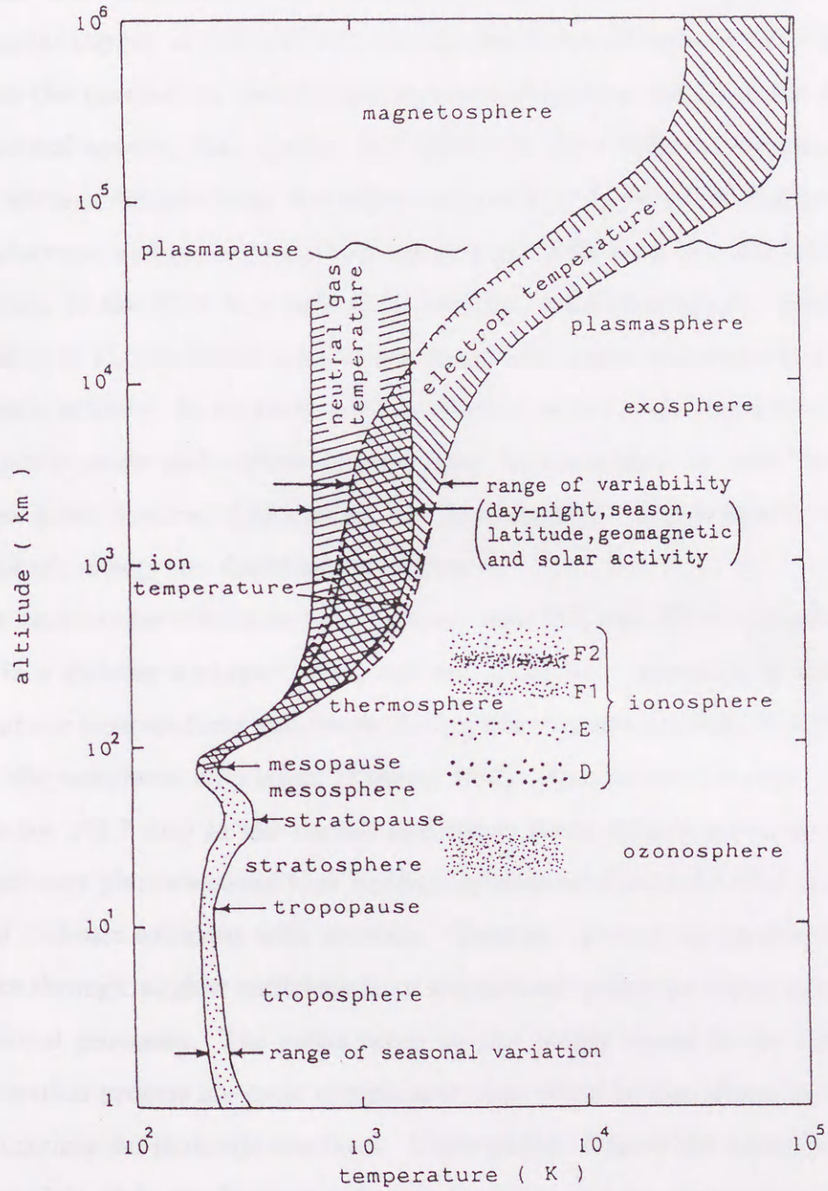

Figure 1.1: Vertical profile of atmospheric temperature and naming of atmospheric regions. [After *Tohmatsu and Ogawa*, 1990.]

of the solar EUV radiation in the Schumann-Runge continuum region ($\sim$ 130 to 175 nm) by the molecular oxygen at 100–130 km, and by absorption of ionizing EUV radiation above 130 km. Since the production, distribution and loss of thermal energy in the thermosphere differ among neutral species, ionic species, and electrons, three different temperatures, i.e., neutral, ion, and electron temperatures are defined separately. As shown in Figure 1.1, thermospheric neutral, electron, and ion temperatures are strongly influenced by solar activity, mainly due to the variation of the EUV flux with solar activity. Joule heating and heating due to particle precipitation at high latitudes are also important heat sources particularly at times of enhanced geomagnetic activity. In addition, cooling effects due to radiatively active minor constituents such as nitric oxide and carbon dioxide must be considered in order to completely model the global mean thermal structure of the thermosphere. The separate sources and sinks of thermospheric energy are discussed as follows.

Of the various thermospheric heat sources, solar UV and EUV radiation are the most important in a globally averaged sense, and are primarily responsible for maintaining the high thermospheric temperatures and for producing the pressure-gradient that drives the basic day-to-night thermospheric circulation [*Killeen*, 1987]. Absorption of a solar EUV photon (wavelength below 102.7 nm) in the middle and upper thermosphere produces ionization, creating ejected primary photoelectrons that undergo subsequent Coulomb collisions with electrons and ions, and inelastic collisions with neutrals. However, most of the photoelectron energy is lost into space through airglow emissions from atomic and molecular states excited through inelastic collisional processes. The paths taken by the energy stored in the ions produced by the photoionization process are more complicated than those for the photoelectrons, involving various exothermis ion-molecule reactions. These paths all have the common feature that every ionization ultimately results in the dissociation of an oxygen molecule into two oxygen atoms which then diffuse downward and release their energy of dissociation into the three-body recombination process at an altitude below the EUV-dominated region in the lower thermosphere and upper mesosphere. Thus, most of the energy carried by the ions goes into direct heating

of the local thermosphere.

In the lower thermosphere, between ~90 and 150 km, absorption of solar radiation in the Schumann-Runge Continuum region (~130 to 175 nm) is the dominant heat source. In this spectral region, photons are able to dissociate molecular oxygen, producing metastable atomic oxygen in the $O(^1D)$ state that is subsequently collisionally quenched, releasing its excess energy which appears as neutral heating. The local heating efficiency of this process is $\sim$ 33%, which denotes that approximately one third of the Schumann-Runge continuum photon energy goes into heating the local neutral gas [*Killeen*, 1987]. In order to improve the understanding and empirical representation of the solar EUV/UV fluxes, significant efforts have been made over the years [*Hedin*, 1979]. It has long been recognized that thermospheric densities and temperatures vary with solar activity and that the variations are qualitatively similar to those of the solar decimetric (F10.7) flux. Although this radio flux, which has been cataloged continuously over many years, does not act directly on the upper atmosphere itself. It can, however, be used as a representative index of the intensity of the solar UV and EUV fluxes, with which experimental data sets of thermospheric temperatures are correlated [*Hernandez*, 1983], in semi-empirical atmospheric models.

It was also discovered that the cooling effect of NO 5.3μm band plays an important role especially at the solar maximum condition by comparing the AE satellite measurement with the data from MSIS empirical model by *Roble and Emery* [1983]. This is considered to be due to the enhancement of NO concentration in the thermosphere at times of solar maximum conditions. On the other hand, the role of infrared radiative cooling effect in the lower thermosphere due to CO_2 is not yet well known, although some works have been made [*Dickinson*, 1984].

As stated above, Joule heating due to differential motion between ion and neutral, and the particle heating due to the collisional slowing-down processes for energetic auroral particles precipitating from the magnetosphere at high-latitudes become important sources of thermospheric heating, particularly at times of enhanced geomagnetic activity. *Perreault and Akasofu*, [1978] suggested that the *AE* (Auroral Electrojet) index could be used as a measure of the global Joule

heat production. A reasonable linear correlation was found between the Joule heat production and the *AE* index, with the constant of proportionally being $\sim 2.3 \times 10^8$ Watts/*AE* by *Ahn et al.*, [1983]. The equivalent constant for particle heating is $\sim 0.2 \times 10^8$ Watts/*AE*.

Foster et al., [1983] determined the average pattern of Joule heating over the polar caps for various geophysical conditions using empirical models of particle precipitation, electrical conductivity, and electric fields. Their results indicate that high-latitude Joule heating occurs in a roughly-oval pattern consisting of three distinct heating regions, i.e., dayside cleft, the region of sunward ion convection at dawn and dusk, and the midnight sector. The hemisphere-averaged Joule heating at equinox is $\sim 2.5 \times 10^{10}$ Watts for the Kp=1 condition and $\sim 8.5 \times 10^{10}$ Watts for Kp=4, with a linear variation with Kp's. The study of Joule heating by *Foster et al.*, [1983] is based on electric field measurement and it generally neglects effects due to neutral winds. The existence of neutral wind can modify the Joule heating rate by reducing or enhancing the ion-neutral differential velocity. These effects have been considered, however, in the simulation studies using the TGCMs, which are the numerical, three-dimensional, time-dependent general circulation models of the thermosphere. Two kinds of the TGCM have been developed; one is the National Center for Atmospheric Research model (NCAR-TGCM) developed by *Dickinson et al.*, [1981] and *Roble et al.*, [1982], and the other is the University College London model (UCL-TGCM) developed by *Fuller-Rowell and Rees*, [1980]. The study of Joule heating using the TGCMs [*Roble et al.*, 1983; *Rees et al.*, 1985; *Killeen and Roble*, 1986] has provided estimates of $\sim 0.3 - 1.5 \times 10^{11}$ Watts, depending on the level of geomagnetic activity and value for the cross-cap potential used in the calculations. The estimates of the total global thermospheric heating due to particle precipitation based on recent satellite measurements of the averaged precipitating particle fluxes are typically lower than those for Joule heating, which is in the approximate range of $\sim 0.05 - 0.6 \times 10^{11}$ Watts, depending on solar and auroral activity [*Hardy et al.*, 1985; *Gussenhoven et al.*, 1984].

Fuller-Rowell and Evans [1987] analyzed the TIROS/NOAA satellite data to provide average maps of energy influx in latitude and local time, that can be used to provide the statistical

pattern of auroral particle heating in theoretical models.

Rees, M.H. et al., [1983] have discussed the neutral and ion gas heating by auroral electron precipitation and have calculated the neutral heating efficiency for a range of typical auroral spectra, using a sophisticated electron energy degradation and transport code. They found the altitude profile of the heating efficiency is relatively independent of the electron spectrum, but sensitive to changes in the neutral atmosphere composition and temperature. Over 50% of the energy input associated with the energetic particle precipitation was found to go into neutral heating.

There are other minor heat sources of the thermosphere. One of them is due to the low- and mid-latitude precipitation of energetic neutral particles produced through charge exchange reactions with ions in the ring current [*Rohrbaugh et al.*, 1983]. However, global average heating of the thermosphere by this source is not yet well quantified. Energy is also transferred into the thermosphere from below, through the upward propagation of tides and gravity waves generated at lower altitudes. *Groves and Forbes* [1985] have made estimates of the global thermospheric heating due to tidal dissipation and presented the mean heating rates as a function of altitude and latitude in order to facilitate the parametrization of this energy source in general circulation models. They found that the tidal heating is less than the heating due to radiation at all altitudes, except below 90 km where the tidal heating maximizes and the solar UV is already attenuated. The global integrated tidal heating from 150 to 400 km is $\sim 6 \times 10^9$ Watts, which amounts to $\sim 7\%$ of the EUV energy deposition rate assumed in their analysis. These results suggest that tidal heating plays a secondary, but significant role in the energy budget of the thermosphere, although the effect of tidal heating on the global circulation and compositional structures does not yet receive much attention for the present.

The effects of gravity wave dissipation on the global thermospheric heat budget also have not been well quantified yet, although theoretical treatment for gravity wave breaking have been reported [*e.g., Garcia and Solomon*, 1985, and references within it]. In Figure 1.2, altitude distributions for some of the global average heating and cooling rates are plotted for comparison,

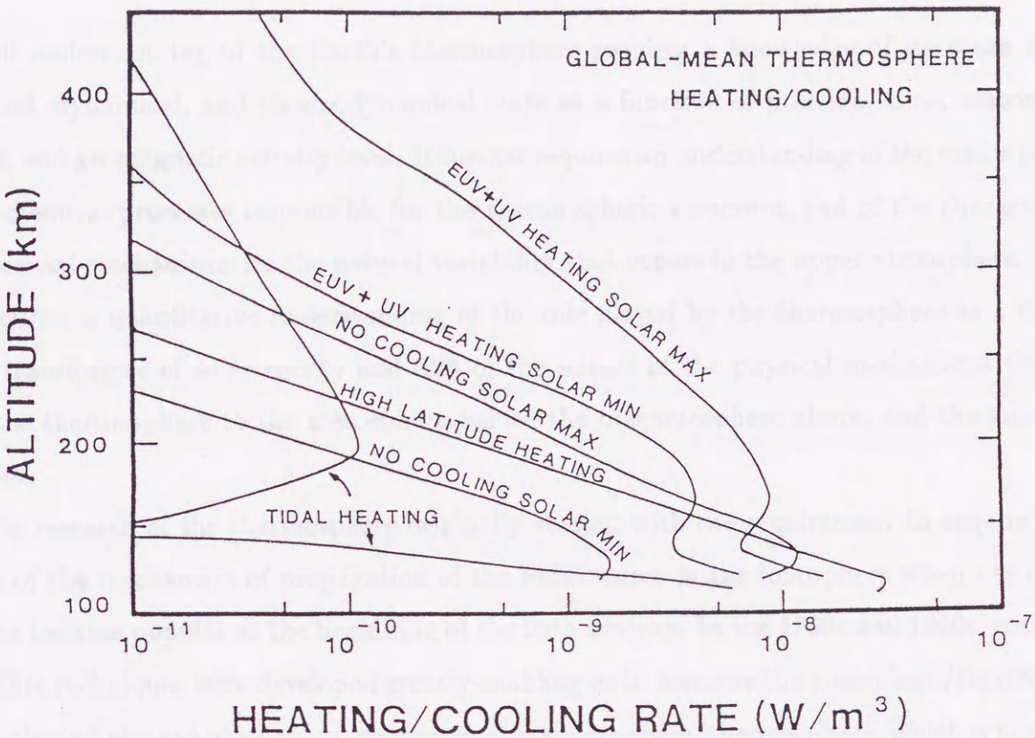

Figure 1.2: Global mean sources and sinks of energy to the thermosphere as a function of altitude (information taken from *Roble and Emery* [1983] and *Groves and Forbes* [1985]). The main sink of energy is due to the relatively slow process of downward conduction of heat. [After *Killeen*, 1987.]

based on the studies of *Roble and Emery* [1983] and *Groves and Forbes* [1985] (After *Killeen*, [1987]). Some indication of the large degree of variability in these sources and sinks can be seen in the contrast between solar maximum and solar minimum. The net heating is balanced by downward heat conduction. Since the high-latitude heat sources are localized and not uniformly distributed over the globe, their influence on the thermospheric dynamics and structure will be much greater than would be expected from the simple comparison of global mean values.

1.2 Observations of the Earth's Thermosphere

A full understanding of the Earth's thermosphere requires a knowledge of its mean compositional, dynamical, and thermodynamical state as a function of position, time, season, solar cycle, and geomagnetic activity level. It further requires an understanding of the major physical and chemical processes responsible for the thermospheric structure, and of the characteristics and causal mechanisms for the natural variability that occurs in the upper atmosphere. Lastly, it requires a quantitative understanding of the role played by the thermosphere as a modifier and transformer of solar energy and also of the nature of the physical mechanisms that couple the thermosphere to the mesosphere below, the magnetosphere above, and the ionosphere within.

The research of the thermosphere originally started with the requirement to acquire knowledge of the mechanism of propagation of the radio waves in the ionosphere when use of radio waves became popular at the beginning of the 20th century. In the 1950s and 1960s, rocket and satellite techniques were developed greatly enabling us to measure the ionosphere/thermosphere directly and also the physics and chemistry of the ionosphere/thermosphere, which is now called the 'upper atmosphere'. The stratosphere and mesosphere are now called the 'middle atmosphere'.

Until recently, the lower thermosphere was the least explored region of the atmosphere since it was too high for balloon experiments and too low for in-situ satellite measurements. Recently, significant progress towards providing quantitative information on the parameters described at the beginning of this section, including the lower thermosphere, has been made. One of the reasons of progress is due to the comprehensive nature of new data-sets provided by NASA's Dynamics Explorer spacecraft (DE-1 and DE-2), as well as the ground-based network of optical Fabry-Perot interferometer observatories and incoherent scatter radar facilities which utilizes the technique of remote sensing, from space and from the ground. The other reason is the development of the numerical, three-dimensional, time-dependent general circulation models

(TGCMs) of the thermosphere as introduced in Section 1.1. The upper thermosphere is qualitatively well understood due to extensive observations by a variety of instruments over a period of many years. Recently a more quantitative approach has been employed, with many of the old assumptions being questioned. There has also been a realization that many of the outstanding problems can only be solved by the simultaneous application of multiple diagnostics, often on a global scale, as reflected in some of the globally coordinated campaigns [*Crowley*, 1991].

In the following sections, recent results of ground-based observations with both Fabry-Perot interferometers and incoherent scatter radars are reviewed. In the first part, observations on the F-region thermosphere are reviewed, then space-borne observations of thermosphere are overviewed, and at the last part, observations on lower thermosphere are mentioned.

1.2.1 Ground-based observations on the F-region thermosphere

The thermosphere consists of several constituents. N_2, O, O_2, H, and He are the major neutral species, the altitudinal distribution of which are mainly determined by the diffusive equilibrium, although it widely varies according to solar activity, geomagnetic activity, and season, which is empirically given by the empirical models. These neutral species interact with a weak plasma consisting of various ions, mostly O^+ and NO^+. The three states of thermosphere, i.e., dynamical, thermodynamical, and compositional states depend on various dynamical forcings and neutral-plasma interactions with neutral winds. These effects induce diffusive changes in composition and thereby modifying the pressure gradients due to the temperature variations. While significant work over the past decade has been devoted to characterizing the temperature and compositional structure of the thermosphere, it has been only recently that instruments have been deployed in space and on the ground to map the dynamical state of the Earth's upper atmosphere on a global-scale.

The ground-based observations of thermospheric parameters have been made using the Fabry-Perot interferometers and the incoherent backscatter radar facilities. First, Fabry-Perot obser-

vations of F-region thermosphere are reviewed.

The practical observations of the thermospheric neutral wind velocities and temperatures using the Fabry-Perot interferometers started in the late 1960s. In the early stage, *Armstrong* [1969] observed the neutral wind velocities in the $F2$-layer by measuring the Doppler shift in the night airglow emission of OI 630.0 nm atomic oxygen emission line [$O(^1D) - O(^3P)$] at Camden, N.S.W.[1]. He succeeded in observing winds in the order of 100 m/s with diurnal changes in wind directions. The measurement of the thermospheric neutral temperatures using the Doppler broadening of the OI 630.0 nm emission line was performed by *Biondi and Feibelman* [1968]. It has been shown that nighttime, ground-based observations of this emission line are a realistic measure of the exospheric temperature [*Roble et al.*, 1968]. *Hays et al.* [1969] measured the Doppler temperatures of OI 630.0 nm emission line using a 6-inch Fabry-Perot interferometer during the magnetic storm period of October 30 to November 2, 1968. They showed that the obtained Doppler temperatures give a realistic indication of the storm-time variation of the exospheric temperature and compared the change of temperatures with the model predictions.

Since then, a number of observations of using Fabry-Perot interferometers have been made. For example, observations of neutral wind velocities have been done by *Hays and Roble* [1971] at Ann Arbor, Michigan[2], *Sipler and Biondi* [1978] at Kwajelein Atoll, Marshall Islands[3], *Friedman and Herrero* [1982] at Arecibo, Puerto Rico[4], *Hernandez* [1982a] at Fritz Peak Observatory, Colorado[5], *Rees et al.* [1982] at Kiruna, Sweden, *Abreu et al.* [1983] at Calgary, Canada[6], *Sipler et al.* [1983] at Roi Namur Island, Kwajalein Atoll, *Hernandez and Roble* [1984a] at Fritz

[1]Camden, N.S.W. : 34.07°S, 150.67°W, geographic

[2]Ann Arbor, Michigan : 42.27°N, 83.73°W, geographic

[3]Kwajelein Atoll, Marshall Islands : 9.40°N, 167.48°E, geographic

[4]Arecibo, Puerto Rico : 18.3°N, 66.7°W, geographic

[5]Fritz Peak, Colorado : 39.89°N, 105.5°W, geographic

[6]Calgary, Canada : 51.08°N, 114.1°W, geographic

Peak, Colorado, *Rees et al.* [1984c] at Skibotn, Northern Scandinavia[7], Kiruna, Sweden[8], and at Longyearbyen, Svalbard[9], *Stewart et al.* [1985] at Halley, Antarctica[10], *Yagi and Dyson* [1985b] at Beveridge, Australia[11], *Meriwether et al.* [1986] at Arequipa, Peru[12] *Burnside and Tepley* [1987] at Arecibo, Puerto Rico, *Meriwether et al.* [1988] at Thule, Greenland[13], *Burnside and Tepley* [1989] at Arecibo, Puerto Rico, *Biondi et al.* [1990] at Arequipa, Peru, and *Crickmore et al.* [1991] at Halley, Antarctica.

Observations of neutral temperatures were made by *Roble et al.* [1970] at Ann Arbor, *Truttse and Yurchenko* [1971] at Zvenigorod Observatory[14], *Feibelman et al.* [1972] at Laurel Ridge[15], *Biondi and Meriwether* [1985] at Arequipa, Peru, *Yagi and Dyson* [1985a] at Beveridge, Australia, *Okano and Kim* [1986a; 1986b] at Albany[16], and *Sridharan et al.* [1991] at Mt. Abu[17].

Observations of both neutral wind velocities and temperatures were made by *Hays and Atreya* [1971] at Ann Arbor, *Hernandez and Roble* [1976a; 1976c] at Fritz Peak Observatory, *Hernandez* [1977; 1978] at Fritz Peak, Colorado, *Jacka et al.* [1979] at Mt. Torrens, Australia[18], *Okano and Kim* [1979] at Albany, New York, *Sipler and Biondi* [1979] at Laurel Ridge, Pennsylvania, *Burnside et al.* [1981] at Arecibo, Puerto Rico, *Hernandez et al.* [1982b] at Fritz Peak, Colorado, *Sipler et al.* [1982] at Laurel Ridge, Pennsylvania, *Hernandez and Roble* [1984b] at Fritz

[7]Skibotn, Northern Scandinavia : 68°N, 21°E, geographic

[8]Kiruna, Sweden : 67.0°N, 21.5°E, geographic

[9]Longyearbyen, Svalbard : 78.2°N, 15.6°E, geographic

[10]Halley, Antarctica : 75.5°S, 26.8°W, geographic

[11]Beveridge, Australia : 37.47°S, 145.36°E, geographic

[12]Arequipa, Peru : 16.5°S, 71.5°W, geographic

[13]Thule, Greenland : Λ=86

[14]Zvenigorod Observatory, USSR : 56°N, 37°E, geographic

[15]Laurel Ridge, Pennsylvania : 40.16°N, 79.17°W, geographic

[16]Albany, New York : 42.68°N, 73.82°W, geographic

[17]Mt. Abu, India : 24.6°N, 72.72°E, geographic

[18]Mt. Torrens, Australia : 35°S, 139°E, geographic

Peak, Colorado, *Biondi and Sipler* [1985] at CLFBI rocket launching base near Natal, Brazil[19], *Okano et al.* [1985] at Albany, New York, *Yagi and Dyson* [1985c; 1985d] at Beveridge, Australia, *Sica et al.* [1986a; 1986b] at College, Alaska[20] *Murty and Kim* [1988a; 1988b] at Albany, New York, *Sica et al.* [1989] at College, Alaska, *Hernandez et al.* [1990] at Amundsen-Scott Base, Antarctica[21], *Kim et al.* [1990], at Albany, New York, and *Sica* [1991] at College, Alaska.

Simultaneous observations of an incoherent scatter radar or a medium-frequency radar and a Fabry-Perot interferometer were made by *Cogger et al.* [1970] at Arecibo, *Hernandez et al.* [1975] using data of Jicamarca Radio Observatory, *Hays et at.* [1979] at Ester Dome Observatory near College, Alaska using the Chatanika incoherent scatter radar data, *Rees et al.* [1984b] at Kiruna using the EISCAT data, *Wickwar et al.* [1984] at Ester Dome Observatory using the Chatanika radar data, *Winser et al.* [1988] at Kiruna using the EISCAT radar data, *Larsen et al.* [1989] at Søndre Stømfjord, Greenland, *Lloyd et al.* [1990] at Saskatoon[22] using medium-frequency radar data, *Basu et al.* [1991] at Arequipa, Peru, using a 50-MHz radar at Jicamarca[23], *Hagan and Sipler* [1991] using the Millstone Hill[24] radar data, *Manson et al.* [1991] at Saskatoon using a medium frequency radar data, *Rees et al.* [1991] at Kiruna using the EISCAT radar data, and *Sipler et al.* [1991] using the data at Millstone Hill.

Recently, new kinds of data sets from the upgraded UCL Doppler Imaging System (DIS), a field-widened imaging Fabry-Perot interferometer, which was developed specifically for the detection of small scale thermospheric wind velocity structures with correspondingly short time scales were presented by *Rees et al.* [1984a], *Batten et al.* [1988], *Batten and Rees* [1990], *Rees et al.* [1990], *Aruliah et al.* [1991], and *Aruliah et al.* [1991]. These data confirmed that

[19]Natal, Brazil : 5.9°S, 35.2°W, geographic

[20]College, Alaska : 64.8°N, 147.8°W, geographic

[21]Amundsen-Scott Base, Antarctica : geographic south pole

[22]Saskatoon, Canada : 52°N, 107°W, geographic

[23]Jicamarca, Peru : 11.95°S, 76.86°W, geographic

[24]Millstone Hill, Massachusetts : 42.6°N, 71.5°W, geographic

the thermosphere is very dynamic, with a high degree of variability even at small spatial (50 km) and temporal (10 min) scales. Typical eddy scale sizes of 100–300 km were observed near midnight.

1.2.2 Space-borne observations on the F-region thermosphere

The successful NASA Dynamics Explorer-2 (DE-2) mission (August 1981 – February 1983) provided comprehensive data sets including direct, global-scale measurements of temperatures, composition and vector wind fields as well as ionospheric parameters relevant to the important thermospheric neutral-plasma processes. Henceforth, space-borne observations and studies on low-latitude, mid-latitude and high-latitude thermosphere are described, mainly relating to the DE-2 observational results.

The low-latitude thermosphere is primarily controlled by the in-situ processes of solar heating, tidal forcing and large-scale ion-neutral interactions. The last process includes dynamo interactions, ion drag and dynamical coupling processes due to ions being forced into regions with various recombination rates. In addition to these important processes, energy and momentum can be transferred to low latitudes by waves and meridional winds, particularly during large geomagnetic storms. Comprehensive global-scale measurements of low latitude thermospheric winds and temperatures have been realized recently from the DE-2 spacecraft. *Wharton et al.* [1984] analyzed zonal wind data from the Wind and Temperature Spectrometer (WATS) instrument on board the DE-2 to obtain average profiles of the equatorial zonal wind for different levels of solar flux and altitude intervals. The theoretical results indicate that the mean circulation at low latitudes is driven primarily by the momentum sources associated with the diurnal tide. *Herrero et al.* [1983] used temperature data from AE-E in a tidal analysis to investigate the latitudinal, diurnal, and seasonal variations in the thermospheric temperature

at two latitudes; −17.5° and +17.5°. The nighttime temperature enhancements were found to occur earlier in the night in summer than in winter.

The mid-latitude thermosphere at F-region altitudes is controlled by the solar EUV and UV heating during geomagnetic quiet times. During disturbed periods, however, it is strongly perturbed by the high-latitude heat sources since convection electric fields penetrate to lower latitudes, and gravity waves, launched by high-latitude processes, propagate through the mid-latitude region. In general, the quiet-time, mid-latitude thermosphere, driven by the EUV/UV heat source, exhibits antisunward motion of $\sim$ 50–100 m/s during the day and $\sim$ 100–200 m/s during the night. The faster speed during the night is due to the reduction in ion drag in the lower ionosphere. Thermospheric temperatures are dependent on solar activity, season and geomagnetic activity, and display a semi-annual variation. *Oliver et al.* [1984] combined the incoherent scatter radar data at Millstone Hill with other radar facilities and from the HILAT satellite to provide maps of the latitudinal and temporal structure of the exospheric temperature. *Miller et al.* [1984] have used data from the DE-2 to investigate the storm time response of the midlatitude thermospheric composition. They found that the $[O]/[N_2]$ ratio is directly correlated with the topside electron density and the exospheric temperature, as a result of the enhanced heating.

The high-latitude thermosphere is intrinsically more variable than at lower latitudes, because of the strong and extremely variable auroral forcing processes. The high-latitude cellular convection of ions, driven by electric fields mapped down from the magnetosphere, provides an important momentum source via ion drag to the neutral gas, which set up vortices in the neutral circulation that are superimposed on the solar EUV/UV driven antisunward transpolar flow. The high and variable ionospheric ion convection velocities also provide an important energy source to the high-latitude thermosphere through Joule heating. These sources of energy and momentum are further modulated by variations in auroral particle precipitation that serve to modify ion-neutral collision frequencies and to increase the ionospheric conductivity in the auroral region.

The Fabry-Perot interferometer, FPI [*Hays et al.*, 1981], and the Wind and Temperature Spectrometer, WATS [*Spencer et al.*, 1981], on the DE-2 have provided neutral wind measurements along the track of the polar orbiting spacecraft that can be combined to yield the vector wind at F-Region altitudes [*Killeen et al.*, 1982]. Vector neutral wind data from seven orbital passes over the northern and southern polar regions were plotted in geomagnetic polar coordinates by *Killeen et al.* [1982] to illustrate the twin-cell neutral circulation pattern in the neutral gas which is driven by ion-drag. *Killeen et al.* [1983] then performed a statistical analysis of 58 orbital passes over the southern hemisphere polar cap to illustrate the basic diurnal coherence of variations in the neutral wind pattern as seen from the polar orbit. *Spencer et al.* [1982] presented WATS zonal and vertical wind measurements in the polar region that demonstrated the existence of strong vertical winds, having velocities of 100–150 m/s at times, which correlated with strong zonal winds. *Hays et al.* [1984] conducted a comprehensive study of the average high-latitude thermospheric wind and temperature field for both summer and winter hemispheres as observed from DE-2 during October and November/December, 1981. *Rees, D.* [1983] compared data from seven polar passes of DE-2 with the predictions of the UCL-TGCM. *Roble et al.* [1983] performed a similar study using the NCAR-TGCM and were able to obtain good qualitative agreement with the DE-2 data. A series of model runs was used to improve the agreement between the measured winds, temperatures and composition of both summer and winter polar regions. A conclusion of this study was that, to obtain agreement with the observations, it is necessary to incorporate realistic electron, soft cusp and polar cap precipitation sources [*Fuller-Rowell et al.*, 1984]. Geomagnetic forcing of the high-latitude thermosphere can not be explained purely by polar convective electric fields, while the thermal and ionizing properties of the polar and auroral electron sources are crucial components of the total geomagnetic input. *Killeen et al.* [1984] compared results of DE-2 vector wind measurements over Svalbard, Norway with simultaneous measurements from the ground using the Ulster College Fabry-Perot interferometer. The agreement for common volume measurements was good, indicating that both ground-based and space-borne techniques were measuring the same basic flow properties

satisfactorily. *McCormac et al.* [1985] used both single orbit data as well as averaged data from many DE-2 orbits to illustrate the By dependence of the neutral circulation pattern. *Killeen et al.* [1986] collated all available F-region neutral wind data from seven ground-based Fabry-Perot interferometers as well as from seven hundred orbital passes of DE-2 taken during December 1981. Since weather conditions at the ground stations limited the number of occasions when simultaneous measurements were possible, they adopted the technique of averaging all available data by UT to describe the mean diurnal behavior of the thermospheric wind pattern in the northern hemisphere. They proceeded to assemble 12 thermospheric 'climatological' maps for every two hours of UT during a 'mean day' in December, 1981. The averaged data sets were compared with output from the NCAR-TGCM for a diurnally-reproducible model run and very good agreement was obtained. This study demonstrated that multiple station measurements could be used to provide consistent descriptions of the global-scale thermospheric circulation and furthermore, that the mean diurnal wind pattern in the northern hemisphere could be well modeled using appropriate inputs for the mean thermospheric forcings. *Killeen et al.* [1988] compared DE-2 neutral wind and ion drift observations with simultaneous measurements of the global-sale auroral distribution observed by the Spin-scan Auroral Imager (SAI) on the high-altitude DE-1 spacecraft. The result clearly shows the direct morphological relationship between the neutral circulation in the polar region and the auroral oval.

1.2.3 Observations on the lower thermosphere

The dynamics of the lower thermosphere (from the mesopause to $\sim$ 200 km) are relatively unexplored by comparison with the upper thermosphere. The physical processes that control the lower thermosphere are also quite different in character from those that control the atmosphere at F-region heights and most of the sources of energy to the thermosphere peak in this region, including the variable high-latitude auroral heat source (see Figure 1.2). Furthermore, the lower thermosphere is under the strong influence of semidiurnal tides and gravity waves

which propagate upwards from below [*Dickinson et al.*, 1981; *Roble and Emery*, 1983; *Groves and Forbes*, 1985]. The balance of forces which control the circulation of the neutral air in the upper thermosphere, such as ion drag, becomes less dominant in the lower thermosphere while the Coriolis and pressure gradient forces become the major competing terms. The semidiurnal tides are dissipated in the lower thermosphere by molecular thermal conduction, viscosity and ion drag, as their influence is progressively attenuated at the higher levels. Unlike the upper thermosphere, the lower thermosphere neutral winds appear to blow from the low-temperature to the high-temperature regions because of the phase properties of the tides. Typical wind speeds are 100 m/s. Due to the dominant effect of the tides, there is little evidence of temperature and wind effects from high latitude auroral forcing. Any picture of the lower thermosphere which neglects upward propagating tides is therefore somewhat incomplete.

Below ~120 km, neutral winds have been measured on a long-term basis by meteor radars [e.g., *Clarke*, 1983; *Dartt et al.*, 1983] and by the partial reflection technique [e.g., *Manson and Meek*, 1984]. *Dartt et al.* [1983] have collected data on winds in the 90–100 km region, from meteor radar observations over nearly 30 years in order to investigate the seasonal and solar cycle wind variations. These observations have shown strong tidal control of the winds at the base of the thermosphere.

Fabry-Perot interferometer measurements of thermospheric E-region neutral temperature at an altitude range of ~95–140 km began with the early upper limit estimates of the line width of the atomic oxygen OI 557.7 nm line emission of the night sky by *Babcock* [1923]. Photoelectric measurement of the neutral temperature in E-region is reported under normal and disturbed ionospheric conditions [*Hernandez and Turtle*, 1965; *Hilliard and Shepherd*, 1966].

Similar measurements at mid-latitude observatory at Laurel Ridge, Pennsylvania from twilight and nighttime airglow were made to determine the neutral temperatures by *Feibelman et al.* [1972]. Their result shows that measured temperatures of E-region ranged from 200–220 K on quiet night to 500–600 K during geomagnetic storms. The same kind of observation using

the annular slit system was made at mid-latitude observatory at Zao Observatory, Japan[25] by *Kamiyama et al.* [1975], showing a variation of E-region temperature of 200–250 K. *Hernandez* [1976] compiled as much as 5200 measurements (spread over 63 lunar periods and 193 days) of E-region neutral temperatures from 1965 to 1973 to show the existence of solar and magnetic activity modulation of atmospheric temperature at the height of emission of the OI 557.7 nm line as well as the presence of significant variations with 5-, 2.5-, 1-, and 0.5-year periods. He then deduced an empirical formula which provides E-region neutral temperatures by using $F10.7$ cm flux, AP value and day numbers from observations. *Cogger et al.* [1985] used 75 nights of measurements of the Doppler shift of the OI 557.7 nm emission at Calgary, Canada to investigate the E-region neutral wind. They found the wind field to be very variable, with speeds approaching 200 m/s on geomagnetically disturbed days. Stable wind patterns over several hundred kilometers were seen at times, while at other times, there was little coherence with the measured winds.

Twilight and daytime observations of the sodium layer using a Fabry-Perot spectrometer at Mt. Torrens, Australia over two years and also at Mawson Station, Antarctica[26] for the austral summer in 1989 are reported by *Greet and Jacka* [1989a; 1989b]. A winter mean temperature of 199 K and a summer mean temperature of 150 K are determined from the Mt. Torrens data, while the Antarctic data showed 157±7 K for January 1989. This technique is shown to be promising for the study of the dynamics of the 90 km region which is otherwise difficult to observe. Recently, the influence of geomagnetic activity on the lower thermosphere in the auroral zone was estimated by *Price and Jacka* [1991] using the vertical wind, temperature and emission intensity data taken at Mawson Station, Antarctica. Their results show that large upward winds of approximately 30 m/s at altitudes less than 100 km appear to be a direct response of the neutral atmosphere to intense auroral events. They suggested that the

[25]Zao Observatory, Japan : 38.09°N, 140.56°W, geographic

[26]Mawson Station, Antarctica : 67.6°S, 62.9°E, geographic

observed upwelling is a result of particle heating at heights below the principal emission height. Then they concluded that the upwelling is produced due to a combination of Joule and particle heating effects.

1.3 Purpose of This Thesis

In order to understand the coupling mechanisms between the ionosphere and the thermosphere in which a variety of dynamical and chemical processes take place in response to the variations of energy input, we have developed a new optical instrument: the Fabry-Perot Doppler Imaging System (FPDIS). The FPDIS measures the Doppler shifts and widths of aurora and/or airglow emission lines of OI 557.7 nm and OI 630.0 nm over a wide field of view (165°) to obtain two-dimensional distributions of winds and temperatures. It is possible to study several interesting subjects concerning the thermospheric dynamics and chemistry, e.g., 1) dynamical coupling processes between the ionosphere and the thermosphere, 2) dynamical response of the polar thermosphere to the energy input from the magnetosphere through the Joule heating and particle heating of auroral particles and 3) wave phenomena in the lower thermosphere.

The second point is focused especially on the present study and observations of thermospheric neutral temperatures and winds which have been carried out at Syowa Station, Antarctica[27] for a period of one austral winter in 1990 in cooperation with National Institute of Polar Research. Since Syowa Station is located just under the auroral zone (invariant latitude is $-66.12°$ and L = 6.10), the site is quite suitable to make observations to study relationships between thermospheric dynamics and auroral activity. Another advantage of Syowa Station is that several kinds of observations on upper atmospheric physics were being carried out simultaneously with the FPDIS observations. These include the following observations.

1. Optical auroral observations using an all-sky camera, a SIT camera, a monochro-

[27]Syowa Station, Antarctica : 69.00°S, 39.58°E, geographic

matic (557.7 nm and 630.0 nm) CCD camera, and several (scanning, zenith, north 30 degrees, south 30 degrees, and multi-color) photometers.

2. Observations of the geomagnetic field using ground-based fluxgate and induction magnetometers as well as a proton magnetometer. These instruments acquire magnetic data with a time resolution of 1 sec which can be used to estimate magnetic and auroral activity as well as to calculate K-indices at Syowa Station.

3. Ionospheric observations using an ionosonde, an auroral radar, a conventional riometer a multi-beam riometer, and a VHF Doppler radar. These observations provide valuable information on the ionosphere.

4. In-situ and photometric observations on several physical parameters related to auroral phenomena by the Akebono (EXOS-D) satellite which was launched on February 22, 1989. The data of the Akebono satellite are acquired at Syowa Station using a multi-purpose antenna system with a diameter of 11 m.

The data from simultaneous observations by these instruments and satellites can be utilized to understand the physical processes which take place in the thermosphere.

The main purpose of this study is to understand the neutral thermospheric response in both F- and E-regions to the auroral activity. The response of the thermosphere to the auroral breakup event is examined in detail for several auroral breakup events. The characteristics of this study are its high temporal and spatial resolution of the thermospheric data analysis. The maximum time resolution is as high as 1 data in every 3 min while the typical spatial resolution is about 100 km at the F-region altitude and about 50 km at the E-region altitude.

The reasoning behind this thesis is as follows.

The principle and analytical description of a Fabry-Perot interferometer is given in Chapter 2, along with descriptions of the FPDIS and of several peripheral instruments used in this study. In Chapter 3, the method of data processing of image data acquired by the FPDIS is described and

the necessity for several kinds of data calibration is pointed out with the actual methods of these procedures given. In Chapter 4, installation of the FPDIS at Syowa Station will be explained and observational results of the FPDIS over Syowa Station will be given. In Chapter 5, the results of Chapter 4 will be discussed by comparing them with the thermospheric parameters derived from the empirical model and with previous works, along with the discussion on the possible errors of the results in this study. Then the response of the thermosphere to the auroral energy input from the magnetosphere will be studied. Finally, the conclusions of this study will be presented in Chapter 6.

Chapter 2

INSTRUMENTATION

2.1 Introduction to a Fabry-Perot Interferometer

A Fabry-Perot interferometer is a very useful spectroscopic tool owing to its inherent property. The Fabry-Perot interferometer is distinguished from other spectroscopic devices in that it is the most luminous instrument available for a given resolving power. This feature indicates the reason for its continued and wide use in high-resolution spectroscopy of extremely faint radiation sources, such as airglow, auroras and astronomical sources.

2.1.1 Basic principle of the Fabry-Perot interferometer

The basic principle of the Fabry-Perot interferometer is outlined as follows. A typical configuration of the device consists of a collimator lens, a Fabry-Perot etalon and a focusing lens as shown in Figure 2.1. A Fabry-Perot etalon (we call it 'a F-P etalon' or simply 'an etalon', hereafter) is a combination of two optical flats which are placed in parallel with a separation

The analytical formulation of the Fabry-Perot interferometer presented in this chapter is after [*Hernandez*, 1986] and [*Kudo*, 1985].

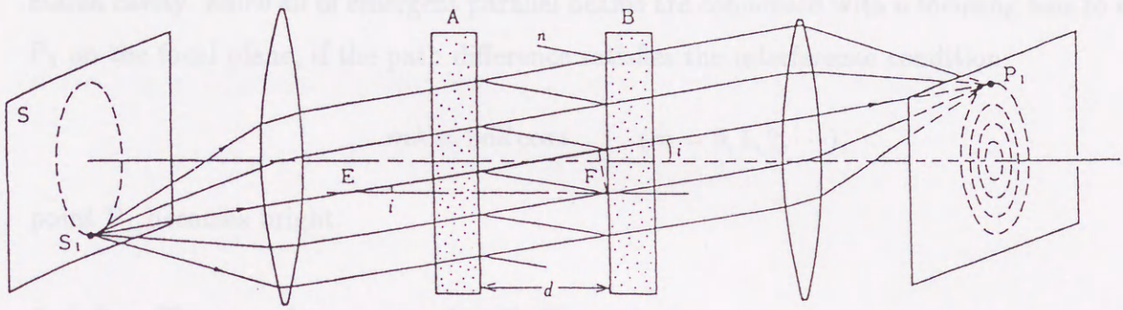

Figure 2.1: Schematic diagram showing the optical paths of the Fabry-Perot interferometer. The optical path difference of adjoining rays is given by the relation $\mathrm{EF} = 2nd\cos i$.

of d. Their facing (inner) surfaces are coated with semi-transparent material of high refractive index, such as dielectric multi-layered films. The coating is made in a way such that the surfaces partly reflect and partly transmit light. When a monochromatic beam with wavelength λ is incident upon the etalon at an angle i to the normal as indicated in Figure 2.1, the beam incident on plate B is divided into two beams, one reflected and the other transmitted, and the division process of the beam remaining in the cavity between the plates (etalon cavity) continues as shown in the figure. The optical path difference between two adjoining beams emerging from plate B is $2nd\cos i$. Here, n denotes the refractive index of the medium in the etalon cavity. Since all of emergent parallel beams are condensed with a focusing lens to a point P_1 on the focal plane, if the path difference satisfies the interference condition

$$m\lambda = 2nd\cos i \qquad (m = 0, 1, 2, \cdots), \tag{2.1}$$

point P_1 becomes bright.

2.1.2 Transmittance of a F-P etalon

The transmittance of a F-P etalon is calculated as follows. As is indicated in Figure 2.1, we assume that a monochromatic beam is incident upon the F-P etalon at an angle i. We also assume that the reflectivity of surfaces A and B are identical. We denote the total amplitude transmittance of light for the reflective coating as $t = \sqrt{T}e^{i\psi}$, the amplitude reflectivity of light which comes from the inner side of the plates as $r = \sqrt{R}e^{i\phi}$, the optical spacing of the F-P etalon as d, the refractive index of the medium in the F-P etalon cavity as n, and the amplitude of incident light as 1. We then get the amplitude of light τ which comes out of the F-P etalon as

$$\tau = t^2 + t^2r^2e^{-i2\Delta} + t^2r^4e^{-i4\Delta} + \cdots = \frac{t^2}{1 - r^2e^{-i2\Delta}} \tag{2.2}$$

where 2Δ denotes the phase difference of the optical path difference ($2nd\cos i$) of adjoining beams coming out of the F-P etalon as

$$2\Delta = \frac{2\pi}{\lambda} 2nd\cos i. \tag{2.3}$$

Now the transmittance of light $T_F = \tau\tau^*$ is given by

$$T_F = \frac{T^2}{(1-R)^2 + 4R\sin^2\delta} \tag{2.4}$$

where

$$\delta = \frac{\pi}{\lambda} 2nd\cos i - \phi = \Delta - \phi. \tag{2.5}$$

According to Equation 2.3, the transmittance has a maxima at $\delta = m\pi$, i.e.,

$$\left(m + \frac{\phi}{\pi}\right)\lambda = 2nd\cos i \qquad (m = 0, 1, 2, \cdots) \tag{2.6}$$

and a minima at $\delta = (2m+1)\pi/2$, i.e.,

$$\left(m + \frac{1}{2} + \frac{\phi}{\pi}\right)\lambda = 2nd\cos i \qquad (m = 0, 1, 2, \cdots). \tag{2.7}$$

Equation 2.6 is called 'the wavelength formula of an interferometer'. When the area of the light source is sufficiently large, interference fringes produced in the focal plane are ring shaped according to Equation 2.6. These fringes are called 'the Haidinger's fringes'. Although phase shift due to reflection is less than π, the order m becomes very large since the optical spacing d is much larger than the wavelength of light.

2.1.3 Angular dispersion of a F-P etalon

Although a F-P etalon is usually used as an interference spectrometer, it also intrinsically has an angular dispersion. When the extended light source emits the light of wavelength λ and that of $\lambda+\Delta\lambda$, and if we assume that the refractive index of the medium in the etalon cavity is nearly independent on the wavelength and further that m and d are constants, then a bright fringe for

wavelength λ and that for $\lambda + \Delta\lambda$ are produced at different position on the focal plane. In this case, as can be seen from Equation 2.6, the rays which cause the different fringes are emitted from different positions on the light source. This means that the wavelength of emitted light λ is dispersed corresponding to a change of the incident angle i, in other words, to a channel of emitting position on the light source. This dispersion is fundamentally different from that of other dispersion elements, such as prisms or gratings; in these elements, the wavelength is dispersed even when the incident angle does not change. The angular dispersion D_I for a F-P etalon, which is derived by differentiating Equation 2.6 by wavelength λ, is defined as

$$D_I = \left|\frac{di}{d\lambda}\right| = \frac{m + \frac{\phi}{\pi}}{2nd \sin i} = \frac{1}{\lambda \tan i} = \frac{\sigma}{\tan i} \tag{2.8}$$

where σ denotes the wavenumber $[cm^{-1}]$. It is obvious from this equation that the angular dispersion D_I of the F-P etalon has following characteristics.

1. D_I is unrelated to the optical spacing d.
2. D_I becomes larger as the incident angle i becomes smaller and thus D_I is the largest at the center of the fringe.
3. D_I becomes larger as the wavelength becomes smaller.

2.1.4 Order separation of interference fringes of a F-P etalon

When λ, n, d are constants, we get the following equation by differentiating Equation 2.6 by the order number m,

$$\left|\frac{di}{dm}\right| = \frac{1}{(m + \frac{\phi}{\pi}) \tan i}. \tag{2.9}$$

This equation means that the alteration of incident angle necessary for changing one order of m number becomes larger as the order number m becomes smaller and also the incident angle i becomes smaller, while it is independent of the wavelength λ of the incident beam. The order number of the fringe on the focal plane is the biggest for the innermost fringe. Since the order

number m is usually very large, the effect of a change in one order of m number is almost negligible in Equation 2.9 and only the change in incident angle i is important. Accordingly, the separation between adjoining interference fringes of the F-P etalon is the largest at the center of the fringe, and it becomes shorter for outer fringes. The configuration of interference fringes of the F-P etalon is shown in Figure 2.2.

2.1.5 Free spectral range of a F-P etalon

A region where the order numbers of fringes do not overlap is called 'free spectral range' $\Delta\lambda_R(\Delta\sigma_R)$. When an interference fringe of m-th order is formed at an incident angle of i with an interference condition of $(m + \frac{\phi}{\pi})\lambda = 2nd\cos i$, the interference fringe of $m + 1$-th order is formed at an incident angle of $i - \Delta i$, i.e.,

$$\left(m + 1 + \frac{\phi}{\pi}\right)\lambda = 2nd\cos(i - \Delta i). \tag{2.10}$$

Assuming that a beam with the wavelength of $\lambda + \Delta\lambda$ forms an interference fringe of m-th order at the same incident angle of $i - \Delta i$, the following equation is satisfied by

$$\left(m + \frac{\phi}{\pi}\right)(\lambda + \Delta\lambda) = 2nd\cos(i - \Delta i). \tag{2.11}$$

Equation 2.11 is another expression of Equation 2.8 giving the angular dispersion of a F-P etalon, that is, Equation 2.11 gives the difference of incident angle Δi_R between neighboring fringes with one order number difference. Therefore, the free spectral range $\Delta\lambda_R$ is given by

$$\Delta\lambda_R = \frac{d\lambda}{di}\Delta i_R = \frac{2nd\sin i}{m + \phi/\pi} \cdot \frac{\lambda}{2nd\sin i} = \frac{\lambda}{m + \phi/\pi} = \frac{\lambda^2}{2nd\cos i} \simeq \frac{\lambda^2}{2nd}\ [\mathrm{cm}]. \tag{2.12}$$

It is apparent from this equation that the free spectral range becomes larger as the wavelength λ becomes longer and the value of nd becomes smaller. Equation 2.12 is represented by using the wavenumber as

$$\Delta\sigma_R = \frac{1}{2nd\cos i}\ [\mathrm{cm}^{-1}]. \tag{2.13}$$

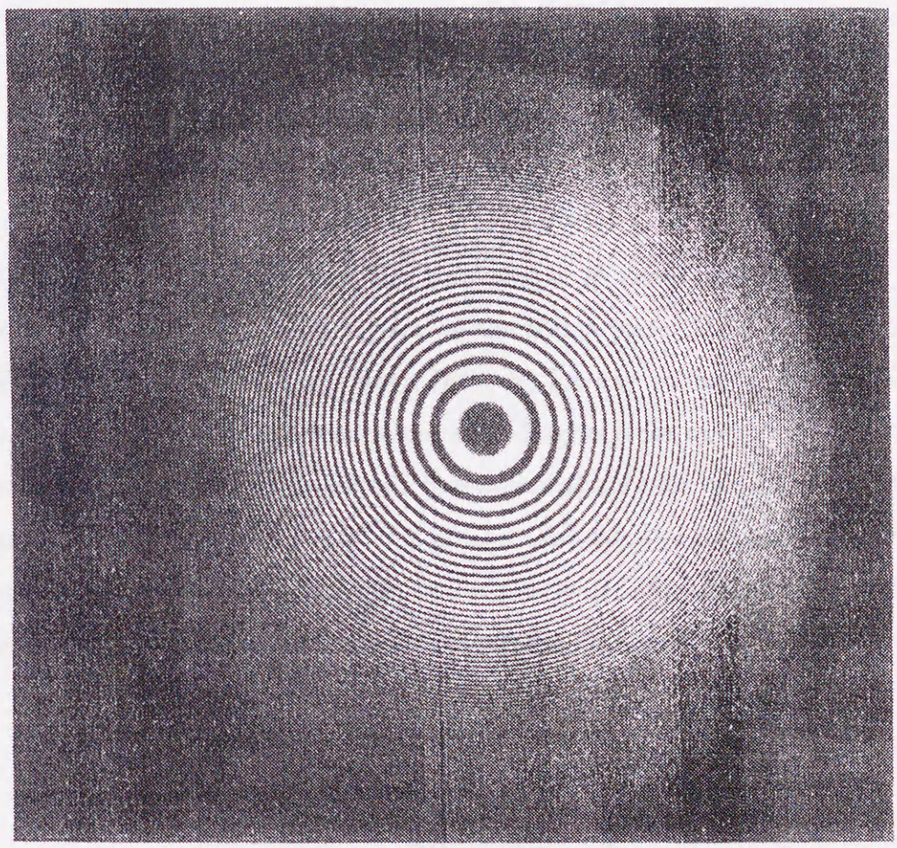

Figure 2.2: An example of interference fringes of a F-P etalon. These are fringes of a mercury discharge lamp source with a etalon of 1.5 cm spacer and a reflectivity of 0.85.

2.1.6 Theoretical resolving power of a F-P etalon

The transmittance of a F-P etalon T_F given by Equation 2.4 can be transformed to

$$T_F = B \cdot \frac{1}{1 + H \sin^2 \delta} \tag{2.14}$$

where

$$B \equiv \frac{T^2}{(1-R)^2} \tag{2.15}$$

$$H \equiv \frac{4R}{(1-R)^2}. \tag{2.16}$$

In most cases, B is almost constant and the value of H varies largely with R. Note that R is the reflectivity of light at the film surface on the etalon plate. From Equation 2.14, it is found that T_F has the same maximum value ($T_F = B$) for any values of R when $\delta = m\pi$ ($m = 0, \pm 1, \pm 2, \cdots$), while it has different values according to R for other δ values. Figure 2.3 shows transmittance curves of a F-P etalon as a function of phase δ for various values of the reflectivity R as parameters. When the value of R is greater than 0.9, the transmittance of the F-P etalon has a very sharp peak around $\delta = m\pi$, and is nearly zero for other values of δ. Now we look into the shape of transmittance curves of interference fringes. Putting

$$\delta = m\pi \pm \Delta\delta \tag{2.17}$$

and

$$\frac{4R}{(1-R)^2} = H = \frac{4}{\Gamma^2} \tag{2.18}$$

from Equation 2.14, we get

$$T_F = B \cdot \frac{(\Gamma/2)^2}{(\Delta\delta)^2 + (\Gamma/2)^2}. \tag{2.19}$$

The shape of Equation 2.19 is similar to the Lorentzian profile with the full-width-at-half-maximum (FWHM) given by

$$\Gamma = \frac{2}{\sqrt{H}} = \frac{1-R}{\sqrt{R}}. \tag{2.20}$$

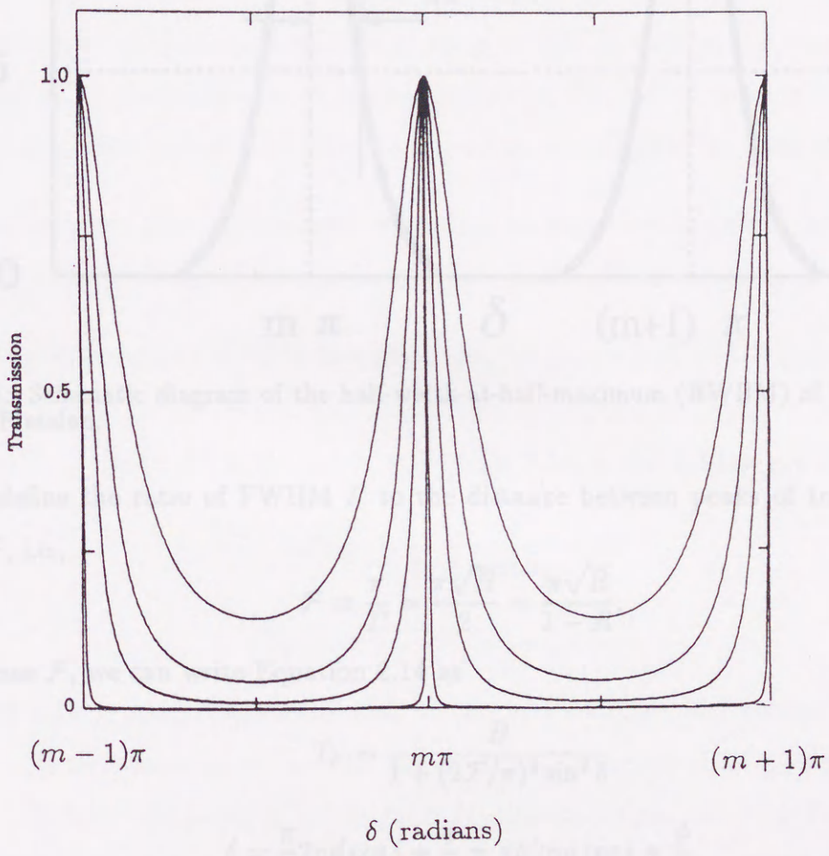

Figure 2.3: Transmittance of a Fabry-Perot etalon as a function of the phase retardation of the beams and for various values of reflectivity R. The values of R are changes as 0.98, 0.81, 0.65, and 0.45. The narrowest and widest profiles correspond to R =0.98 and 0.45, respectively.

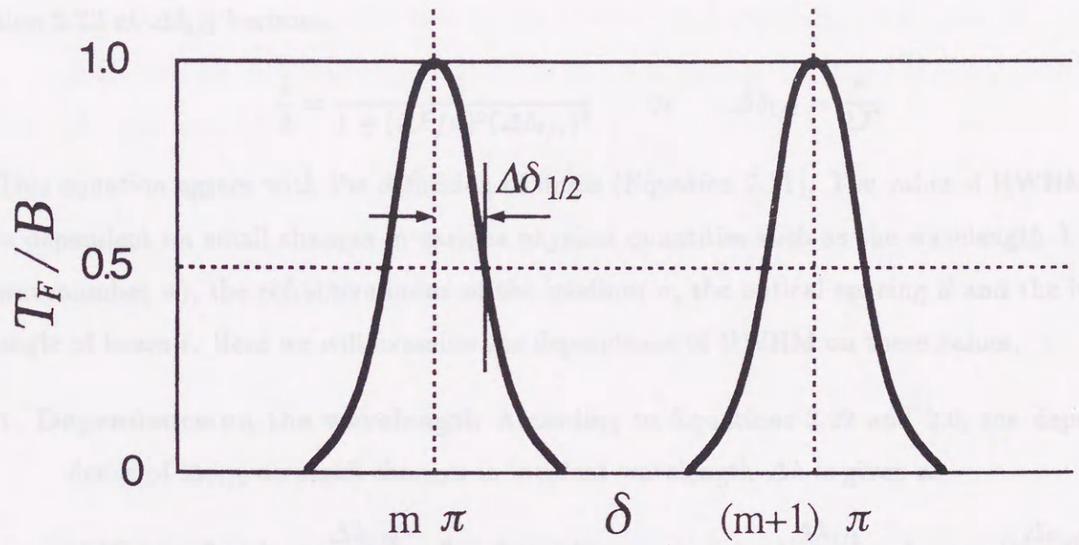

Figure 2.4: Schematic diagram of the half-width-at-half-maximum (HWHM) of transmittance T_F of a F-P etalon.

Now, we define the ratio of FWHM Γ to the distance between peaks of transmittance π as 'finesse' $\mathcal{F}$, i.e.,

$$\mathcal{F} \equiv \frac{\pi}{\Gamma} = \frac{\pi\sqrt{H}}{2} = \frac{\pi\sqrt{R}}{1-R}. \tag{2.21}$$

Using finesse $\mathcal{F}$, we can write Equation 2.14 as

$$T_F = \frac{B}{1 + (2\mathcal{F}/\pi)^2 \sin^2\delta} \tag{2.22}$$

$$\delta = \frac{\pi}{\lambda} 2nd\cos i + \frac{\phi}{\pi} = \pi\sigma 2nd\cos i + \frac{\phi}{\pi}. \tag{2.23}$$

Now, we estimate the resolving power of a F-P etalon using Equations 2.22 and Equations 2.23. As is shown in Figure 2.4, the transmittance T_F becomes half of the peak value when

$$\delta = m\pi \pm \Delta\delta_{1/2} \tag{2.24}$$

where $\Delta\delta_{1/2}$ is the half-width-at-half-maximum (HWHM). Since $\Delta\delta_{1/2}$ is very small, Equa-

tion 2.22 at $\Delta\delta_{1/2}$ becomes

$$\frac{1}{2} = \frac{1}{1+(2\mathcal{F}/\pi)^2(\Delta\delta_{1/2})^2} \quad \text{or} \quad \Delta\delta_{1/2} = \frac{\pi}{2\mathcal{F}}. \tag{2.25}$$

This equation agrees with the definition of finess (Equation 2.21). The value of HWHM $\Delta\delta_{1/2}$ is dependent on small changes in various physical quantities such as the wavelength λ (or the wavenumber σ), the refractive index of the medium n, the optical spacing d and the incident angle of beam i. Here we will examine the dependence of HWHM on these values.

1. **Dependence on the wavelength** According to Equations 2.23 and 2.6, the dependence of $\Delta\delta_{1/2}$ on small changes in incident wavelength $\Delta\lambda$ is given as

$$|\Delta\delta_{1/2}| = 2\pi nd\cos i\frac{\Delta\lambda_{1/2}}{\lambda^2} = 2\pi nd\cos i\Delta\sigma_{1/2} = (m\pi+\phi)\frac{\Delta\lambda_{1/2}}{\lambda} = (m\pi+\phi)\frac{\Delta\sigma_{1/2}}{\sigma}. \tag{2.26}$$

Using Equations 2.25, 2.21, and 2.26, FWHM $2\Delta\sigma_{1/2}$ and $2\Delta\lambda_{1/2}$ are represented as

$$2\Delta\sigma_{1/2} = \frac{1-R}{2\pi nd\sqrt{R}\cos i}[\mathrm{cm}^{-1}] \tag{2.27}$$

$$\frac{2\Delta\lambda_{1/2}}{\lambda} = \frac{2\Delta\sigma_{1/2}}{\sigma} = \frac{1-R}{\pi\sqrt{R}(m+\phi/\pi)} \tag{2.28}$$

where $2\Delta\lambda_{1/2}$ and $2\Delta\sigma_{1/2}$ are the full widths in wavelength and wavenumber, respectively. If we substitute $c\sigma$ for σ in this equation, the width of frequency is obtained. Now, the resolving power of a F-P etalon $\mathcal{R}_F$ can be defined using the Taylor criterion (see Appendix A.1 about the Taylor criterion) by $\lambda/2\Delta\lambda_{1/2}$ or $\sigma/2\Delta\sigma_{1/2}$, since the interference fringe of the wavelength λ or the wavenumber σ can be distinguished from that of the wavelength $\lambda+2\Delta\lambda_{1/2}$ or the wavenumber $\sigma-2\Delta\sigma_{1/2}$. The theoretical resolving power of a F-P etalon for non-monochromatic beams $\mathcal{R}_F$ is therefore given by

$$\mathcal{R}_F = \frac{\lambda}{2\Delta\lambda_{1/2}} = \frac{\sigma}{2\Delta\sigma_{1/2}} = \left(m+\frac{\phi}{\pi}\right)\mathcal{F} = \left(m+\frac{\phi}{\pi}\right)\frac{\pi\sqrt{R}}{1-R}. \tag{2.29}$$

2. **Dependence on the refractive index of the medium** Using Equations 2.23 and 2.25, we get the dependence of $\Delta\delta_{1/2}$ on small changes in the refractive index of the medium Δn as

$$\Delta\delta_{1/2} = 2\pi\sigma(\Delta n_{1/2})d\cos i = \frac{\pi}{2\mathcal{F}}. \tag{2.30}$$

The change in σ according to the change in n can be derived from the wavelength formula (Equation 2.6) as

$$n\Delta\sigma + \sigma\Delta n = 0. \tag{2.31}$$

By substituting the above equation into Equation 2.30 and using Equation 2.6, we get Equation 2.29.

3. **Dependence on the optical spacing** From Equations 2.23 and 2.25, the dependence of $\Delta\delta_{1/2}$ on small change in optical spacing Δd is represented as

$$\Delta\delta_{1/2} = 2\pi\sigma n\Delta d_{1/2}\cos i = \frac{\pi}{2\mathcal{F}}. \tag{2.32}$$

From the wavelength formula (Equation 2.6),

$$d\Delta\sigma + \sigma\Delta d = 0. \tag{2.33}$$

Thus the resolving power formula (Equation 2.29) is obtained.

4. **Dependence on the incident angle of a beam** Using Equations 2.23 and 2.25, the dependence of $\Delta\delta_{1/2}$ on a small change in incident angle of a beam Δi is given as

$$\left|\Delta\delta_{1/2}\right| = 2\pi\sigma nd\sin i\Delta i_{1/2} = \frac{\pi}{2\mathcal{F}}. \tag{2.34}$$

Since the relation

$$\Delta\sigma\cos i - \sigma\sin i\Delta i = 0 \tag{2.35}$$

is obtained from the wavelength formula, we can get the resolving power formula (Equation 2.29) again. Further, another expression for the resolving power is derived.

The angular deviation from the peak position of the fringe corresponding to $\Delta\sigma$ is $\delta(\cos i)$, we get

$$\left|2nd\delta(\cos i)\right| = \frac{\Delta\sigma}{\sigma^2}\left(m + \frac{\phi}{\pi}\right) \tag{2.36}$$

from the wavelength formula. Using Equation 36 and the wavelength formula, we get

$$\left|\frac{\sigma}{\Delta\sigma}\right| = \frac{\cos i}{\delta(\cos i)} = \mathcal{R}'_F. \tag{2.37}$$

2.2 The Fabry-Perot Doppler Imaging System (FPDIS)

The Fabry-Perot Doppler Imaging System (FPDIS) is a newly developed two-dimensional Fabry-Perot interferometer system with an extremely high spectroscopic resolution and a high temporal and spatial resolution. Compared with conventional Fabry-Perot interferometers, the FPDIS has the following characteristics;

- The FPDIS employs an all-sky fish-eye objective lens ahead of the instrument to match the field of view of the interference fringes on the focal plane of the photon detector to a wide field of view (FOV = 165°) in the sky.
- The FPDIS employs a very sensitive two-dimensional photon detector which consists of a Photon Imaging Head (PIH) and a Charge Coupled Device (CCD) detector.

The use of a high-sensitivity photon detector and a wide angle objective lens enables us to study spatial distributions of Doppler temperatures and line-of-sight wind velocities. These quantities are derived from Doppler fringe data of airglow or aurora emissions. In this study, we have derived the spatial distributions of auroral zone thermospheric neutral temperatures and wind velocities from FPDIS observation data of the two atomic oxygen emission lines OI 630.0 nm and OI 557.7 nm.

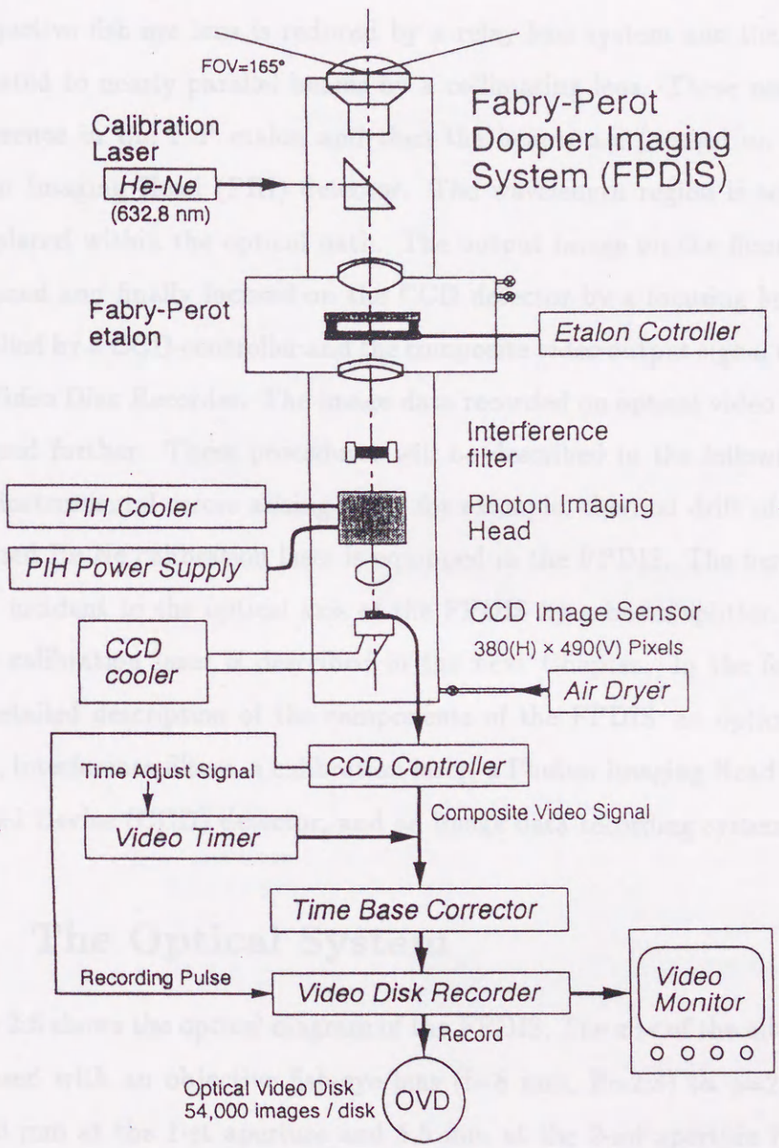

Figure 2.5: System diagram of the Fabry-Perot Doppler Imaging System (FPDIS)

The system diagram of the FPDIS is shown in Figure 2.5. The all-sky image focused by an objective fish-eye lens is reduced by a relay lens system and then the incident beams are collimated to nearly parallel beams by a collimating lens. These nearly parallel beams cause interference in the F-P etalon and then the beams are focused on the photocathode of the Photon Imaging Head (PIH) detector. The wavelength region is selected by an interference filter placed within the optical path. The output image on the fluorescent screen of the PIH is reduced and finally focused on the CCD detector by a focusing lens. The CCD detector is controlled by a CCD-controller and the composite video output signal is monitored and recorded by a Video Disk Recorder. The image data recorded on optical video disks are reproduced and processed further. These procedures will be described in the following Chapter. In order to check instrumental errors arising from, for example, thermal drift of the etalon parameters, a stabilized He-Ne calibration laser is equipped in the FPDIS. The beam of the laser is diffused and is incident to the optical axis of the FPDIS by a beam splitter. The practical operation of the calibration laser is described in the next Chapter. In the following sections, we will give detailed description of the components of the FPDIS: an optical system, a Fabry-Perot etalon, interference filters, a calibration laser, a Photon Imaging Head (PIH) detector, a Charge Coupled Device (CCD) detector, and an image data recording system.

2.3 The Optical System

Figure 2.6 shows the optical diagram of the FPDIS. The size of the all-sky image (FOV = 165°) is focused with an objective fish-eye lens (f=8 mm, F=2.8) to ϕ=24.0 mm then reduced to ϕ=12.0 mm at the 1-st aperture and 5.5 mm at the 2-nd aperture by using an aspheric lens (f=35.7 mm, F=0.89) and a relay lens (f=50 mm, F=1.2), respectively. The beams are then collimated by a collimating lens (f=240 mm, F=2.0) so that the beams incident upon the Fabry-Perot etalon are nearly parallel light with a maximum incident angle of 0.66 degrees. Since this foreoptics covers the sky with an approximately 165° full angle, individual sectors of

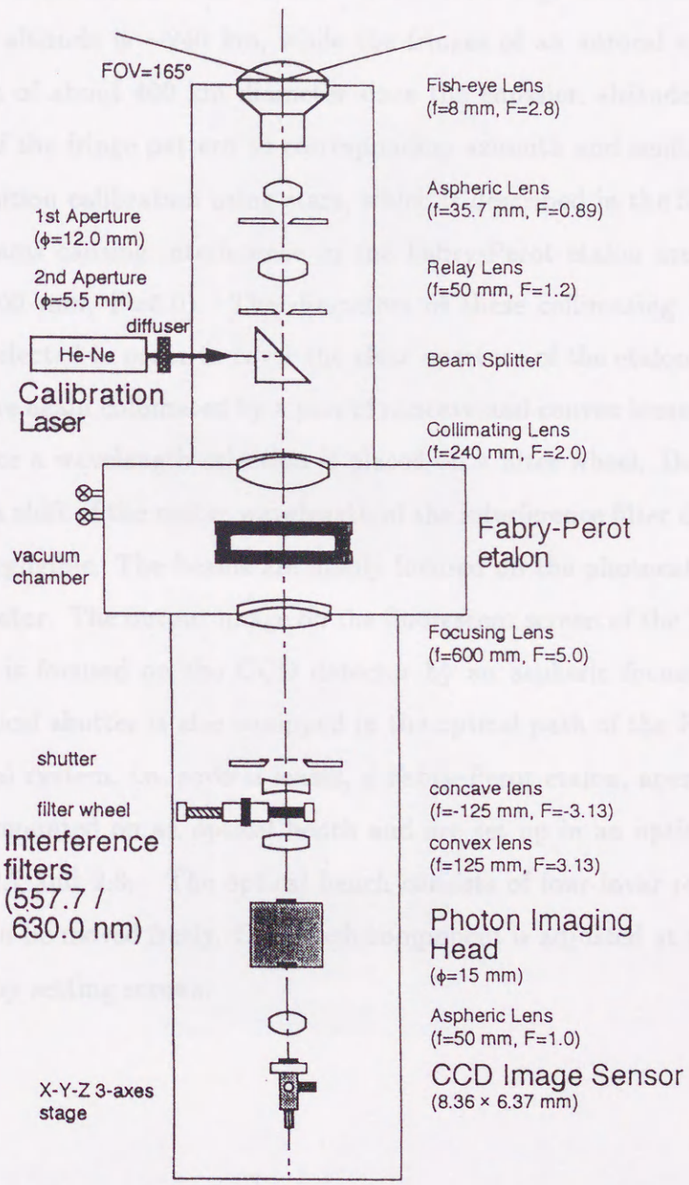

Figure 2.6: Optical diagram of the Fabry-Perot Doppler Imaging System (FPDIS)

individual Fabry-Perot fringes correspond to widely separated regions of the sky. For example, the fringes of an auroral emission of OI 630.0 nm cover a region of about 900 km diameter since the emission altitude is ~240 km, while the fringes of an auroral emission of OI 557.7 nm covers a region of about 400 km diameter since the emission altitude is ~ 110 km. The correct matching of the fringe pattern to corresponding azimuth and zenith angles is made by performing the position calibration using stars, which is described in the following Chapter.

The incident beams causing interference in the Fabry-Perot etalon are then focused by a focusing lens (f=600 mm, F=5.0). The diameters of these collimating and focusing lenses (D=120 mm) are selected in order to cover the clear aperture of the etalon (D=116 mm). The converged beams are again collimated by a pair of concave and convex lenses, between which an interference filter for a wavelength selection is placed on a filter wheel. Due to the conversion to parallel beams, a shift of the center wavelength of the interference filter due to a difference in incident angle is negligible. The beams are finally focused on the photocathode of the Photon Imaging Head detector. The output image on the fluorescent screen of the PIH is reduced with a ratio of 2:1 and is focused on the CCD detector by an aspheric focusing lens (f=50 mm, F=1.0). A mechanical shutter is also equipped in the optical path of the FPDIS.

The entire optical system, i.e. several lenses, a Fabry-Perot etalon, apertures, a filter wheel and detectors are mounted on an optical bench and are set up in an optical container box as shown in Figures 2.7 and 2.8. The optical bench consists of four invar rods along which the mounting plates can be moved freely. Once each component is adjusted at the correct position, it is firmly locked by setting screws.

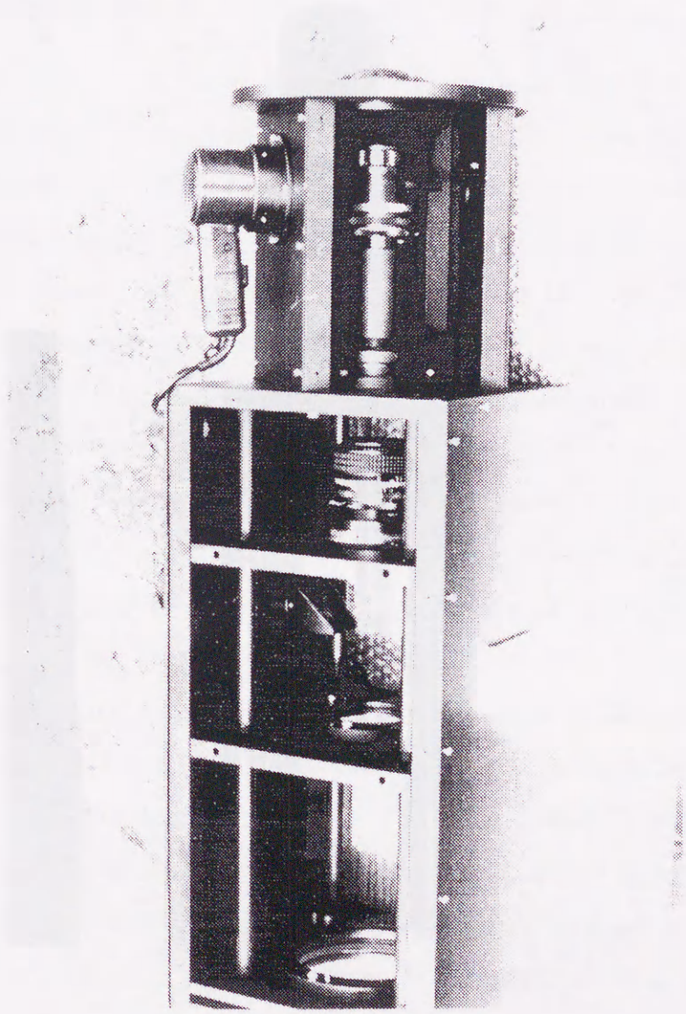

Figure 2.7: Front end of the FPDIS. Several lenses including an objective fish-eye lens, a relay lens, and a collimating lens are seen. A blower is equipped at the top of the optical container box in order to prevent the surface of the objective lens from dewing by blowing hot air.

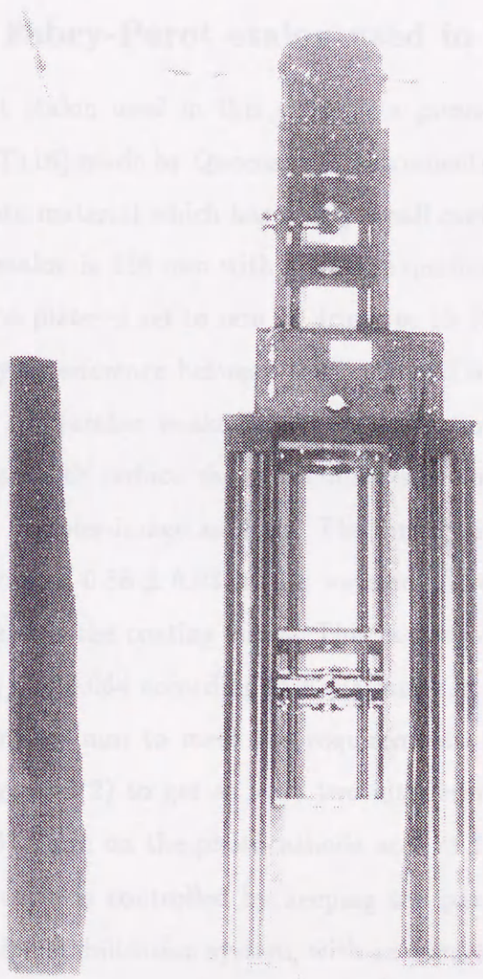

Figure 2.8: View of the whole optical system of the FPDIS. The etalon chamber shown at the center of the apparatus is put between two optical container boxes (the side panels of the boxes are removed in order to show the inside components). The two-dimensional photon detector removed from the optical system in this picture.

2.4 The Fabry-Perot Etalon

2.4.1 The Fabry-Perot etalon used in this study

The Fabry-Perot etalon used in this study is a piezo-electrically tuned and servo-stabilized etalon (model ET116) made by Queensgate Instruments Ltd. It uses standard fused silica (FS) as the etalon plate material which has a very small coefficient of thermal expansion. The clear aperture of the etalon is 116 mm with a surface quality of $\lambda/100$ at $\lambda = 546.1$nm. The wedge angle of the etalon plates is set to zero ± 1 fringe or 10-15 arc minutes. This offsets the parasitic fringes caused by interference between the inner and outer surfaces of the etalon plates. The parasitic fringes are further weakened by anti-reflection coating on the outer surfaces of the plates. These methods reduce the ghost images of the Fabry-Perot fringes to a level being negligible in the Doppler-image analysis. The inner surface of the etalon is coated as required to set a reflectivity of 0.88 ± 0.03 in the wavelength region between the 557.7 nm and 630.0 nm. Figure 2.9 shows the coating curve. This corresponds to the theoretical finesse $\mathcal{F}$ of 24.6 and HWHM $\Delta\delta_{1/2}$ of 0.064 according to Equations 2.21 and 2.25. The nominal optical spacing is selected to be 12.0 mm to meet the requirements: 1) to get the maximum resolution of interference fringe and 2) to get at least two interference fringes, at both the wavelengths of 630.0 nm and 557.7 nm on the photocathode area of the Photon Imaging Head. The optical spacing of the etalon is controlled by keeping the parallelism of the etalon plates using the piezo electric etalon stabilization system, with an accuracy of as much as 3 μm (nominal). This system is described in detail in the next section. A view of the etalon is shown in Figure 2.10.

2.4.2 The etalon stabilization system used in this study

The spacing and parallelism of the ET116 etalon are controlled by the CS100 stabilization system made by Queensgate Instruments Ltd. The CS100 is a three-channel balanced bridge system which uses capacitance micrometers included in the etalon to detect error signals when

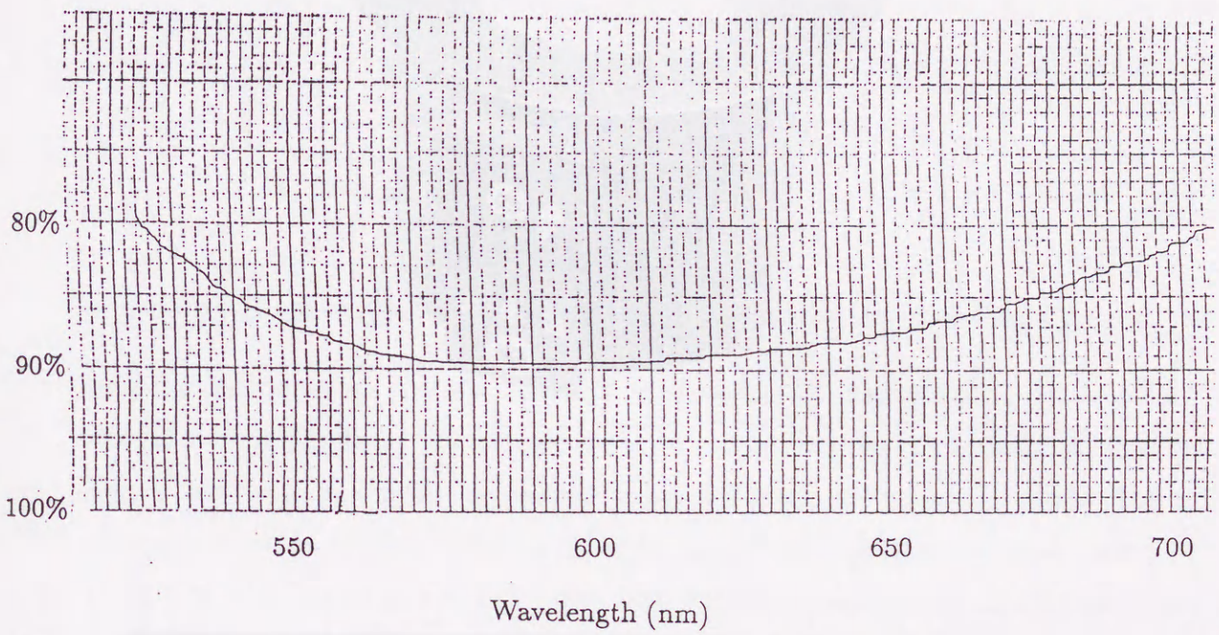

Figure 2.9: Dependence of the reflectivity of the etalon coating used in this study on the wavelength of incident light. The abscissa represents the wavelength, while the ordinate represents the reflectivity.

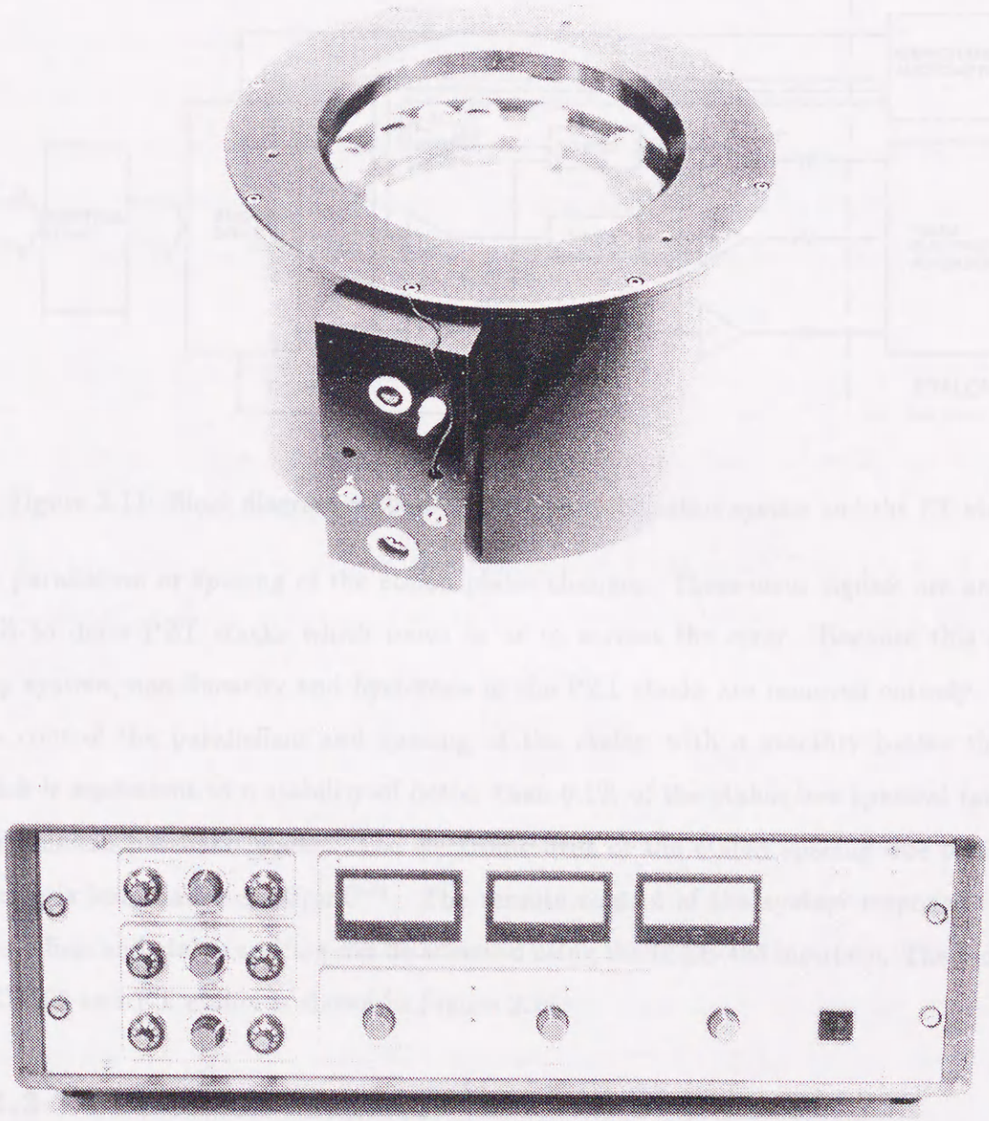

Figure 2.10: View of the servo-stabilized Fabry-Perot etalon and its controller. Several connectors which are seen on the side of the etalon container are used for cables connecting the servo-control circuit to keep the two etalon surfaces parallel.

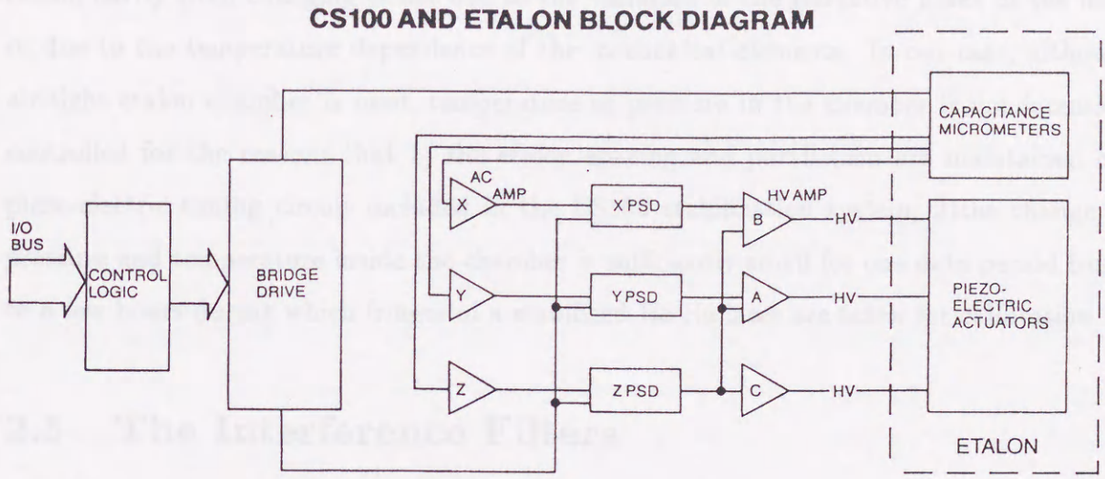

Figure 2.11: Block diagram of the CS100 etalon stabilization system and the ET etalon

the parallelism or spacing of the etalon plates changes. These error signals are amplified and used to drive PZT stacks which move so as to correct the error. Because this is a closed-loop system, non-linearity and hysteresis in the PZT stacks are removed entirely. The CS100 can control the parallelism and spacing of the etalon with a stability better than $\lambda/2000$, which is equivalent to a stability of better than 0.1% of the etalon free spectral range and the transmission passband width. The electronic drift of the etalon spacing due to temperature change is less than $0 \pm 50\,\mathrm{pm}C^{-1}$. The remote control of the system response time, etalon parallelism and etalon spacing can be achieved using the IEEE-488 interface. The block diagram of CS100 and ET etalon is shown in Figure 2.11.

2.4.3 The etalon chamber

In the cases that fixed spacers are used, an etalon is usually mounted within a temperature- and pressure-controlled chamber in order to scan the optical spacing nd. In such cases, temperature and pressure in the etalon chamber must be controlled to prevent the optical path within the

etalon cavity from changing either due to the variation of the refractive index of the medium or due to the temperature dependence of the mechanical elements. In our case, although an air-tight etalon chamber is used, temperature or pressure in the chamber is not intentionally controlled for the reasons that 1) the etalon spacing and parallelism are maintained by the piezo-electric tuning circuit included in the CS100 stabilization system; 2)the change of air pressure and temperature inside the chamber is sufficiently small for one data period from one to a few hours during which fringes of a stabilized He-Ne laser are taken for calibration.

2.5 The Interference Filters

Two interference filters are used to select the wavelength of auroral emissions. In general, the center wavelength of the interference filter depends on the incident angle. Consider a beam incident upon an interference filter at an angle i to the normal. When the incident angle i is small, the shift of the center wavelength of the interference filter, $\Delta\lambda$, as a function of i, is expressed as

$$\Delta\lambda = \lambda \cdot \frac{i^2}{2n^2} \tag{2.38}$$

where n denotes the refractive index of the medium in the cavity of the interference filter. In our case, since beams are collimated by a concave lens as shown in Figure 2.6, the maximum incident angle is identical to that of the Fabry-Perot etalon, i.e., 0.66 degrees. Using the values of the maximum incident angle (0.66 degrees) and the refractive index of the interference filter (1.45), we get the shift of the center wavelength of transmittance $\Delta\lambda = 0.020$nm for $\lambda = 630.0$nm and 0.018 nm for $\lambda = 557.7$nm. The shift is so small compared with the width of transmission of the filters that we can neglect the effect of the shift.

The nominal center wavelength and full-width-at-half-maximum (FWHM) of the filters used in this study are given in Table 2.1. Although the No. 1 filter passes an unwanted OH(9, 3)$P_1(3)$ emission line at 630.68 nm [*Armstrong*, 1969], the contribution of this line is considered to be

Table 2.1: Transmission characteristics of the interference filters used in the FPDIS.

Filter No.	Center Wavelength	FWHM
1	630.0 nm	3.15 nm
2	557.7 nm	2.23 nm

almost negligible since it is much weaker than the OI 630.0 nm emission line at high latitudes.

A filter wheel, on which the filters are mounted, is equipped to quickly insert the necessary filter into the optical path of the FPDIS. The filter wheel is controlled by electric signals from a control box.

2.6 The Photon Imaging Head (PIH) Detector

Since the spectral brightness of the object of observation is extremely low, the FPDIS uses a combination of two types of imaging detectors, i.e., a Photon Imaging Head and CCD detectors. Firstly, the characteristics of the Photon Imaging Head detector are given below.

The Photon Imaging Head (PIH) is a highly sensitive two-dimensional photon detector (type C2166-01) made by Hamamatsu Photonics Corporation. The application of a two-dimensional photon detector enables us not only to acquire two-dimensional images, but also to get a light gathering capability much better than a photomultiplier. A schematic diagram of the PIH is shown in Figure 2.12. A photocathode, a pair of electric lenses, micro-channel plates (MCPs) and a fluorescent screen are assembled in a vacuum tube. Photoelectrons which are emitted by the photoelectric effect of an incident photon at the photocathode are focused on the MCP by a pair of electric lenses. These electrons are multiplied by more than several thousand times on the MCP. Since the PIH includes two-stage MCPs, the electron amplification factor represents a single square of the MCP. Then electrons bombard the fluorescent screen, yielding

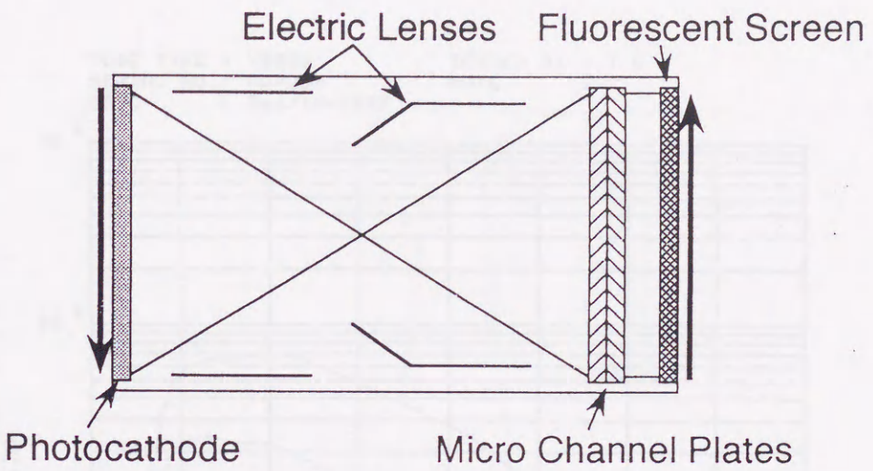

Figure 2.12: A diagram of the Photon Imaging Head (PIH) detector

an optical image. The photocathode and the fluorescent screen of the PIH are made of multi-alkali and P-20, respectively, while the windows are made up of borosilicate glass and fiber-plate, respectively. The effective diameters of the photocathode and the fluorescent screen are both 15 mm. The radiant sensitivity and the quantum efficiency of the photocathode is shown in Figure 2.13 while the relative emission intensity and the relative afterglow intensity of the fluorescent screen (P-20) are shown in Figures 2.14 and 2.15, respectively. The ratio of photo-electrons emitted from the photocathode to incident photons is defined as the quantum efficiency (QE), which is written, in this case, by using the radiant sensitivity χ_k and the wavelength λ [nm] as

$$QE = \frac{\chi_k}{\lambda} \times 1240 \times 100 \ [\%]. \tag{2.39}$$

It is clear from Figure 2.13 that the radiation sensitivity of the PIH is about 25 mA/W for $\lambda = 630.0$ nm and is about 40 mA/W for $\lambda = 557.7$ nm. The dark count of the multi-alkali photocathode is greatly reduced by using an electronic cooler which utilizes the Peltier effect. When the photocathode is cooled down to $-15°C$, the maximum dark count becomes

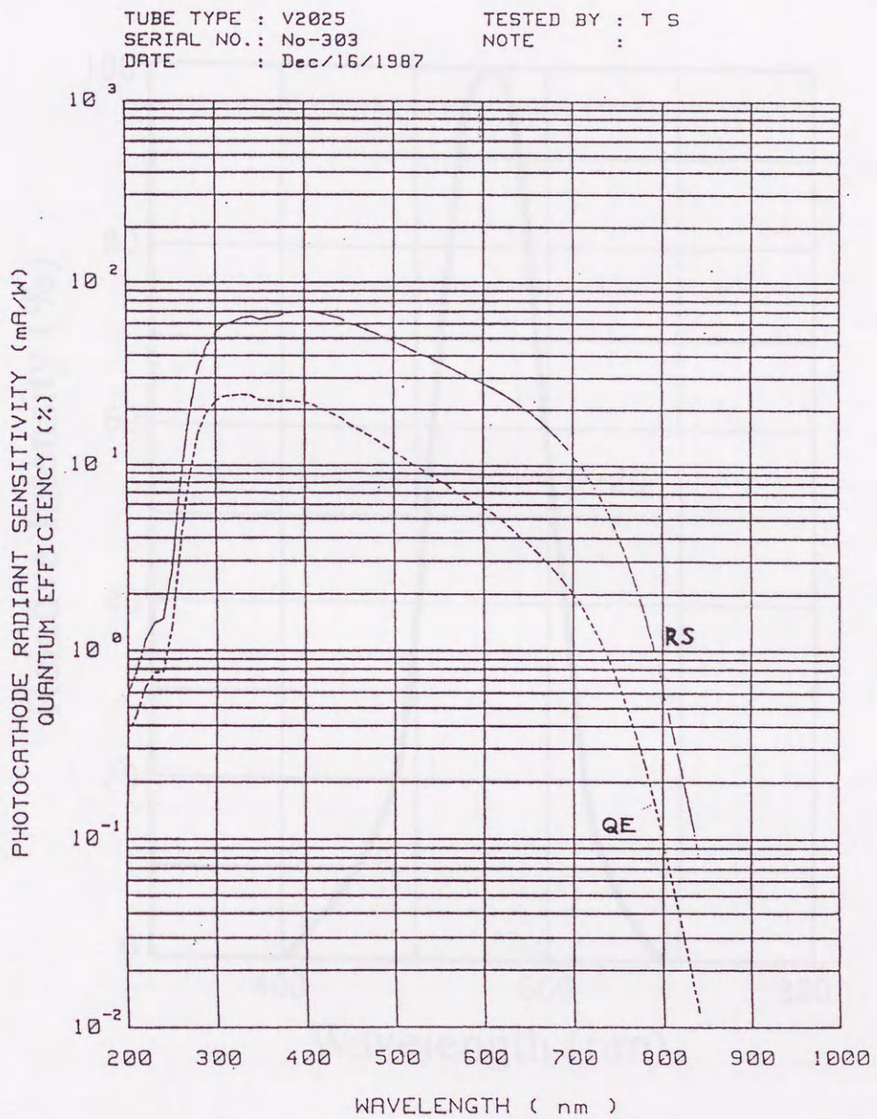

Figure 2.13: Radiant sensitivity and quantum efficiency of the photocathode as a function of wavelength. The photocathode used for the PIH is sensitive between 250 and 850 nm.

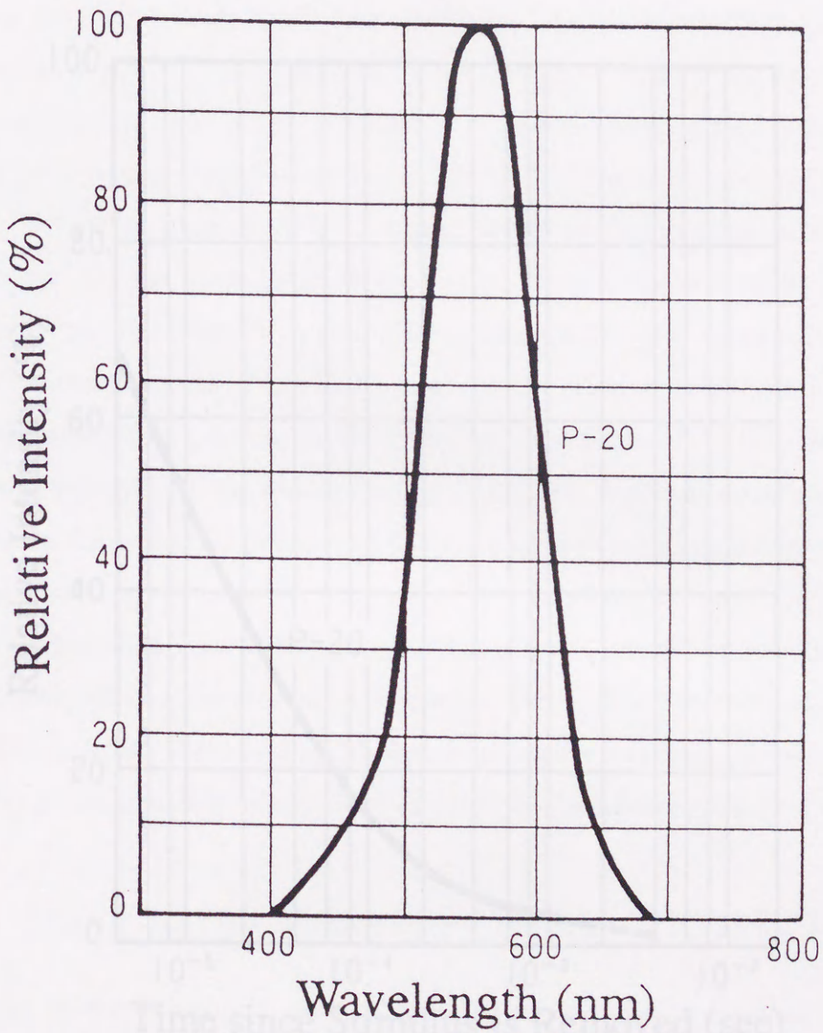

Figure 2.14: Relative emission intensity of the fluorescent screen (P-20) as a function of wavelength. It has an emission peak near 560 nm.

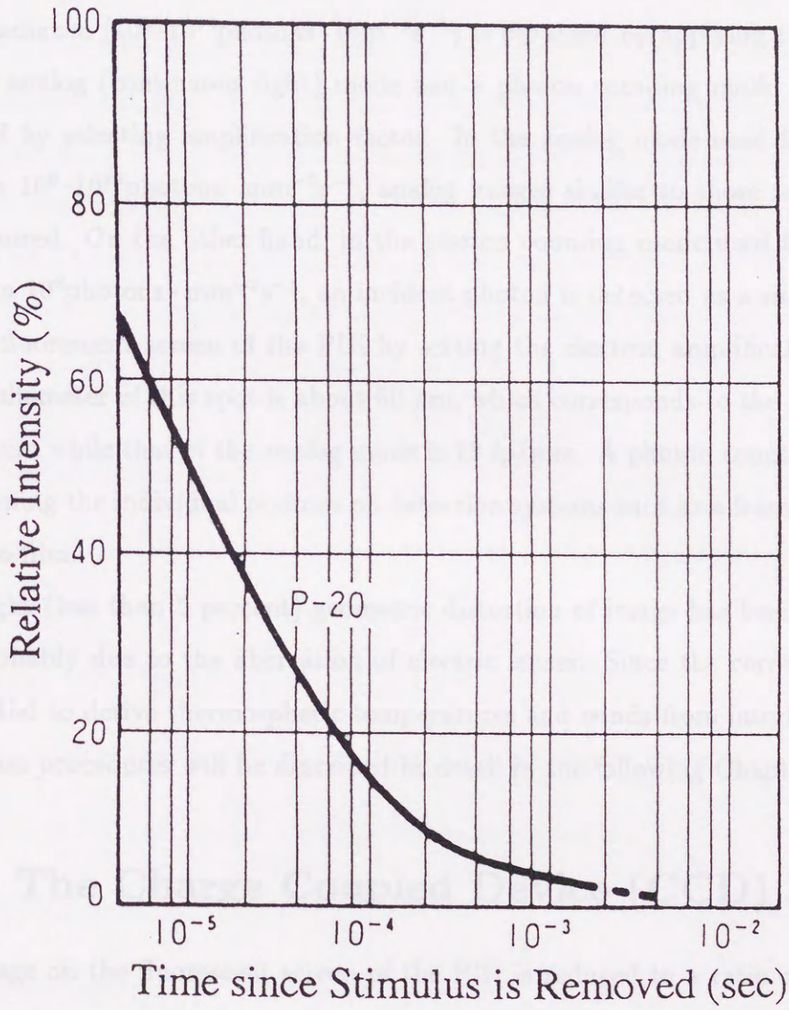

Figure 2.15: Relative afterglow intensity of the fluorescent screen (P-20) as a function of time after removing stimulation. The fluorescence disappears quickly with a time scale of milliseconds.

0.5 counts $\cdot$ $mm^{-2}sec^{-1}$.

The electron amplification factor of the PIH can be controlled from 100 to 1,000,000 by changing the high voltage applied to the MCPs. An extremely wide dynamic range of surface irradiance (10^0–10^{10}photons $\cdot$ $mm^{-2}s^{-1}$) is obtained by applying two modes of operation, i.e., an analog (continuous light) mode and a photon counting mode which are continuously changed by selecting amplification factor. In the analog mode used for the irradiance range between 10^6–10^{10}photons $\cdot$ $mm^{-2}s^{-1}$, analog images similar to those taken by a SIT detector are acquired. On the other hand, in the photon counting mode used for the irradiance range less than 10^6photons $\cdot$ $mm^{-2}s^{-1}$, an incident photon is detected as a single photon spot on the output fluorescent screen of the PIH by setting the electron amplification factor to 10^6. The typical diameter of this spot is about 60 μm, which corresponds to the resolution of 15 *l*p(line-pairs)/mm while that of the analog mode is 18 *l*p/mm. A photon counting image is then taken by summing the individual photons on detection systems such as a frame memory, a CCD chip, or photo-film.

A slight (less than 5 percent) geometric distortion of image has been detected on this PIH. It is probably due to the aberration of electric lenses. Since the correction of this distortion is essential to derive thermospheric temperatures and winds from interference image data, the correction procedures will be described in detail in the following Chapter.

2.7 The Charge Coupled Device (CCD) Detector

The image on the fluorescent screen of the PIH is reduced to a ratio of 2:1 and focused on a CCD image sensor located at the bottom of the FPDIS with an aspheric focusing lens as shown in Figure 2.6. Characteristics of the CCD detector used in this study are presented in this section.

2.7.1 The principle of a CCD image sensor

Since their invention [*Boyle and Smith*, 1970] and their experimental investigation [*Amelio et al.*, 1970], charge-Coupled Devices (CCD's), are characterized by low dispersive, analog delay lines with low-noise signal propagation and high dynamic range. When the CCD analog delay line is utilized in imaging, it is coupled with a monolithic photosensor, such as a semitransparent silicon-gate CCD or a diffused photodiode and a low-noise monolithic preamplifier to provide low light level imaging. Although the CCD was originally developed as a linear delay line or a linear photo-sensor, two-dimensional application of CCD's has many advantages in imaging technique over conventional image pickup tubes [*Shiraki*, 1980]. That is to say, the CCD's;

1. have no afterimages,
2. have little distortion in images,
3. attain high resolution with not so many pixels since each pixel is independent of each other,
4. attain high signal to noise (S/N) ratios,
5. are small in size and weight and consume low electric power,
6. have no burned images even by intense incident light,
7. are long-lived,
8. become inexpensive when mass-produced.

There are two schemes of charge transfer for two-dimensional CCD sensors, i.e., 1) a frame transfer scheme and 2) an interline transfer scheme. The characterization of these transfer schemes was presented by *Shiraki* [1980] and *White et al.* [1974].

2.7.2 The CCD image sensor used in this study

In this study, an interline transfer type two-dimensional CCD sensor (type TCD-203C) [*Ono et al.*, 1987; *Ono et al.*, 1988] with an effective imaging area of $8.36(H) \times 6.37(V)$mm composed of $380(H) \times 490(V)$ pixels is used to take image data. The pitch of each pixel is $22(H) \times 13(V)\mu$m with an aperture ratio of about 35% on the CCD image plane. The output of signals from individual pixels are successively achieved by a 2:1 interlace method, which makes it possible to get clear images without blur at high sensitivity. The exposure time of the CCD is changeable among 0.53, 1.06, 2.13, 4.26, and 8.58 sec. Although the virtual sensitivity of the CCD increases while adopting a long exposure time, the signal to noise (S/N) ratio decreases due to accumulation of dark current noise. Since the amount of dark current also depends on the temperature of the device, the CCD is equipped with a refrigerator which chills the device to about $-20°C$.

2.7.3 The CCD data processor used in this study

The signals from the CCD image sensor are fed into a CCD data processor. Description of the CCD data processor used in this study is given by *Ono et al.* [1987]. A block diagram of the CCD data processor is given in Figure 2.16. The output of image signals from the pixels of the CCD image sensor are successively synchronized with the CCD's clock signal. The image signals are fed to a dual sample and hold (S/H) amplifier and are converted to the digital data by an 8-bit high speed analog to digital (A/D) converter. The digitized signals from the A/D converter are stored in the frame memory with the capacity of 191.1 kbytes. The data in the frame memory are read out and fed to two processing systems. One makes a composite video signal and the other makes a PCM digital signal. The composite video signal is recorded in an optical video disk using a video disk recorder, while the PCM digital signal is recorded in a magnetic tape using a data recorder. In this study, we used the composite video data for the reasons that 1) it requires a huge amount of magnetic tapes to record the PCM signals (the

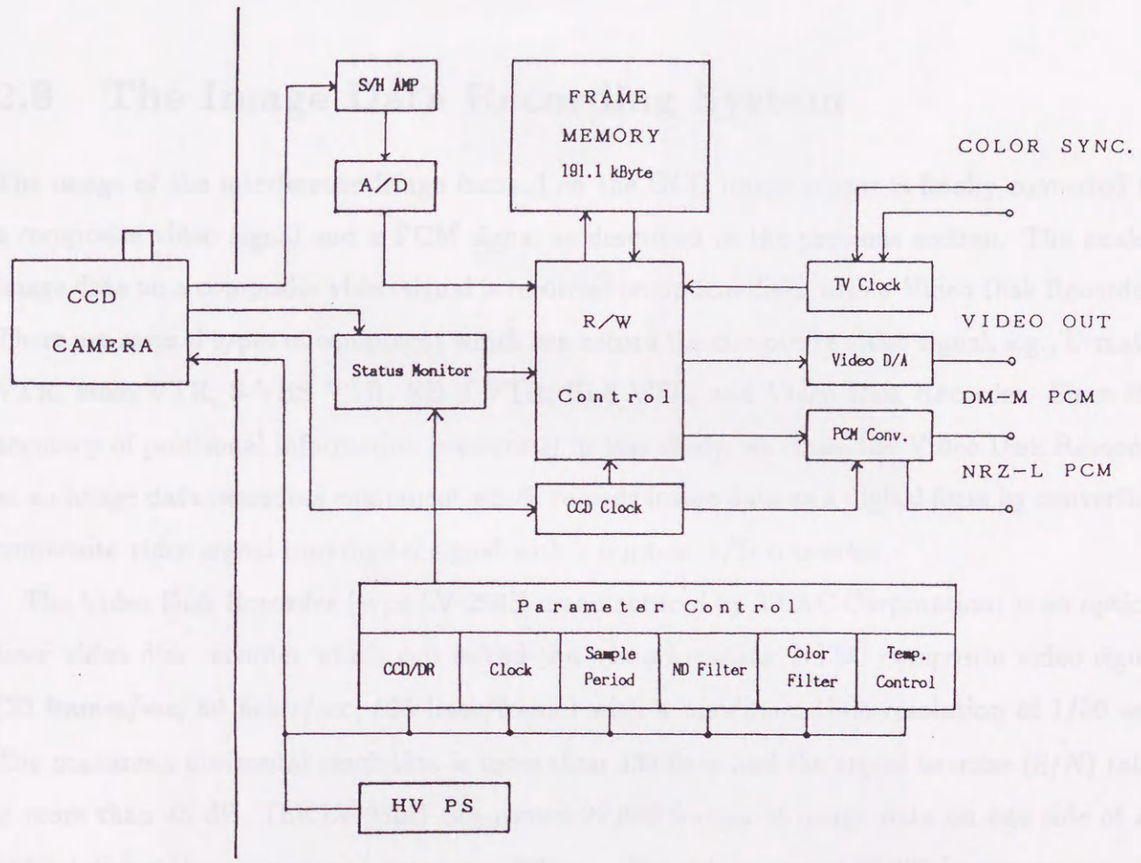

Figure 2.16: Block diagram of the CCD data processor. An output signal from the CCD image sensor is converted to digital values by an A/D converter, and the digital data are memorized in a frame memory. A composite video signal is then generated by the video D/A converter with a speed of 30 frames per second. A PCM signal is also generated by the PCM converter which reads out the memorized data synchronizing it with the CCD clock signal. The CCD data processor also controls the selection of the CCD clock rate and the sampling rate.

maximum data rate is 2.86 Mbit/sec) and it is unrealistic to record all of them; 2) although the composite video signal is an analog signal, the video disk recorder records it after digitizing it by a built-in A/D converter, and hence it is considered that the data quality is not reduced. A view of the CCD data processor along with its power supply is shown in Figure 2.17.

2.8 The Image Data Recording System

The image of the interference fringe focused on the CCD image sensor is finally converted to a composite video signal and a PCM signal as described in the previous section. The analog image data on a composite video signal is recorded on optical disks with a Video Disk Recorder. There are several types of equipment which can record the composite video signal, e.g., U-matic VTR, 8mm VTR, S-VHS VTR, ED-β VTR, Hi-8 VTR, and Video Disk Recorder. Since the accuracy of positional information is essential in this study, we chose the Video Disk Recorder as an image data recording equipment which records image data as a digital form by converting composite video signal into digital signal with a built-in A/D converter.

The Video Disk Recorder (type LV-250H manufactured by TEAC Corporation) is an optical laser video disk recorder which can record the monochromatic NTSC composite video signal (30 frames/sec, 60 fields/sec, 525 lines/frame) with a maximum time resolution of 1/30 sec. The maximum horizontal resolution is more than 550 lines and the signal to noise (S/N) ratio is more than 45 dB. The LV-250H can record 27,000 frames of image data on one side of an optical disk with a diameter of about $\phi = 300$mm. The still images of 27,000 frames correspond to 15 min of moving images. When image data are recorded every second, images for 450 min (7.5 hours) can be recorded on one side of an optical disk.

Since the LV-250H is equipped with an external recording control circuit, a recording signal pulse taken from the CCD data processor is given to the LV-250H in order to synchronize image frames. The recording pulse is adjusted to meet the requirement of the LV-250H (see Figure 2.18) by adding an single-shot multi vibrator circuit (Figure 2.19) to the CCD data

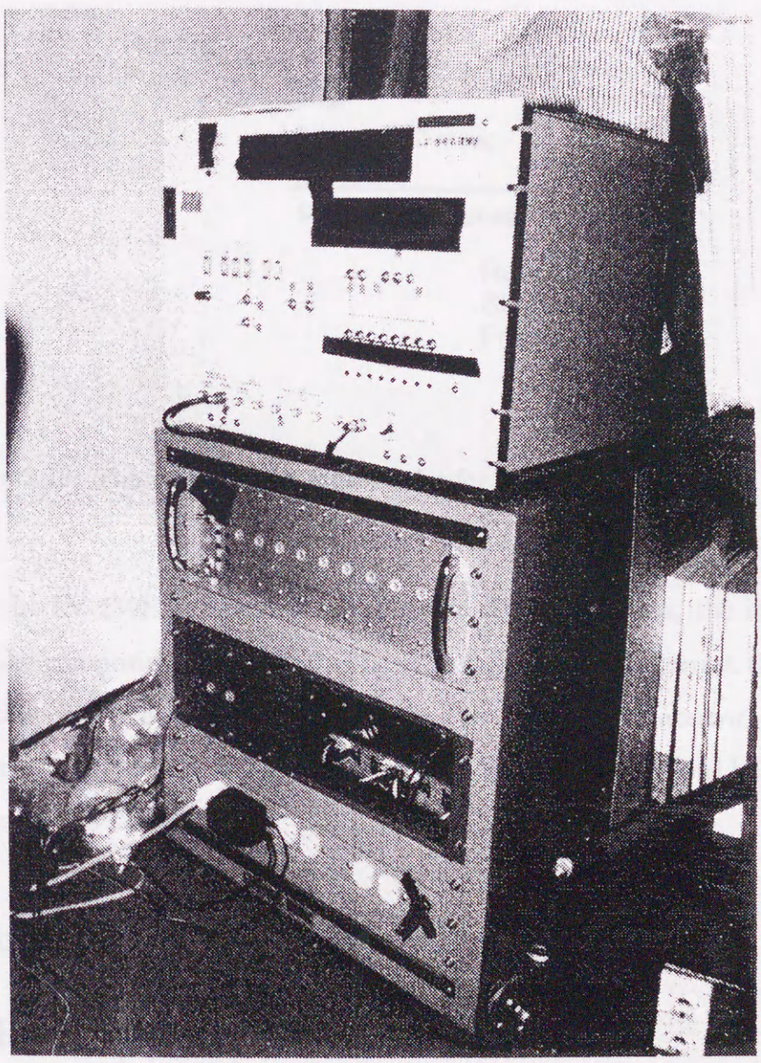

Figure 2.17: View of the CCD data processor (top) and its power supply (bottom). Some parts of the front panel of the CCD data processor are masked by black tapes to prevent the light of LED indicators from disturbing the observation.

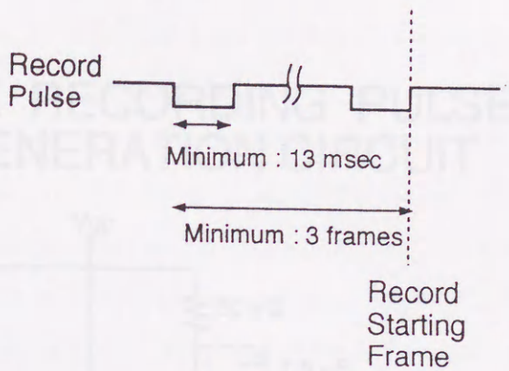

Figure 2.18: Timing chart of a record pulse for the requirement of the LV-250H.

processor.

Although the LV-250H can record very high quality image data, the input requirement for accuracy of the composite video signal is fairly high. In order to correct the time base error of the NTSC composite video signals produced by the CCD data processor, we inserted a digital time base corrector (type FA-300 manufactured by HOEI Corporation) between the CCD data processor and the LV-250H.

2.9 Auxiliary Experimental Apparatus

2.9.1 The calibration laser

A stabilized He-Ne laser (λ = 632.8nm) is used to calibrate the parameters of the etalon and also to monitor the drift of optical spacing of the etalon. For laser calibration, the laser equipment which consists of a stabilized He-Ne laser tube, a diffuser and a beam splitter is inserted into the optical path of the FPDIS as shown in Figure 2.6. During calibration, sky

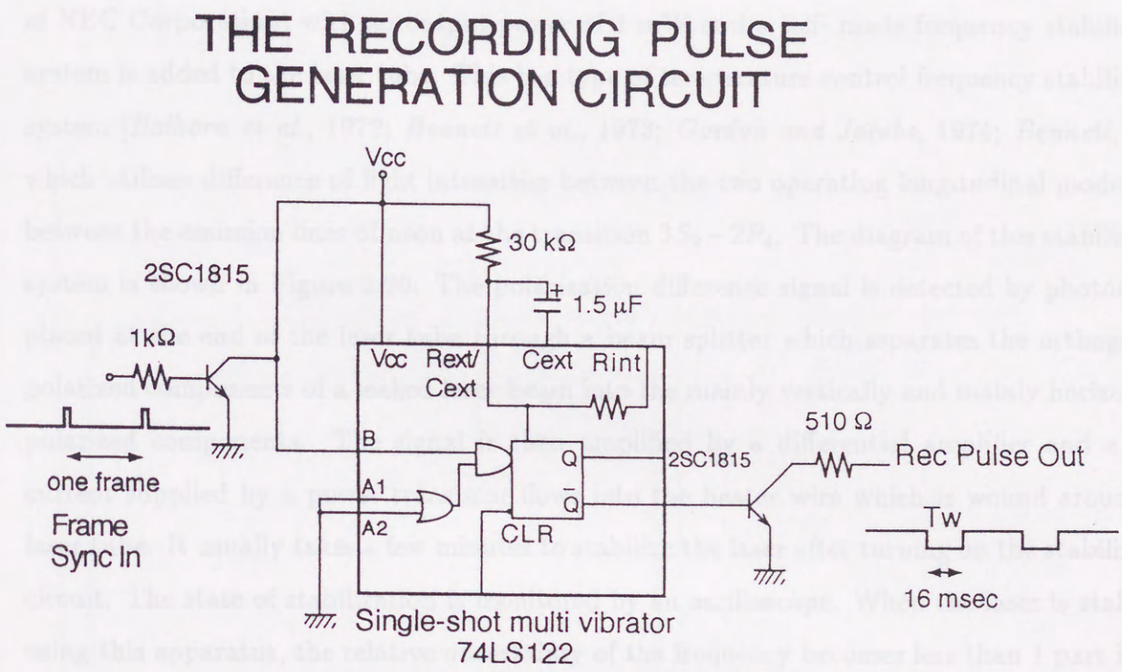

Figure 2.19: A circuit added to the CCD data processor to generate a recording pulse.

light is prevented from entering by covering the objective lens with a lens cap. The beam splitter reflects about 5 percent of the incident laser beam which is diffused by the diffuser to cover the full field of view of the FPDIS. The laser itself is a random polarization laser (type GLG5230 of NEC Corporation) with an output power of 1 mW and a self- made frequency stabilization system is added to the laser tube. This is a type of temperature-control frequency stabilization system [*Balhorn et al.*, 1972; *Bennett et al.*, 1973; *Gordon and Jacobs*, 1974; *Bennett*, 1974] which utilizes difference of light intensities between the two operating longitudinal modes, i.e., between the emission lines of neon at the transition $3S_2 - 2P_4$. The diagram of this stabilization system is shown in Figure 2.20. The polarization difference signal is detected by photodiodes placed at the end of the laser tube through a beam splitter which separates the orthogonally polarized components of a leaked laser beam into the mainly vertically and mainly horizontally polarized components. The signal is then amplified by a differential amplifier and a servo current supplied by a power transistor flows into the heater wire which is wound around the laser tube. It usually takes a few minutes to stabilize the laser after turning on the stabilization circuit. The state of stabilization is monitored by an oscilloscope. When the laser is stabilized using this apparatus, the relative uncertainty of the frequency becomes less than 1 part in 10^7, i.e., $\Delta f/f < 1 \times 10^{-7}$.

2.9.2 The air dryer apparatus

Since the photocathode of the PIH detector and the surface of the CCD sensor are cooled at -10 to $-20°C$ in order to reduce thermal noise, water vapor tends to condense on their surfaces. In order to prevent the water vapor condensation, dry air is supplied into the optical container box in which the PIH, the CCD and other optics are installed. Dry air is made by an air dryer apparatus shown in Figure 2.21. Air taken from an intake of the diaphragm air compressor is sent to the heatless air dryer. The dry air is then sent to the optical container box through a flow meter with a flow valve by which the flow rate of dry air is controlled.

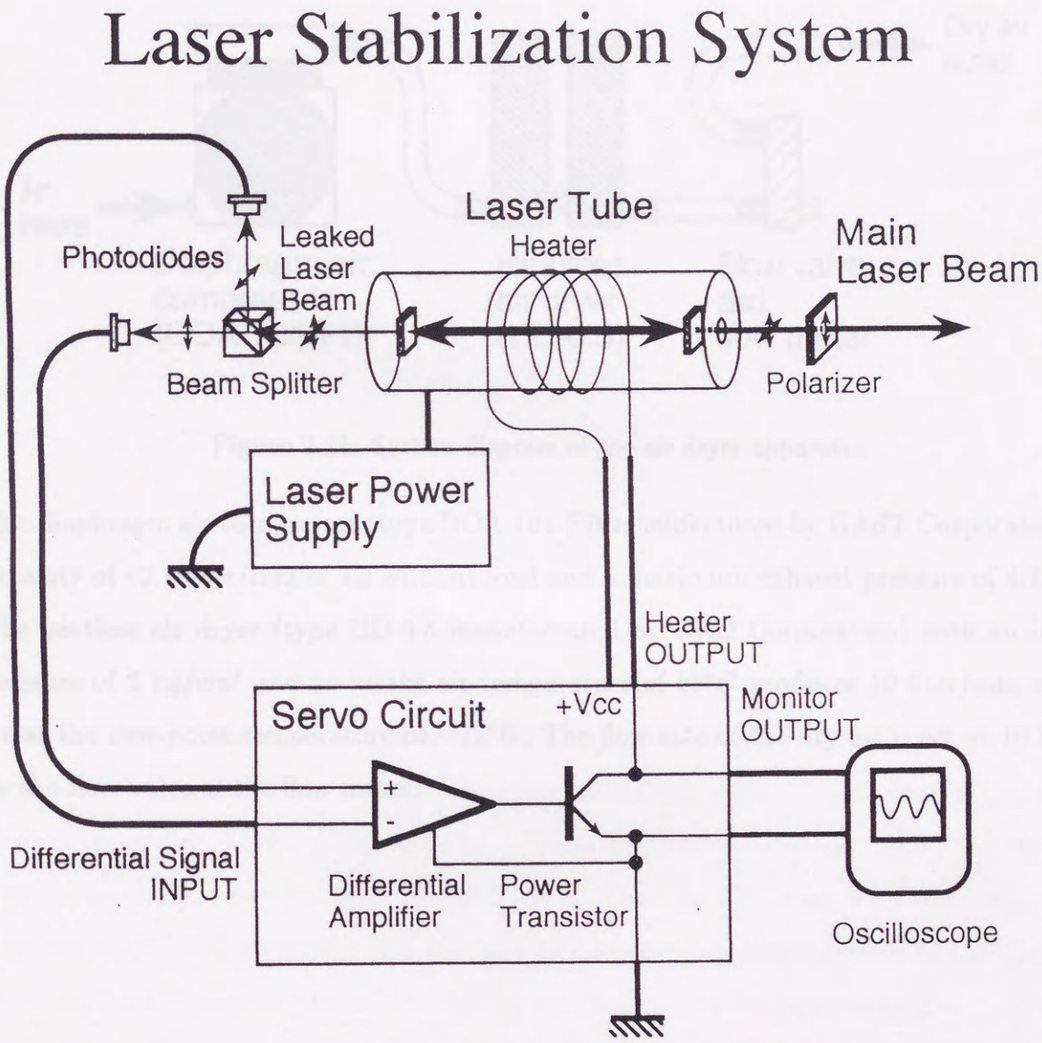

Figure 2.20: System diagram of the laser stabilization system

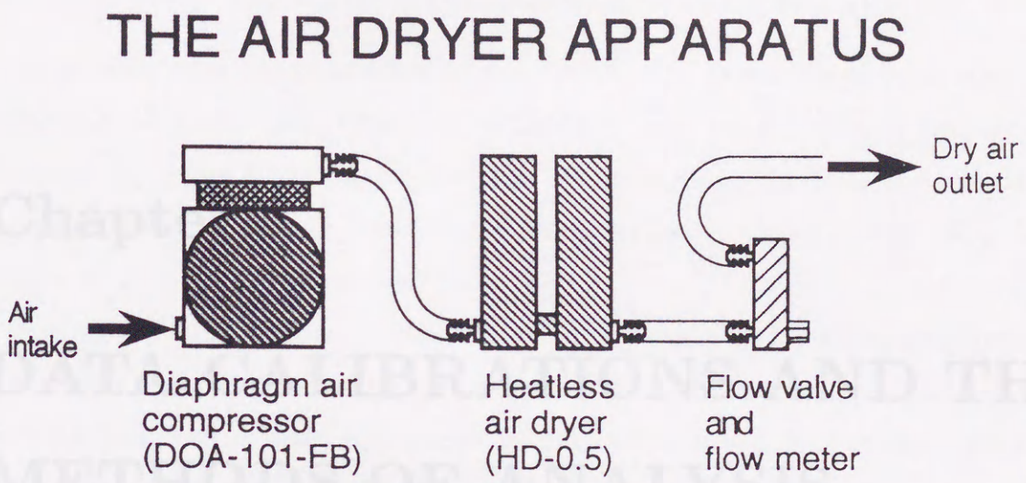

Figure 2.21: System diagram of the air dryer apparatus

The diaphragm air compressor (type DOA-101-FB manufactured by GAST Corporation) has a capacity of 42.1 liter/min of air without load and a maximum exhaust pressure of 4.2 kg/cm^2. The heatless air dryer (type HD-0.5 manufactured by CKD Corporation) with an intake air pressure of 2 kg/cm^2 and an intake air temperature of 18°C produces 10 liter/min of dry air for at the dew-point temperature of $-72°C$. The flow rate of the dry air is set at 10 liter/min by the flow valve of the flow meter.

Chapter 3

DATA CALIBRATIONS AND THE METHODS OF ANALYSIS

3.1 Image Data Processing

In this chapter, the method of calibration and analysis of the FPDIS data taken at Syowa Station is described. First of all, the procedure of image data processing is described.

The original image data taken by the FPDIS are stored in optical video disks in the NTSC composite video format as stated in the previous chapter. Since these data are in analog form, it is necessary to digitize them in order to perform image processing. There are two steps on the image data processing of the FPDIS data. The first step is an A/D conversion and data summation for a data period of 1 min and the second step is corrections to the digital image data and analysis to retrieve winds and temperatures. The former is executed on the so called 'ARSAD system' at the World Data Center-C2 (WDC-C2) for Aurora in National Institute of Polar Research (NIPR), while the latter is executed on a work station (DEC-Station 5000/125) at the Upper Atmosphere and Space Research Laboratory, Tohoku University. The principle and method of these procedures are described in the following sections in detail.

3.1.1 Image data reproduction by the ARSAD system

Various kinds of image data taken by the FPDIS, e.g., aurora fringe data, laser calibration data, star calibration data, cloudy calibration data, etc. are stored in 17 optical video disks. The first procedure of the image processing is reproduction and digitization of these data to transform them into digital image data. This procedure is carried out by using the ARSAD system at WDC-C2 for Aurora in NIPR.

The ARSAD (Automatic Retrieval System for Auroral Data) system was originally constructed to handle various auroral data including all-sky camera data, magnetometer data and satellite data automatically with simple instructions by users. It is a combination of a work station (Toshiba AS-3260) and various video signal processing systems including the Optical Video Disk (OVD) recorder / reproducer. The system diagram of the ARSAD system is shown in Figure 3.1. The composite video signal read by the OVD is digitized and stored in an Image Frame Memory (called the Image-Σ). This image data is then sent to the host work station (AS-3260) through the GPIB interface. Although some programs which execute image processing are installed in the system, it was necessary to develop some new computer programs on the host computer to process the image data taken by the FPDIS.

The procedures to process the FPDIS image data are as follows.

1. First, the image data digitized by the Image-Σ are read by the host computer in a data format of 640 $\times$ 480 $\times$ 8-bits (1-byte) data through the GPIB interface.

2. Secondly, these data are superposed for a data period of 1 min after subtracting the bias value of the image data. The nominal values of the exposure time for FPDIS data can be selected from 0.53, 1.06, 2.13, 4.26 and 8.58 sec according to the selected CCD clock, but is set at 1.06 sec in most observations. The measured exposure time is 1.068062 sec, corresponding to 56.1765 frames/min data. Therefore, 56 images have to be superposed to obtain 1 min FPDIS data.

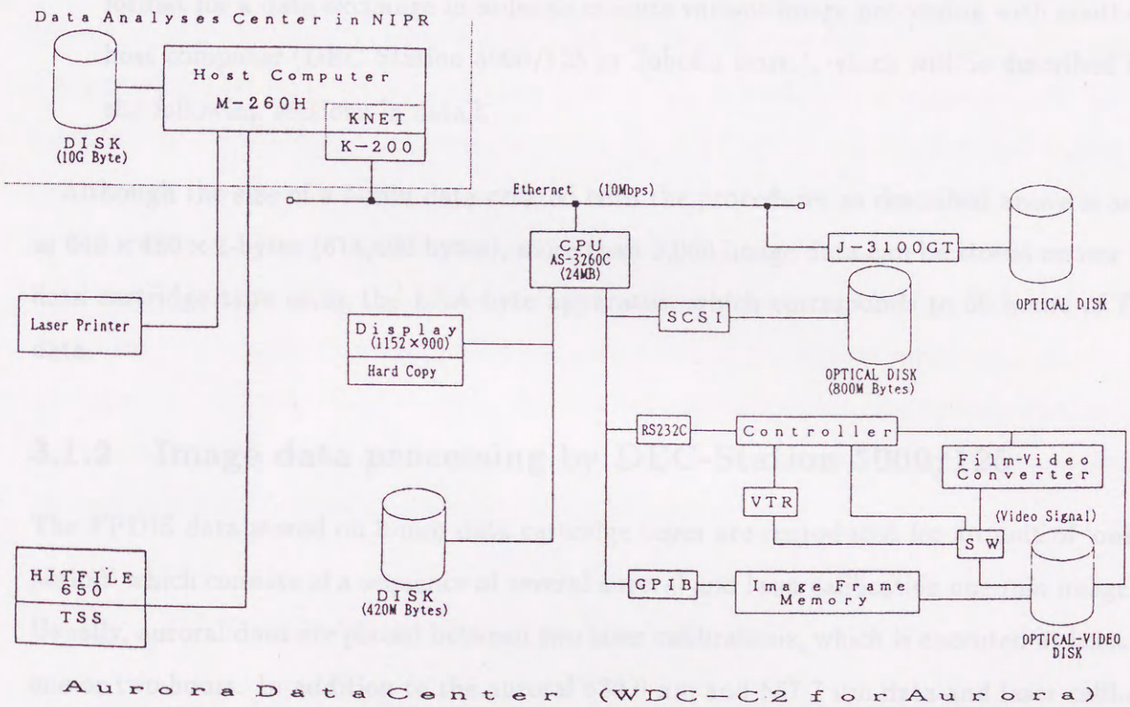

Figure 3.1: A system diagram of the ARSAD (Automatic Retrieval System for Auroral Data) installed at the World Data Center-C2 for Aurora in National Institute of Polar Research.

3. Thirdly, these data are stored on a magnetic disk of the host computer in a data format of $640 \times 480 \times 16$-bits (2-bytes). The procedures described above are controlled by a single program developed exclusively for this purpose.

4. Finally, the data stored in a magnetic disk of the host computer are transferred to 8-mm data cartridge tapes using an EXA-byte data storage apparatus in a 'tar' data format for a data exchange in order to execute various image processing with another host computer (DEC-Station 5000/125 in Tohoku Univ.), which will be described in the following sections in detail.

Although the size of a 1-min data created with the procedures as described above is as large as $640 \times 480 \times 2$-bytes (614,400 bytes), more than 3,000 image data can be stored on one 8-mm data cartridge tape using the EXA-byte apparatus, which corresponds to 50 hours of FPDIS data.

3.1.2 Image data processing by DEC-Station 5000/125

The FPDIS data stored on 8-mm data cartridge tapes are reproduced for an unit of 'one data period' which consists of a sequence of several auroral and laser calibration one-min image data. Usually, auroral data are placed between two laser calibrations, which is executed at least every one or two hours. In addition to the auroral 630.0 nm and 557.7 nm data and laser calibration data, several kinds of FPDIS data are also stored on 8-mm tapes. They are grid calibration data, star calibration data, cloudy day calibration data and z-spacing calibration data. Use of these data will be described later.

The first step of data processing on these data is to co-add a few one-min image data sets to make a single image data. This procedure is executed in order to improve the S/N ratio of an image by increasing signal and smoothing random noise due to the photon counting statistics. For auroral fringe data, 6 temporary successive images, which correspond to 6 min exposure

time, are usually co-added at an interval of every 3 min in order to make a running mean of 6 min of image data with a time resolution of 3 min. For a laser calibration data, at least 5 images are co-added and when successive laser calibration data are available, up to a maximum of 10 images are co-added.

Since these images contain non-linear image distortion as will be described in Section 3.2, correction of images have to be executed before analysis. For every FPDIS image data, this correction is performed by using a computer program which converts a distorted image into a linear image by referencing a parameter file which is made by other procedures as will be described in Section 3.2. Then images are sliced in 6 directions (12 azimuthal angles which corresponds to every 30 degrees in azimuth) from the center of the image which is determined by the center of a laser calibration fringe. The sliced data are then subjected to the analysis of the Doppler temperatures and velocities. The derived values of line-of-sight wind velocities are converted to the horizontal component using the result of geometrical calibration which will be described in Section 3.3 and assuming that the vertical component of the wind velocity is zero.

The details of above procedures including image correction, several kinds of calibration, data analysis and wind conversion are described as follows.

3.2 Correction of Image Distortion

The existence of non-linear distortion in an image taken by the FPDIS was first detected by executing a grid calibration for which an optical grid was placed at the 2nd aperture of the FPDIS (shown in Figure 2.6) as shown in Figure 3.2. This distortion is inherent in the FPDIS and it is mostly attributed to the aberration of electric lenses in the PIH detector as mentioned in the previous chapter. Since the correction of this distortion is essential to the precise analysis of a fringe data, the method of correction, which is called 'the grid calibration', is described in detail as follows.

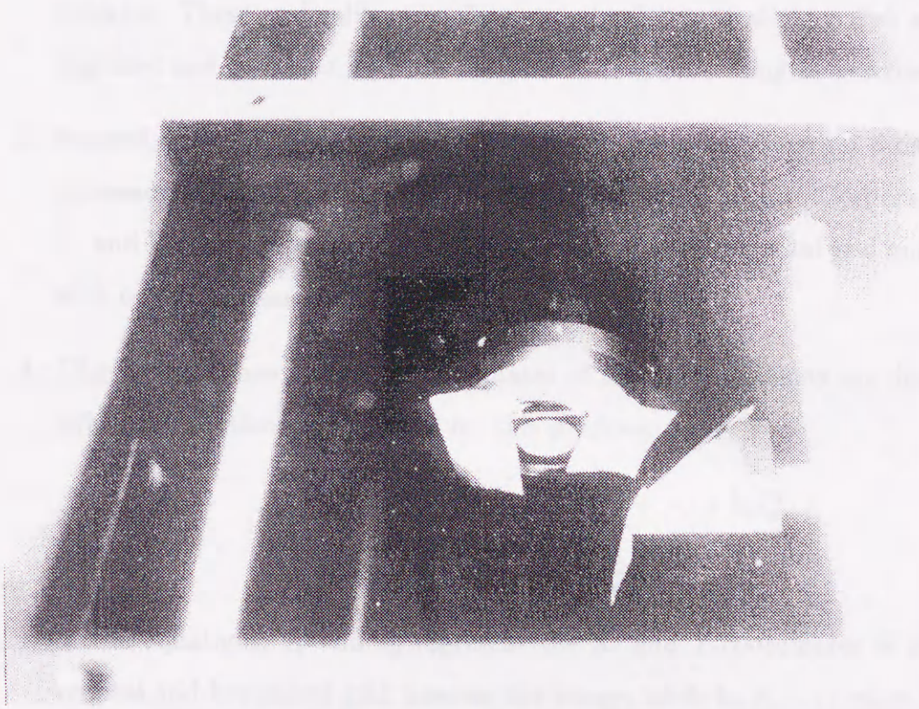

Figure 3.2: A picture of an optical grid placed on the 2nd aperture ($\phi = 5.5$mm) of the FPDIS. When executing a grid calibration, the image of optical grid is taken by weakly illuminating white paper placed behind the transparent optical grid with a diffused He-Ne laser beam.

1. First, an image of the optical grid is placed on the 2-nd aperture ($\phi = 5.5$mm) of the FPDIS, and the image of the grid is taken by weakly illuminating a sheet of white paper placed behind the transparent optical grid by a diffused He-Ne laser beam and is stored on an optical video disk. The interval between lines of this grid is 0.25 mm and about 20 lines in both X- and Y- directions are in the field of view of the detector. These grid calibration data stored on an optical video disk are reproduced, digitized and co-added with the method of data processing as described above.

2. Secondly, the grid calibration image data is displayed using a 2-dimensional image processor (called EXCEL manufactured by Nippon Avionics Corporation) and then X- and Y-coordinates of intersections of vertical and horizontal grid lines are obtained with one-pixel resolution.

3. Thirdly, functions to fit the coordinates of these intersections are determined. The following functions are selected for this purpose.

$$I_y = b_0 + b_1 I_x + b_2 I_x^2 + \cdots + b_n I_x^n \tag{3.1}$$

$$I_x = c_0 + c_1 I_y + c_2 I_y^2 + \cdots + c_n I_y^n \tag{3.2}$$

In the equations, I_x and I_y represent the X- and Y-coordinates of intersections of vertical and horizontal grid lines on the image, while $b_0, b_1, \ldots,\ c_0, c_1, \ldots$ are the regression coefficients. The maximum order n is determined by comparing the standard deviation of regression coefficients σ with the residuals of the fitting $\sigma(b_n)$ or $\sigma(c_n)$. In our case, when n is larger than 2, both values of σ and $\sigma(b_n)$ or $\sigma(c_n)$ become greater than those for $n = 2$. Therefore, the maximum value of n is taken to be 2 and the fitting functions become

$$I_y = b_0 + b_1 I_x + b_2 I_x^2 \tag{3.3}$$

$$I_x = c_0 + c_1 I_y + c_2 I_y^2. \tag{3.4}$$

4. Fourthly, the regression coefficients b_0, b_1, b_2 and c_0, c_1, c_2 are determined by fitting the Equations 3.3 and 3.4 to the X- and Y-coordinates of intersections for both vertical and horizontal directions of grid lines in a least squares sense.

5. Next, a 2-dimensional plane spline interpolation method is applied to interpolate X- and Y-coordinates over the whole region of the image. In practice, spline functions of 3-rd order are used to give the regression coefficients of Equations 3.3 and 3.4. Then, the interpolation is executed in a required resolution and a lot of interpolated lines are determined. Further, intersections of these lines are calculated using the Newton's method and a coordinates conversion table is completed.

The grid data which are used for this calibration are taken twice on August 12, 1990 and December 20, 1990 at Syowa Station, Antarctica. In Appendix B.1, the actual values of grid calibration, i.e., coordinates of intersections of grid lines on the original image, calculated regression coefficients, an example of regression lines and interpolated lines for the grid data taken on August 12, 1990 are given.

Figure 3.3 shows; (a) an example of a grid image used for the grid calibration and (b) the image corrected by the method as stated above. It is clear that distorted and/or curved grid lines are corrected to straight lines which are orthogonal to each other.

Since the optical grid is placed on the 2-nd aperture of the FPDIS, distortion of the images arising from the fish-eye lens, the aspheric lens, and the relay lens can not be corrected by this method. Although slight distortion of image may occur due to these optics, it is not so essential for the analysis of the Doppler temperatures and velocities since these optics are located before the etalon which produces the interference. The geometrical calibration for the effect arising from whole optics of the FPDIS has been performed using stars and its details will be described in the following section.

(a)

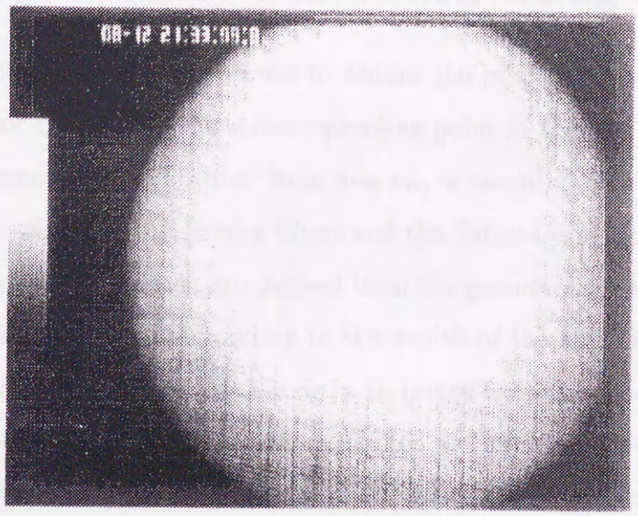

(b)

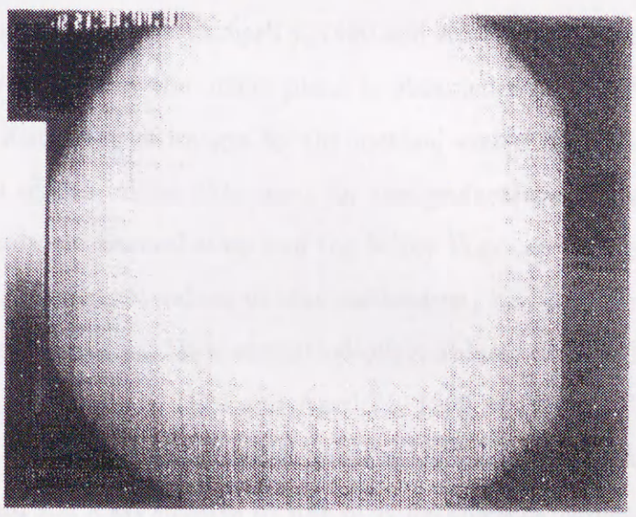

Figure 3.3: (a) An example of a grid image used for the grid calibration. Since the data contains noise and because of limited resolution in the image, the read values may contain errors. However, these errors are thought to be minimized by using the grid calibration method as stated in the text. (b) The image which has been corrected by the grid calibration method. It is apparent that distortions and non-linearity of the image are eliminated.

3.3 The Geometrical Calibration Using Stars

A geometrical calibration is made in order to obtain the relation of a point on a Fabry-Perot fringe in the detector image plane to a corresponding point in the sky. This calibration, which we will call 'the geometrical calibration' from now on, is executed based on the images of stars taken by the FPDIS with the interference filters and the Fabry-Perot etalon being removed from the optical path. Coefficients which are derived from the geometrical calibration are: a position on the detector image plane corresponding to the zenith of the sky, (IX_0, IY_0) (pixels), offset angle of the azimuthal direction of the Y-axis in an image from the geographic north direction, O_{AZ} (radian) and 'the A-parameter', which is defined as the ratio of positional distance in the image plane from the zenith position (pixels) to the zenith angle in the sky; A (pixels/radian). These coefficients can be calculated by any pairs of stars[1]. Since a few pairs of stars can usually be used to determine the coefficients, statistical analysis of these coefficients can also be made.

This calibration was done twice on April 4, 1990 and April 21, 1990 at Syowa Station, Antarctica. The positions of stars in the image plane is obtained with the EXCEL image processor after removing the distortion of images by the method stated in Section 3.2. Figures 3.4 and 3.5 shows examples of the image data used for the geometrical calibration displayed by the EXCEL image processor. Several stars and the Milky Way can be identified in these Figures.

In Appendix B.2, the actual values of star calibration, i.e., positions of stars in an image, calculated zenith position (IX_0, IY_0), azimuthal offset values, O_{AZ} and the A-parameter using star data taken both on April 4, 1990 and April 21, 1990 are given. Figures 3.6, 3.7, 3.8, and 3.9 show variations of the calculated zenith position (IX_0, IY_0), the A-parameters, azimuthal offset values O_{AZ} and the least squares fit line of A-parameters, respectively.

The variations of the values are attributed to 1) the error in the positions of stars, which is

[1]This calculation is executed by giving names of a pair of stars, time of observation, and pixel values of the stars in the image in addition to the geographical location of the observation site to a program named `dcent.f`.

Figure 3.4: An example of the star image data taken at 21:22 UT on April 4, 1990 by the FPDIS with the interference filter and the Fabry-Perot etalon being removed from the optical path.

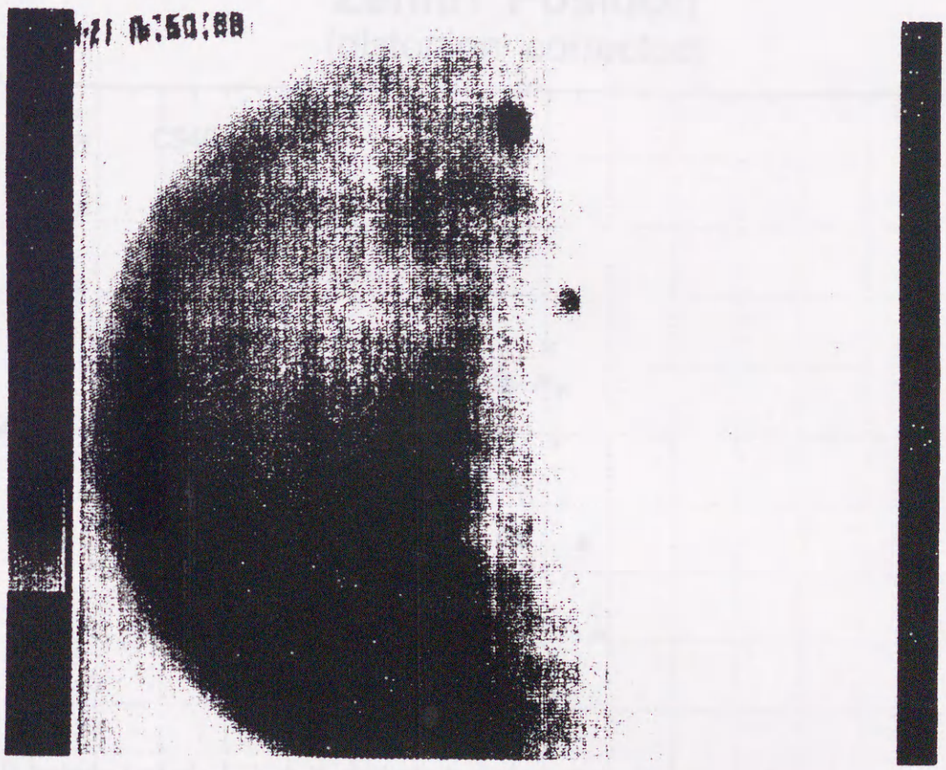

Figure 3.5: Same as Figure 3.4 but for at 16:50 UT on April 21, 1990.

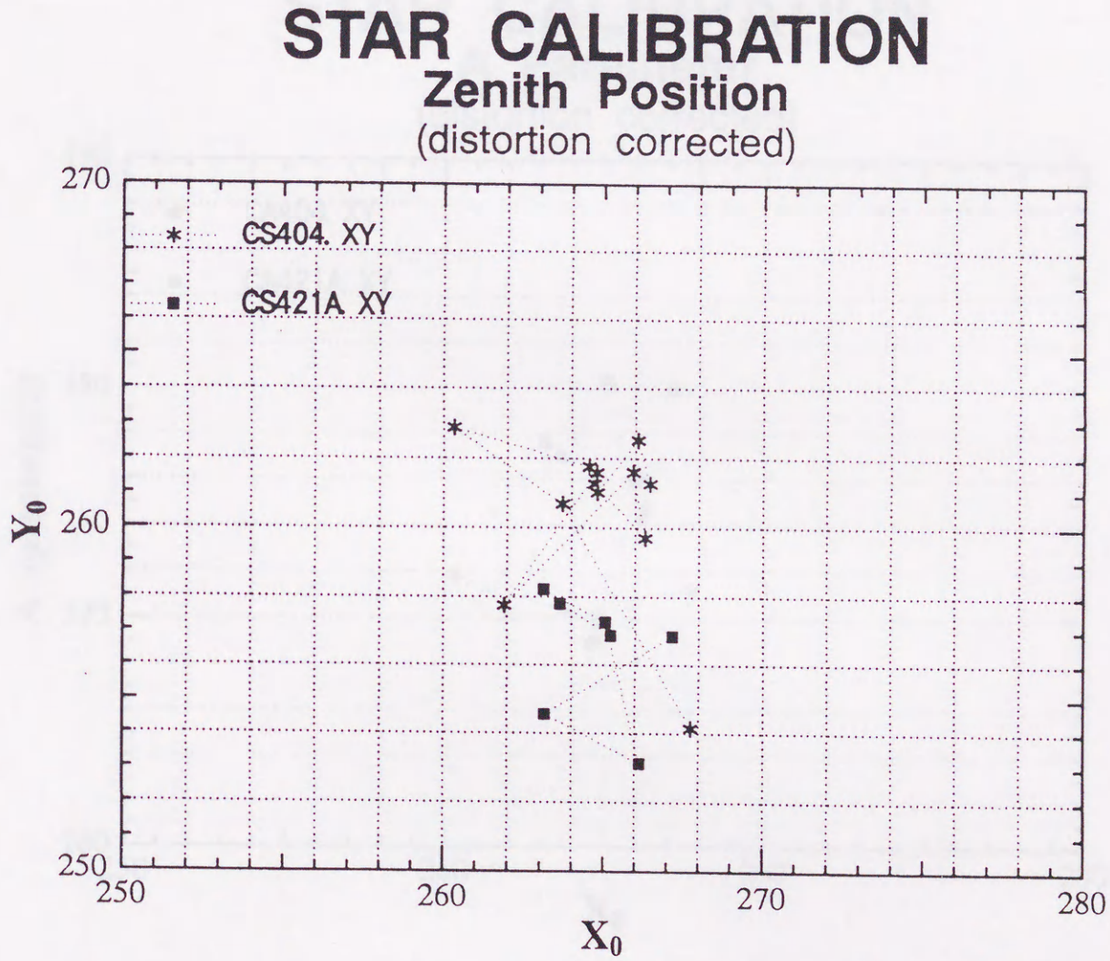

Figure 3.6: Variations of calculated zenith positions on an image data using several pairs of stars for the star calibration.

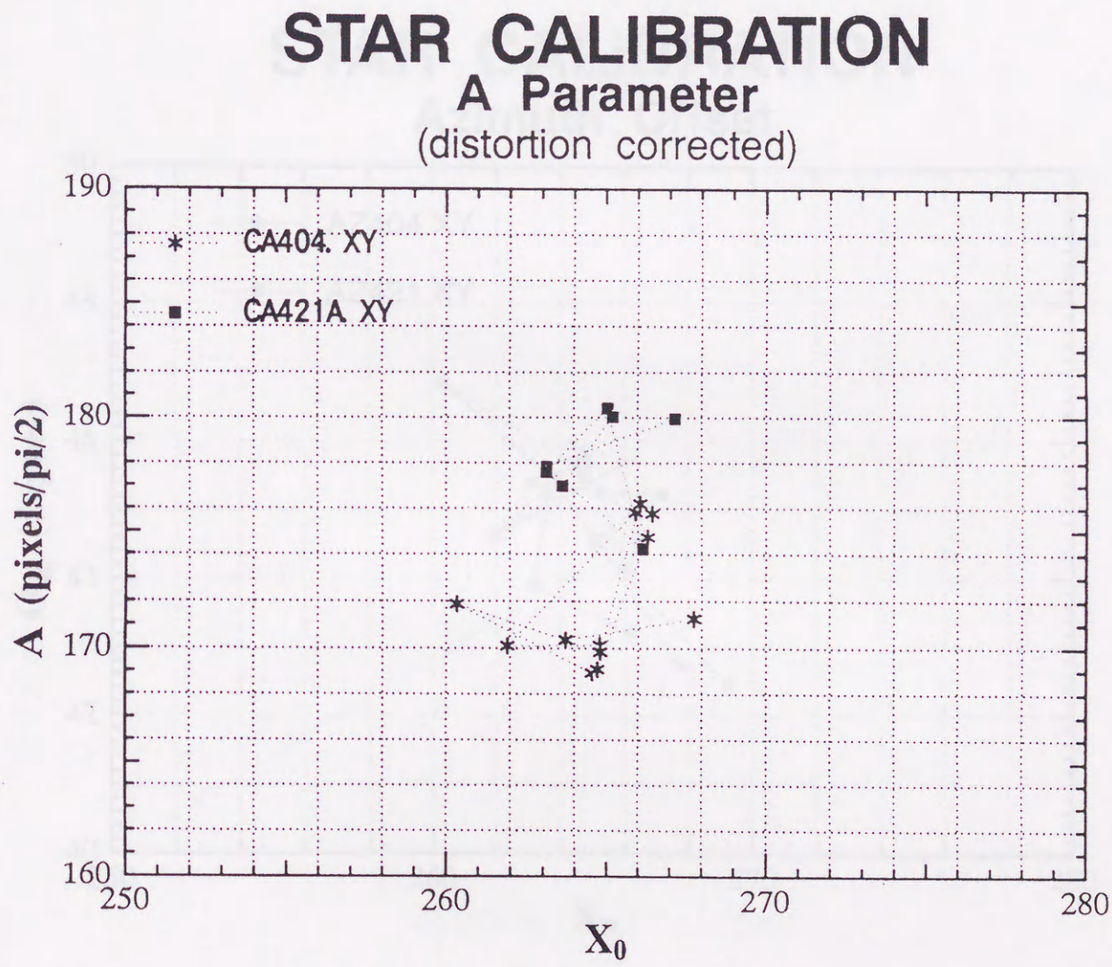

Figure 3.7: Variations of calculated A-parameters using several pairs of stars for the star calibration.

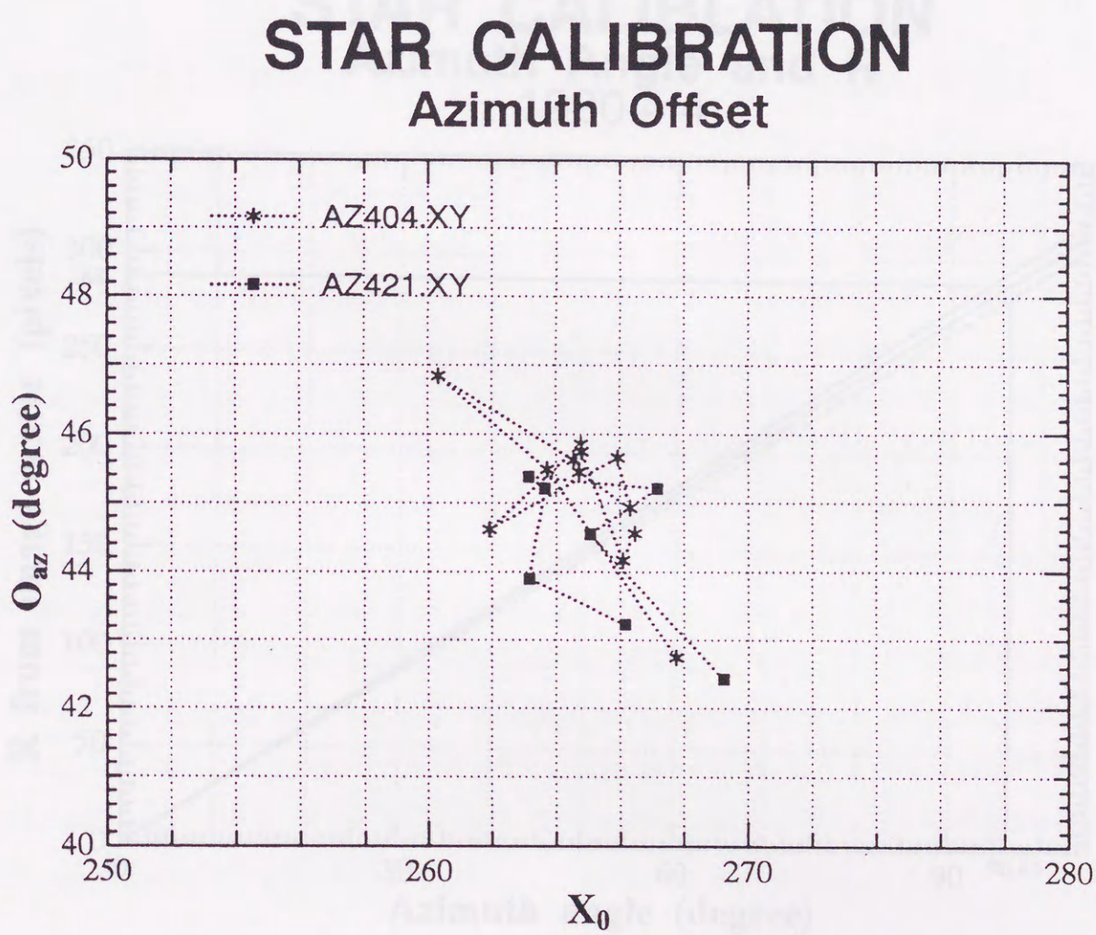

Figure 3.8: Variations of calculated azimuthal offset values using several pairs of stars for the star calibration.

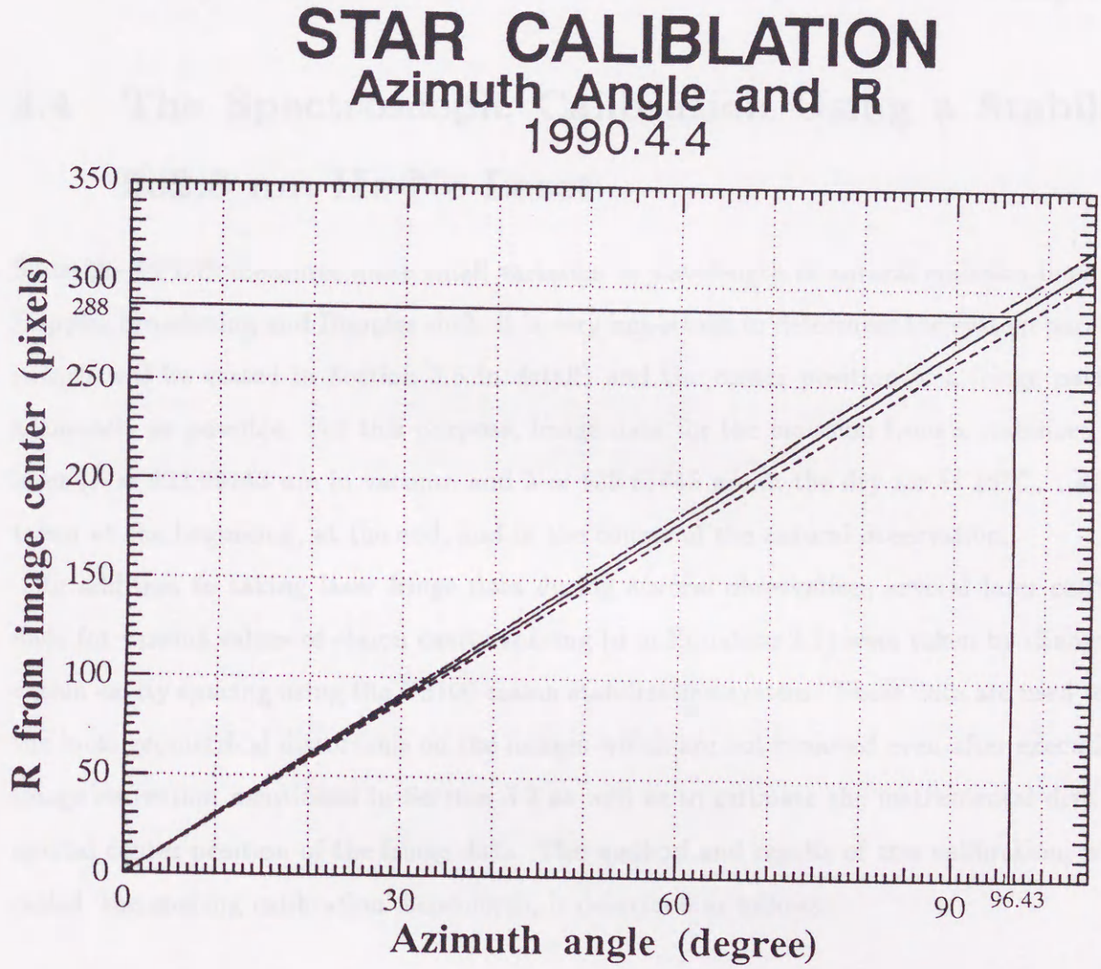

Figure 3.9: Linear conversion of the distance in pixel number from the zenith position on the image data plane into the zenith angle of the sky. The straight line represents the mean conversion line derived from mean A-parameter, while broken and dotted lines represent the conversion lines of mean plus standard deviation (S.D.) of A-parameter and that of mean minus S.D., respectively.

considered to be less than 3 pixels and to 2) the error in the calculation which is thought to become large when the separation between the two stars is small. Although the values vary as shown in the figures, the mean value is used to calibrate the position of auroral fringe data.

3.4 The Spectroscopic Calibration Using a Stabilized 632.8 nm He-Ne Laser

Since the FPDIS measures quite small variation in wavelength of auroral emission lines due to Doppler broadening and Doppler shift, it is very important to determine the system parameters (which will be stated in Section 3.5 in detail) and the center position of a fringe pattern as accurately as possible. For this purpose, fringe data for the emission from a stabilized He-Ne laser (λ = 632.99143 nm in vacuum and λ = 632.81645 nm in the dry air at 15°C, 1 atm) are taken at the beginning, at the end, and in the course of the auroral observation.

In addition to taking laser fringe data during auroral observation, several laser calibration data for various values of etalon cavity spacing (d in Equation 2.1) were taken by changing the etalon cavity spacing using the CS100 etalon stabilization system. These data are used to check the local geometrical distortions on the images which are not removed even after executing the image correction mentioned in Section 3.2 as well as to estimate the instrumental drift of the optical center position of the fringe data. The method and results of this calibration, which is called 'the spacing calibration' henceforth, is described as follows.

3.4.1 Determination of the optical center of the image data

The procedures to make a superposed image data from laser calibration data for different spacings are the same as described in Section 3.1. Ten 1-min images are co-added for the spacing calibration.

The next step in the spacing calibration is to find the center position of the fringe. Each

laser calibration data can be used for this purpose. The procedure to find the optical center position is as follows.

1. First, an image data of the laser fringe is sliced in the horizontal direction using an initial guess for the Y-coordinate of the center position. Accuracy of the order of 10 pixels is sufficient for the initial Y-position. In order to reduce noise in the image data, image data of a few successive lines—5 lines in most cases—are co-added and the mean profile along the X-direction is used for the calculation. An example of such profile data is shown in Figure 3.10. We define these sliced data as 'the sliced (image value) function' $S(r)$ where r represents the X-position in the image data.

2. Secondly, each fringe peak of the sliced function is subjected to fit to a Gaussian function, as given below, using a non-linear least squares method;

$$G(r) = A \exp\left(- \frac{(r - P)^2}{B^2} \right). \tag{3.5}$$

The values A, B, and P, are determined by the fitting. This fitting is executed to every peak of the sliced function. For example, four peaks are seen in Figure 3.10 and these values are designated as $A_x(1), B_x(1), P_x(1)$ for the first peak, $A_x(2), B_x(2), P_x(2)$ for the second peak, and so on. Then, the X-value for the center, C_x, of this sliced data is determined as

$$C_x = \frac{1}{2}\left(\frac{P_x(3) + P_x(2)}{2} + \frac{P_x(4) + P_x(1)}{2} \right). \tag{3.6}$$

This means that the mean value of the center position is determined from a pair of inner fringes and a pair of outer fringes.

3. Thirdly, image data of the laser fringe is sliced again along $X = C_x$, which has been determined in the previous step of this procedure. A few successive vertical lines are co-added in this step to reduce noise in the image data.

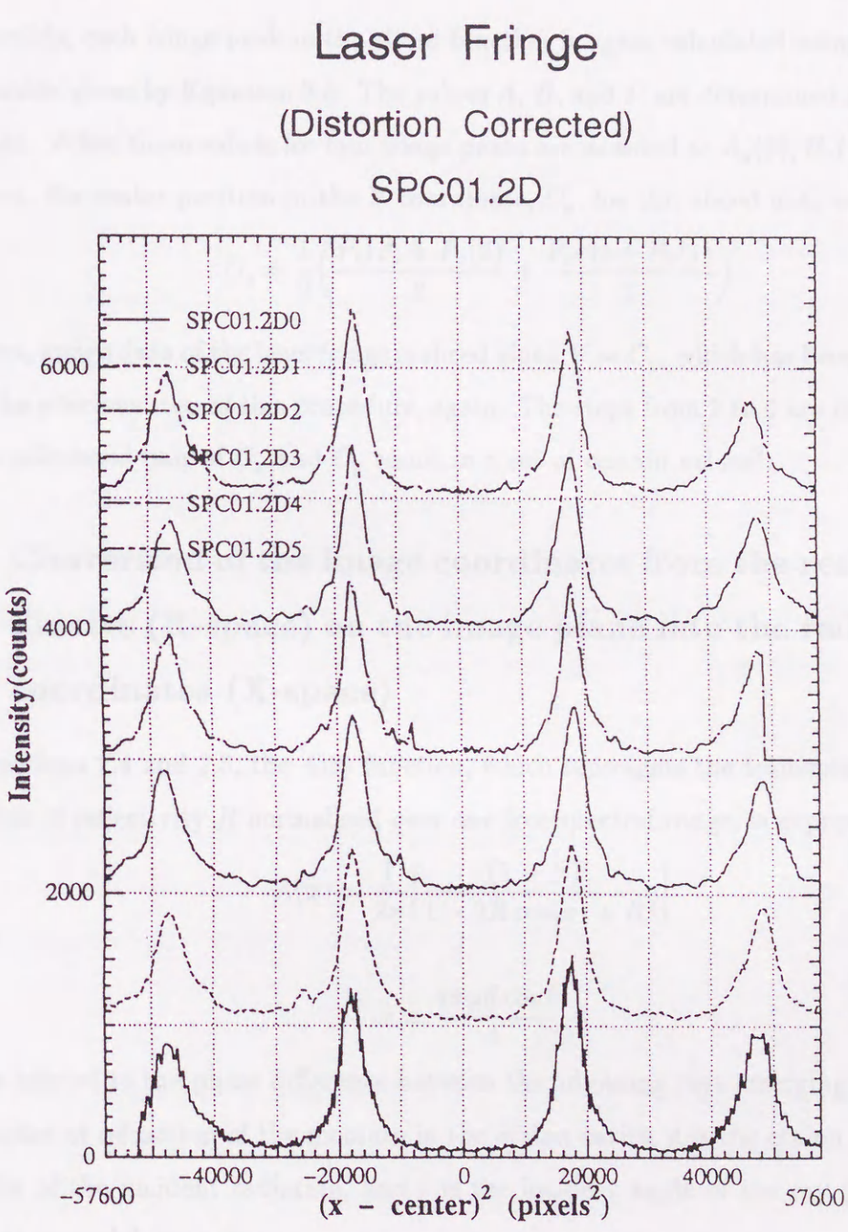

Figure 3.10: An example of the sliced He-Ne laser calibration image data in 6 directions. The abscissa represents the X-position in the image data, while the ordinate represents the count number of the image data.

4. Fourthly, each fringe peak in the sliced function is again calculated using a Gaussian function given by Equation 3.5. The values A, B, and P are determined by the fitting again. When these values for four fringe peaks are denoted as $A_y(1), B_y(1), P_y(1)$ and so on, the center position in the Y-coordinate, C_y, for this sliced data is given by

$$C_y = \frac{1}{2}\left(\frac{P_x(3) + P_x(2)}{2} + \frac{P_x(4) + P_x(1)}{2}\right). \tag{3.7}$$

5. Then, image data of the laser fringe is sliced along $Y = C_y$, which has been determined in the previous step of this procedure, again. The steps from 2 to 5 are repeated until the calculated pair of C_x and C_y result in a set of certain values[2].

3.4.2 Conversion of the image coordinates from the real pixel coordinates (R-space) on the image plane into the radius-squared coordinates (X-space)

From Equations 2.4 and 2.5, the Airy function, which represents the transmission profile of an ideal etalon of reflectivity R normalized over one free spectral range, is expressed as

$$A(x) = \frac{1}{2\pi}\left[\frac{(1-R)^2}{1 - 2R\cos(x) + R^2}\right] \tag{3.8}$$

where

$$x = \frac{4\pi\mu d\cos i}{\lambda}. \tag{3.9}$$

Here, x is related to the phase difference between the adjoining rays emerging from the etalon, μ is the index of refraction of the medium in the etalon cavity, d is the etalon spacing, λ is the wavelength of the incident radiation, and i is the incident angle of the ray [*Hays and Roble*, 1971]. Now, a useful parameter

$$N_R = \frac{\pi\sqrt{R}}{1-R} \tag{3.10}$$

[2]These procedures including step 1 to step 5 are executed automatically by giving a name of an image file and values of the initial guess value for the center position to a single program named `sliga.c`.

is redefined as 'the reflective finesse' N_R which was simply defined as the 'finesse' in Equation 2.21. The free spectral range $\Delta\lambda$ is given as

$$\Delta\lambda = \lambda^2/2\mu d\cos i. \tag{3.11}$$

By an analytical theory of a Fabry-Perot spectrometer [*Hernandez*, 1966], the output profile Y is defined as the convolution of the source profile B with the instrumental broadening function I, and Y is symbolically expressed as

$$Y = B * I = Y(x) = \int_{-\infty}^{\infty} B(y)I(x-y)dy \tag{3.12}$$

where B, the source function under consideration is a convolution of a Lorentzian $\mathcal{L}$ with a Doppler profile $\mathcal{G}$. I, the instrumental function, is also a convolution of the Airy function of an ideal etalon, A, with its surface defect functions, D_f (spherical curvature) and D_g (microscopic flatness imperfections) and with the exploring diaphragm. Therefore, the output profile Y is written as

$$Y = B * I = \mathcal{L} * \mathcal{G} * A * D_f * D_g * F. \tag{3.13}$$

Although analytical description of these parameters will be given in Section 3.5, it is clear from Equations 3.13, 3.8, and 3.9 that the output profile of the etalon has a period of $2\pi x = \frac{4\pi\mu d}{\lambda}\cos i$. Expanding Equation 3.9 by Taylor series, we get

$$x = \frac{4\pi\mu d}{\lambda}\left(1 - \frac{i^2}{2!} + \frac{i^4}{4!} - \cdots\right). \tag{3.14}$$

When i is small, i can be written as $i \simeq \tan i = \frac{r}{f}$, where r is the distance of a position from the center of a fringe on the detector and f is the focal length of the focusing lens (nominal value is 600 mm as shown in Figure 2.6. Using this relationship, Equation 3.14 can be rewritten as

$$x = \frac{4\pi\mu d}{\lambda}\left(1 - \frac{r^2}{2f^2} + \frac{r^4}{24f^4} - \cdots\right). \tag{3.15}$$

Since $f \gg r$, the 3-rd and following terms in the parentheses of Equation 3.15 can be neglected. When n, d, λ, and f are constants, x is proportional to r^2. Therefore, it is convenient to use

r^2 instead of r as a variable which represents the position in a fringe, in order to deal with the output profile of a Fabry-Perot spectrometer. We call this conversion as the conversion of the image coordinates from the real pixel coordinates (R-space) on the image plane into the radius-squared coordinates (X-space). Figure 3.11 shows an example of sliced image data in 6 directions, already shown in Figure 3.10 displayed in X-space. The coordinate conversion described above is made for the procedure described below.

The center position of a fringe determined by the method described in Section 3.4.1 is used for slicing the image data. Image data of the laser fringe is now sliced in the 12-directions with 30 degree separations. In order to reduce noise in the image data, image data of a few successive lines—5 lines in most cases—are co-added and the mean value is used for the calculation of the sliced values. The variable representing the distance r from the center of this sliced data is then converted into the squared distance in the X-position (X-space) from the center of the sliced image data as $X = (r - C_x)^2$. This conversion is executed in each of the 12-directions. This procedure which converts sliced image data into an expression of X-space is called the 'X-slice procedure' from now on[3].

It is clear from Figure 3.11 that the peaks of the laser fringes are equally separated in X-space. The difference in peak heights of the fringes is probably due to the limb darkening of the optics. When this figure is examined in detail, it is apparent that the FWHM value is larger for the outer fringes than for the inner fringes. This is due to the effect corresponding to the term of the exploring diaphragm F which appeared in Equation 3.13 which derives from the limited number of image pixels in the 2-dimensional detector. This effect in dealing with the auroral data will be discussed in Section 3.5.

[3]This procedure is executed by giving the center position of a image data and a name of an image file to a program named `xslice.c`.

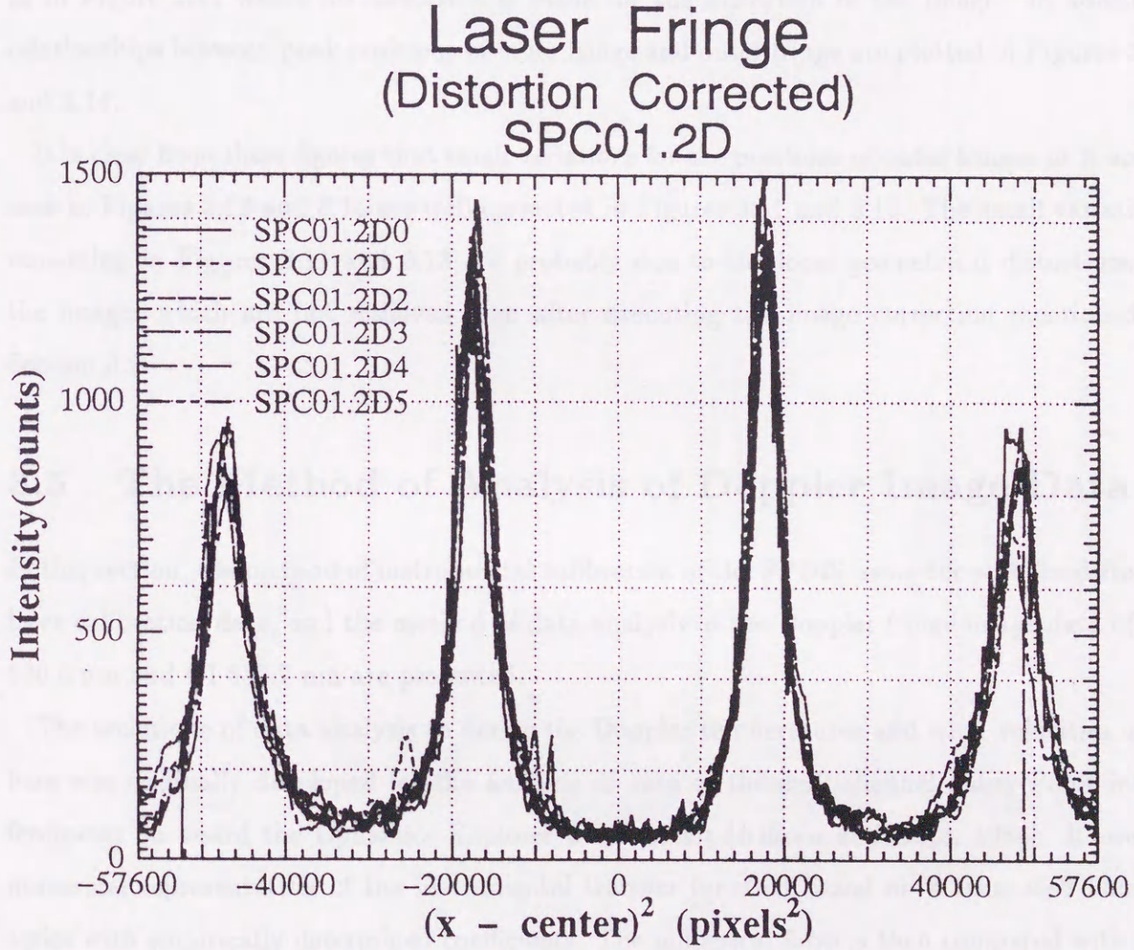

Figure 3.11: An example of the sliced He-Ne laser calibration image data in 6 directions displayed in the radius-squared coordinates (X-space). The abscissa represents the squared distance of X-position from the center of the fringe.

3.4.3 Efficacy of the correction of distortion in the image data

After executing the X-slice procedure, efficacy of the correction of distortion mentioned in Section 3.2 is evaluated. Figure 3.12 shows the X-sliced image data in 6 directions same as in Figure 3.11 where no correction is made for the distortion in the image. In addition, relationships between peak positions of inner fringe and outer fringe are plotted in Figures 3.13 and 3.14.

It is clear from these figures that small variations for the positions of outer fringes in X-space seen in Figures 3.12 and 3.14 are well corrected in Figures 3.11 and 3.13. The small variations remaining in Figures 3.11 and 3.13 are probably due to the local geometrical distortions on the images which are not removed even after executing the image correction mentioned in Section 3.2.

3.5 The Method of Analysis of Doppler Image Data

In this section, the method of instrumental calibration of the FPDIS using the stabilized He-Ne laser calibration data, and the method of data analysis of the Doppler fringe image data of OI 630.0 nm and OI 557.7 nm are presented.

The technique of data analysis to derive the Doppler temperatures and wind velocities used here was originally developed for the analysis of data of the multichannel Fabry-Perot interferometer on board the Dynamics Explorer 2 spacecraft [*Killeen and Hays*, 1984]. It uses a numerical representation of the instrumental transfer function based on a truncated Fourier series with empirically determined coefficients. The numerical form is then compared with the conventional analytic form. The Fourier coefficients describing the instrument function are generated at the wavelength of a stabilized He-Ne laser and are translated to different wavelengths of observation using an interpolation technique for both phase and power. The use of a quasi-linear least-squares fitting process involving the use of matrices permit a rapid and accurate

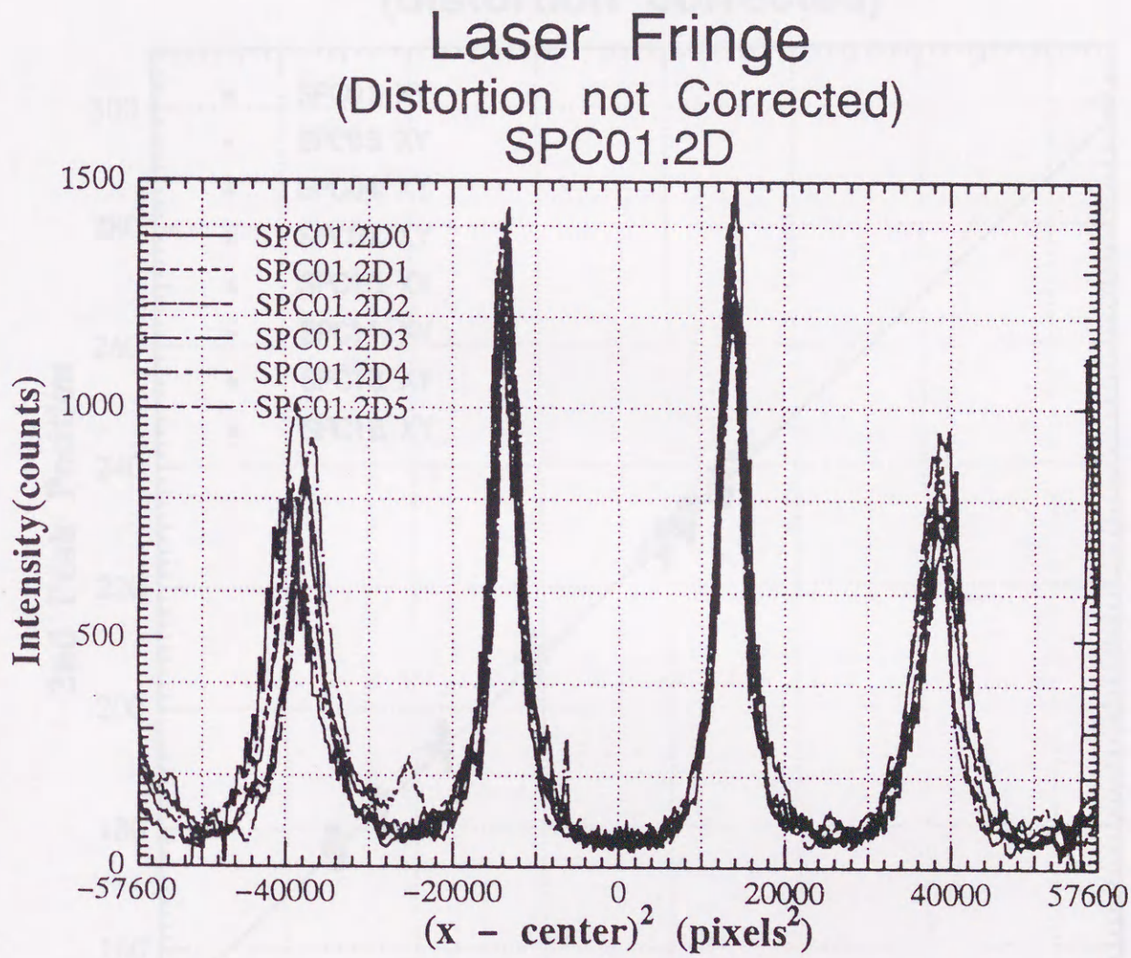

Figure 3.12: An example of the sliced He-Ne laser calibration image data displayed in the radius-squared coordinates (X-space). The abscissa represents the squared distance of X-position from the center of the fringe. The correction for the distortion in the image is not executed.

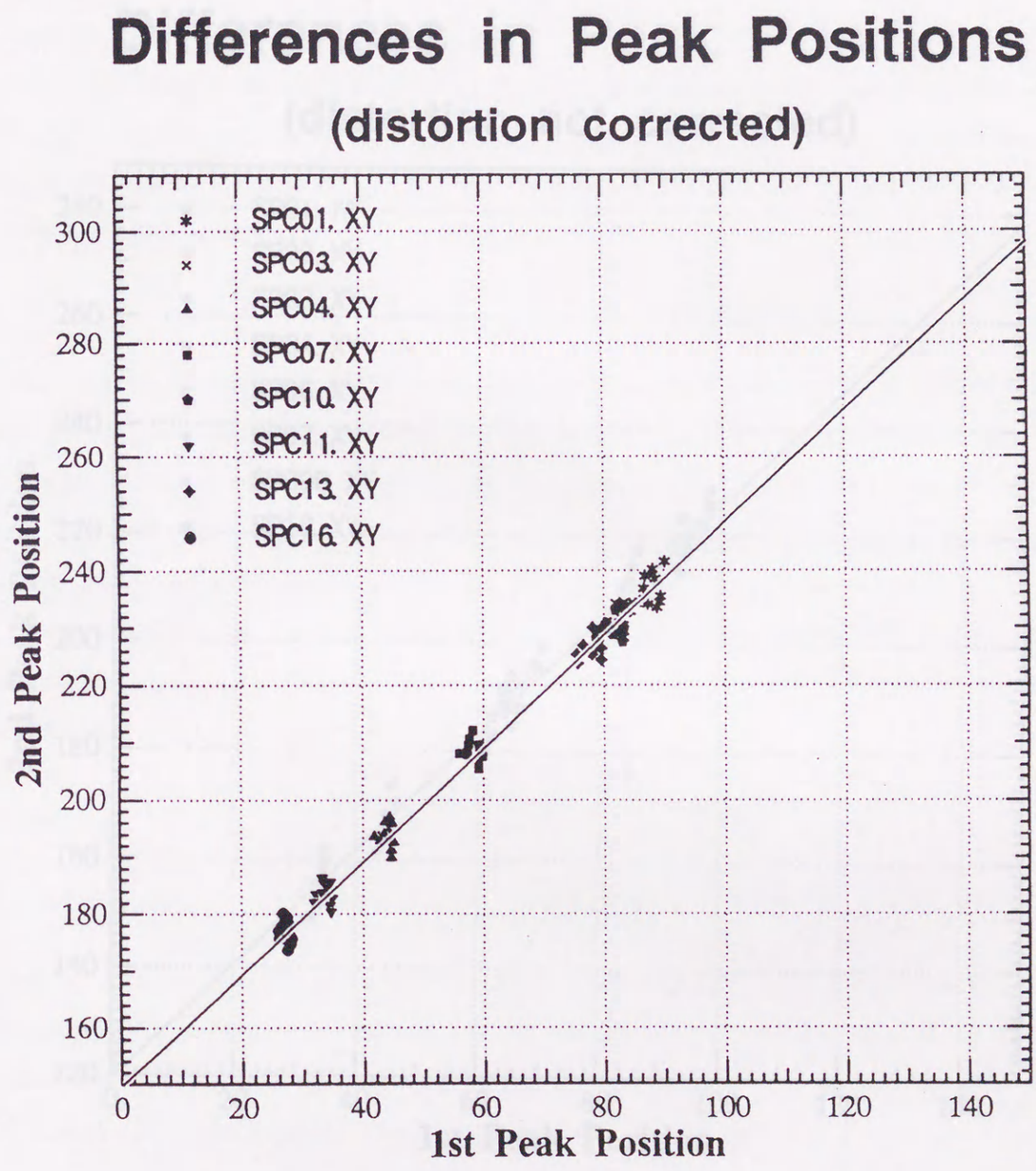

Figure 3.13: Relationships between peak positions of inner fringes (1-st peak) and outer fringe (2-nd peak) plotted in X-space both in abscissa and in ordinate. Correction for the distortion in image is made for these data.

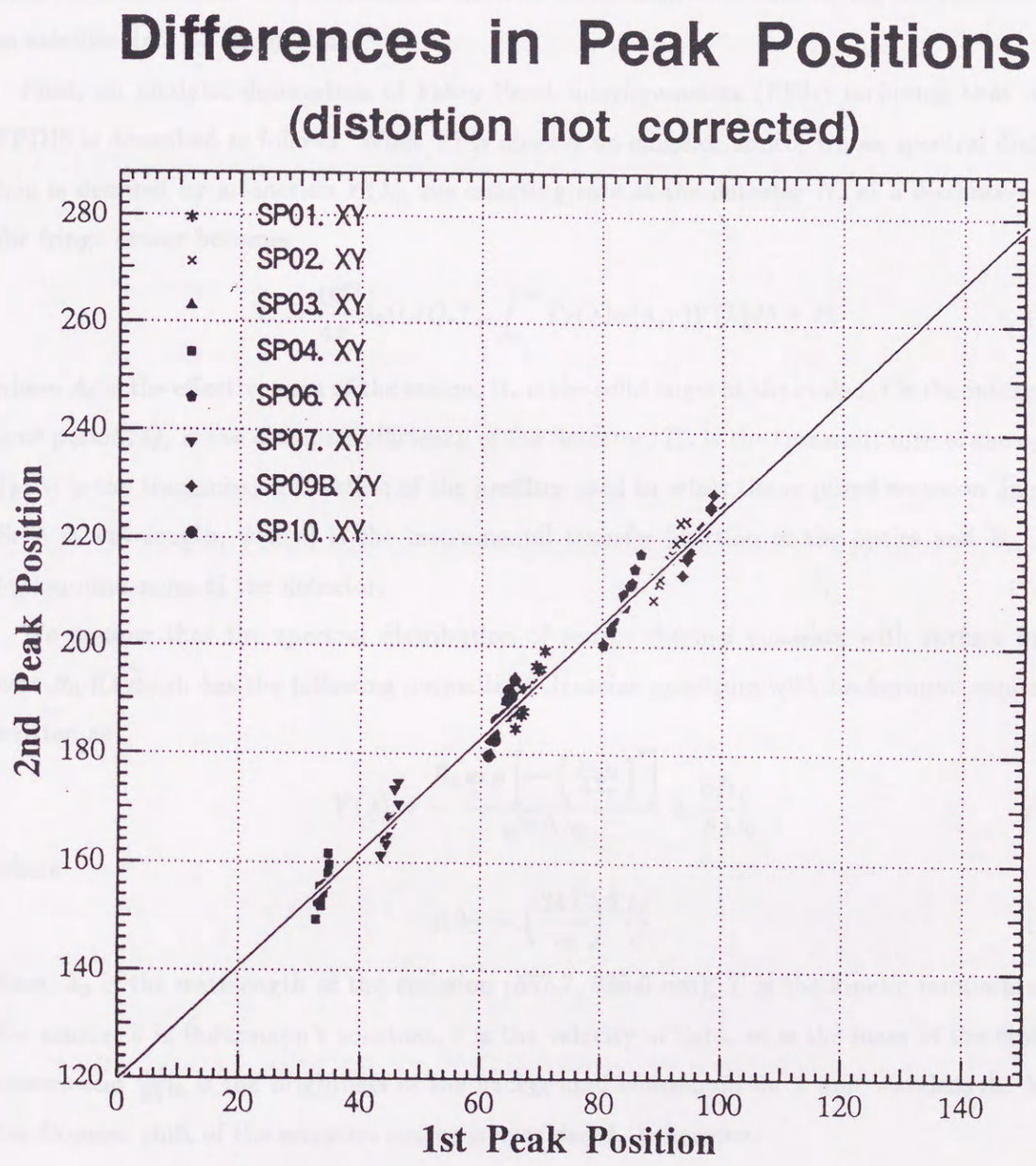

Figure 3.14: Same as Figure 3.13 but without correction for the distortion in images. Small variations appeared in each set of data (SP**.XY) are probably due to the non-linearity of the image which differs in each direction.

data reduction and is very suitable for the case where numerous data fitting are required such as satellite data or image data.

First, an analytic description of Fabry-Perot interferometers (FPIs) including that of the FPDIS is described as follows. When FPIs observe an emission source whose spectral distribution is denoted by a function $Y(\lambda)$, the counting rate at the detector N_r at a distance r from the fringe center becomes

$$N_r = \frac{10^6}{4\pi} A_0 \Omega_r t Q_r T_{or} \int_0^\infty T_F(\lambda)\psi(\lambda, r)Y(\lambda)d\lambda + B_r \tag{3.16}$$

where A_0 is the effective area of the etalon, Ω_r is the solid angle at the etalon, t is the integration time period, Q_r is the quantum efficiency of the detector, T_{or} is the transmittance of the optics, $T_F(\lambda)$ is the transmission function of the prefilter used to select the required emission line, and Br λ is wavelength, $\psi(\lambda, r)$ is the instrumental transfer function of the optics and B_r is the background noise of the detector.

We assume that the spectral distribution of source thermal emission with surface brightness R_0 Rayleigh has the following normalized Gaussian spectrum with background continuum written as

$$Y(\lambda) = \frac{R_0 \exp\left[-\left(\frac{\lambda-\lambda_l}{\Delta\lambda_T}\right)^2\right]}{\sqrt{\pi}\Delta\lambda_T} + \left.\frac{\partial R}{\partial\lambda}\right|_0 \tag{3.17}$$

where

$$\Delta\lambda_T = \left(\frac{2kT}{m}\right)^{\frac{1}{2}} \frac{\lambda_l}{c}. \tag{3.18}$$

Here, λ_0 is the wavelength of the emission (557.7, 630.0 nm), T is the kinetic temperature of the source, k is Boltzmann's constant, c is the velocity of light, m is the mass of the emitting species and $\frac{\partial R}{\partial\lambda}|_0$ is the brightness of the background continuum for a unit wavelength. When the Doppler shift of the emission source is considered, λ_l becomes

$$\lambda_l = \lambda_0\left(1 + \frac{v}{c}\right), \tag{3.19}$$

where v is the relative velocity of the bulk motion of the source to the observer.

The analytic form of the instrumental transfer function ψ is given by a convolution of the individual analytic functions for various instrumental broadening effects [*Hays and Roble*, 1971]. They are ;

- 1) reflectivity broadening (Airy function) $A(x)$, which is given by Equations 3.8 and 3.9,
- 2) broadening due to an aperture function, $F(x)$,
- 3) broadening due to microscopic flatness imperfection of the etalon, $D_g(x)$,
- 4) broadening due to spherical defect of the etalon, $D_f(x)$.

Among the above, 2) and 4) can be described by a rectangular broadening function, while 3) is described by a Gaussian function. These functions are analytically written as follows. For the aperture function $F(x)$,

$$F(x) = \frac{\pi(x)}{2\Delta\lambda f} = \frac{N_f}{2\pi}\pi(x) \tag{3.20}$$

where

$$\pi(x) = \begin{cases} 1 & < \frac{\pi}{N_f} \\ \frac{1}{2} & \text{when } |x| = \frac{\pi}{N_f}. \\ 0 & > \frac{\pi}{N_f} \end{cases} \tag{3.21}$$

In these equations, f is the HWHM of the aperture function which is equal to $f = \frac{2\pi}{\lambda}\frac{d^2}{(4L)^2}$, where d is the diameter of the circular aperture, L is the focal length of the objective lens, and N_f is the finesse of aperture function which is given by $N_f = \frac{\pi}{\Delta\lambda f}$.

The broadening due to microscopic flatness imperfection of the etalon, $D_g(x)$, is given by

$$D_g(x) = \frac{1}{\sqrt{\pi}D}\exp\left(-\frac{x^2}{D^2}\right) \tag{3.22}$$

where

$$D = \frac{\Delta\lambda d_g}{\sqrt{\ln 2}} = \frac{\pi}{N_{D_g}\sqrt{\ln 2}}. \tag{3.23}$$

In these equations, d_g is the HWHM of the Gaussian function (Equation 3.22) and is equal to $d_g = \frac{\pi}{\Delta\lambda N_{D_g}}$, N_{D_g} is the finesse of microscopic defect function which is written by $N_{D_g} = \frac{n^*}{4.7}$ where n^* is a constant which is related to the mean shift of the microscopic defects in the order $\frac{\lambda}{n^*}$.

For broadening due to spherical defect of the etalon, $D_f(x)$, is given by

$$F(x) = \frac{\pi(x)}{2\Delta\lambda d_f} = \frac{N_{D_f}}{2\pi}\pi(x) \tag{3.24}$$

where

$$\pi(x) = \begin{cases} 1 & < \frac{\pi}{N_{D_f}} \\ \frac{1}{2} \quad \text{when } |x| & = \frac{\pi}{N_{D_f}}. \\ 0 & > \frac{\pi}{N_{D_f}} \end{cases} \tag{3.25}$$

In these equations, d_f is the HWHM of the spherical defect function of the etalon plates which is equal to $d_f = \frac{\pi}{\lambda N_{D_f}}$, N_{D_f} is the finesse of spherical defect function, which is written by $N_{D_f} = \frac{m^*}{2}$ when etalon plates have a spherical curvature of sagitta $\frac{\lambda}{m^*}$.

Now, the evaluation of Equation 3.16 can be made more conveniently by expanding the Airy function $A(x)$ (Equation 3.8) into its equivalent Fourier series [*Hernendez*, 1966] as

$$A(x) = \frac{1-R}{1+R}\left\{1 + 2\sum_{n=1}^{\infty} R^n \cos(2\pi n x)\right\}. \tag{3.26}$$

Convoluting these functions and designating $\mathrm{sinc}(\beta) = \sin(\pi\beta)/(\pi\beta)$, we get the instrumental transfer function $\psi(\lambda, r)$ as

$$\psi(\lambda, r) = \frac{1-R}{1+R}\left\{1 + 2\sum_{n=1}^{\infty} R^n \mathrm{sinc}\left(\frac{n}{N_{D_f}}\right)\mathrm{sinc}\left(\frac{n}{N_f}\right)\exp\left(-\frac{n^2 D^2}{4}\right)\cos(2\pi n x)\right\}. \tag{3.27}$$

We may now further evaluate Equation 3.16 in the analytic approximation by performing the integration using Equations 3.17 and 3.27. First, we note that the filter transmission function may be expanded in a Taylor series

$$T_F(\lambda) = T_{F_0}(\lambda_l) + T'_{F_0}(\lambda - \lambda_l) + \ldots \tag{3.28}$$

and also that

$$\int_0^\infty T_F(\lambda)d\lambda = \overline{\Delta\lambda_F}, \tag{3.29}$$

where $\overline{\Delta\lambda_F}$ is the filter integral width in nm. If we take only the first term in the filter expansion, which is equivalent to assuming that the filter transmission is constant over the etalon bandpass, the counting rate of an emission at the detector at a distance r from the fringe center N_r is given by

$$\begin{aligned} N_r &= C_{or}t\frac{1-R}{1+R}\left[\left.\frac{\partial R}{\partial\lambda}\right|_0 \overline{\Delta\lambda_F}\right. \\ &\quad \left. + R_0 T_{F_0}\left\{1 + 2\sum_{n=1}^{\infty} R^n \cos(2\pi n x)\mathrm{sinc}\left(\frac{n}{N_f}\right)\exp\left(-\frac{n^2[D^2+G^2]}{4}\right)\right\}\right] + B_r. \end{aligned} \tag{3.30}$$

Here, C_{or} represents the absolute intensity of the emission, $1 + 2\sum_{n=1}^{\infty} R^n \cos(2\pi nx)$ represents the Airy function , $\mathrm{sinc}(\frac{n}{N_f})$ comes from the spherical defect, D^2 from the microscopic defect, and G^2 from the Gaussian width corresponds to the kinetic temperature of the source. Measured line profiles may be fitted to Equation 3.30 in a nonlinear least-square sense to provide estimates for the geophysically significant parameters v, T, and R_0.

Although Equation 3.30 gives a complete form of an analytic expression of the counting rate of an emission at the detector, there is a large problem in the use of this equation because it is quite difficult to quantify the various included broadening terms separately from experiments. In the past, experimenters have used etalon manufacturers' specifications for the microscopic defects of etalon plates, the first-order spherical plate curvature has been estimated, and the aperture physical dimension has been used to give the aperture broadening [*Killeen and Hays*, 1984]. Usually, trial and error procedures are employed by changing these parameters until the calculated transmission, generally characterized by a working finesse, matches the measured transmission. However, there sometimes occur that an agreement between the calculated and measured finesse may be obtained with quite a different set of parameters.

Now, we suggest here that a more appropriate way to represent the FPDIS transfer function using a numerical technique where all broadening functions are subsumed into a full Fourier

series representation with empirically calculated coefficients. This approach is described as follows.

The form of Equation 3.30, which is essentially a cosine Fourier series convolved with a Gaussian source function, suggests the use of a full Fourier series to describe the instrument transfer function. The coefficients of such a series would contain implicit information on all the operative broadening effects. Therefore, the instrumental transfer function $\psi(x)$ can be written with x being a variable as

$$\psi(x) = a_0 + \sum_{n=1}^{\infty} \Big\{ a_n \cos(2\pi n x) + b_n \sin(2\pi n x) \Big\} \tag{3.31}$$

where a_n and b_n are the Fourier coefficients. Then the counting rate of an emission N_r is written by

$$\begin{aligned} N_r \;=\; & C_{or} a_0 t \Big[\frac{\partial R}{\partial \lambda}\Big|_0 \overline{\Delta\lambda_F} + R_0 T_{F_0}(\lambda_l) \Big\{ 1 + \sum_{n=0}^{\infty} \frac{a_n}{a_0} \cos\Big(\frac{4\pi n \mu d}{\lambda_l} \cos\theta \Big) \\ & + \frac{b_n}{a_0} \sin\Big(\frac{4\pi n \mu d}{\lambda_l} \cos\theta \Big) \Big\} \exp\Big\{ -n^2 \pi^2 \Delta\lambda_T^2 \Big(\frac{2\mu d}{\lambda_l} \Big)^2 \Big\} \Big] + B_r, \end{aligned} \tag{3.32}$$

where μ is the refractivity in the etalon cavity, and d is the etalon spacing. Then a_0, a_n, and b_n can be determined from the He-Ne calibration laser data, which is thought to satisfy the equations $\frac{\partial R}{\partial \lambda}|_0 = 0$ and $\Delta\lambda_T \simeq 0$. In this formulation, the coefficients a_n and b_n contain all the information necessary to describe the whole instrument functions including sensitivity differences as well as all the etalon and optical defects in the FPDIS.

The extraction of the winds, temperatures, source brightness, and continuum background intensity from a measured spectrogram may be achieved by performing a nonlinear least-square fit to Equation 3.32, e.g., the parabolic search technique of *Hays and Roble* [1971]. This method, however, has the disadvantage of being computationally intensive and is, therefore, unsuitable for the analysis of numerous spectrograms obtained by the FPDIS. Instead, we use a matrix technique that retains the accuracy of the full nonlinear least-squares fit and has the advantage of simplicity and speed described by *Killeen and Hays* [1984]. Then, observed data are analyzed

to evaluate line-of-sight bulk wind velocity of the emission v, kinetic temperature T, surface brightness R_0, and brightness of the background continuum for a unit wavelength $\frac{\partial R}{\partial \lambda}|_0$ using the Fourier coefficients determined by the analysis of laser calibration data. The comparison between results of v, T, R_0 by matrix technique and by parabolic search technique shows good agreement in values deduced by these two methods [*Killeen and Hays*, 1984].

3.6 Another Analytic Method of Wind Velocity Determination

In Section 3.5, we have described the method of data analysis of the Doppler fringe data of OI 630.0 nm and OI 557.7 nm emissions taken by the FPDIS using a technique based on a truncated Fourier series whose coefficients, which is thought to describe the instrument function of the optics, are generated by using a stabilized He-Ne calibration laser. Then, physical parameters such as wind velocity, kinetic temperature, and surface brightness of the emission are determined using a matrix nonlinear least-squares fit technique. In this section, another method to determine wind velocities of the emission is described. It is a simpler method than the matrix nonlinear least-square method and is called the 'Gaussian fit method'. The basic principle of this method is as follows. In order to estimate the bulk wind velocity of the emission, the Doppler shift of emission wavelength, which is thought to be represented by the shift of peak position of each fringe peak, is determined by fitting each fringe profile of sliced image data which is represented in the X-space (see Section 3.4.2) by a Gaussian function

$$y = A \exp\left(-\frac{(x - P_0)^2}{B^2}\right) \tag{3.33}$$

using a non-linear least squares method. Then, after translating the difference of emission wavelength, the derived peak position P_0 is compared to the reference He-Ne laser peak position, and bulk wind velocity is determined.

The purpose of introducing another analytical method of wind velocity is given as follows.

First, the reliability and errors of wind velocities derived by these two methods can be estimated by performing another analytic method.

Secondly, it is possible to decide absolute wind velocities by using the Gaussian fitting method and wind-zero data derived from 557.7 nm and 630.0 nm emissions taken on a totally cloudy night. Since the emissions of 557.7 nm and 630.0 nm scattered by clouds are thought to be completely isotropic, the line-of-sight component of wind velocity estimated from the Doppler shift of the emission is thought to be zero on an average. Wind velocities derived by the matrix method described in Section 3.5 are relative values, because an absolute zero-wind reference is not considered in the analysis and, therefore, there may remain some arbitrary decisions on wind velocity.

The third reason is that it is easier and faster to derive wind velocities from the Doppler fringe data than using the matrix method, in which one sometimes faces a difficulty in executing a nonlinear least-squares fit to Equation 3.32 which often diverges especially when the count rate of a fringe is low.

Now, we start with Equations 3.8 and 3.9 since the peak position of each fringe described in Equation 3.16 is determined by the peaks of the Airy function (Equation 3.8). Considering that $A(x)$ in Equation 3.8 has its peaks at $x = 0, \pm\pi, \pm 2\pi, \ldots$, we will remark on x from now. Since $f \gg r$, i.e. the focal length of a focusing lens is much larger than the distance in detector, we can approximate Equation 3.15 as

$$x = \frac{4\pi\mu d}{\lambda_e}\left(1 - \frac{R^2}{2f_0^2}\right) \tag{3.34}$$

by neglecting the third and following terms inside the parentheses in Equation 3.15, where R represents the distance from the optical center on the detector, μ is the refractivity in the etalon cavity, d is the etalon spacing, λ_e is the wavelength of the object emission, and f_0 is the focal length of the focusing lens of the FPDIS. If we write Equation 3.34 by order number m instead of x, we get

$$m = \frac{2\mu d}{\lambda_e}\left(1 - \frac{R^2}{2f_0^2}\right) \tag{3.35}$$

where $m = \frac{x}{2\pi}$. If we use the substitution used in Section 3.4.2, i.e., $X = (r - C_x)^2 = R^2$, Equation 3.35 becomes

$$m = \frac{2\mu d}{\lambda_e}\left(1 - \frac{X}{2f_0^2}\right), \tag{3.36}$$

namely,

$$\begin{aligned} X(= R^2) &= 2f_0^2\left(1 - \frac{m\lambda_e}{2\mu d}\right) \\ &= -\frac{f_0^2 m}{\mu d}\lambda_e + 2f_0^2. \end{aligned} \tag{3.37}$$

Now, we consider that the wavelength of emission is shifted by the Doppler effect of the bulk motion of the emission relative to the observer, and the resulting wavelength comes to $\lambda_e + \Delta\lambda$. At that time, the position of the emission on the detector X' becomes

$$X' = -\frac{f_0^2 m}{\mu d}(\lambda_e + \Delta\lambda) + 2f_0^2. \tag{3.38}$$

When subtracting Equation 3.38 from Equation 3.37, we get

$$X - X' = \frac{f_0^2 m}{\mu d}\Delta\lambda \tag{3.39}$$

namely,

$$\Delta\lambda = \frac{\mu d}{f_0^2 m}(X - X'). \tag{3.40}$$

We now estimate the line-of-sight component of the relative bulk motion of the emission, which is designated as v (m/s). Since the shift of wavelength of an emission in Equation 3.40 is considered to be due to the Doppler effect of v, we can write the relationship between v and $\Delta\lambda$ by taking positive values of v for the away direction from the observer as

$$\frac{\lambda + \Delta\lambda}{\lambda} = \frac{c + v}{c} \tag{3.41}$$

namely,

$$v = c\frac{\lambda + \Delta\lambda}{\lambda} - c = \frac{c}{\lambda}\Delta\lambda. \tag{3.42}$$

Putting Equation 3.40 to this equation, we get

$$v = \frac{c}{\lambda}\frac{\mu d}{f_0^2 m}(X - X') \tag{3.43}$$

where X is the position of a zero-wind fringe peak and X' is that of relative velocity v.

Now actual procedures in order to derive neutral wind velocities from He-Ne calibration laser data, auroral fringe data, and cloudy day's calibration data are described. First, we consider that a fringe of a stabilized He-Ne calibration laser ($\lambda = 632.8164$ nm in the dry air at $15°C$, 1-atm) of m-th order m_L is observed at the peak position of x_{L_0} on cloudy calibration data, and $x_{L_0} + \delta x_L$ on the observation day of attention as shown in Figure 3.15 (a). From Equation 3.36, it can be written as

$$m_L = \frac{2\mu d_0}{\lambda_L}\left(1 - \frac{x_{L_0}}{2f_0^2}\right) = \frac{2\mu d_0(1+\delta_d)}{\lambda_L}\left(1 - \frac{x_{L_0} + \delta x_L}{2f_0^2}\right) \tag{3.44}$$

where d_0 and $d_0(1+\delta)$ represent the etalon spacing of those days which may change a little due to the environmental condition, such as air pressure and/or humidity within the range of an order of m of interference fringes.

For a fringe of auroral 630.0308 and/or 557.7345 nm emission, the same kind of relation exists but for another order number $m_{63(55)}$ as shown in Figure 3.15 (b). And it can be written as

$$m_{63(55)} = \frac{2\mu d_0}{\lambda_{63(55)}}\left(1 - \frac{x_{63(55)}}{2f_0^2}\right) = \frac{2\mu d_0(1+\delta_d)}{\lambda_{63(55)}}\left(1 - \frac{x_{63(55)} + \delta x_{63(55)}}{2f_0^2}\right). \tag{3.45}$$

Now, writing $\mu d_0 = t_0$ and $\mu d_0(1+\delta d) = t_0(1+\delta t)$, Equation 3.44 can be written as

$$m_L = \frac{2t_0}{\lambda_L}\left(1 - \frac{x_{L_0}}{2f_0^2}\right) = \frac{2t_0(1+\delta_t)}{\lambda_L}\left(1 - \frac{x_{L_0} + \delta x_L}{2f_0^2}\right) \tag{3.46}$$

Then, δt is derived as

$$\delta t = \frac{\delta x_L}{2f_0^2 - x_{L_0} - \delta x_L}. \tag{3.47}$$

Similarly, δt is derived from auroral fringe data as

$$\delta t = \frac{\delta x_{63(55)}}{2f_0^2 - x_{63(55)} - \delta x_{63(55)}}. \tag{3.48}$$

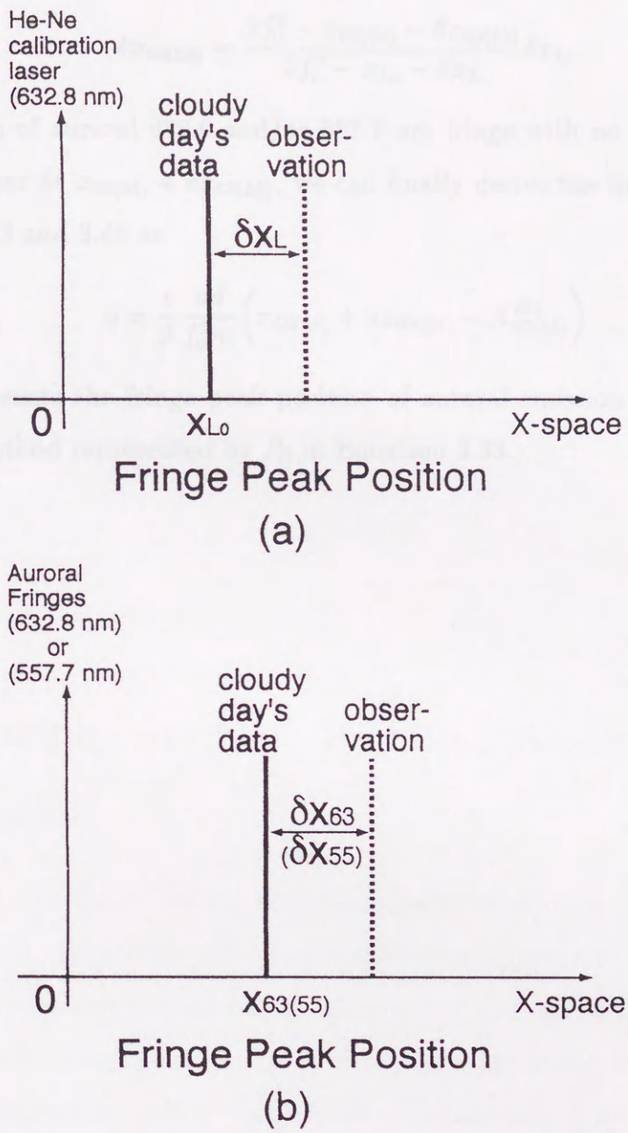

Figure 3.15: Schematic figures which describe peak positions of He-Ne calibration laser fringe peaks on cloudy day's data (x_{L_0}) and on the observation day of attention ($x_{L_0} + \delta x_L$) (a), and those for auroral fringes ($x_{63(55)}$ and $x_{63(55)} + \delta x_{63(55)}$) (b).

From Equations 3.47 and 3.48, we can get the following relation as

$$\delta x_{63(55)} = \frac{2f_0^2 - x_{63(55)} - \delta x_{63(55)}}{2f_0^2 - x_{L_0} - \delta x_L} \delta x_L. \tag{3.49}$$

Since peak position of auroral 630.0 and/or 557.7 nm fringe with no Doppler shift ($v = 0$) is thought to be appear at $x_{63(55)} + \delta x_{63(55)}$, we can finally derive the line-of-sight wind velocity from Equations 3.43 and 3.49 as

$$v = \frac{c}{\lambda} \frac{\mu d}{f_0^2 m} \left(x_{63(55)} + \delta x_{63(55)} - X^{obs}_{63(55)} \right) \tag{3.50}$$

where $X^{obs}_{63(55)}$ represents the fringe peak position of auroral emission which is determined by the Gaussian fit method represented by P_0 in Equation 3.33.

Chapter 4

OBSERVATIONS OVER SYOWA STATION, ANTARCTICA

Observations over Syowa Station is described in this Chapter.

4.1 Installation of the FPDIS at Syowa Station, Antarctica

After fine adjustments to the optics and test observations were performed at Zao Observatory, Japan in August, 1989, the FPDIS was disassembled into its components, i.e., PIH and CCD detectors, Fabry-Perot etalon, fore-optics, imaging-optics, and etalon chamber. These components were packed and transported, first, to Tokyo where the research vessel of the Japanese Antarctic Research Expedition called 'Shirase' left for Antarctica. The packages of the FPDIS were then carefully shipped on the Shirase. The Shirase left Harumi wharf, Tokyo port on November 14, 1989 and arrived at Syowa Station, Antarctica after a one-month voyage. The packages were transported to the 'Information Processing hut' of Syowa Station where the FPDIS was reconstructed. Installation of the FPDIS was accomplished by the following proce-

dures described below.

1. A roof opening for observation was constructed on the roof of the Information Processing hut from which the top of the FPDIS, i.e., the objective fish-eye lens protruded. The appearance of this opening is shown in Figure 4.1.

2. The FPDIS was then reconstructed inside the Information Processing hut and peripheral equipment was also installed as shown in Figures 4.2 through 4.4. Figure 4.2 shows the appearance of the FPDIS with the picture taken from the floor up. Figure 4.3 shows the FPDIS and peripheral equipment, e.g., the laser stabilization system, the filter wheel controller, the HV controller of the PIH, the refrigerator to cool the CCD, and the CS100 etalon stabilization system. Figure 4.4 shows the video disk image data recorder LV-250H and the 2-dimensional image processor EXCEL with a PC-9801 personal computer which controls the EXCEL.

3. Then fine adjustments to the optics in the FPDIS were performed by following the procedures described below;

   - First, a focus of the fore-optics is adjusted so that an image of outer scenery is focused onto the 2-nd aperture position by watching the image on a diffuser paper pasting on the 2-nd aperture.
   - Secondly, the optical center position of the optics and that of the etalon are matched by adjusting the slant angle of the etalon.
   - Thirdly, the etalon plates are aligned to almost parallel by adjusting the CS100 etalon controller by following the instructions manual.
   - Fourthly, a focus of the imaging-optics is adjusted so that interference fringes are focused onto the photocathode of the PIH.

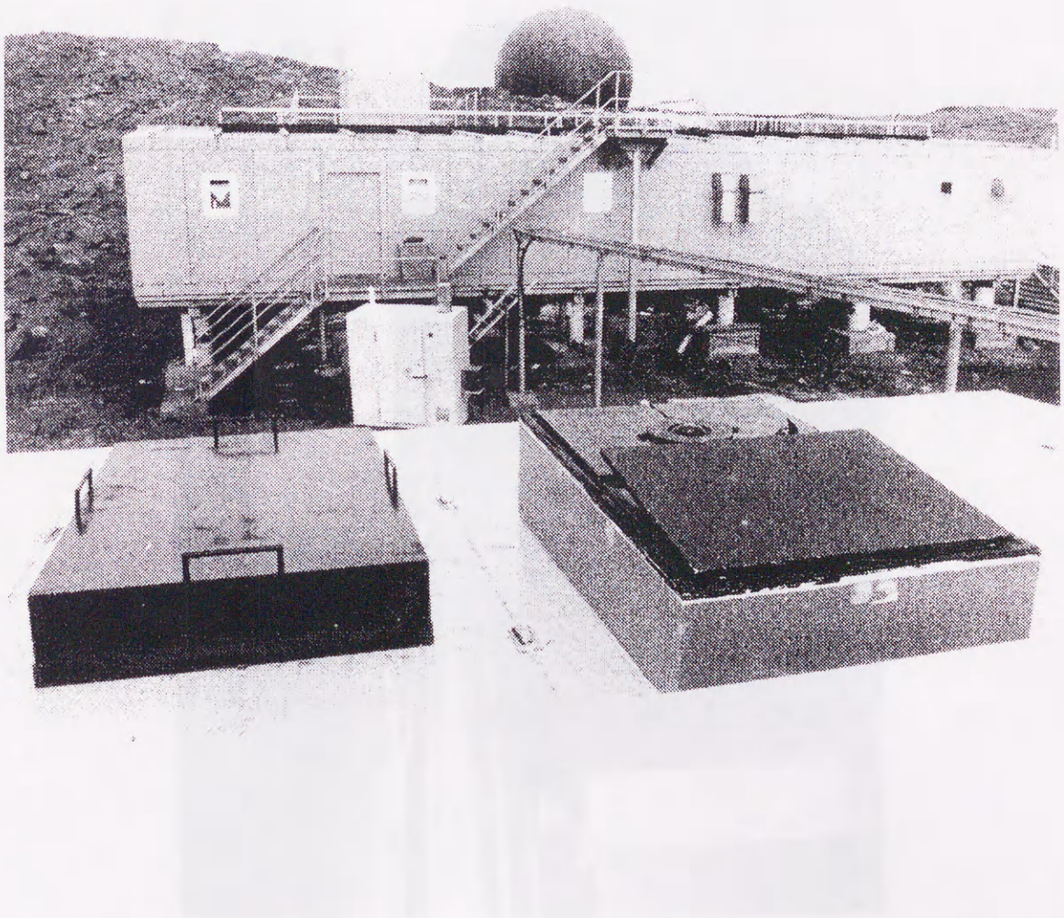

Figure 4.1: The appearance of the roof opening for observation constructed on the roof of the Information Processing hut at the Syowa Station, Antarctica. The objective fish-eye lens of the FPDIS can be seen at the far side of the opening. The plate in the opening can be opened in order to check the condition of the objective lens, from dewing or frosting, from inside the hut. The opening is covered with a cover shown on the left side of the picture. The Satellite Tracking hut and the Radome of multi-purpose antenna system are seen on the back.

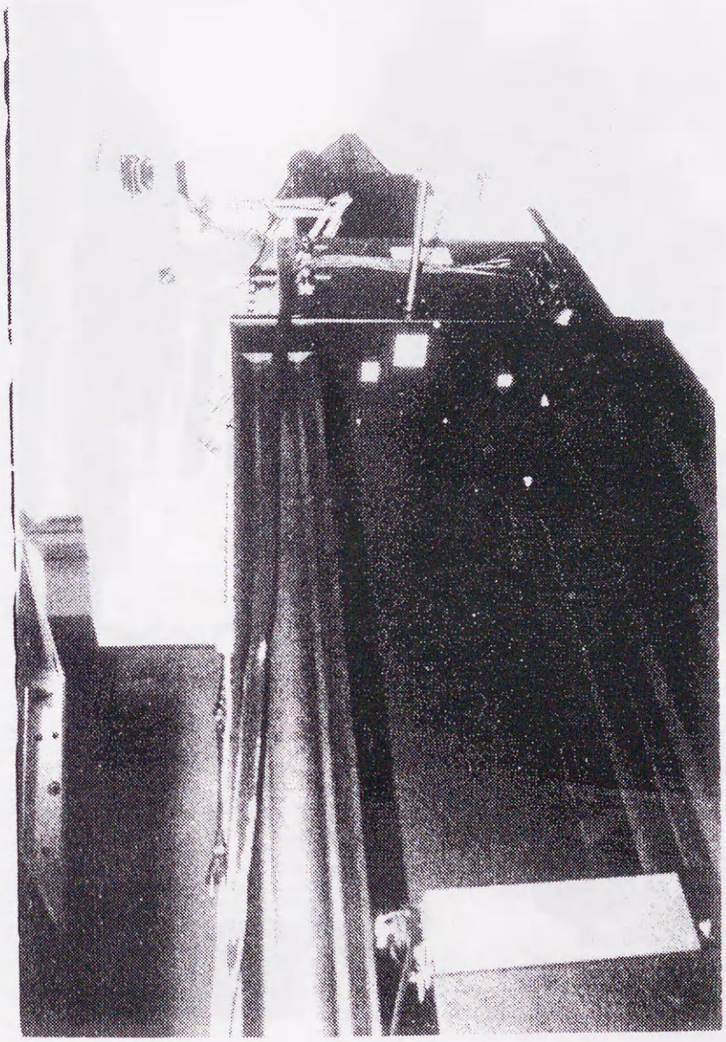

Figure 4.2: The appearance of the FPDIS installed in the hut with its fore-optics protruding out of the roof opening.

Figure 4.3: The FPDIS and its peripheral equipment. The FPDIS is on the upper right side of the picture, while the laser stabilization system is seen at the bottom of the FPDIS. On the left side, the filter wheel controller, the HV controller of the PIH, the refrigerator to cool the CCD, and the CS100 etalon stabilization system are mounted, from top to the bottom, respectively.

Figure 4.4: The equipment for image data processing and data storage for the FPDIS. The video disk image data recorder LV-250II, the 2-dimensional image processor EXCEL, the video printer, the video timer and two monitors are shown from the bottom to the top on the left side, while PC-9801 personal computer which controls the EXCEL is shown on the right side of this picture.

- Finally, a focus of the aspheric lens which projects an output image of the PIH onto the CCD is adjusted in addition to adjusting the X-Y stage to an adequate position on which the CCD image sensor is mounted.

4. Then, the electric gain of the CCD detector is adjusted in order that the maximum signal to noise ratio is acquired when taking photon counting images.

The installation of the FPDIS was executed from February to March, 1990. Then observations of thermospheric winds and temperatures began in April, 1990 when dark nights began to appear at Syowa Station.

4.2 Summary of Observations at Syowa Station

Fabry-Perot Doppler imaging observations of thermospheric winds and temperatures by the FPDIS have been carried out at Syowa Station, Antarctica for a period of one austral winter in 1990. The observations were made on 46 clear nights from April 1, 1990 to September 20, 1990 covering various auroral conditions. Summary of the observations is given in Table 4.1. Among them, several kinds of data which are used for calibrations described in Chapter 3 were taken along with auroral observations. For example, all-sky star images were taken on April 4 and April 20, 1990, optical grid images were taken on August 12 and December 20, 1990, and calibration laser fringe data were taken for various values of etalon cavity spacing on January 7, 1991. On July 13, 1990, fringe data of 630.0 nm and 557.7 nm all-sky images in addition to those of He-Ne calibration laser were taken under totally cloudy condition in order to determine the wind-zero position of the interference fringe which is used to derive the absolute wind velocity by the method described in Section 3.6.

On April 19 and June 23, 1990, the focus of the optics was re-adjusted, while on June 23, 1990, CCD gain was re-adjusted. The data taken from July 23 to July 26 may contain large errors since we were not aware of the presence of numerous dew drops on the aspheric lens just

Table 4.1: Summary of the Fabry-Perot Doppler Imaging observations at Syowa Station, Antarctica from April to September, 1990. The symbol 'o' indicates that full observation/calibration is made, while '◇' indicates that observation/calibration is made partially. OD I.D. is the identifier of the optical video disk on which image data of the day are recorded. The notation $\sum$K Pr/Ne represents the summation of K-indices at Syowa Station for the day and the next day, while $\sum$Kp Pr/Ne represents those of Kp-indices.

No.	Date YearMM.DD	TD	Time(UT) Start	End	Total Time	Obs.Wave 5577	6300	Mode FP	I	Cal	OD I.D.	$\sum$K Pr/Ne	$\sum$Kp Pr/Ne
1	1990. 4. 1	91	00:04	01:43	01:39	o	o	o	o	–	900301(1-B)	12/12	13/20
2	4. 2	92	19:47	01:03	05:16	o	o	o	o	–	"	12/21	20/25
3	4. 4	94	21:21	01:32	04:11	o	o	o	◇	o	"	19/13	18/17
4	4. 19	109	19:29	20:34	01:05	o	o	o	◇	◇	900401(2-A)	18/29	17/25
5	4. 20	110	17:52	23:38	05:46	o	o	o	◇	◇	"	29/18	25/18
6	4. 21	111	16:50	00:46	07:56	o	o	o	◇	–	900402(2-B)	18/21	18/23
7	4. 22	112	17:12	21:42	04:30	◇	o	o	–	–	"	21/33	23/35
8	4. 25	115	23:04	02:06	03:02	o	o	o	–	–	900403(3-A)	26/24	27/20
9	4. 26	116	17:40	01:16	07:36	o	o	o	–	–	900404(3-B)	24/29	20/24
10	4. 27	117	18:00	03:11	09:11	o	o	o	–	–	"	29/31	24/27
11	4. 28	118	19:11	02:05	06:54	o	o	o	–	–	900405(4-A)	31/35	27/32
12	5. 17	137	17:35	20:37	03:02	o	o	o	–	–	"	6/26	9/30
13	5. 18	138	16:06	22:43	06:37	o	o	o	◇	–	900501(4-B)	26/24	30/26
14	5. 20	140	14:48	03:06	12:18	o	o	o	–	–	"	28/27	27/26
15	5. 21	141	19:30	02:13	06:43	o	o	o	–	–	900502(5-A)	27/34	26/34
16	6. 23	174	18:17	00:07	05:50	o	o	o	–	–	"	14/10	13/16
17	6. 27	178	19:46	03:26	07:40	o	o	o	–	–	900601(5-B)	16/15	17/15
18	6. 28	179	21:22	03:33	06:11	o	o	o	–	–	"	15/15	15/15
19	6. 29	180	23:20	03:56	04:36	o	o	o	–	–	900602(6-A)	15/ 8	15/ 7
20	6. 30	181	01:50	03:12	01:22	o	o	o	–	–	"	8/10	7/20
21	7. 13	194	16:42	20:42	04:00	o	o	–	–	o	"	26/21	21/20
22	7. 23	204	14:31	19:16	04:45	o	o	o	–	–	900701(6-B)	12/ 9	8/ 8
23	7. 24	205	18:32	04:11	09:39	o	o	o	–	–	900702(7-A)	9/ 4	8/ 8
24	7. 25	206	18:45	03:30	08:45	o	o	o	–	–	"	4/11	8/16
25	7. 26	207	19:50	03:01	07:11	◇	o	o	–	–	900703(7-B)	11/16	16/17
26	7. 27	208	21:18	03:04	05:46	–	o	o	–	–	900704(8-A)	16/40	17/48
27	7. 28	209	23:22	03:33	04:11	–	o	o	–	–	"	40/42	48/45
28	8. 12	224	22:33	03:05	04:32	–	o	o	–	◇	900801(8-B)	21/26	14/21
29	8. 13	225	16:14	02:08	09:54	o	o	o	–	–	900802(9-A)	26/26	21/25
30	8. 14	226	18:08	03:31	09:23	o	o	o	–	–	900803(9-B)	26/31	25/29
31	8. 19	231	22:08	03:10	05:02	–	o	o	–	–	900804(10-A)	27/28	23/26
32	8. 20	232	17:00	03:16	10:16	o	o	o	–	–	900805(10-B)	28/33	26/33
33	8. 21	233	16:42	03:04	10:22	o	o	o	–	–	900806(11-A)	33/39	33/40
34	8. 22	234	16:23	03:05	10:42	o	o	o	–	–	900807(11-B)	39/46	40/46
35	8. 23	235	18:37	02:59	08:22	o	o	o	–	–	900808(12-A)	46/27	46/27
36	8. 24	236	22:10	02:39	04:29	o	o	o	–	–	900809(12-B)	27/15	27/13
37	9. 10	253	18:20	19:54	01:34	–	o	o	–	–	900810(13-A)	23/26	17/30
38	9. 11	254	17:25	01:14	07:49	–	o	o	–	–	900901(13-B)	26/29	30/27
39	9. 12	255	17:27	01:38	08:11	o	–	o	–	–	900902(14-A)	29/27	27/26
40	9. 13	256	17:28	01:12	07:44	–	o	o	–	–	900903(14-B)	27/28	26/27
41	9. 14	257	17:42	01:29	07:47	o	–	o	–	–	900904(15-A)	28/28	27/28
42	9. 15	258	17:17	01:16	07:59	–	o	o	–	–	900905(15-B)	28/28	28/28
43	9. 17	260	20:47	00:04	03:17	o	–	o	–	–	"	22/22	22/26
44	9. 18	261	18:00	01:21	07:21	–	o	o	–	–	900906(16-A)	22/28	26/24
45	9. 19	262	18:02	00:52	06:50	o	–	o	–	–	900907(16-B)	28/25	24/20
46	9. 20	263	18:43	01:04	06:21	–	o	o	–	–	900908(17-A)	25/25	20/24
47	12. 20	354	–	–	–	–	–	–	–	o	901201(17-B)	–	–
48	1991. 1. 7	7	–	–	–	–	–	◇	–	o	"	–	–

under the objective fish-eye lens which are caused by the blizzard and are thought to have bad influence on the data.

In this thesis, observational results on September 11/12, September 12/13, and September 13/14, 1990 are presented. Geophysical and solar data for September, 1990 are listed in Table 4.2. As shown in Table 4.2, ΣKp values on September 11, 12, 13 are $30^+, 27^-, 26$, indicating that geomagnetic conditions in the auroral region on those days are moderate to active.

4.3 Observational Results on Thermospheric Neutral Temperatures and Wind Velocities on September 11/12, 1990

In this section, results on thermospheric neutral temperature and line-of-sight velocities derived from the FPDIS image data taken on September 11/12, 1990 are presented. On this night, Doppler fringe data of auroral OI 630.0 nm emission were taken in a period from 17:25 UT on September 11 to 01:14 UT on September 12, while calibration fringe data using the stabilized He-Ne laser as a source were taken 4 times, at the beginning, around the middle, and the end of the auroral observation data period, respectively. As summary of observations on this day is shown in Table 4.3.

4.3.1 Auroral activities on September 11 / 12, 1990

The three-hourly Kp-indices are 3^-, 3^+, 4, 4^-, 4, 4, 4, 5^- for September 11 and 4, 4, 3, 3^+, 3^-, 3, 4^-, 3 for September 12, respectively. The K-indices at Syowa Station determined from the Syowa magnetometer data are 3, 3, 3, 3, 2, 3, 3, 6 for September 11 and 5, 5, 5, 2, 2, 3, 4, 3 for September 12, respectively. The fluxgate triaxial magnetometer and CNA data at Syowa Station for September 11 are shown in Figure 4.5. Figure 4.6 shows the same data with an

Table 4.2: Geophysical and solar parameters for September, 1990, edited by [*Coffey, H.E.*, 1991].

Geomagnetic and Solar Data

HELEN E. COFFEY, EDITOR

World Data Center A for Solar-Terrestrial Physics, NOAA, Boulder, Colorado 80302

SEPTEMBER 1990

Day		Kp Three-Hourly Indices 1 2 3 4	5 6 7 8	Sum	Ap	Cp	Km Three-Hourly Indices 1 2 3 4	5 6 7 8	Am	aa Provisional N	S	M	
1	D4	2+ 3- 1 4	7- 4 3- 1+	25-	26	1.2	2+ 3- 1 3+	6- 4- 3- 2-	38	34	38	24	47
2	Q1	1- 0+ 0+ 1-	1- 0 1- 0	3+	2	0.0	1 1- 0 1-	1- 0+ 1- 0+	4	9	4	8	5 C
3	Q2	0 1- 1- 2-	2- 1- 1 1	7+	4	0.1	0+ 1- 1 1+	1+ 1- 1+ 1	6	12	3	6	9 CC
4	Q6A	1- 1- 1 2	2 3- 2+ 3+	15-	8	0.4	1 1- 1 2	2 3- 2 3	15	19	20	11	29
5		3+ 3- 2+ 2+	3- 2+ 2 2+	20	11	0.6	4- 3- 2+ 3-	3- 2+ 2- 3-	22	26	17	24	19
6		3 2 3+ 3	3- 2+ 2+ 2+	21	12	0.7	3- 2 3+ 3-	3- 2 3- 3-	23	26	24	27	23
7		3 3- 3 3+	3+ 4- 1+ 2	22+	14	0.8	3 2+ 3 3	3+ 3 1+ 2-	26	25	29	28	26
8	Q7A	2+ 2 2- 2-	2- 2+ 2+ 3	17	8	0.5	2 2- 2- 2-	2- 2 2+ 3	16	29	14	14	30
9	Q9A	3- 2+ 1+ 3-	3- 2 3- 2+	19-	10	0.5	2 2- 1- 2	2 2+ 3- 3-	16	25	12	15	22
10	Q10A	3 2+ 2+ 0+	1- 1 3 4+	17	11	0.6	3 2+ 3- 1-	1- 1 3 4	21	22	21	17	25
11	D1	3- 3+ 4 4-	4 4 4 5-	30+	25	1.2	3- 3+ 4 4-	4- 3 4- 4+	43	48	41	40	49
12		4 4 3 3+	3- 3 4- 3	27-	19	1.0	3+ 4 3 3+	3- 2+ 4- 3-	33	35	32	34	33
13		5- 3 2- 3+	3+ 3+ 3- 4	26	19	1.0	4+ 3- 2+ 3+	3 3+ 3- 3+	33	42	27	36	33
14		4 4 3+ 3+	3+ 3+ 3+ 2+	27	19	1.0	4- 3+ 3 3+	3 3 3 2	32	50	28	42	36
15	D3	3+ 4 3 4	5- 4- 3+ 2+	28+	22	1.1	3 4- 3- 4	4 4- 3 2+	39	38	51	42	48
16	D2	4- 3+ 4 5	4 3+ 2 3	28+	23	1.1	4- 3- 4- 4+	4- 3- 2- 3-	35	40	30	42	28
17		3- 3 3 3-	2+ 2 3 3	22-	12	0.7	2+ 2 3- 2	2+ 2- 3- 3	19	26	16	19	23
18		1 3- 3+ 4	4- 4 4 3+	26	19	1.0	1 2 3 4	3 4- 4- 3+	33	37	31	28	40
19		4+ 3+ 3- 2-	2- 4- 3- 4-	24-	16	0.9	4- 3- 3- 2	2- 4- 3- 3+	28	36	19	24	31
20		4 2 1 1+	1+ 2 3 5+	20	16	0.9	3+ 2- 1 1	2- 3 3+ 5-	27	31	22	16	36
21		4- 2+ 2+ 3+	3 3- 3 3+	24-	15	0.8	3 2+ 2 3	3+ 3- 3 3	27	28	25	21	32
22	D5	3+ 4 4- 2	3+ 4- 4- 4-	27+	20	1.0	3- 3+ 3+ 2+	3 3+ 3- 3+	31	40	28	26	41
23		4- 4 3 2+	2 3- 1+ 1+	20+	13	0.7	3 3+ 3- 2+	2- 3- 2 2	22	24	20	20	16
24		1+ 3- 3+ 2+	3+ 4- 3- 2	21+	13	0.7	1+ 2 3 2+	4- 3 3- 2-	23	27	25	20	32
25		3+ 3+ 2+ 2+	1 2- 3+ 3-	19+	11	0.7	3 3- 2+ 1+	1 1+ 3+ 3-	20	27	12	19	21
26		2+ 3 2 2	3 3 3+ 2	21-	12	0.7	2 2 2- 2	3 3- 3 2	19	29	17	17	29
27	Q5A	3- 2+ 3- 2-	2+ 2- 1 1+	16-	8	0.4	3- 2 3- 1+	3- 2 1+ 1+	15	21	11	15	17
28	Q8A	3+ 3 1 2+	3- 1- 1+ 2-	16	9	0.5	3 2+ 1- 2+	2+ 1 1+ 2-	15	20	17	22	14
29	Q4A	3- 2+ 2 2	1+ 0 1+ 2+	14	7	0.3	2+ 2- 2- 2-	1+ 0 1+ 2+	12	16	11	17	11 K
30	Q3	2+ 1- 1- 1-	1- 1- 2 2-	9+	5	0.2	2 1 1 0+	1- 0+ 2- 2	8	13	5	10	9 CC
Mean					14	0.71			23.4	28.5	21.7		25.1

Day	Kn Three-Hourly Indices 1 2 3 4	5 6 7 8	An	Ks Three-Hourly Indices 1 2 3 4	5 6 7 8	As	Sa	Prov Ri	Ra	Rs	IMF
1	2+ 3 1 3+	6 4 2+ 2-	41	2 3- 1 3+	5+ 3+ 3- 1+	34	171.4	126	125	123	
2	1+ 1- 0+ 0+	0+ 0 1- 0	3	1- 1- 0 1-	1 0+ 1- 1-	4	168.9	116	124	120	
3	0 1- 1+ 1+	2- 1 1+ 2-	8	0+ 1- 1- 1+	1- 1- 1 1-	5	162.6	131	135	114	
4	1 1- 1 2+	2+ 3- 2 3	16	1 1- 1 2-	2 3- 2 3	14	158.2*	134	141	109	
5	3 3- 3- 3-	3- 3- 2- 3-	24	4+ 3- 2 2	2 2- 1+ 2	21	157.5	118	119	108	
6	2+ 2 3+ 3	3- 2+ 3- 3-	24	3 2- 4- 2+	3- 2 3- 2+	23	157.6	118	114	108	
7	3- 2 3+ 3	4 3+ 2- 2-	27	3+ 3- 3 3	3 3- 1+ 2-	24	165.1	103	107	116	
8	2 2- 2- 1+	2- 2 3- 3+	17	2+ 2- 2 2	2- 2- 2+ 3	16	163.5	112	104	115	
9	2+ 2- 1 2+	2+ 3- 3- 3-	18	2- 2- 1- 2-	2 2- 3- 3-	14	170.4	113	112	122	
10	3- 2+ 2 1-	1- 1 3+ 4+	21	3+ 2+ 3 0+	0+ 1- 3- 4-	21	171.2	121	118	123	
11	3- 3+ 4 4	4+ 3+ 4- 4	48	3- 4- 3+ 3+	3+ 3 3+ 5-	39	180.6	116	113	133	
12	4- 4- 3+ 3+	3 3- 4- 3-	36	3+ 4 3- 3	3- 2 4- 3-	31	193.3	124	127	147	
13	5- 3- 2+ 3+	3 4- 3- 4-	36	4+ 2 2 3+	3 3 3- 3	30	198.0	142	139	152	
14	3+ 4- 3+ 3+	3+ 3+ 3+ 2	34	4- 3 3- 3+	3 3 3 2-	29	209.4*	178	164	164	
15	3 4- 3- 4	4+ 4 3 3-	41	3+ 3+ 3- 4+	4 3 3- 2+	37	207.3	162	158	162	
16	3+ 2+ 4- 4	4 3 2 3	35	4- 3- 4- 5-	4- 3- 2- 2	35	205.2	156	162	160	
17	3- 2+ 3- 2+	3- 2- 3 3	22	2 2 2+ 2	2- 2- 2+ 3-	16	210.7	142	144	166	
18	1 2 3 4+	3+ 4 4 3+	37	1- 2 3- 4-	3 3+ 4- 3+	30	207.5	136	138	162	
19	4- 3- 3- 2	2 4- 3 3+	29	4- 3- 3- 2	2- 3+ 2+ 3+	26	213.8	151	143	169	
20	3 2 1+ 1	2- 3- 3 4+	25	3+ 1 1- 1	1+ 3 4- 5-	28	204.0	135	142	158	
21	3 2+ 2+ 3+	3+ 3 3 3	28	3+ 2 2 3	3+ 2 3 3	25	203.2	139	138	157	
22	3- 3 3+ 2	3 4- 3 3+	30	3 4- 3+ 2+	3 3+ 3- 3	31	195.3	130	133	149	
23	3- 3 3 2	2- 3 2 2+	22	3 3+ 3- 3-	2- 2+ 2 2-	21	185.4	110	113	138	
24	1+ 2+ 3 2+	4 3+ 3- 2-	25	1+ 2- 3- 2	3+ 3 3- 2	20	178.7	101	101	131	
25	3 3- 2+ 1+	1+ 2- 3 3-	20	3+ 3- 2 2-	1- 1+ 3+ 3-	20	167.1	101	97	118	
26	2+ 2+ 2- 2-	3 3- 3+ 2	20	2 2 1+ 2+	3 3- 3- 2-	18	159.6	93	98	110	
27	2+ 2 3- 2-	3- 2 2- 1+	16	3 2 2+ 1+	2+ 2- 1- 1+	15	152.6	77	95	103	
28	3- 2+ 1 2-	2 1- 1+ 2-	13	3+ 3- 1- 3-	3- 1 1+ 2	17	152.1	113	119	102	
29	2+ 2- 2- 2-	1- 0 1+ 2+	11	3- 1+ 2- 2	2- 0+ 1+ 2+	12	150.1	119	127	100	
30	2 1- 1- 0+	1- 1- 2- 2	8	2 1 1 1-	1- 0+ 2- 2-	7	157.8	124	118	108	
Mean			24.5			22.1	179.3	124.7	125.6	131.6	

The Geophysikalisches Institut, University of Gottingen, prepares the quiet (Q) and disturbed (D) days, the geomagnetic planetary 3-hour-range indices (Kp), the average amplitude (Ap) and the magnetic character figures (Cp). The 10 most quiet days (Q1-Q10) and the five most disturbed days (D1-D5) are ordered from most quiet and from most disturbed, respectively. A and K mark quiet days that are not really quiet; an asterisk marks disturbed days that are not really disturbed. Geomagnetic 3-hour indices Km, Kn, Ks; daily mean values Am, An, As; and indices aa are prepared by M. Menvielle of the Institut de Physique du Globe, Paris, France. For the aa indices, daily north (N) and south (S) values and half-daily antipodal mean (M) values are given; quiet 24- and 48-hour intervals centered on 1200 UT are indicated by C if they are really quiet and by K if they are quiet with some slightly disturbed 3-hour periods.

Solar flux adjusted to 1 AU (Sa) are prepared by the National Research Council, Ottawa. An asterisk denotes flux adjusted for burst; b = ice on antenna. Provisional sunspot numbers (Ri) are prepared by A. Koeckelenbergh, Observatoire Royal de Belgique, Bruxelles. Sunspot numbers (Ra) are prepared by the American Association of Variable Star Observers. Sunspot numbers (Rs) are computed from the daily Sa values by WDC-A for Solar-Terrestrial Physics.

The inferred interplanetary magnetic field (IMF) directions are prepared from Vostok observations for the first half-day by the Institute for Terrestrial Magnetism, Ionosphere and Radio Propagation, Moscow, USSR when available. T = toward sun, A = away from sun, * = effect doubtful or not discernible, - = missing data.

These data are reprinted from the monthly publication SOLAR-GEOPHYSICAL DATA issued by World Data Center A for Solar-Terrestrial Physics, NOAA. SOLAR-GEOPHYSICAL DATA is available on either a data exchange or subscription basis. For information write to Eric A. Kihn, NOAA E/GC2, 325 Broadway, Boulder, Colorado 80303, USA. This table is also available on a subscription basis.

Table 4.3: Summary of observations on September 11/12, 1990.

I.D. of Data Period	Start Time (UT)	End Time (UT)	Data Period (hh:mm:ss)	Object	OVD I.D.	Start Frame	End Frame	Number of Frames	Filter (nm)	CCD CK	Fish-eye Aperture F	Room Temp (℃)
911L1	17:00:00	17:19:35	00:19:35	Laser Cal	900810(13-A)	08101	09200	1100	–	4	–	22.8
911F2	17:25:00	19:34:56	02:09:56	OI630.0nm	900810(13-A)	09201	16500	7300	630	4	16∼22	22.5
911L3	19:36:00	19:43:07	00:07:07	Laser Cal	900810(13-A)	16501	16900	400	–	4	–	22.6
911F4	19:44:02	22:43:50	02:59:48	OI630.0nm	900810(13-A)	16901	27000	11100	630	4	11∼22	22.4
911L5	22:49:00	23:15:38	00:26:38	Laser Cal	900901(13-B)	00004	01500	1497	–	4	–	22.9
911F6	23:17:00	01:14:28	01:57:28	OI630.0nm	900901(13-B)	01501	08100	8100	630	4	22∼16	22.9
911L7	01:19:00	01:29:40	00:10:40	Laser Cal	900901(13-B)	08101	08700	8700	–	4	–	23.1

expanded time scale to show more detailed magnetic perturbations for the observation period of the FPDIS from 20:00 to 24:00 on September 11.

It can be seen in Figures 4.5 and 4.6 that a great negative bay in the H-component with magnitude of 800 nT occurred around 21:30 UT, September 11. It corresponds to an auroral breakup event beginning at 21:38 UT which were observed by the all-sky SIT, CCD, and film cameras. The auroral morphology based on the monochromatic CCD camera [*Ono et al.*, 1987] data taken simultaneously at Syowa Station during the time of this event will be given in Section 4.3.4. The large disturbance seen in the magnetogram subsided by 23:00 UT although small variations still remained thereafter.

4.3.2 Result on thermospheric neutral temperatures

Now, results on thermospheric neutral temperatures obtained with the method described in Chapter 3 are given in this section. The number of points in an image for which temperatures are calculated is 24. These points are on the inner and outer fringes in 12 azimuthal directions for every 30 degrees. Notation of these points is defined in two different ways, as shown in Figures 4.7 (a) and (b).

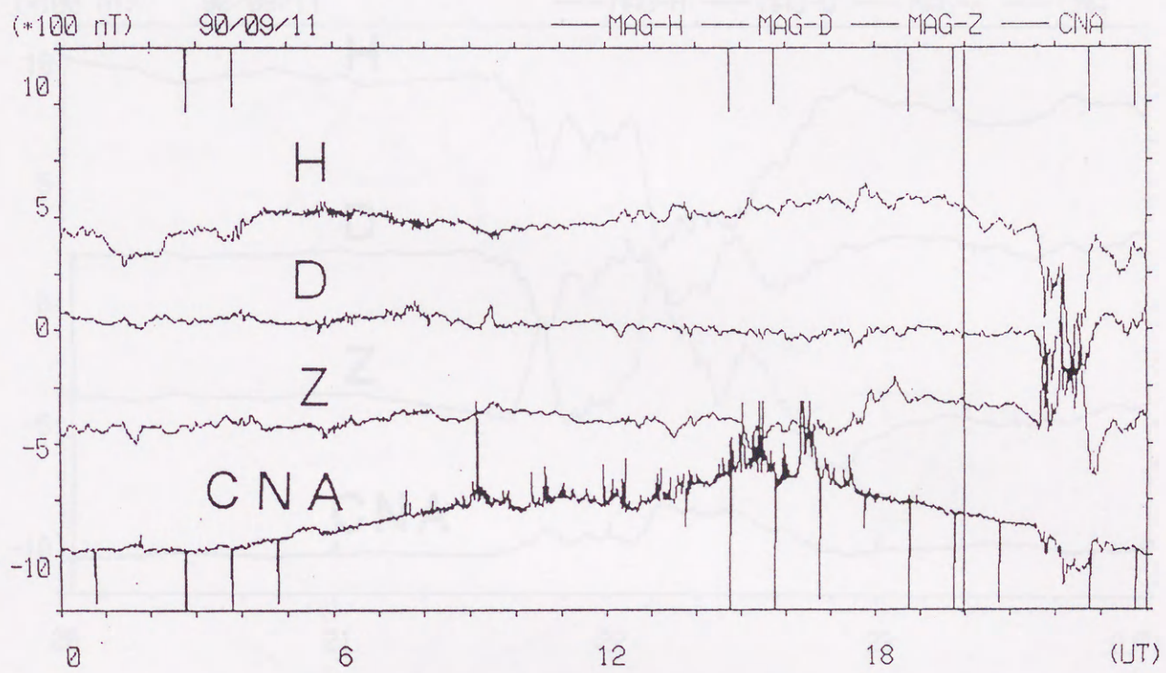

Figure 4.5: Triaxial magnetometer and CNA data at Syowa Station on September 11, 1990.

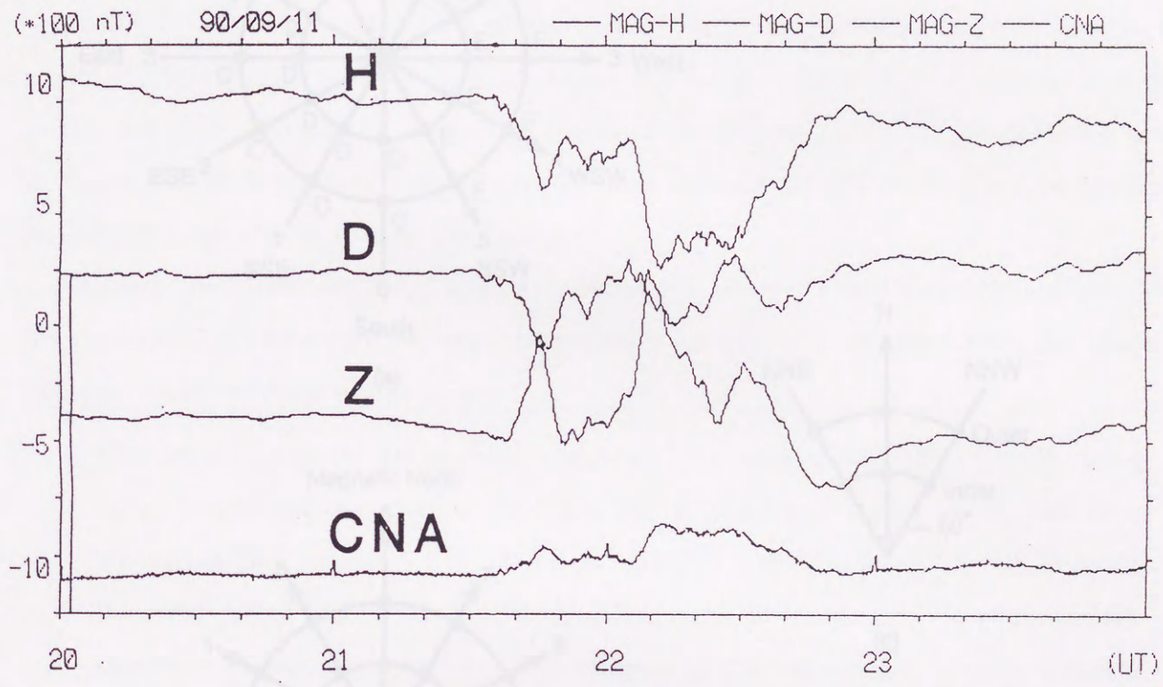

Figure 4.6: Triaxial magnetometer and CNA data at Syowa Station from 20:00 to 24:00 UT on September 11, 1990.

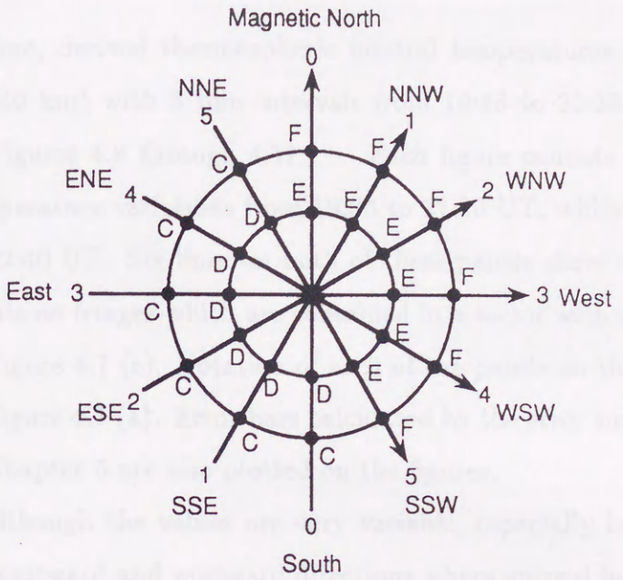

(a)

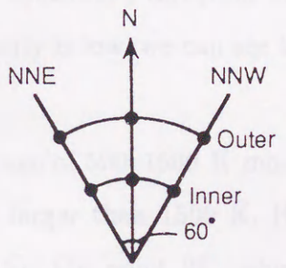

(c)

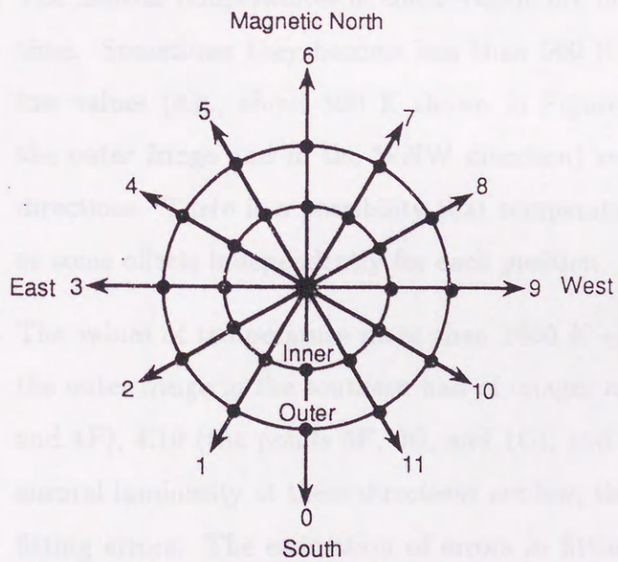

(b)

Figure 4.7: (a) and (b) are two different ways to that note the points for which analyses of the fringes data were performed; and (c) is a sector which is a part of (a) or (b) and contain 6 points. This sector is an example for the (magnetic) north direction.

Here, derived thermospheric neutral temperatures at the emission height of OI 630.0 nm (~240 km) with 3 min intervals from 19:48 to 22:39 UT on September 11, 1990 are shown in Figures 4.8 through 4.11. Each figure consists of two panels. The upper panel shows temperature variations from 19:30 to 21:00 UT, while the lower panel shows those from 21:00 to 22:40 UT. Six lines on both of these panels show variations of neutral temperatures at six points on fringes which are contained in a sector with an included angle of 60 degrees as shown in Figure 4.7 (c). Notation of each of the points on the fringes is given by the definition given in Figure 4.7 (a). Error bars calculated by the error simulation method which will be described in Chapter 5 are also plotted on the figures.

Although the values are very variable, especially in the southward direction and partly in the eastward and westward directions where auroral luminosity is low, we can see the following features in the temperature variation;

1. The neutral temperatures in the F-region are in a range of 500–1500 K most of the time. Sometimes they become less than 500 K and larger than 1500 K. However, low values (e.g., about 500 K shown in Figure 4.9 for the point 2F, which is on the outer fringe and in the WNW direction) seem to be observed at some certain directions. There is a possibility that temperature values contain systematic errors or some offsets independently for each position.

2. The values of temperature more than 1500 K are sometimes observed at points on the outer fringe in the southern half of images as seen in Figures 4.9 (the points 3F and 4F), 4.10 (the points 5F, 0C, and 1C), and 4.11 (the points 3D and 2C). Since auroral luminosity at these directions are low, these values are considered to contain fitting errors. The estimation of errors in fitting will be discussed using the error simulation in Chapter 5.

3. Short time-scale (in period of 15 to 25 min) periodic variations in neutral temperatures are seen in the northward section as seen in Figure 4.8.

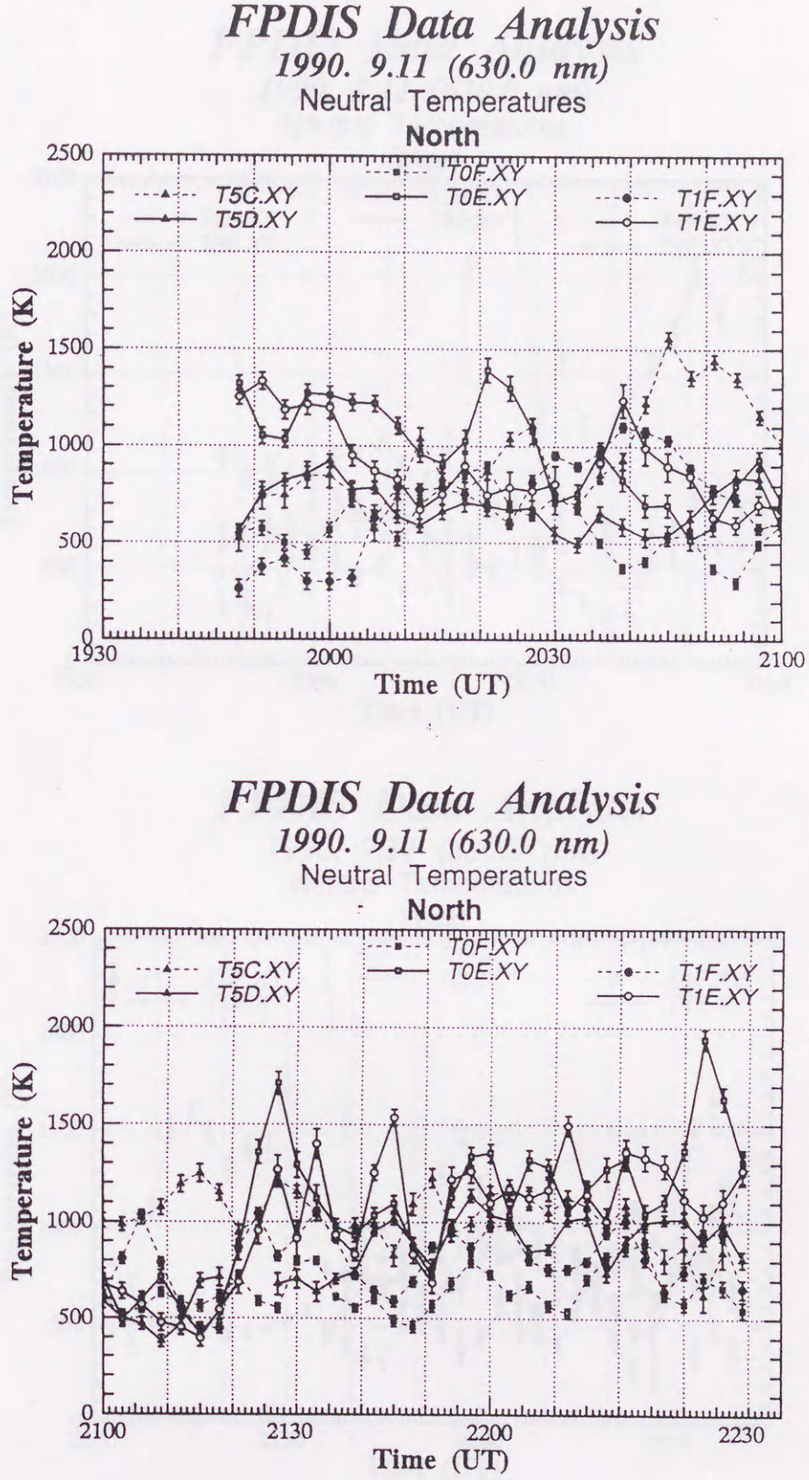

Figure 4.8: Variations of thermospheric neutral temperatures derived from the FPDIS Doppler fringe data. This figure shows the variations of 6 points in the (magnetic) Northward direction from 19:48 to 21:00 (upper panel) and from 21:00 to 22:39 (bottom panel) on September 11, 1990. Error bars are also shown on the figure.

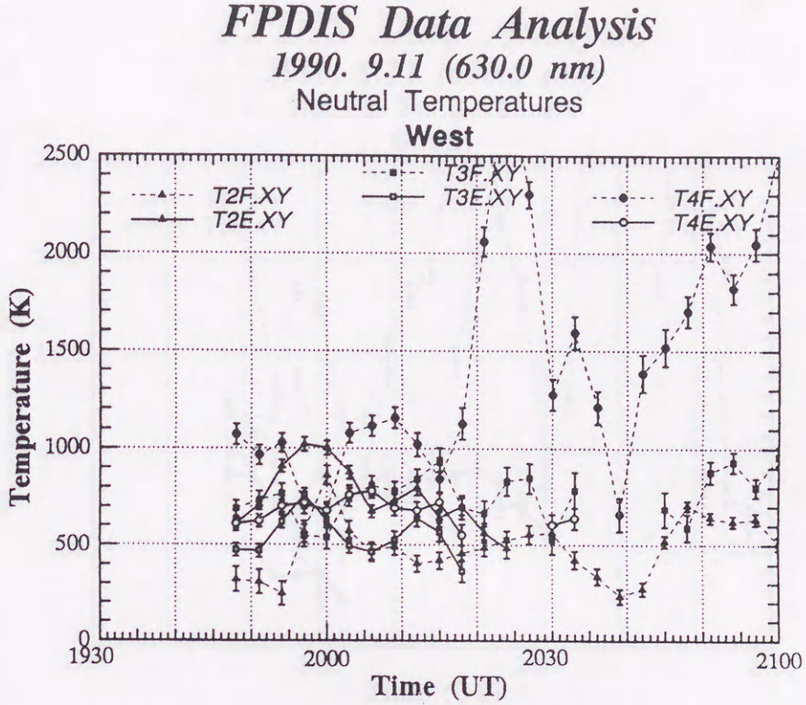

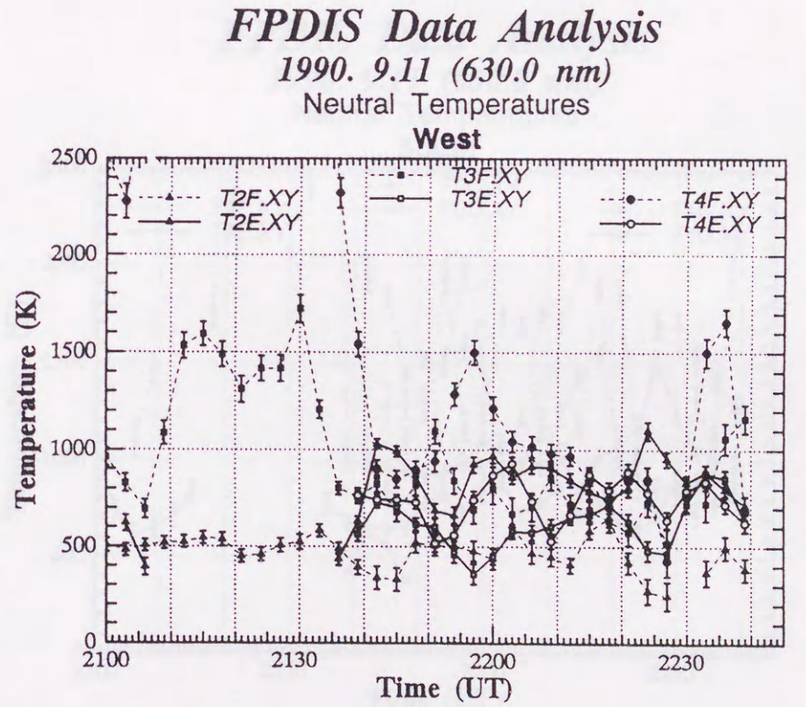

Figure 4.9: Same as Figure 4.8 but for the (magnetic) Westward direction.

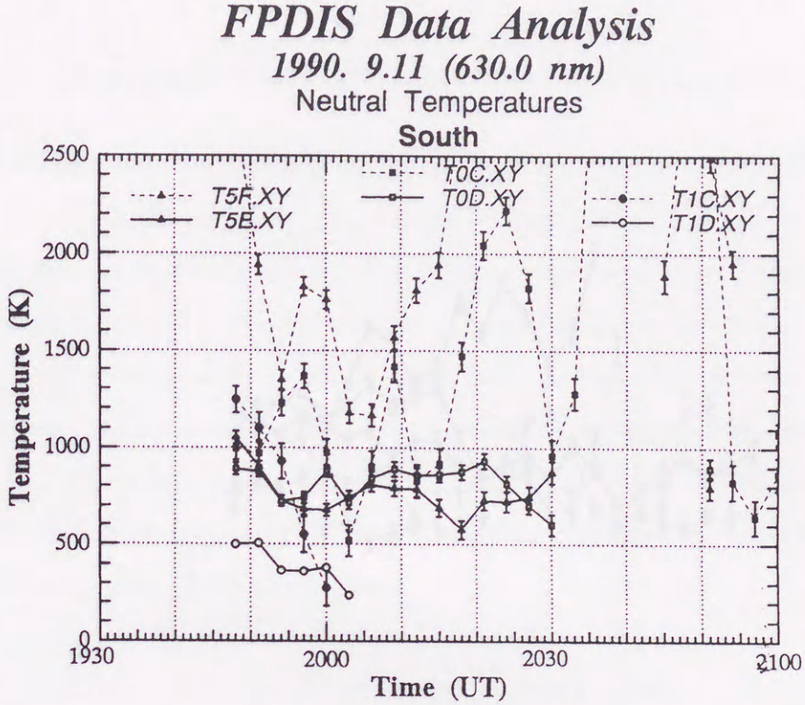

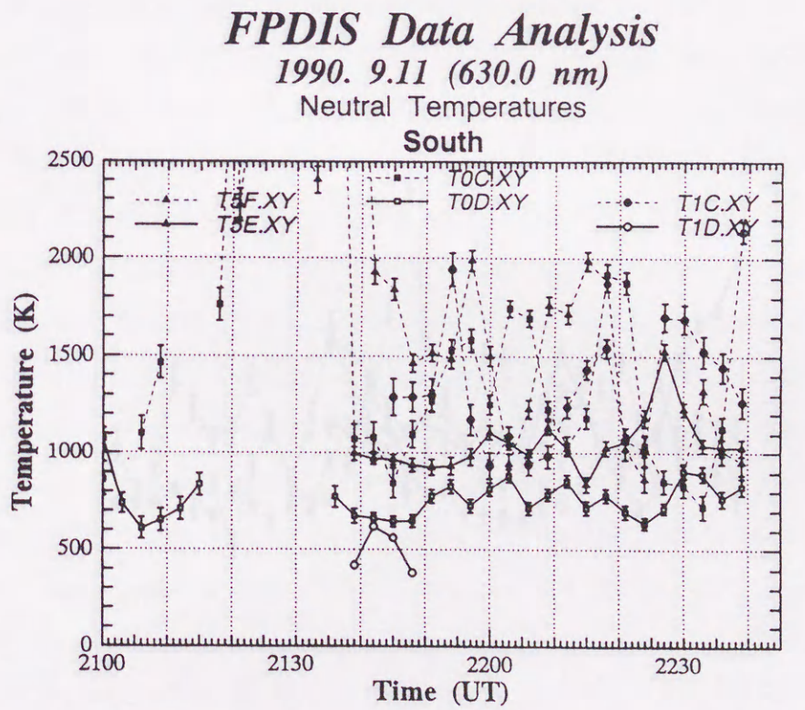

Figure 4.10: Same as Figure 4.8 but for the (magnetic) Southward direction.

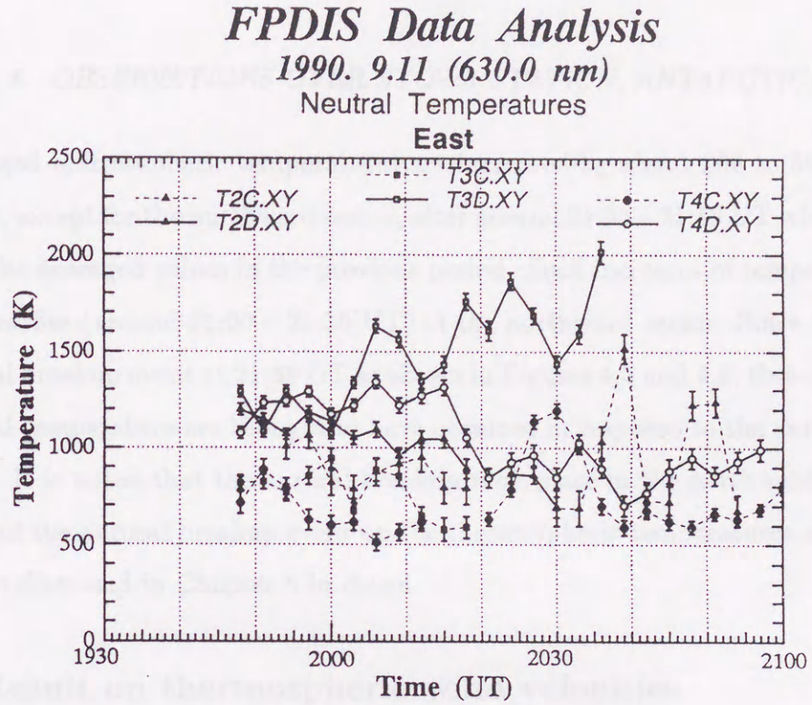

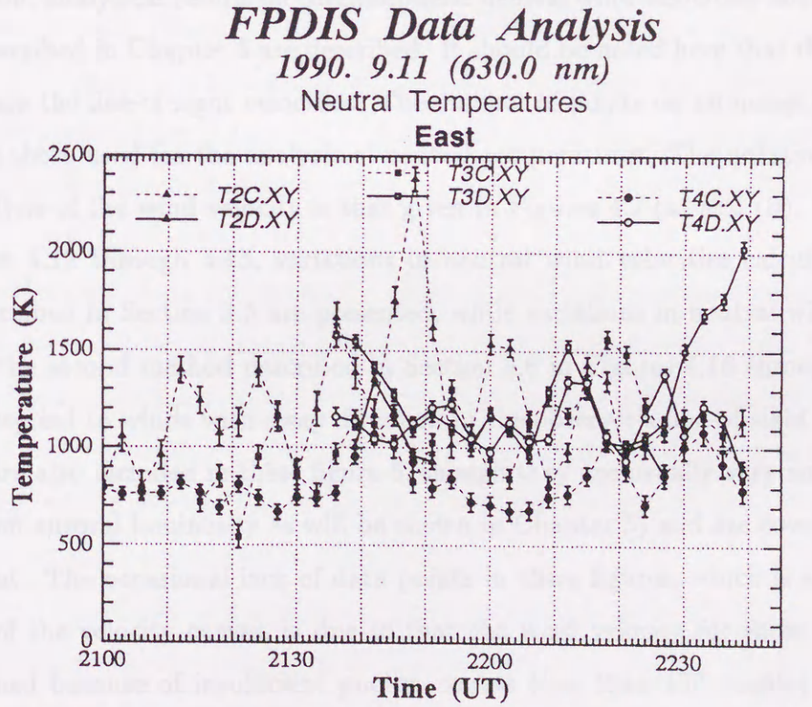

Figure 4.11: Same as Figure 4.8 but for the (magnetic) Eastward direction.

4. Averaged thermospheric temperatures are increased by about 200 to 500 K at most points, except for the northward sector, after around 21:35 – 21:40 UT when compared with the averaged values in the previous period. Such increases of temperature occur a bit earlier (around 21:00 – 21:30 UT) in the northward sector. Since there was an auroral breakup event at 21:38 UT as shown in Figures 4.5 and 4.6, these variations in neutral temperature are thought to have occurred in response to the auroral breakup event. It is noted that the auroral breakup took place in the northward sector. The effect of the auroral breakup event on the thermospheric temperatures and velocities will be discussed in Chapter 5 in detail.

4.3.3 Result on thermospheric wind velocities

In this section, analytical results on thermospheric neutral wind velocities calculated by the two methods described in Chapter 3 are described. It should be noted here that the wind velocities given here are the line-of-sight velocities. The number of points on an image to be analyzed is 24, same as those used for the analysis of neutral temperatures. The notation of those points for the analysis of the wind velocity is that given in Figures 4.7 (a) and (b).

In Figures 4.12 through 4.15, variations in neutral wind velocities calculated by the first method described in Section 3.5 are presented, while variations in neutral wind velocities calculated by the second method described in Section 3.6 in Figures 4.16 through 4.19. Positive values correspond to winds with away direction in the observer's line-of-sight component. The error bars are also included in these figure 5, though they are usually very small (~20–50 m/s depending on auroral luminosity as will be shown in Chapter 5) and are covered by the marks of each point. The occasional lack of data points in these figures, which is shown by the discontinuity of the velocity curves, is due to that the wind velocity for those points could not be determined because of insufficient photon counts (less than 150 counts) arising from the raw luminosity in the sky corresponding to those points. Some points are plotted on a line of

zero-wind velocity because of the impossibility of wind determination due to the divergence in data fitting calculation. The differences in calculated wind velocities between the two analysis methods are described first and then the variations of wind velocities are given.

First, the differences in wind velocities calculated by the two methods are compared. When variations in wind velocities for each individual points in Figures 4.12 through 4.15 are compared with those in Figures 4.16 through 4.19, it is clear that the trends of variation resemble closely each other. However, it is also clear that the absolute values of line-of-sight wind velocities in Figures 4.12 though 4.15 and in Figures 4.16 though 4.19 have large differences from each other, and moreover, the magnitudes of difference (offset values) are not same for various directions. The reason for these differences in absolute wind velocity may be attributed to the lack of calibration of the Doppler zero wind velocity for the first method of retrieval wind velocity retrieval, whereas the calibration was executed for the second method using the fringe data of a cloudy night. Since the relative agreement between the wind velocities, determined independently by the two different methods thought to prove the pertinence of these two methods of analysis, we will use the results of the second method of analysis hereafter because it is thought to have less errors in absolute wind velocities after executing the calibration using the data of a cloudy night.

It can be seen that there still exists the offset of wind velocities for the inner fringe data in Figures 4.16 through 4.19. Although it looks like an alternation from normal (it seems that the divergence of wind field exists at the inner fringe), we use these data without correction in this section in way that attention is paid only on the relative changes in wind speed at each point. The correction of the offset of this value will be made in the next section. The possible reason of the offset will also be discussed in Chapter 5.

Now, the characteristics of variations of neutral wind velocities are discussed. A significant auroral breakup event occurred at 21:38 UT as mentioned before. First, changes of wind velocities associated with this event at each image point are summarized as follows. At the points in the northward sector, as shown in Figure 4.16, wind velocities in inner fringe positions

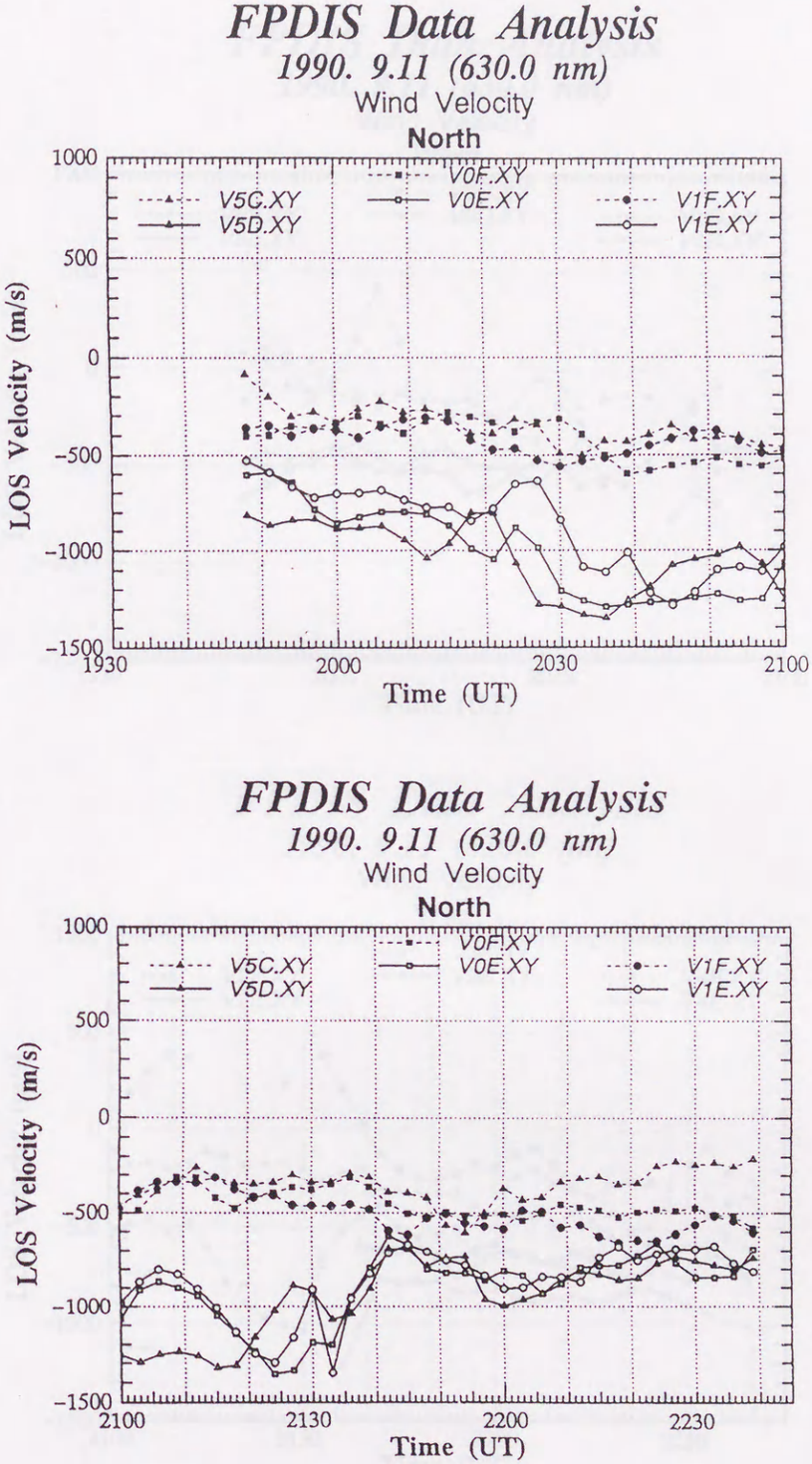

Figure 4.12: Variations of line-of-sight component of thermospheric neutral wind velocities derived from the FPDIS Doppler fringe data. The method described in Section 3.5 was used to determine the wind velocity. This figure shows the variations at 6 points in the (magnetic) northward sector from 19:48 to 21:00 (upper panel) and from 21:00 to 22:39 (bottom panel) on September 11, 1990.

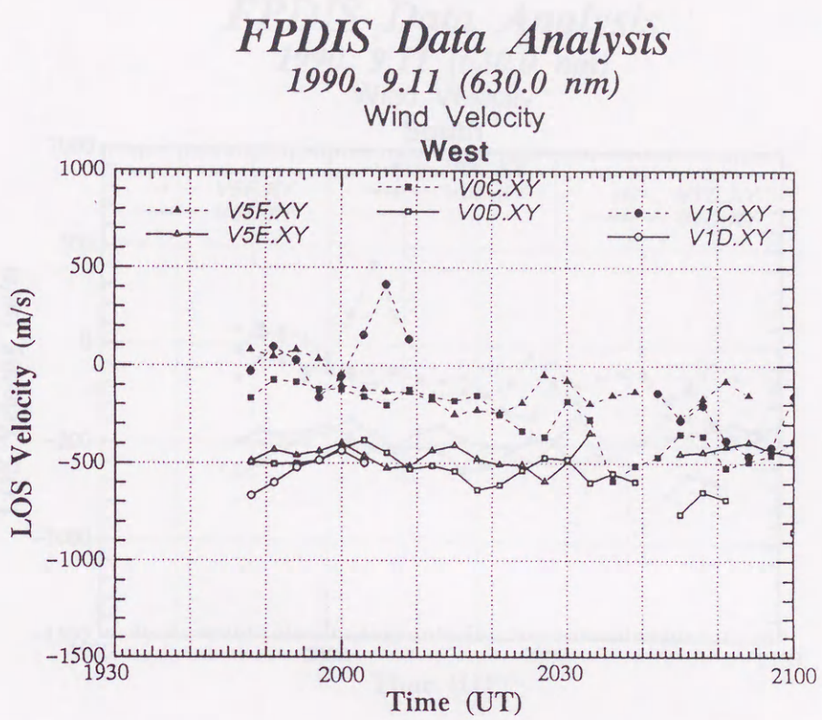

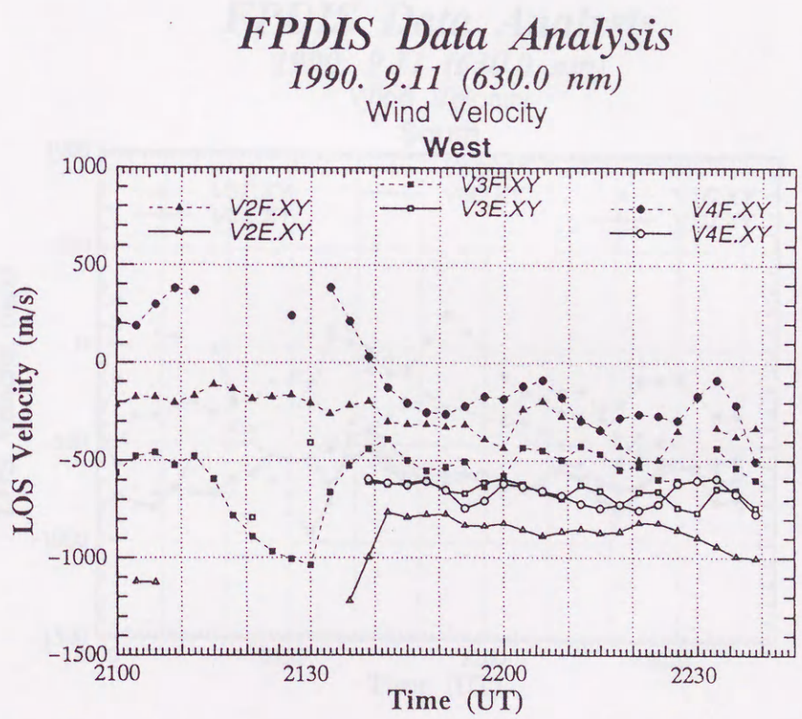

Figure 4.13: Same as Figure 4.12 but for the (magnetic) westward section.

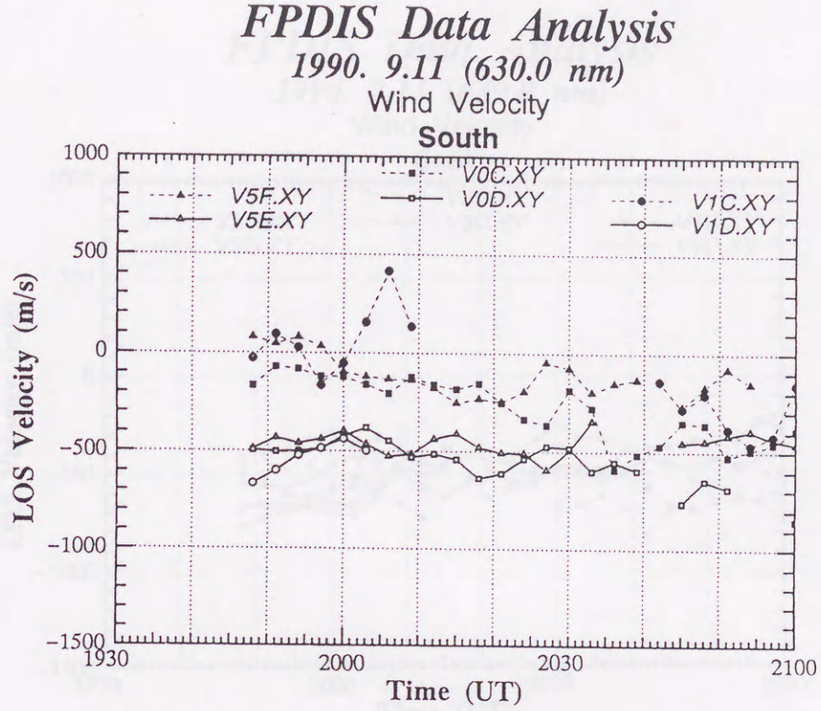

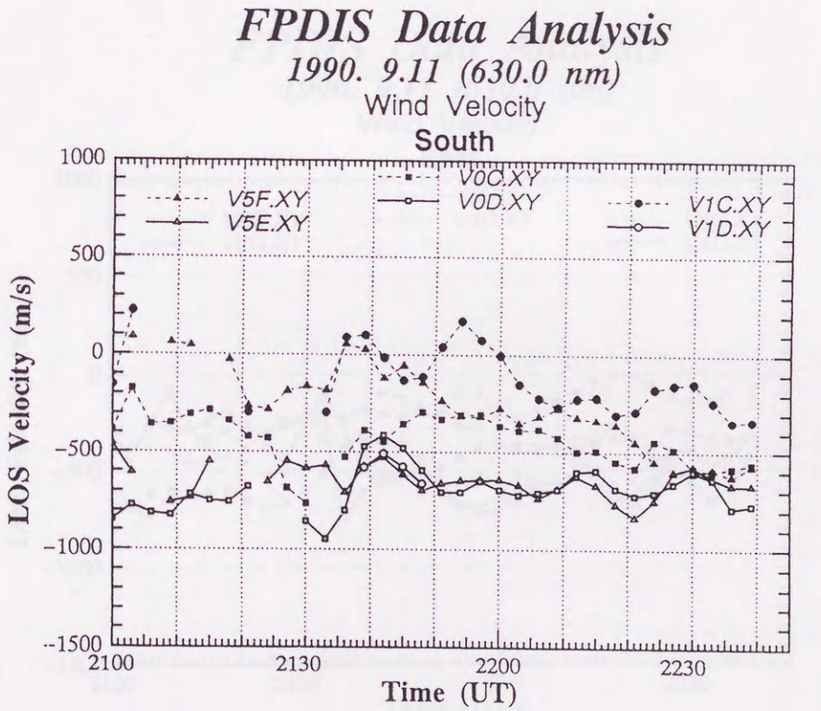

Figure 4.14: Same as Figure 4.12 but for the (magnetic) southward sector.

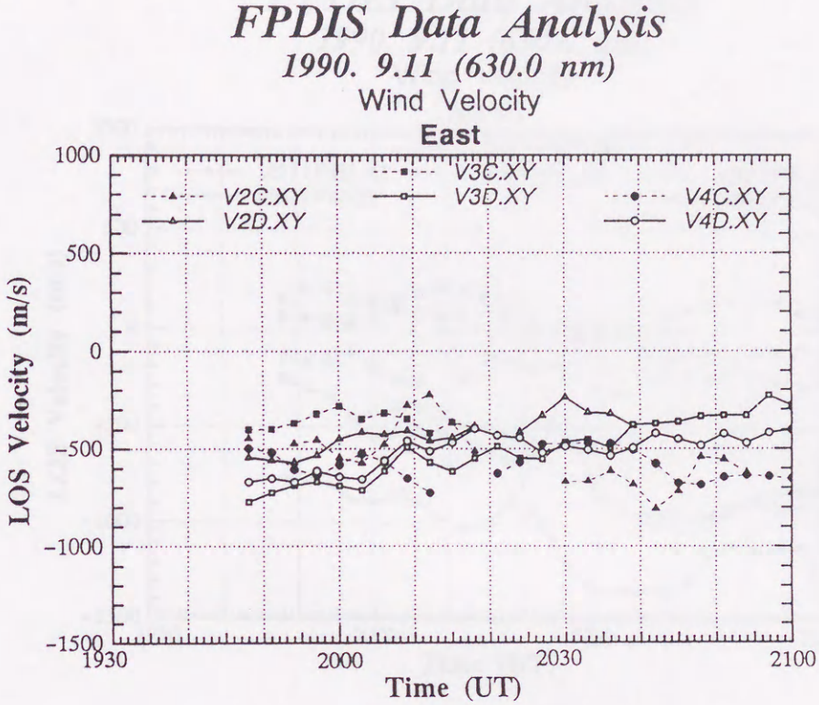

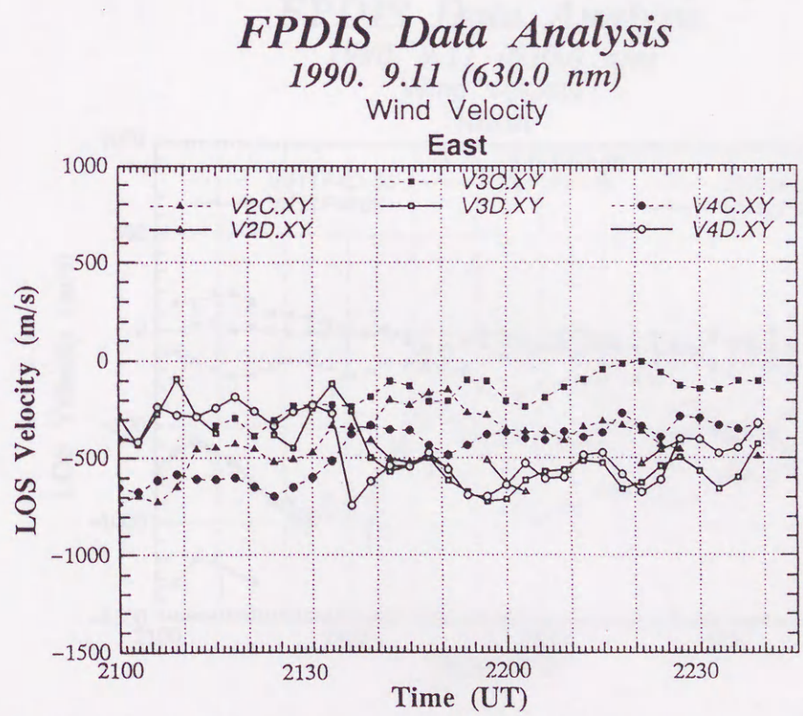

Figure 4.15: Same as Figure 4.12 but for the (magnetic) eastward sector.

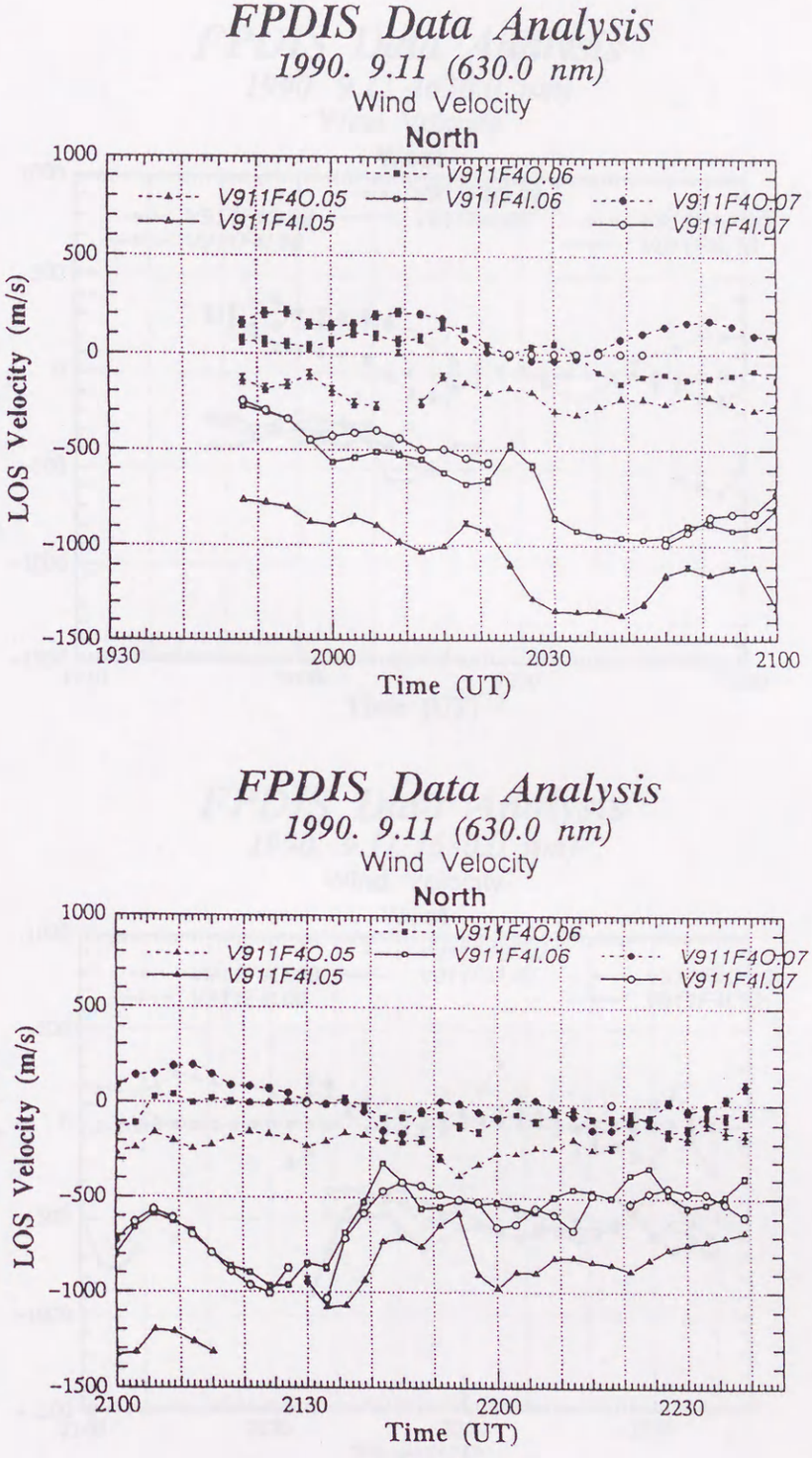

Figure 4.16: Variations of line-of-sight component of thermospheric neutral wind velocities derived from the FPDIS Doppler fringe data. The method described in Section 3.5 was used to determine the wind velocity. This figure shows the variations at 6 points in the (magnetic) northward sector from 19:48 to 21:30 (upper panel) and from 21:30 to 22:39 (bottom panel) on September 11, 1990.

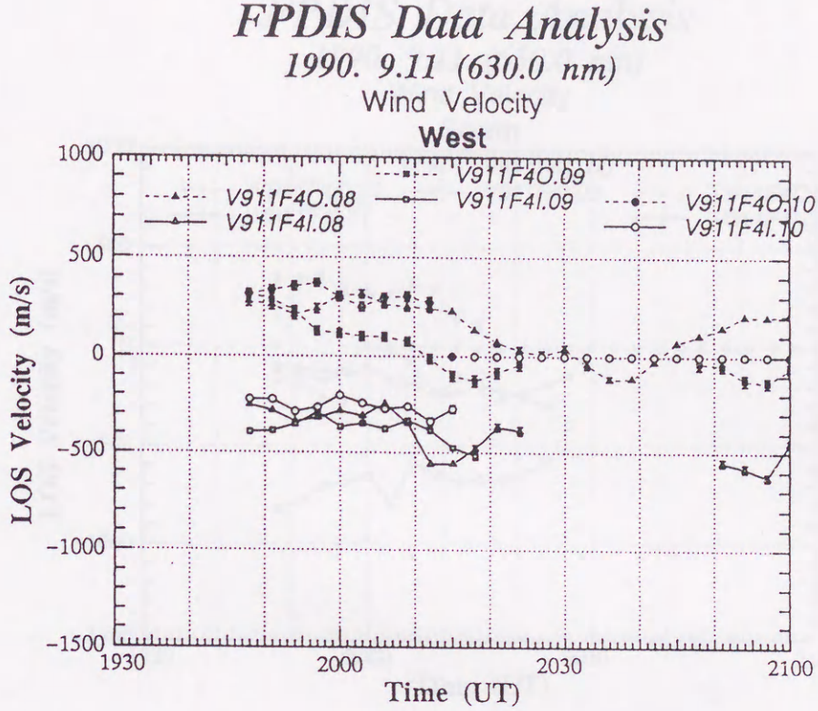

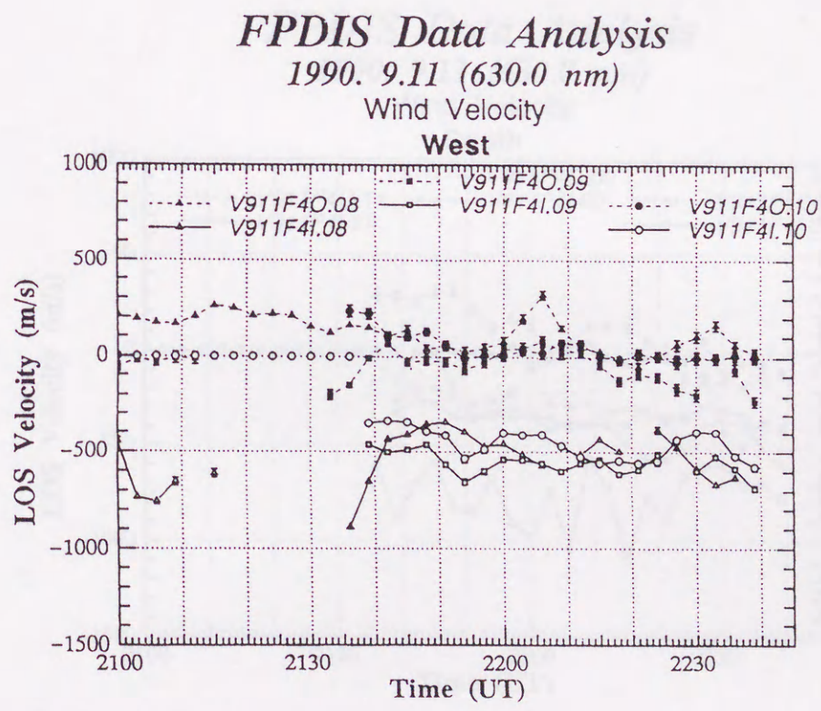

Figure 4.17: Same as Figure 4.16 but for the (magnetic) westward sector.

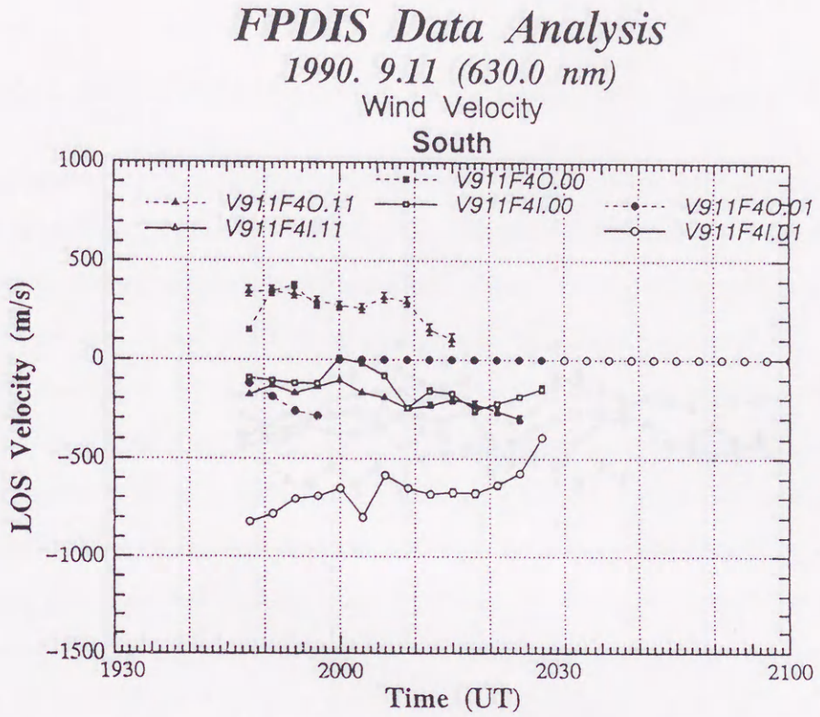

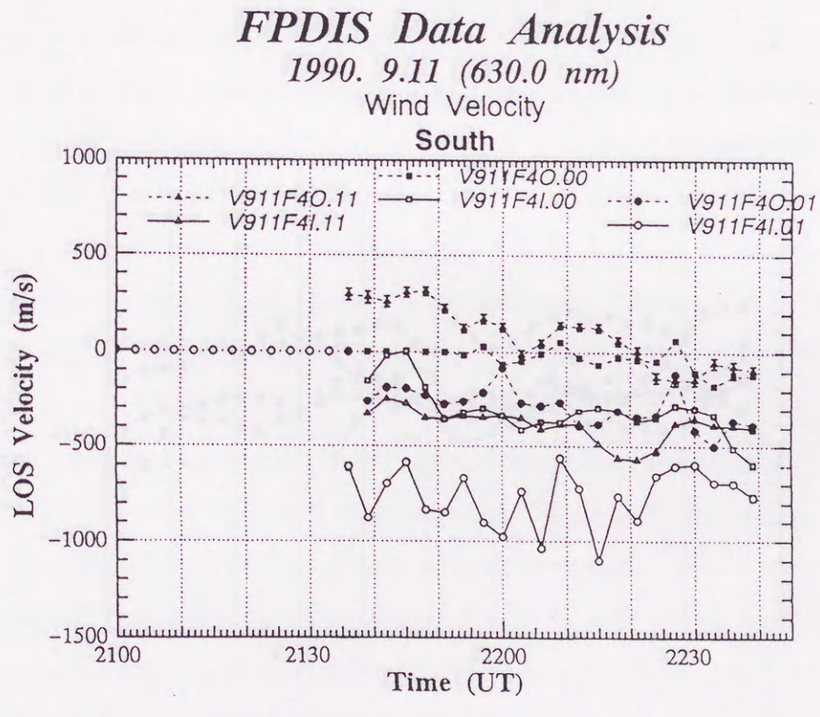

Figure 4.18: Same as Figure 4.16 but for the (magnetic) southward sector.

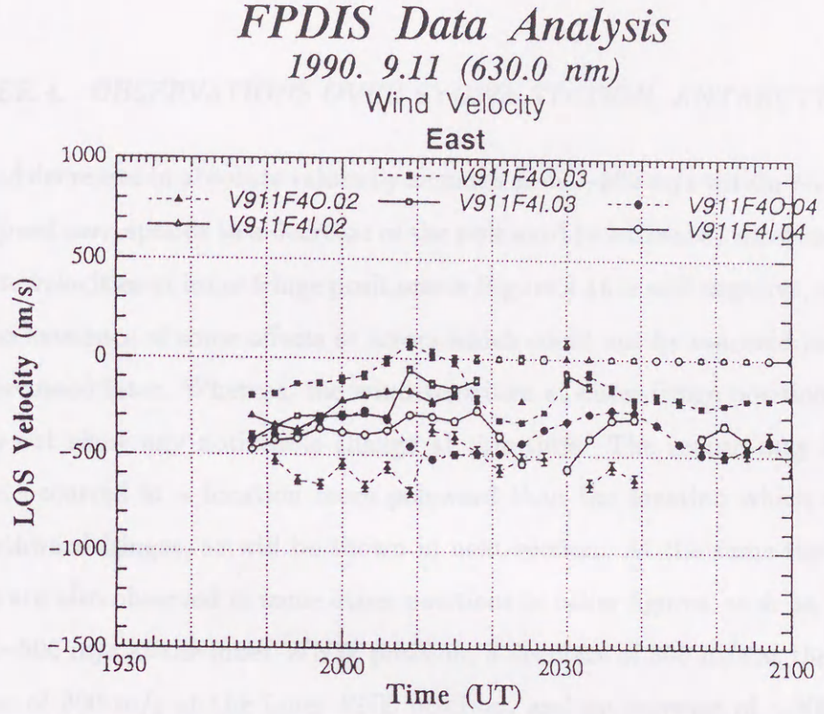

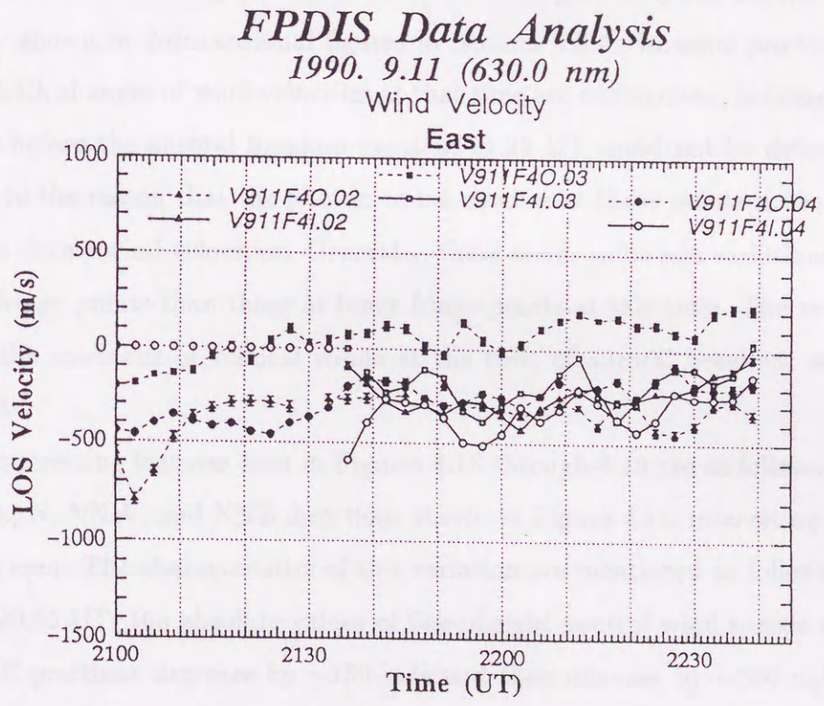

Figure 4.19: Same as Figure 4.16 but for the (magnetic) eastward sector.

show rapid decreases in absolute values by as much as 400–600 m/s within ~10 min. This change in wind speed corresponds to a decrease of the poleward (southward) wind component. The sign of absolute velocities at inner fringe positions in Figure 4.16 is still negative, and this is probably due to the existence of some offsets or errors which could not be removed in calculation, which will be discussed later. Whereas, the wind velocities at outer fringe positions in the northward sector do not show any noticeable change at this time. The reason may be that an auroral expansion occurred at a location more poleward than the location which corresponds to the outer northward fringes, as will be shown in next section. At the same time, changes of wind velocities are also observed in some other positions in other figures, such as, a decrease of wind speed in ~500 m/s at the inner WNW position, a decrease of 300 m/s at the outer W position, a decrease of 300 m/s at the inner ENE position, and an increase of ~200 m/s at the inner ESE position. Those changes in wind velocities accompanied by the auroral breakup event will be clearly shown in 2-dimensional figures in Section 4.3.4. In some positions in Figures 4.17 through 4.19, changes of wind velocities at that time are not so clear, because the values of wind velocities before the auroral breakup event at 21:38 UT could not be determined from image data due to the reason that the photon count number at those points is too low (less than 150 counts) to derive wind velocities. Generally, there seems to be less variations in wind velocities at outer fringe points than those at inner fringe points at this time. The reason of this, which suggests the existence of vertical winds at the time of auroral breakup, will be discussed in Chapter 5.

Other interesting features seen in Figures 4.16 through 4.19 are as follows. In the northward sector, i.e., N, NNW, and NNE directions shown in Figure 4.16, interesting variations in wind speed are seen. The characteristics of this variation are mentioned as follows. In a time period of 20:15–20:35 UT, the absolute values of line-of-sight neutral wind speeds at the inner N and inner NNE positions decrease by ~150 m/s and then increase by ~500 m/s in 5–10 min. In addition, there is a time lag of about 5–6 min for this rapid change in wind velocity, i.e., the change at the inner NNE position precedes that at the inner N position by 5–6 min. Whereas,

the changes in wind velocities at outer fringe positions are small, i.e., 50–100 m/s, and are, moreover, in the opposite phase compared with those in the NNW direction. These changes in wind velocity correspond to auroral arc activity in the north direction, as will be shown in the next section. The changes in wind velocity gradually were resumed around 20:40 at the inner NNE position, and around 21:00 when next interesting change occurred.

From ~21:00 to 21:20 UT, the wind velocities at the inner N and NNW positions gradually increase by about 400 m/s, while at outer positions in the same direction they show little (less than 150 m/s) change. This gradual increase corresponds to a gradual movement of the auroral edge which is shown in next Section.

In the westward, i.e., W, WNW, and WSW sector shown in Figure 4.17, small variations in wind velocity at the inner WNW and W positions occurred around 20:10-20:20 UT preceding those in the northward sector by about 5 min.

In the eastward sector shown Figure 4.19, periodic variations in wind velocity with a period of 20–25 min seem to exist after the onset of auroral breakup event at 21:38 UT. The amplitude of this variation is 200–300 m/s at inner positions, and 150–200 m/s at outer positions. The difference of the amplitude of this periodic variations will be discussed in Chapter 5. When variations in wind velocity shown in Figure 4.17 are carefully examined, same kind periodic variations with a period of 15–20 min and an amplitude of 50–200 m/s at all inner positions (W, WNW, WSW) are identified.

The variations in wind velocities in the southward sector (S, SSW, SSE) are not so clear since auroral intensity in this region is relatively law before the auroral breakup event occurred and wind velocities can not be determined in a period of 20:30–21:33 UT as shown in Figure 4.18. After the breakup, small variations are observed at outer S, SSW, and SSE positions, though their periods are not certain. Although relatively large (300 m/s in amplitude) variations in wind velocity with a short (8–10 min) period are observed only at the inner SSE position, they are uncertain because of the reason mentioned in Chapter 5.

4.3.4 Summary plot of FPDIS results on September 11/12, 1990

In Sections 4.3.2 and 4.3.3, derived thermospheric neutral temperatures and line-of-sight wind velocities at various positions were presented as a function time. Although it is a good way to see the temporal variations of temperatures and wind velocities at a certain point, it is hard to get two-dimensional information from these plots. In this section, three kinds of thermospheric data, i.e., neutral temperatures, line-of-sight wind velocities, and monochromatic image data of auroral emission taken by the FPDIS and by the monochromatic CCD camera at Syowa Station are superposed on each figure to represent the view of all-sky image every 3 minutes. In Figures 4.20 though 4.24, examples of such data for periods of 20:12–20:27, 20:30–20:45, 21:24–21:39, 21:42–21:57, and for 22:00–22:15 UT, September 11, 1990 are shown, respectively. The upper side of each images is the magnetic northward, which is about 47° west of geographic north at Syowa Station, and the right is westward. In these figures, velocities at inner fringe positions are corrected so as to have an offset value of −500 m/s. Moreover, since the wind velocities at the inner NNE and inner SSE positions are thought to contain large errors, the velocity arrows in these directions are painted out by blue colors in order to distinguish from others. Two-dimensional information on the three kinds of data over the field of view of the FPDIS is easily comprehended from these figures. On those figures, inner fringe positions correspond to a zenith angle of 22 degrees, while those of outer fringe correspond to a zenith angle of 70 degrees, respectively, which are read from Figure 3.9 by using the mean peak position of the auroral fringe.

In Figures 4.20 and 4.21, the following characteristics are clearly shown. Throughout the data period shown in these figures, a thin auroral arc in 630.0 nm exists at the magnetic northern part (equatorward) of the image. At 20:21 UT, the auroral arc is intensified at the east to east north part of the sky, which continues until around 20:33 UT. According to this auroral intensification, two distinct changes in wind velocities are shown. One of them started around 20:24 UT at the east part of the image. The line-of-sight wind velocities at E and ENE positions

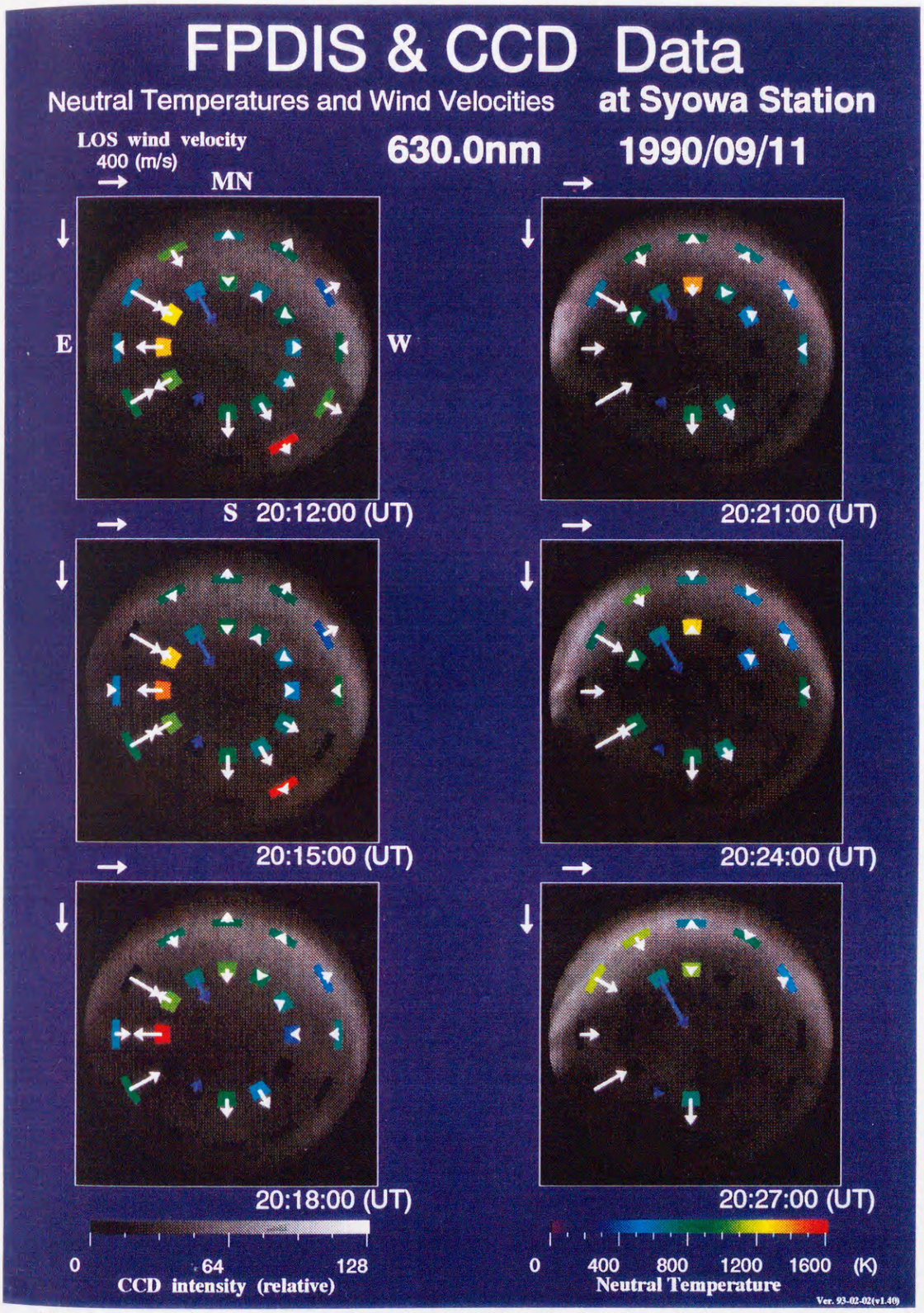

Figure 4.20: Variations of the line-of-sight thermospheric neutral wind velocities and neutral temperatures displayed on a monochromatic CCD image taken at Syowa Station, Antarctica. Each 3-min data are plotted from 20:12 to 20:27 UT, September 11, 1990. Magnetic north direction (which is about 47° west of geographic north at Syowa Station) is the upside, and west is the right side. Length of small arrows on the left upper corner of each panel represent the wind speed of 400 m/s. Monochromatic auroral intensity and neutral temperatures are shown in gray and color codes, respectively

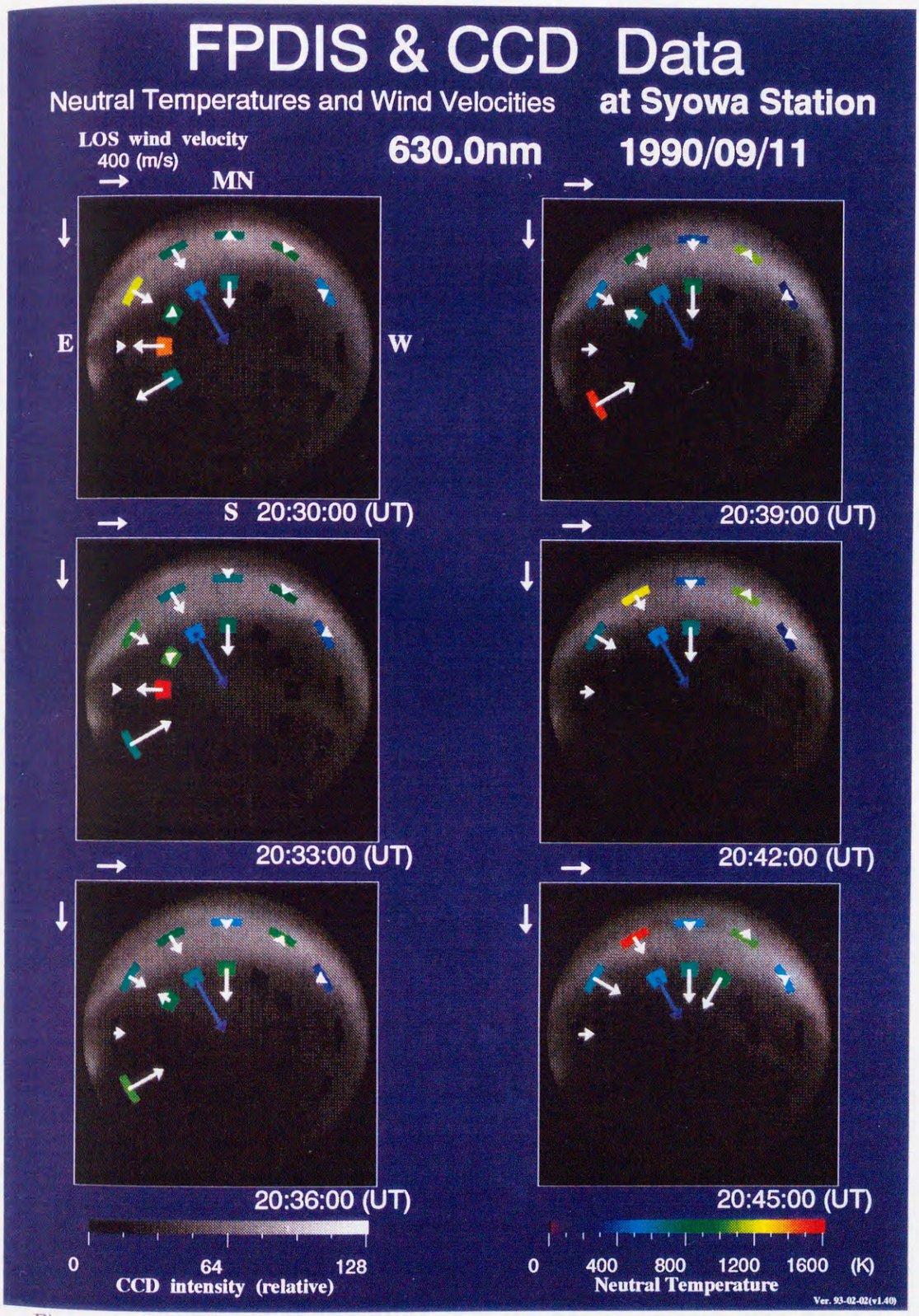

Figure 4.21: Same as Figure 4.20 but for 20:30–20:45 UT, September 11, 1990. Intensification of 630.0 nm auroral arc is shown for images from 20:21 to 20:33 UT.

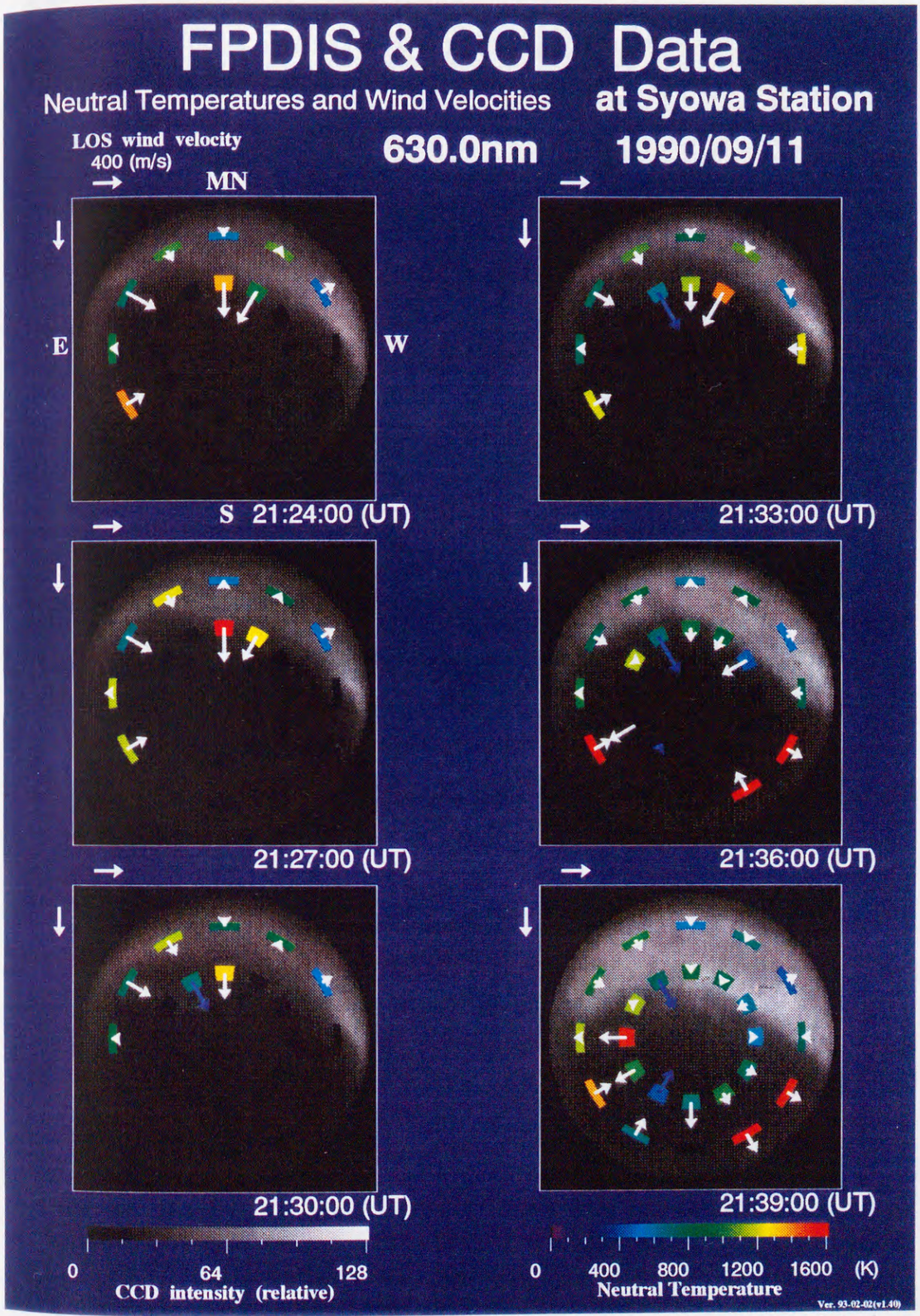

Figure 4.22: Same as Figure 4.20 but for 21:24–21:39 UT, September 11, 1990. It is shown that auroral breakup starts at the west part of the image around 21:36 UT.

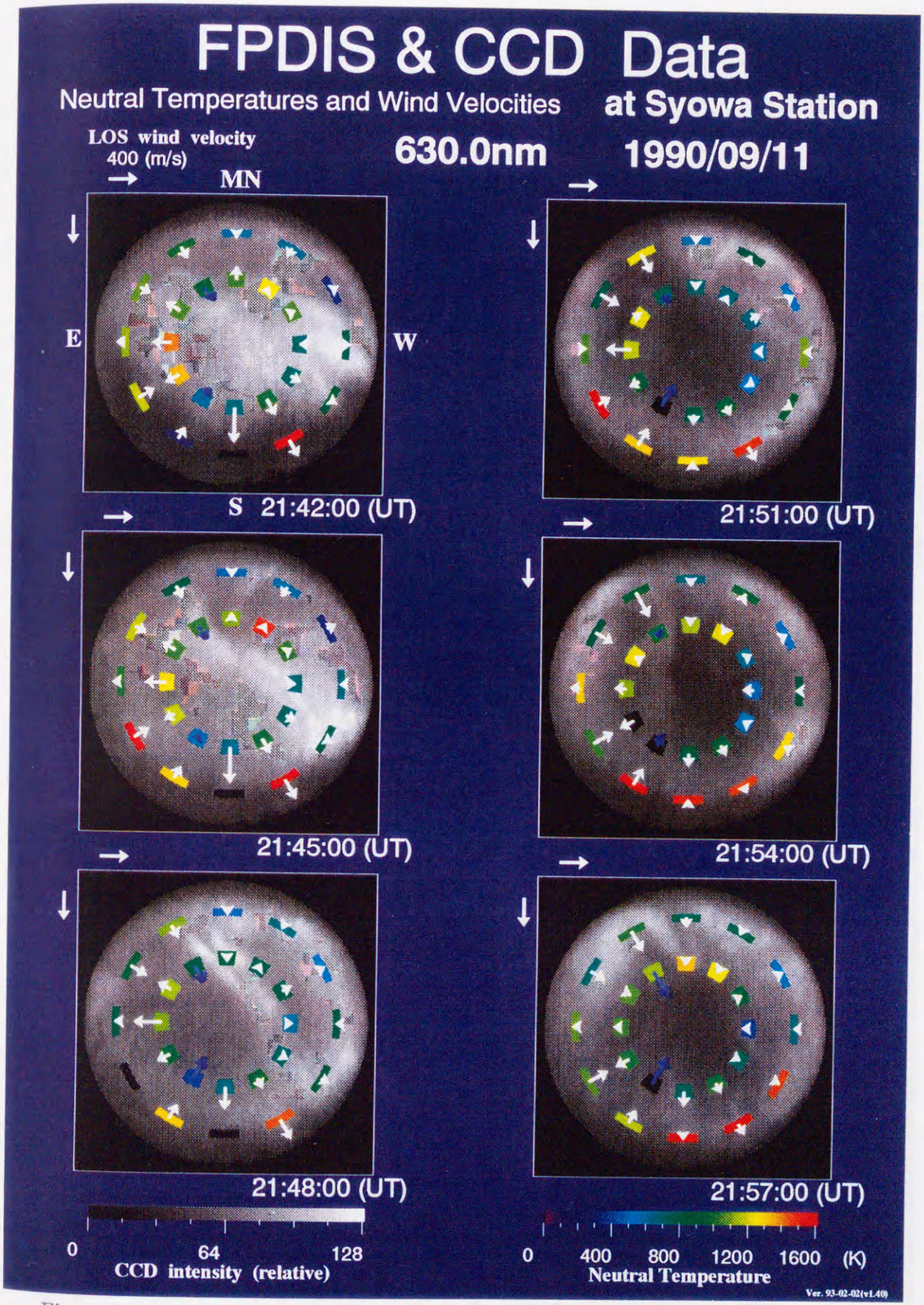

Figure 4.23: Same as Figure 4.20 but for 21:42–21:57 UT, September 11, 1990. It is shown that auroral breakup expands towards southward (poleward) to cover the whole image.

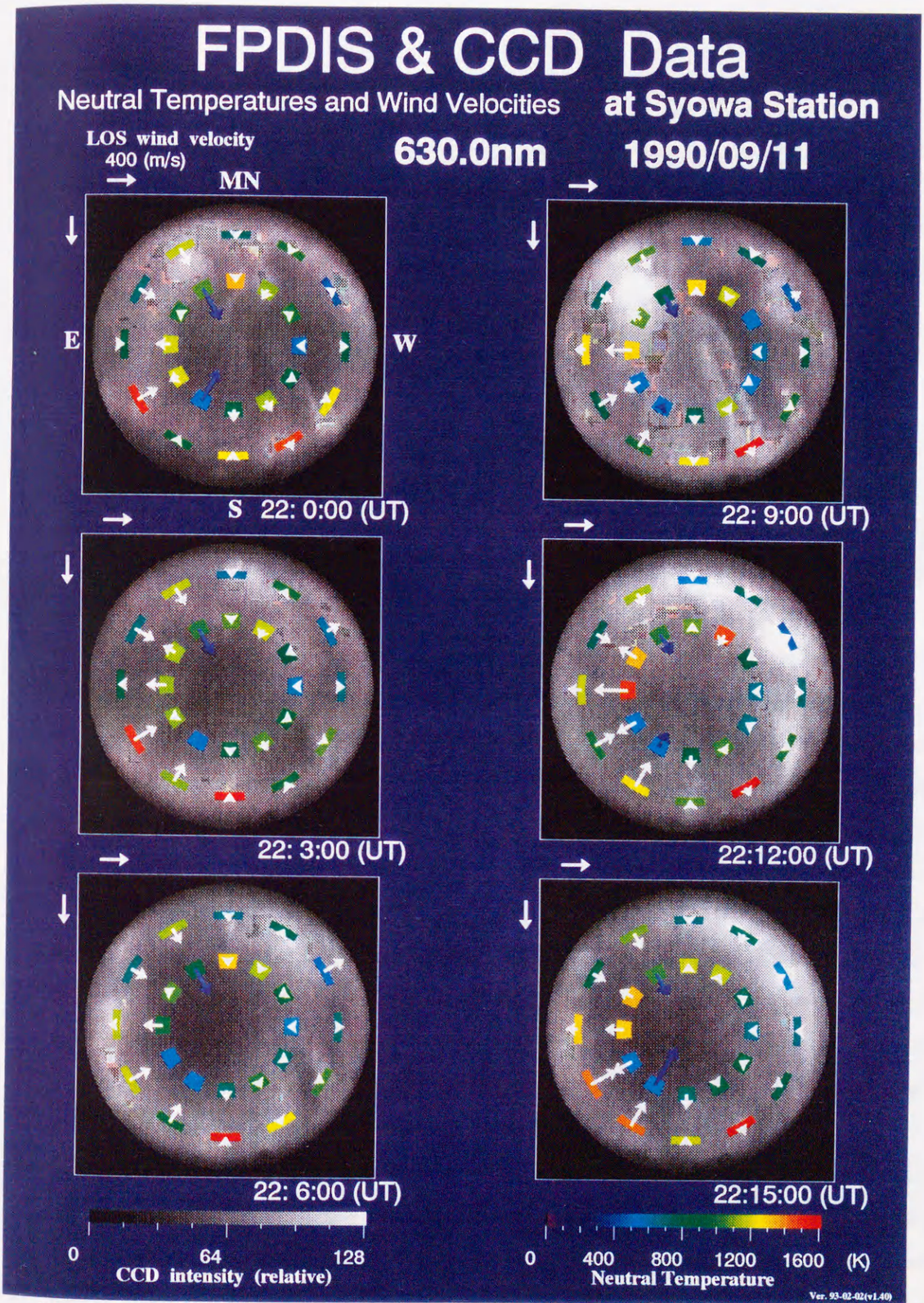

Figure 4.24: Same as Figure 4.20 but for 22:00 22:15 UT, September 11, 1990. Succession of the auroral breakup is shown on the image.

of the outer fringe decreased by 200–300 m/s as we have seen in Figure 4.19. Other distinct change is an increase of wind velocity at the inner N position by 400–500 m/s which begins around 20:30 UT. When we examine these figures carefully, it is clear that these changes in velocities occurred at the edge of an intensifying auroral arc. A possible mechanism of this will be given in Chapter 5.

In Figures 4.22 through 4.24, drastic changes in wind velocity and neutral temperatures around the time of auroral breakup starting at 21:38 UT are clearly shown. In the panel of 21:36 UT in Figure 4.22, it is shown that an auroral arc located in the magnetic north direction of the image is intensified, particularly at the west part of the arc. At this time, large changes in southward wind velocities at the inner N and NNW positions are found to decrease in 300–400 m/s. In the panel of 21:39 UT, it is shown that the auroral breakup begins, accompanied by poleward (southward) expansion of aurora. At this time, large southward component of winds reaching 200–500 m/s at the inner WSW, SSW, S, SSE, E, S and SE positions were observed. The high temperatures (about 1600 K) at the outer SSW, WSW positions are thought to be incorrect due to fitting errors. At 21:42 UT in Figure 4.23, the auroral breakup region spread to the zenith of Syowa Station, and at 21:45 UT, it almost covered almost the whole field of view of the FPDIS. The wind velocities changed little after 21:42 UT except for a decrease of 200 m/s at the inner S position. From 21:48 to 22:15 UT, quasi-periodic changes in wind velocity, which are described in Section 4.3.3, are shown clearly at the east part of the images. Large eastward winds are observed around 21:48 and 21:12 UT at the inner ENE, E, and ESE positions. These variations in wind velocity suggest the existence of some periodic disturbance occurred in the thermospheric wind field at the time of auroral breakup.

The variation in temperature associated with the auroral breakup is not so clear because the variations of temperatures is much more variable and noisy compared with those of wind velocities as shown in Figures 4.8 through 4.11. However, it seems that temperatures at east part of the inner positions show periodic variations similar to that of westward wind component described above. When high wind velocities are observed around 21:48 and around 21:12 UT

Table 4.4: Summary of observations on September 13/14, 1990.

I.D. of Data Period	Start Time (UT)	End Time (UT)	Data Period (hh:mm:ss)	Object	OVD I.D.	Start Frame	End Frame	Number of Frames	Filter (nm)	CCD CK	Fish-eye Aperture F	Room Temp (°C)
913L1	17:15:02	17:25:42	00:10:40	Laser Cal	900902(14-A)	14001	14600	600	–	4	–	20.0
913F2	17:28:00	19:04:07	01:36:07	OI630.0nm	900902(14-A)	14601	20000	5400	630	4	11∼22	20.2
913L3	19:06:00	19:16:40	00:10:40	Laser Cal	900902(14-A)	20001	20600	600	–	4	–	21.3
913F4	19:18:00	21:12:04	01:54:04	OI630.0nm	900902(14-A)	20601	27000	7400	630	4	11∼16	21.3
913L5	21:18:00	21:39:18	00:21:18	Laser Cal	900903(14-B)	00004	01200	1197	–	4	–	21.9
913F6	21:40:00	23:32:08	01:52:08	OI630.0nm	900903(14-B)	01201	07500	6300	630	4	16∼22	22.0
913L7	23:33:00	23:45:27	00:12:27	Laser Cal	900903(14-B)	07501	08200	700	–	4	–	22.6
913F8	23:47:00	01:12:27	01:25:27	OI630.0nm	900903(14-B)	08201	13000	4800	630	4	16∼22	22.6
913L9	01:14:00	01:24:40	00:10:40	Laser Cal	900903(14-B)	13001	13599	599	–	4	–	22.8

at inner E and ENE positions, temperatures at those points seem to increase by 200–400 K.

The estimate of errors in temperatures and line-of-sight velocities will be discussed later in Chapter 5.

4.4 Observational Results on Thermospheric Neutral Temperatures and Wind Velocities on September 13/14, 1990

In this section, analytical results on thermospheric neutral temperatures and line-of-sight velocities deduced by the FPDIS image data taken on September 13/14, 1990 are presented. At this night, Doppler fringe data of auroral OI 630.0 nm emission were taken from 17:28 UT on September 13 to 01:12 UT on September 14, while calibration fringes of the stabilized He-Ne laser were taken 5 times at the beginning, around the middle, and the end of the auroral observation data period, respectively. A summary of observations on this day is shown in Table 4.4.

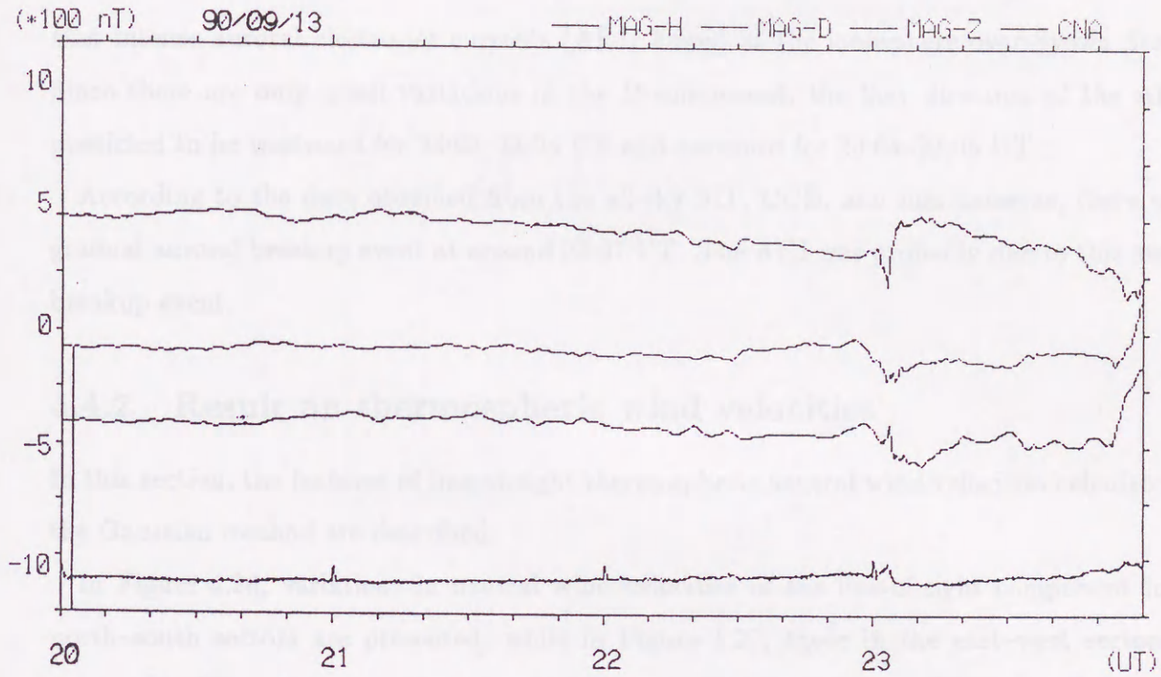

Figure 4.25: Triaxial magnetometer and CNA data at Syowa Station from 20:00 to 24:00 UT on September 13, 1990.

4.4.1 Auroral activities on September 13 / 14, 1990

The three-hourly Kp-indices are 5^-, 3, 2^-, 3^+, 3^+, 3^+, 3^-, 4 for September 13 and 4, 4, 3^+, 3^+, 3^+, 3^+, 2^+ for September 14, respectively. The K-indices at Syowa Station determined from the Syowa magnetometer data are 5, 5, 2, 2, 2, 3, 3, 5 for September 13 and 5, 5, 4, 2, 2, 3, 4, 3 for September 14, respectively. The fluxgate triaxial magnetometer and CNA data at Syowa Station from 20:00 to 24:00 on September 13 are shown in Figure 4.25.

In Figures 4.25, outstanding magnetic deviations in both the H- and Z-components are seen at around 23:00 UT. The magnetic H-component declined by 200 nT within 2 min at 23:02–23:04 UT, and then it suddenly increased by more than 300 nT within 1 min at 23:04–23:05 UT. The magnetic Z-component also shows a sudden increase of about 100 nT at 23:02-23:03 UT and a sudden decrease of the similar amplitude at 23:03-23:04 UT. These deviations suggest

that intense auroral electro-jet currents (AEJ) flowed at the ionosphere over Syowa Station. Since there are only small variations in the D-component, the flow direction of the AEJ is predicted to be westward for 23:02–23:04 UT and eastward for 23:04–23:05 UT.

According to the data obtained from the all-sky SIT, CCD, and film cameras, there was a gradual auroral breakup event at around 23:07 UT. The AEJ was probably due to this auroral breakup event.

4.4.2 Result on thermospheric wind velocities

In this section, the features of line-of-sight thermospheric neutral wind velocities calculated by the Gaussian method are described.

In Figure 4.26, variations in neutral wind velocities of the line-of-sight component in the north–south sectors are presented, while in Figure 4.27, those in the east–west sectors are presented. The notation in these figures is the same as that given in Figure 4.7 (b). From these figures, the following characteristics are clear;

1. Before 22:57 UT, there are not so distinct changes in wind velocities at every analyzed points except for some small (within 300 m/s) wind variations seen around 22:30 UT at the northward section.

2. Absolute wind velocities for each position before 22:57 UT are smaller (-600 to 500 m/s) in the north–south sectors, while they are much larger (-1200 to 1100 m/s) in the east–west sectors. The prominent wind direction is westward before 22:57 UT and line-of-sight wind velocities are 600 to 1000 m/s at the outer fringe position, and 0 to 800 m/s at the inner fringe position. Although these values are corrected by using the cloudy day's calibration data as mentioned in Section 3.6, it is likely that there still exist some offsets for those absolute values, especially at inner fringe positions. Note that since large negative values (~ -1000 m/s) shown at the inner

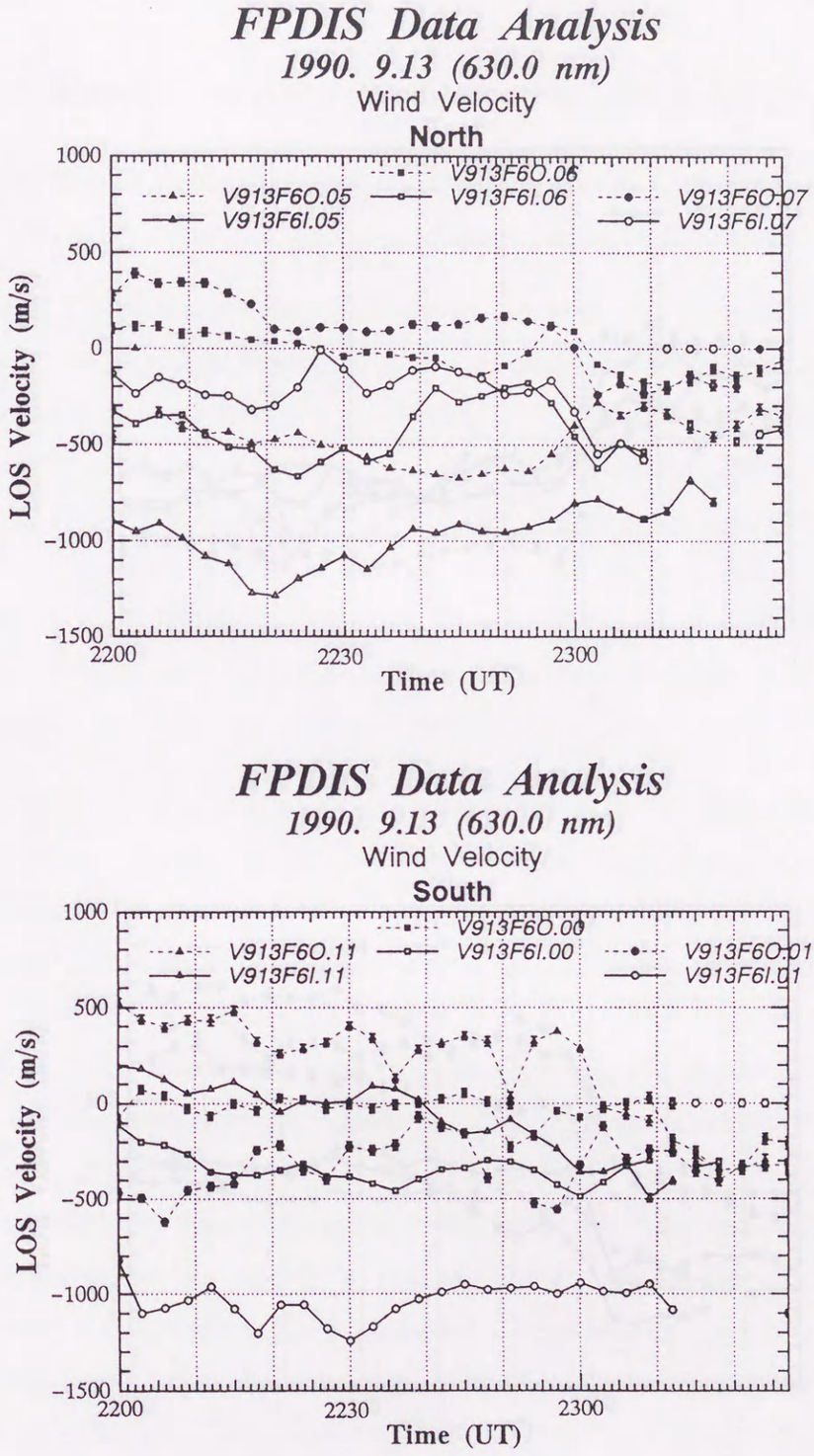

Figure 4.26: Variations of the line-of-sight component of thermospheric neutral wind velocities derived from the FPDIS Doppler fringe data. The upper panel shows variations at 6 points in the (magnetic) northward sector from 22:00 to 23:27 UT on September 13, 1990, while the bottom panel shows those for the southward sector.

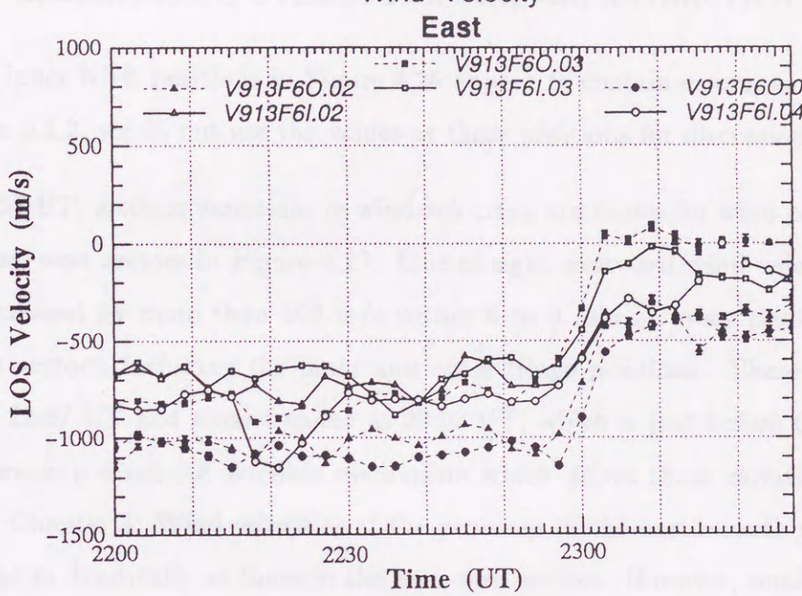

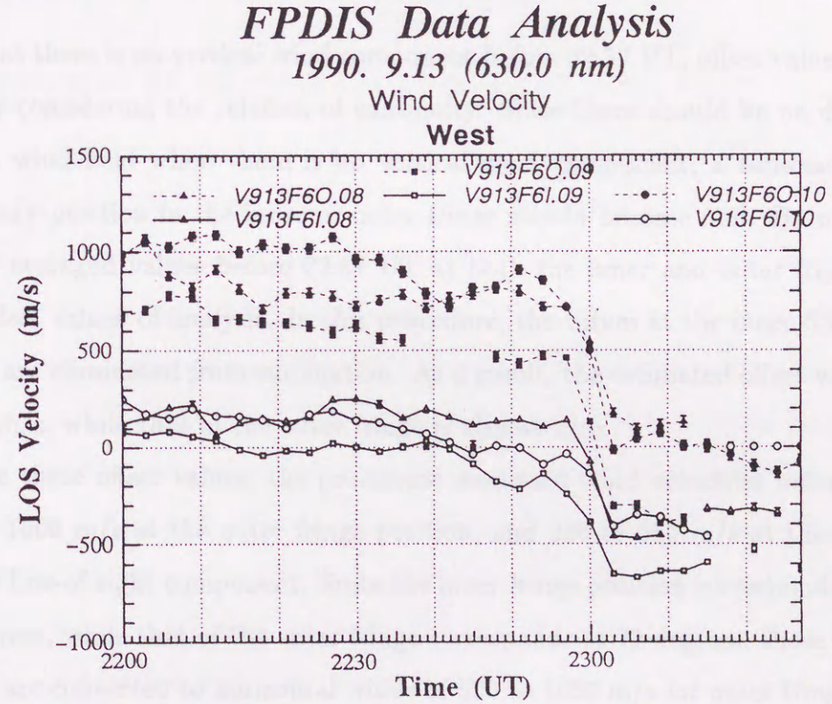

Figure 4.27: Same as Figure 4.26 but for the (magnetic) eastward sector (upper panel) and for the westward sector (bottom panel).

SSE and inner NNE positions in Figure 4.26 appear to contain errors, as mentioned in Section 5.1.2, we do not use the values at those positions for discussion.

3. From 22:57 UT, distinct variations in wind velocities are shown for wind components in the east–west sectors in Figure 4.27. Line-of-sight westward wind velocities suddenly decreased by more than 500 m/s within 6 to 9 min at every position in the east–west sectors, including the inner and outer fringe positions. These variations began at 22:57 UT and almost ended at 23:03 UT, which is just before the time of auroral breakup event. A possible mechanism which drives these variations is discussed in Chapter 5. Wind velocities at the positions in the north–south sectors did not change so drastically as those in the east–west sectors. However, small (300–400 m/s) deviations were observed at the positions in the northward sector.

Assuming that there is no vertical wind component before 22:57 UT, offset values of analysis is estimated by considering the relation of continuity. Since there should be no divergence or convergence in wind field when there is no vertical wind component, a summation of wind velocities at every position in the inner or outer fringe should become null. By making those summation for averaged values before 22:57 UT at both the inner and outer fringes, we can estimate the offset values of analysis. In this procedure, the values at the inner SSE and inner NNE positions are eliminated from summation. As a result, the estimated offset value of inner fringe is -250 m/s, while that of the outer fringe is almost zero.

When we use these offset values, the prominent westward wind velocities before 22:57 UT become 600 to 1000 m/s at the outer fringe position, and 250 to 550 m/s at the inner fringe position for the line-of-sight component. Since the inner fringe position corresponds to a zenith angle of 24 degrees, while that of the outer fringe corresponds to 72 degrees, those line-of-sight wind velocities are converted to horizontal winds of 630 to 1050 m/s for outer fringe positions, and 615 to 1350 m/s for inner fringe positions when the vertical wind component is zero.

Chapter 5

DISCUSSIONS

5.1 Discussion on Errors in Data Analysis

5.1.1 Estimation of errors by a numerical simulation

The method for deriving temperatures and line-of-sight wind velocities was described in Section 3.5 and we call it the 'Killeen's method' henceforth since it has been developed after *Killeen and Hays* [1984]. Although this method is very useful and efficient, possible errors in derived values can not be determined with that method by itself. In order to estimate the possible errors in temperatures and wind velocities determined by the Killeen's method, numerical simulation was executed. The principle of this simulation is described as follows. First, a data set of noise-free experimental fringe is calculated using Equation 3.16 for three kinds of assumed observation conditions; i.e., laser calibration, auroral 630.0 nm, and 577.7 nm. The calculation is made using nominal values of instrumental parameters; i.e., effective aperture of etalon A_0, spacing d, reflectivity R, transmittance of the filter T_F, transmittance of optics ψ, quantum efficiency Q_r and background dark noise count B_r of the detector. The assumed wavelength, λ_0, luminosity of the source R_0, kinetic temperatures of the T_0 and line-of-sight velocity v_0 are given in the calculation as variables. Once a simulated fringe data is constructed, random

noise is superposed on it. When random noise is generated, its standard deviation is set such that its value is equal to the square root of the value of model fringe data considering the statistical theory. In this way, a set of a number of simulated fringe data containing noise, which we call the false observation data, is produced. Then, these false observation data are subjected to the data analysis to derive the temperature T_d and the wind velocity V_d, using the Killeen's method. The difference between a derived value and an assumed value, i.e., $|T_d - T_0|$ for temperature or $|v_d - v_0|$ for wind velocity is taken as error in the analysis. Then the same procedure is repeated by giving another set of random noise with the same standard deviation many times —in our case, 100 times— to get an error value. The standard deviation of derived values for the temperature or the wind velocity determined in this way is thought to represent the error in the analysis using the Killeen's method at a certain temperature and luminosity of the emission source and at a certain position on the detector surface. Then, these values are calculated for various levels of the temperature and luminosity of the source and at various positions on the detector.

Figures 5.1 and 5.2 shows the error values defined as standard deviations of derived temperatures and wind velocities against counts at the fringe peak. These values are for a calculated luminosity of the 630.0 nm source emission and given temperatures at both the inner and outer fringes. It is clearly seen from these figures that errors in the wind velocity for the Killeen's method is relatively small (less than 40 m/s for a peak count of 100), while those of the temperature become larger than 100 K at a peak count less than 100 in the case of a given temperature higher than 1500 K. This is the reason that we did not analyze the data whose peak counts are less than 150.

The results in Figure 5.1 give a close agreement with the result of numerical error analysis by *Hays and Roble* [1971].

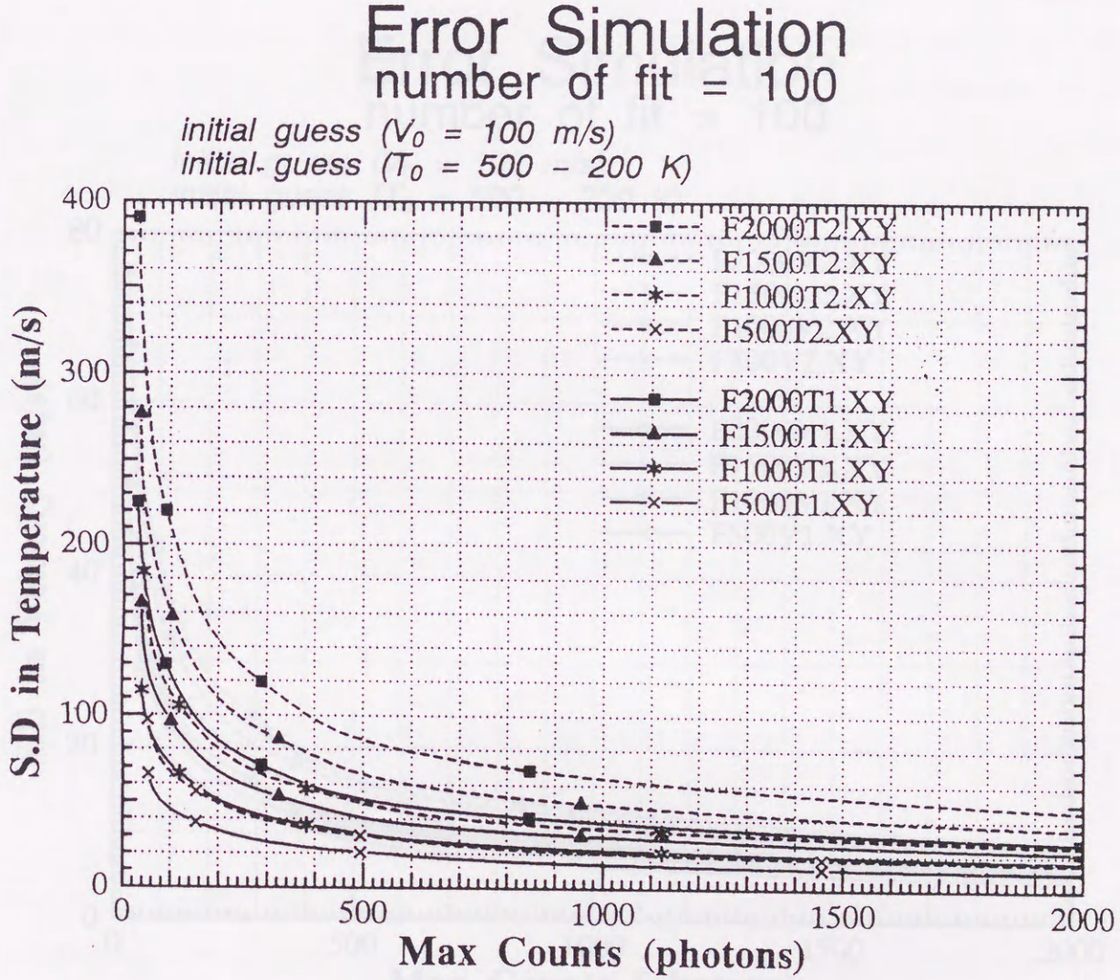

Figure 5.1: Calculated error values defined as the standard deviations of derived temperatures by the Killeen's method versus counts at the fringe peak, which is calculated from the given luminosity of the source and the given temperatures for both inner(solid line) and outer(broken line) fringes and the 630.0 nm emission. The given temperatures are 500, 1000, 1500, 2000 K.

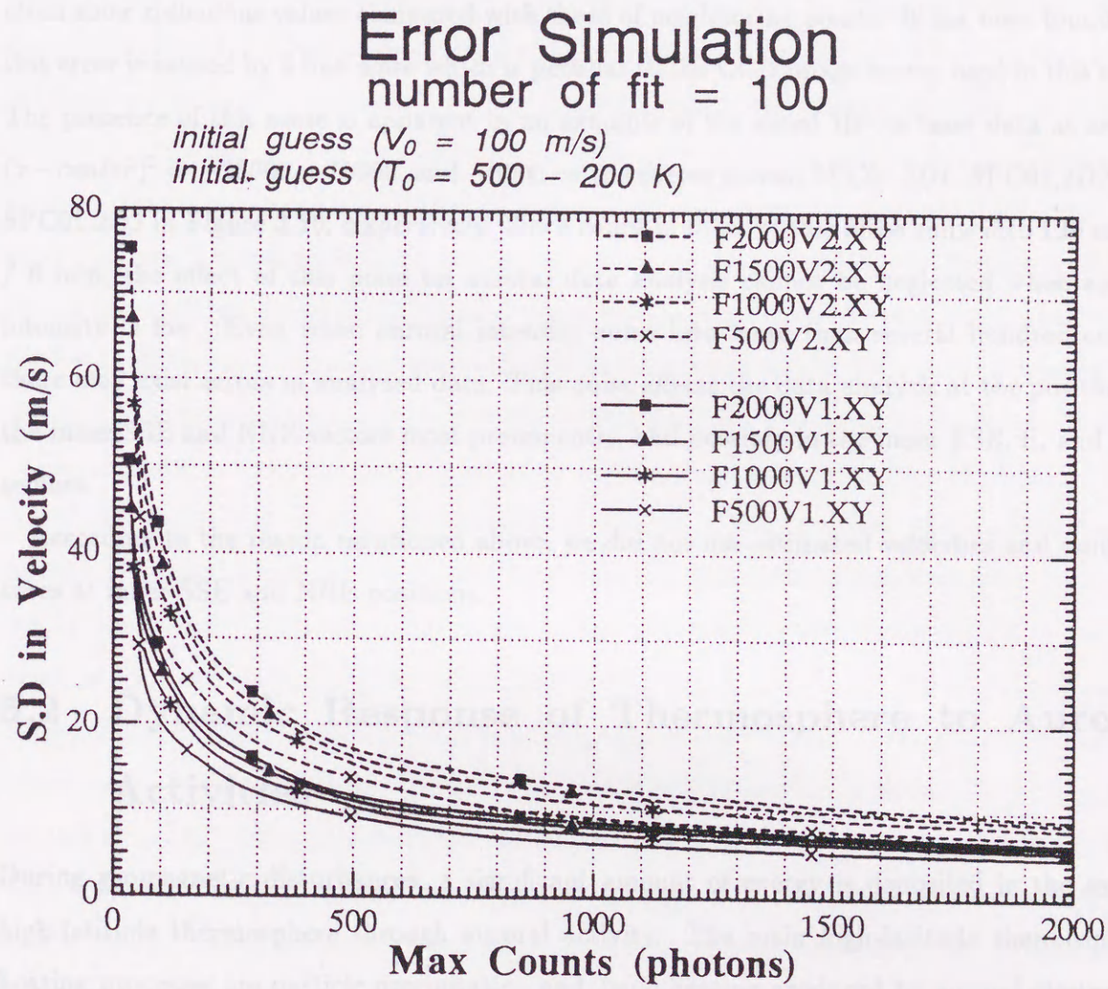

Figure 5.2: Same as Figure 5.1 but for derived wind velocities.

5.1.2 Errors caused by a line noise in the CCD sensor

It has been found that another kind of systematic error exists at specific fringe positions, i.e., at inner SSW and inner NNE positions. Both the velocities and temperatures at these points often show ridiculous values compared with those of neighboring points. It has been found that this error is caused by a line noise which is peculiar to the CCD image sensor used in this study. The presence of this noise is apparent in an example of the sliced He-Ne laser data at around $(x-center)^2 = -26000, -10000$, and -8000 on the curves named SPC01.2D1, SPC01.2D2, and SPC01.2D3 in Figure 3.10, respectively. Since count number of this noise sums into 120 counts / 6 min, the effect of this noise on auroral data analysis cannot be neglected when auroral intensity is low. Even when auroral intensity sums into more than several hundred counts, there may exist errors in analyzed data. This noise affects the data analysis at the positions of the inner SSE and NNE sectors most prominently, and possibly in the inner ESE, E, and ENE sectors.

According to the reason mentioned above, we did not use estimated velocities and temperatures at inner SSE and NNE positions.

5.2 Dynamic Response of Thermosphere to Auroral Activities

During geomagnetic disturbances, a significant amount of energy is deposited in the earth's high-latitude thermosphere through auroral activity. The main high-latitude thermospheric heating processes are particle precipitation and Joule heating produced by auroral electrojets. In addition to the heating, momentum is imparted to the neutral gas as a result of collision processes between drifting ions and neutral molecules and atoms. The energy and momentum sources associated with geomagnetic activity are highly variable in both space and time, and this variability results in a complex atmospheric response. Previous optical observations

made during geomagnetic storms have clarified that temperature and wind significantly change in response to auroral activity [*Biondi and Feibelman*, 1968; *Armstrong*, 1969; *Hays et al.*, 1969; *Roble et al.*, 1970; *Hays and Roble*, 1971; *Blamont and Luton*, 1972; *Hernandez and Roble*, 1976b; *Sipler and Biondi*, 1979; *Hernandez et al*, 1982; *Okano et al*, 1985]. Previous experimental and theoretical studies both indicated that a mid-latitude ground-based station observes a temperature increase poleward of the station due to energy input at high latitudes during geomagnetic storms. In addition, meridional wind flows equatorward in response to pressure gradients generated at high latitudes, and the westward component of zonal wind develops due to the coriolis force acts on enhanced meridional wind, and further sometimes during the early evening hours, due to a westward momentum source associated with magnetospheric convection. However, there are few observational results on wind and temperature changes in accordance with auroral activity at high-latitude or auroral zone stations. The role of geomagnetic activity on the neutral wind flow in the auroral zone was studied by *Wallis* [1974]. He concluded that (1) the meridional wind is primarily driven by solar heating; (2) deviations from this pattern are caused by pressure gradient forces resulting from Joule heating; (3) the zonal wind is primarily driven by ion drag; and (4) the response time of the zonal wind to the ion drift is the order of one-half to two hours. *Sica et al.* [1986b] examined five nights of thermospheric neutral wind and temperature data obtained using a Fabry-Perot interferometer at College, Alaska (L=65°). They concluded that during the recovery phase of an auroral substorm, when the westward electrojet flows is over the observing site, the equatorward meridional wind decreased in magnitude. Though the zonal wind is generally westward in the evening and eastward in the morning, the crossover from westward to eastward flow is a function of the location of the substorm onset and the location of the westward electrojet.

However, since those observations are not two-dimensional, it is very hard to understand the overall deviations in both neutral temperatures and wind velocities even when the direction of the field of view of the Fabry-Perot interferometer is changed successively at four or a bit more directions. Recently, new kinds of data sets from the field-widened imaging Fabry-Perot

interferometer (UCL Doppler Imaging System : DIS) were presented by *Batten et al.* [1988] and *Batten and Rees* [1990]. Although they succeeded to show an existence of small spatial (50 km) and temporal (10 min) scale variability in wind field of the F-region thermosphere, the direct comparison with those structures to auroral activity, i.e., the position of auroras and/or the phase of breakup was not shown.

In our study, deviations of thermospheric neutral temperatures and wind velocities in the F-region altitude corresponding to an auroral breakup event was clearly shown in Chapter 4. The great advantage in our study is simultaneous observation of all-sky aurora images by monochromatic (557.7 nm and 630.0 nm) all-sky CCD cameras [*Ono et al.*, 1987; 1988]. It enable us to study one-to-one correspondence between auroral structures, including auroral activity and phase of breakup events, and thermospheric parameters, i.e., neutral temperatures and wind velocities derived from the FPDIS observations. Another great advantage in our study is the highest time resolution, 3 min, for the derivation of the thermospheric parameters. This time resolution is much shorter than the previous works (for example, 11 min in *Batten et al.* [1990]).

As a result, the dynamic response of line-of-sight velocities of neutral wind and temperature in accordance with an auroral breakup event is clearly shown in Figures 4.20 through 4.24 in Chapter 4. It is apparent from these figures that changes in wind velocities mainly occur at the edge of an auroral arc. Moreover, it has become clear that absolute values of wind velocities decreases in the region where the auroral expansion event occurred as shown in Figure 4.23 and 4.24. This result suggests that when an auroral breakup occurred the quiet-time wind system has been broken almost simultaneously with the auroral expansion within few minutes at the F-region altitude.

In addition, when we examine the variations of wind velocities at the auroral breakup event at 23:07 UT on September 13, 1990, some interesting features are found out. They are summarized as follows;

1. Large changes in wind velocities (> 500 m/s) occurred in less than 5 to 10 min when auroral breakup occurred. This result is completely different from that of *Wallis* [1974] in which the response time of the zonal wind to ion drift is shown to be the order of one-half to two hours. Our result suggests much faster response occurred in the F-region thermosphere when auroral breakup occurred.

2. Since those large changes in velocities occur only in eastward and westward directions, the force which is added to move neutral atmosphere is thought to be the ion drag due to the auroral electrojet current flowing eastward at that time.

3. Since those large changes in velocities occur (22:57 UT) a few minutes prior to the optical auroral breakup (23:07 UT), it is thought that the auroral electrojet current flowed prior to the optical intensification of the auroral arc.

5.3 Effect of Vertical Wind and Periodic Wind Perturbations

Vertical motions of the thermosphere during geomagnetically quiet time are expected to be very small, i.e., less than 10 m/s [e.g., *Hernandez and Roble*, 1976a]. In our result, in Section 4.4 a good coincidence in the horizontal wind components is shown at the inner and outer fringe positions at the same directions before the onset of the auroral breakup event at 23:07 UT on September 13, 1990 on the condition that the vertical wind component is zero. This result also suggests that vertical wind component is relatively small at quiet times.

On the other hand, *Hernandez* [1982] showed the existence of vertical motions in the upper thermosphere at mid-latitudes from high time resolution Doppler shift measurements of the 630.0 nm emission at night. He determined that there exist oscillations with $\sim$ 40 min periodicity and large magnitude (e.g., 50 m/s). He ascribed the behavior of these oscillations to the

passage of gravity waves through the upper atmosphere. *Rees et al.* [1984c] also observed strong vertical thermospheric winds at the auroral zone in Northern Scandinavia and in Svalvard by ground-based Fabry-Perot interferometers. Their result indicates a systematic diurnal pattern of strong downward and upward winds in the noon and midnight sector, whose typical velocities are 30 m/s downward and 50 m/s upward, respectively. They also observed strong vertical winds (height-integrated wind associated with a mean altitude of about 240 km) exceeding 100–150 m/s as a result of intense local heating in the magnetic midnight region of the auroral oval during the expansion phase of geomagnetic disturbances accompanying intense auroral disturbances. They noticed that these disturbances also invariably cause major time-dependent changes of the horizontal wind field with, for example, horizontal wind changes exceeding 500 m/s within 30 min. Changes of vertical and horizontal wind fields are highly correlated, and respond directly to local geomagnetic energy input. The source of auroral substorm expansion is considered to generate strong time-dependent wind features which may propagate globally, and thus directly generates one class of thermospheric gravity waves. *Sica et al.* [1986] also observed very strong vertical winds in the zenith position (whose magnitude reached as much as 200 m/s) on December 21, 1982 as shown in Figure 5.3 (a) and vertical winds with wavelike structure on February 6, 1983 as shown in Figure 5.3 (b) at College, Alaska.

In our results, it is also suggested that vertical winds were generated at the time of the auroral breakup events. We will discuss on the estimation of vertical wind velocities and on the periodic variations both in wind velocities and temperatures after breakup events.

Although it is impossible to derive vertical wind velocities directly from our data as we did not observe Doppler values of the zenith position, it is possible to estimate vertical wind velocities by the method described below. Since we observe two-dimensional distributions of neutral temperatures and line-of-sight wind velocities at 12 points in both inner and outer fringes, horizontal and vertical wind components are estimated by assuming that wind field is continuous and has not a divergence nor a converge inside the field of view. It is thought that this assumption is valid at geomagnetically quiet periods. Actually, continuous horizontal wind

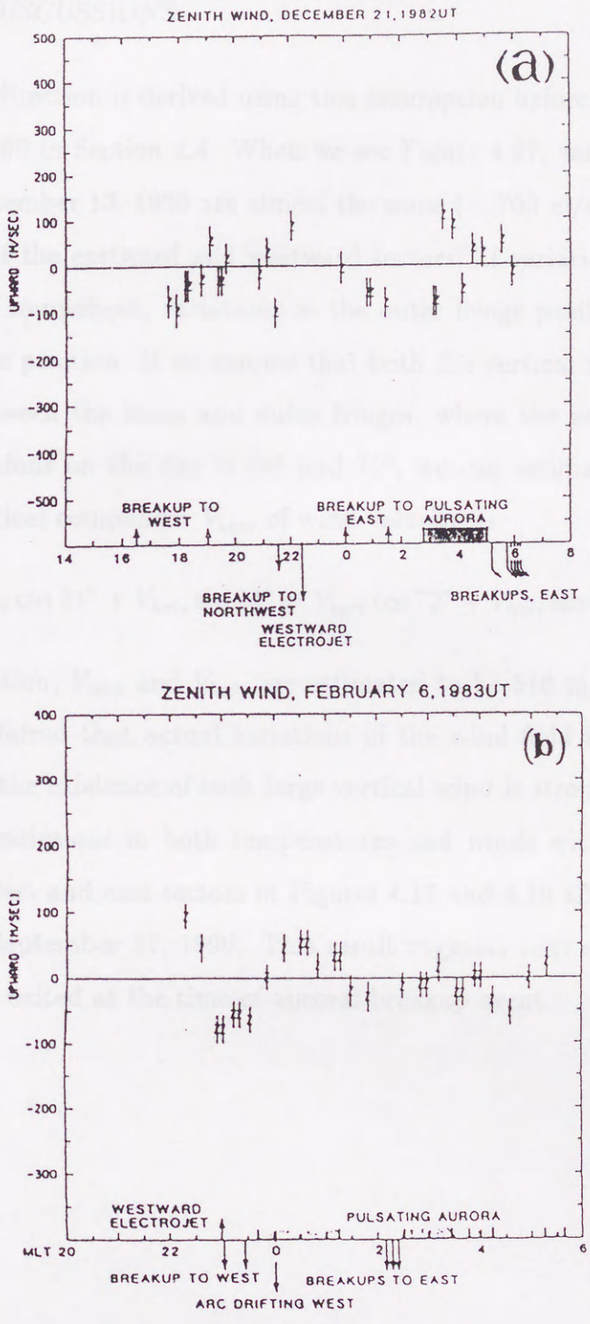

Figure 5.3: Vertical wind measurements on December 21, 1982 (a) and on February 6, 1983 at the zenith position of College, Alaska. (After *Sica et al*, [1986])

in the east–west direction is derived using this assumption before the auroral breakup event on September 13, 1990 in Section 4.4. When we see Figure 4.27, variations in wind speed around 23:00 UT on September 13, 1990 are almost the same ($\sim$ 700 m/s) at both the inner and outer fringe positions of the eastward and westward sectors. If variations in wind speed occur only in the horizontal component, variations at the outer fringe position become more than those at the inner fringe position. If we assume that both the vertical and horizontal wind velocities don't change between the inner and outer fringes, where the zenith angles of the inner and outer fringe positions on the day is 24° and 72°, we can estimate the horizontal component V_{hori} and the vertical component V_{vert} of wind velocity as

$$V_{vert}\cos 24° + V_{hori}\sin 24° = V_{vert}\cos 72° + V_{hori}\sin 72° = 700(\mathrm{m/s}) \tag{5.1}$$

From this equation, V_{vert} and V_{hori} are estimated to be 510 m/s and 570 m/s, respectively. Although it is inferred that actual variations of the wind field is considerably different from this assumption, the existence of such large vertical wind is strongly suggested in any case.

Also periodic variations in both temperatures and winds with a period of 10–20 min are observed in the west and east sectors in Figures 4.17 and 4.19 after the auroral breakup event at 21:38 UT on September 11, 1990. This result suggests that some wave-like variations like gravity waves are exited at the time of auroral breakup event.

Chapter 6

CONCLUSIONS

The conclusions of this thesis is summarized as follows;

1) A new optical instrument, a Fabry-Perot Doppler Imaging System (FPDIS), has been developed. The FPDIS measures the Doppler shift and width of aurora and/or airglow emission lines of OI 557.7 nm and OI 630.0 nm over a wide field of view (165°) to obtain two-dimensional distributions of thermosperic winds and temperatures.

2) Observations of thermospheric winds and temperatures have been carried out at Syowa Station, Antarctica for a period of one austral winter in 1990. Observations were made on 46 clear nights from April 1, 1990 to September 20, 1990 covering various auroral conditions, and 900,000 Doppler image data of OI 557.7 nm and 630.0 nm emission lines as well as the stabilized He–Ne laser calibration data were stored in 17 optical disks.

3) Thermospheric winds and temperatures have been obtained with a high temporal resolution (3 min) as a result of data analysis.

4) The temperatures were observed to increase by 200–500 K associated with an auroral breakup event occurred on September 11, 1990. The line-of-sight wind velocities were observed to change by 400–600 m/s in a time period as short as $\sim$ 10 minutes. Analysis of two dimensional distribution of the wind field suggests periodic changes of winds occurred at most

positions on an image with a period of 10–20 min after the auroral breakup event.

5) From 22:57 UT, September 13, 1990, stable westward winds in 500–800 m/s suddenly decreased by more than 500 m/s within 6 to 9 min at every position in the east–west sectors, including the inner and the outer fringe positions. These variations occurred just before the time of auroral breakup event. It is suggested that neutral particles were forced by the ion drag due to the eastward auroral electrojet current occurred at that time. At the same time, the existence of strong vertical flow is suggested.

Although it have become possible to investigate neutral temperatures and wind velocities in lower (E-region) to middle (F-region) thermosphere from ground, the coverage of this observation is no more than about 2200 km in diameter at 240 km altitude. Whereas, it is impossible to distinguish temporal variations from space-borne observations. When the results on thermospheric dynamics described in this thesis are combined with a variety of space-borne data, we can expect to achieve more clear and comprehensive understanding on the physics of the thermosphere.

Appendix A

TERMINOLOGY

A.1 Two Criteria of Wave Number Width for Defining the Resolving Power

In order to define resolving power of a spectrometer, the width of wave number $\Delta\nu$ which distinguishes two line-spectra is commonly used. When a line-spectra is scanned by a spectrometer which has a finite resolving power, a quasi line-shaped spectra with width $\Delta\nu$ as shown in Figure A.1 is observed according to the instrumental function of the spectrometer. The resolving power $\Delta\nu$ is now defined in two ways. One is called "the Rayleigh criterion" which interprets $\Delta\nu$ as the width from the center of the quasi line-shaped function to the point when the value of that function becomes null for the first time. The other is called "the Taylor criterion" which interprets $\Delta\nu$ as the width of full-width-at-half-maximum (FWHM). The values of $\Delta\nu$ using these two criteria differ a little from each other.

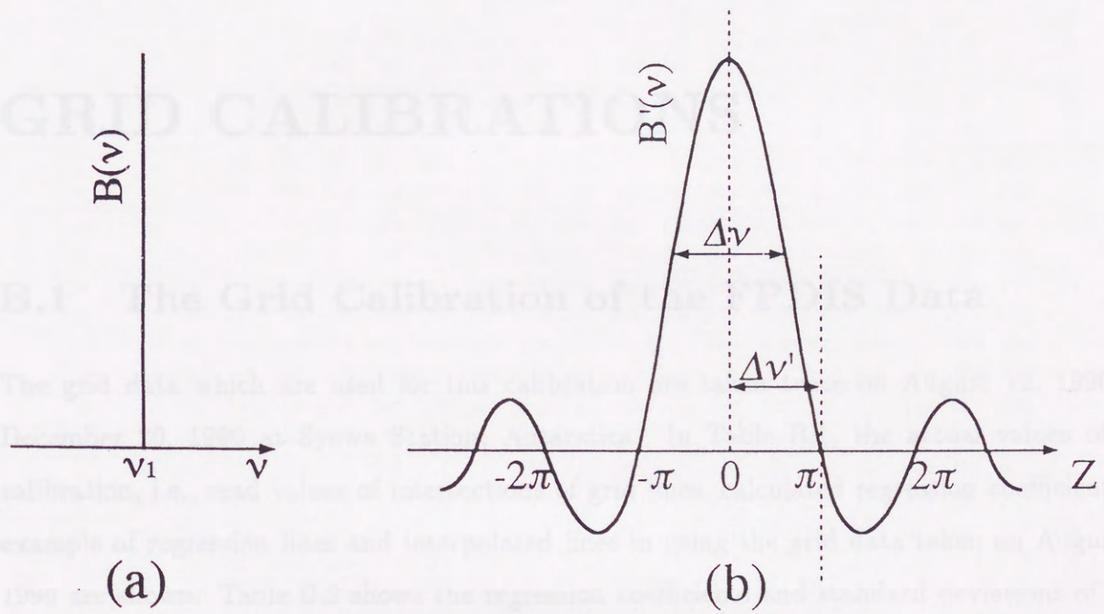

Figure A.1: Schematic diagram of a line-spectra (a) and an example of a quasi line-shaped spectra (b). $\Delta\nu$ represents the resolving power defined by "the Taylor criterion", while $\Delta\nu'$ represents that by "the Rayleigh criterion".

Appendix B

GRID CALIBRATIONS

B.1 The Grid Calibration of the FPDIS Data

The grid data which are used for this calibration are taken twice on August 12, 1990 and December 20, 1990 at Syowa Station, Antarctica. In Table B.1, the actual values of grid calibration, i.e., read values of intersections of grid lines, calculated regression coefficients, an example of regression lines and interpolated lines in using the grid data taken on August 12, 1990 are shown. Table B.2 shows the regression coefficients and standard deviations of them calculated by fitting the values in Table B.1 to the equations 3.3 and 3.4.

Table B.1: Intersections of grid-lines read by the EXCEL image processor from a grid calibration image data taken by the FPDIS shown in Figure 3.3.

		Image-x,y coordinates																			
Grid No.		1	2	3	4	5	6	7	8	9	10	11	12	13	14	15	16	17	18	19	20
1	x	–	–	–	–	–	–	–	–	267	290	311	335	358	379	–	–	–	–	–	–
	y	–	–	–	–	–	–	–	–	26	27	29	29	31	31	–	–	–	–	–	–
2	x	–	–	–	–	179	200	224	245	267	290	310	334	357	377	399	424	444	–	–	–
	y	–	–	–	–	45	45	47	48	50	52	53	54	54	56	57	59	59	–	–	–
3	x	–	–	–	154	178	200	223	245	267	289	310	333	354	377	398	422	443	467	–	–
	y	–	–	–	65	68	70	71	73	74	75	76	77	77	79	81	83	82	82	–	–
4	x	–	–	131	154	177	199	222	244	265	287	309	331	352	375	396	420	442	465	489	–
	y	–	–	85	89	90	92	94	96	98	98	99	102	102	102	106	107	107	107	108	–
5	x	–	–	131	153	176	198	221	243	264	286	308	329	351	374	394	417	441	463	487	–
	y	–	–	110	112	114	116	117	118	120	121	122	124	124	125	129	129	129	130	132	–
6	x	–	104	130	153	176	198	219	242	263	285	307	328	350	373	394	415	440	462	485	508
	y	–	130	132	135	137	138	139	140	142	144	145	146	147	149	151	152	152	153	155	157
7	x	–	106	129	153	176	197	219	241	262	284	306	327	349	370	392	414	439	460	484	507
	y	–	154	155	158	159	160	161	163	164	165	167	168	169	169	174	173	176	176	178	179
8	x	–	105	129	153	175	197	219	241	261	283	304	326	347	368	391	412	436	459	482	507
	y	–	178	179	180	181	182	183	185	185	188	189	190	191	192	196	196	197	199	200	202
9	x	81	105	128	151	175	196	219	238	260	282	303	325	346	368	390	412	434	458	481	507
	y	198	200	201	201	204	205	205	207	208	210	210	211	213	215	218	218	219	221	222	224
10	x	81	104	128	150	173	195	217	237	259	280	302	324	346	367	388	410	433	457	478	506
	y	221	222	223	224	226	226	228	229	231	231	234	234	235	238	240	241	242	244	245	246
11	x	81	103	126	149	171	195	215	236	258	279	301	323	344	366	387	410	433	457	477	504
	y	244	244	246	247	248	249	251	252	253	254	255	256	258	258	263	264	265	266	268	270
12	x	80	102	125	147	170	193	214	235	257	278	300	322	343	365	387	409	433	456	477	502
	y	267	267	268	270	270	270	272	273	275	276	278	279	279	282	285	286	287	290	291	293
13	x	79	101	124	147	168	191	213	234	256	277	299	321	342	364	386	408	432	455	476	500
	y	289	290	291	291	292	293	295	296	297	298	300	302	302	304	305	308	311	312	314	318
14	x	–	100	123	146	166	190	211	233	254	276	298	319	341	363	385	408	432	455	475	–
	y	–	312	314	314	315	316	316	318	320	321	323	324	326	328	328	331	332	334	337	–
15	x	–	100	122	144	165	189	211	231	253	275	296	318	340	362	385	408	432	454	474	–
	y	–	337	337	339	338	339	340	341	343	344	345	346	347	350	352	354	356	359	360	–
16	x	–	–	120	142	165	187	208	229	252	274	296	317	339	361	384	408	430	453	474	–
	y	–	–	362	361	362	362	362	365	366	367	368	370	370	372	374	378	380	382	384	–
17	x	–	–	118	141	162	186	207	227	252	272	294	317	338	361	384	408	429	453	–	–
	y	–	–	385	385	385	385	386	387	389	389	392	394	394	397	397	403	404	405	–	–
18	x	–	–	–	140	160	182	204	224	250	271	294	317	337	360	383	409	428	–	–	–
	y	–	–	–	409	411	410	411	412	413	415	415	418	418	421	421	425	425	–	–	–
19	x	–	–	–	–	–	180	201	222	248	269	294	315	336	359	382	–	–	–	–	–
	y	–	–	–	–	–	434	436	437	437	439	441	442	442	444	446	–	–	–	–	–
20	x	–	–	–	–	–	–	–	223	245	267	293	–	–	–	–	–	–	–	–	–
	y	–	–	–	–	–	–	–	464	466	466	465	–	–	–	–	–	–	–	–	–

Table B.2: Regression coefficients and standard deviations of them calculated by fitting the values in Table B.1 to the equations 3.3 and 3.4.

Line No.	Number of Points to be Used for Fitting	Regression Coefficients			Standard Deviations			
		b_0	b_1	b_2	Fitting(σ)	$\sigma(b_0)$	$\sigma(b_1)$	$\sigma(b_2)$
1	6	-3.799185	0.15651892	-0.00016954	0.50809993	17.27697411	0.10801197	0.00016688
2	13	30.865297	0.08239921	-0.00004143	0.58762939	2.49703597	0.01679314	0.00002676
3	15	51.744101	0.10407908	-0.00008085	0.79606779	2.28341237	0.01561783	0.00002490
4	17	71.528843	0.12205326	-0.00009621	0.86677748	1.77642915	0.01236654	0.00001972
5	17	99.734930	0.08761711	-0.00004541	0.71879266	1.47399114	0.01030405	0.00001650
6	19	121.954399	0.08658782	-0.00003775	0.61340324	0.92081995	0.00656758	0.00001053
7	19	147.525932	0.06309603	-0.00000092	0.76259244	1.15350275	0.00823441	0.00001322
8	19	172.615231	0.04389930	0.00002885	0.63572061	0.95785915	0.00684759	0.00001102
9	20	194.331830	0.04689488	0.00002384	0.68421145	0.82065988	0.00619582	0.00001036
10	20	216.546764	0.04790208	0.00002450	0.65828247	0.78886066	0.00598266	0.00001004
11	20	240.563131	0.03550153	0.00004637	0.75380585	0.89963225	0.00685442	0.00001154
12	20	264.301433	0.02162931	0.00007327	0.68399783	0.81035266	0.00620555	0.00001048
13	20	287.845092	0.01043996	0.00009598	0.58515971	0.68942150	0.00530616	0.00000900
14	18	309.133755	0.02329493	0.00007203	0.61711941	0.95500245	0.00726898	0.00001241
15	18	336.739442	-0.01026349	0.00012759	0.53327052	0.82186386	0.00627753	0.00001074
16	17	362.282049	-0.02764103	0.00015681	0.74689657	1.42549382	0.01040278	0.00001726
17	16	385.601009	-0.02993161	0.00016668	0.96180198	1.94712036	0.01477718	0.00002557
18	14	408.150844	-0.00749168	0.00011315	0.75016726	2.13192635	0.01604540	0.00002800
19	10	426.985817	0.03486331	0.00003655	0.59870899	3.94030929	0.02915793	0.00005174
20	4	371.640719	0.72043273	-0.00137197	0.20780471	12.49532269	0.09751466	0.00018866
		c_0	c_1	c_2	Fitting(σ)	$\sigma(c_0)$	$\sigma(c_1)$	$\sigma(c_2)$
1	5	61.145358	0.18365588	-0.00042198	0.13428548	4.07799721	0.03392782	0.00006956
2	10	102.864719	0.03480939	-0.00013600	0.72075891	3.09734614	0.02791614	0.00005932
3	14	131.515804	0.00206578	-0.00009425	0.36940625	0.65999887	0.00614501	0.00001286
4	16	154.618395	0.00087005	-0.00009374	0.56912296	0.73752855	0.00693857	0.00001435
5	17	179.029365	-0.00731206	-0.00009585	0.74496129	0.75730390	0.00754090	0.00001622
6	18	199.454156	0.00769970	-0.00011820	0.57548255	0.56472227	0.00533069	0.00001086
7	18	223.898823	-0.01111806	-0.00008994	0.76090676	0.75676007	0.00709669	0.00001438
8	19	246.980175	-0.02675276	-0.00006238	0.80462134	0.77094686	0.00682910	0.00001307
9	20	268.527031	-0.03326479	-0.00003217	0.55947307	0.43050179	0.00401760	0.00000798
10	20	291.763378	-0.04420621	-0.00001666	0.42273821	0.32862953	0.00305106	0.00000603
11	20	313.477269	-0.05204104	0.00001344	0.66012284	0.52015631	0.00481590	0.00000949
12	19	337.319685	-0.06725706	0.00003897	0.49523373	0.40733235	0.00393564	0.00000812
13	19	359.892976	-0.07357617	0.00004571	0.46132612	0.38243217	0.00369134	0.00000760
14	19	381.771674	-0.07515858	0.00005451	0.61022535	0.50923190	0.00488080	0.00000998
15	18	403.600403	-0.07945887	0.00007201	0.43896948	0.47803994	0.00426092	0.00000829
16	17	431.397377	-0.13272574	0.00018737	0.40916797	0.47546127	0.00439820	0.00000888
17	17	448.829046	-0.07444154	0.00006420	0.94615948	1.09538692	0.01012757	0.00002043
18	15	473.348151	-0.09035783	0.00010047	0.40029845	0.64478091	0.00581708	0.00001173
19	13	500.927253	-0.12301914	0.00013624	0.50537849	1.21779551	0.01067020	0.00002142
20	8	497.389875	0.12058753	-0.00035446	0.41794270	3.32581716	0.02899113	0.00006081

Appendix C

STAR CALIBRATION

C.1 The Star Calibration of the FPDIS Data

In Table C.1, parameters of each star used for star calibration is shown. In Tables C.2 and C.3, results of geometrical calibration using the star data on April 4, 1990 at 21:22 UT, and on April 21, 1990 at 16:50 UT are shown, respectively.

Table C.1: Introductions and read values of the stars used for the geometrical calibration.

No.	Name of a Star (popular name)	Equatorial Coordinates Right Ascension		Declination		Magnitude	Read Position in Image Plane 21:22UT/April 4, 1990		16:50UT/April 22, 1990	
		hour	min	0	1		I_x(pixel)	I_y(pixel)	I_x(pixel)	I_y(pixel)
1	α-Eri (Achernar)	01	37.7	-57	14	0.5	391	356	405	264
2	α-Car (Canopus)	06	24.0	-52	42	-0.7	397	226	309	185
3	α-CMa (Sirius)	06	45.1	-16	43	-1.5	440	124	272	75
4	α-Vir (Spica)	13	25.2	-11	10	1.0	122	157	–	–
5	β-Centauri	14	03.8	-60	22	0.6	231	265	223	338
6	α-Centauri	14	39.6	-60	50	-0.3	227	277	230	351

Table C.2: Result of the geometrical calibration using the star data on April 4, 1990 at 21:22 UT.

No.	Names of Star Pair	Calculated Zenith Position I_{X_0} (pixels)	I_{Y_0} (pixels)	Azimuth Offset O_{AZ} (degree)	A-Parameter A (pixels/radian)
1	Achernar–Canopus	267.75	254.15	42.75	171.26
2	Achernar–Sirius	263.71	260.67	45.49	170.34
3	Achernar–Spica	260.33	262.87	46.84	171.87
4	Achernar–β-Cen	264.55	261.75	45.62	168.92
5	Achernar–α-Cen	264.71	261.27	45.45	169.09
6	Canopus–Sirius	275.10	265.15	48.27	165.76
7	Canopus–Spica	266.30	259.71	44.93	174.75
8	Canopus–β-Cen	265.93	261.60	45.66	175.84
9	Canopus–α-Cen	268.61	269.02	48.99	175.31
10	Sirius–Spica	261.90	257.75	44.61	170.09
11	Sirius–β-Cen	264.78	261.59	45.85	170.13
12	Sirius–α-Cen	264.80	261.01	45.74	169.85
13	Spica–β-Cen	266.07	262.51	44.16	176.18
14	Spica–α-Cen	266.45	261.26	44.55	175.77
15	β-Cen–α-Cen	263.13	262.16	45.14	161.61
	mean	265.61	261.50	45.60	171.12
	S.D.(σ)	3.26412	3.11571	1.48814	3.94303

Table C.3: Result of the geometrical calibration using the star data on April 21, 1990 at 16:50 UT.

No.	Names of Star Pair	Calculated Zenith Position I_{X_0} (pixels)	I_{Y_0} (pixels)	Azimuth Offset O_{AZ} (degree)	A-Parameter A (pixels/radian)
1	Achernar–Canopus	266.14	253.13	43.24	174.22
2	Achernar–Sirius	263.15	254.56	43.90	177.82
3	Achernar–β-Cen	263.65	257.80	45.21	176.98
4	Achernar–α-Cen	263.14	258.22	45.38	177.58
5	Canopus–Sirius	267.17	256.85	45.21	179.94
6	Canopus–β-Cen	270.28	259.13	47.83	181.01
7	Canopus–α-Cen	280.61	263.92	55.62	181.54
8	Sirius–β-Cen	265.22	256.87	44.59	180.02
9	Sirius–α-Cen	265.05	257.25	44.54	180.40
10	β-Cen–α-Cen	269.23	256.78	42.43	183.96
	mean	267.36	257.45	45.80	179.35
	S.D.(σ)	4.98320	2.71290	3.54962	2.60980

References

Abreu, V. J., G. A. Schmitt, P. B. Hays, J. W. Meriwether, Jr., Ca. A. Tepley, and L. L. Cogger, Atmospheric scattering effects on ground-based measurements of thermospheric winds, *Planet. Space Sci.*, **31**, 303–310, 1983.

Ahn, B. -H, S. -I. Akasofu, and Y. Kamide, The Joule heat production rate and the particle energy injection rate as a function of geomagnetic indices AE and AL, *J. Geophys. Res.*, **88**, 6275–6287, 1983.

Amelio, G. F., M. F. Tompsett, and G. E. Smith, Experimental verification of the charge coupled device concept, *Bell Syst. Tech. J.*, **49**, 593–600, 1970.

Armstrong, E. B., Doppler shifts in the wavelength of the OI λ 6300 line in the night airglow, *Planet. Space Sci.*, **17**, 957–974, 1969.

Aruliah, A. L., D. Rees, and T. J. Fuller-Rowell, The combined effect of solar and geomagnetic activity on high latitude thermospheric neutral winds. Part I. Observations, *J. Atmos. Terr. Phys.*, **53**, 467–483, 1991a.

Aruliah, A. L., D. Rees, and A. Steen, Seasonal and solar cycle variations in high-latitude thermospheric winds, *Geophys. Res. Lett.*, **18**, 1983–1986, 1991b.

Babcock, H. D., A study of the green auroral line by the interference method, *Astrophys. J.*, **57**, 209–221, 1923.

Balhorn, R., H. Kunzmann, and F. Lebowsky, Frequency stabilization of internal-mirror helium-neon lasers, *Appl. Opt.*, **11**, 742–744, 1972.

Basu, S., S. Basu, E. Kudeki, H. P. Zengingonul, M. A. Biondi, and J. W. Meriwether, Zonal irregularity drifts and neutral winds measured near the magnetic equator in Peru, *J. Atmos. Terr. Phys.*, **53**, 743–755, 1991.

Batten, S., and D. Rees, Thermospheric winds in the auroral oval: observations of small scale structures and rapid fluctuations by a Doppler Imaging System, *Planet. Space Sci.*, **38**, 675–694, 1990.

Batten, S., D. Rees, D. Wade, and A. Steen, Observations of thermospheric neutral winds by the UCL Doppler imaging system at Kiruna in northern Scandinavia, *J. Atmos. Terr. Phys.*, **50**, 861–888, 1988.

Bennett, S. J., Modification of inexpensive multimode lasers to produce a stabilized single frequency beam. II. Reply, *Appl. Opt.*, **13**, 231–231, 1974.

Bennett, S. J., R. E. Ward, and D. C. Wilson, Comments on: Frequency stabilization of internal mirror He-Ne lasers, *Appl. Opt.*, **12**, 1406–1406, 1973.

Biondi, M. A., and W. A. Feibelman, Twilight and nightglow spectral line shapes of oxygen λ 6300 and λ 5577 radiation, *Planet. Space Sci.*, **16**, 431–443, 1968.

Biondi, M. A., and J. W. Meriwether, Jr., Measured response of the equatorial thermospheric temperature to geomagnetic activity and solar flux changes, *Geophys. Res. Lett.*, **12**, 267–270, 1985.

Biondi, M. A., and D. P. Sipler, Horizontal and vertical winds and temperatures in the equatorial thermosphere: measurements from Natal, Brazil during August-September 1982, *Planet. Space Sci.*, **33**, 817–823, 1985.

Biondi, M. A., J. W. Meriwether, Jr., B. G. Fejer, and S. A. Gonzalez, Seasonal variations in the equatorial thermospheric wind measured at Arequipa, Peru, *J. Geophys. Res.*, **95**, 12243–12250, 1990.

Blamont, J. E., and J. M. Luton, Geomagnetic effect on the neutral temperature of the F-region during the magnetic storm of September 1969, *J. Geophys. Res.*, **77**, 3534–3556, 1972.

Boyle, W. S., and G. E. Smith, Charge coupled semiconductor devices, *Bell Syst. Tech. J.*, **49**, 587–593, 1970.

Burnside, R. G., and C. A. Tepley, Optical observations of thermospheric neutral winds at Arecibo between 1980 and 1987, *J. Geophys. Res.*, **94**, 2711–2716, 1989.

Burnside, R. G., F. A. Herrero, J. W. Meriwether, Jr., and J. C. G. Walker, Optical observations of thermospheric dynamics at Arecibo, *J. Geophys. Res.*, **86**, 5532–5540, 1981.

Clark, R. R., Upper atmosphere wind observations of waves and tides with the UNH Meteor Radar System at Durham 43°N (1977, 1978 and 1979), *J. Atmos. Terr. Phys.*, **45**, 621–627, 1983.

Coffey, H. E. (editor), Geomagnetic and Solar Data, *J. Geophys. Res.*, **96**, 297–297, 1991.

Cogger, L. L., G. J. Nelson, M. A. Biondi, R. D. Hake, Jr., and D. P. Sipler, Coincident F-region temperature determinations from incoherent backscatter and Doppler broadening of (OI) 6300 Å, *J. Geophys. Res.*, **75**, 4887–4889, 1970.

Cogger, L. L., J. S. Murphree, C. A. Tepley, and J. W. Meriwether, Jr., Measurements of the E region neutral wind field, *Planet. Space Sci.*, **33**, 373–379, 1985.

Crickmore, R. I., J. R. Dudeney, and A. S. Rodger, Vertical thermospheric winds at the equatorward edge of the auroral oval, *J. Atmos. Terr. Phys.*, **53**, 485–492, 1991.

Crowley, G., Dynamics of the earth's thermosphere: a review, *Rev. Geophys., Suppl.*, 1143–1165, 1991.

Dartt, D., G. Nastrom, and A. Belmont, Seasonal and solar cycle wind variations, 80-100 km, *J. Atmos. Terr. Phys.*, **45**, 707–718, 1983.

Dickinson, R. E., Infrared radiative cooling in the mesosphere and lower thermosphere, *J. Atmos. Terr. Phys.*, **46**, 995–1008, 1984.

Dickinson, R. E., E. C. Ridley, and R. G. Roble, A three-dimensional general circulation model of the thermosphere, *J. Geophys. Res.*, **86**, 1499–1512, 1981.

Feibelman, W. A., R. D. Hake, Jr., D. P. Sipler, and M. A. Biondi, Twilight and nighttime ionospheric temperatures from oxygen λ 6300 and λ 5577 spectral-line profiles, *J. Geophys. Res.*, **77**, 1869–1877, 1972.

Foster, J. C., J. -P. St.-Maurice, and V. J. Abreu, Joule heating at high latitudes, *J. Geophys. Res.*, **88**, 4885–4896, 1983.

Friedman, J. F., and F. A. Herrero, Fabry-Perot interferometer measurements of thermospheric neutral wind gradients and reversals at Arecibo, *Geophys. Res. Lett.*, **9**, 785–788, 1982.

Fuller-Rowell, T. J., and D. S. Evans, Height-integrated Pedersen and Hall conductivity patterns inferred from the TIROS-NOAA satellite data, *J. Geophys. Res.*, **92**, 7606–7618, 1987.

Fuller-Rowell, T. J., and D. Rees, A three-dimensional time-dependent global model of the thermosphere, *J. Atmos. Sci.*, **37**, 2545–2567, 1980.

Fuller-Rowell, T. J., D. Rees, S. Quegan, G.J. Bailey, and R.J. Moffett, The effect of realistic conductivities on the high-latitude neutral thermospheric circulation, *Planet. Space Sci.*, **32**, 469–480, 1984.

Garcia, R. R., and S. Solomon, The effect of breaking gravity waves on the dynamics and chemical composition of the mesosphere and lower thermosphere, *J. Geophys. Res.*, **90**, 3850–3868, 1985.

Gordon, S. K., and S. F. Jacobs, Modification of inexpensive multimode lasers to produce a stabilized single frequency beam. I, *Appl. Opt.*, **13**, 231–231, 1974.

Greet, P., and F. Jacka, Observations of the sodium layer using a Fabry-Perot spectrometer: twilight temperature variations, *J. Atmos. Terr. Phys.*, **51**, 91–99, 1989a.

Greet, P., M. Conde, and F. Jacka, Daytime observation of the sodium layer with a Fabry-Perot spectrometer at Mawson, Antarctica, *Geophys. Res. Lett.*, **16**, 871–874, 1989b.

Groves, G. V., and J. M. Forbes, Mean zonal and meridional accelerations and mean heating induced by solar tides for equinox and solstice conditions, *Planet. Space Sci.*, **33**, 283–293, 1985.

Gussenhoven, M. S., D. A. Hardy, N. Heinemann, and R. K. Burkhardt, Morphology of the polar rain, *J. Geophys. Res.*, **89**, 9785–9800, 1984.

Hagan, M. E., and D. P. Sipler, Combined incoherent scatter radar and Fabry-Perot interferometer measurements of frictional heating effects over Millstone Hill during March 7-10, 1989, *J. Geophys. Res.*, **96**, 289–296, 1991.

Hardy, D. A., M. S. Gussenhoven, and E. Holeman, A statistical model of auroral electron precipitation, *J. Geophys. Res.*, **90**, 4229–4248, 1985.

Hays, P. B., and S. K. Atreya, The influence of thermospheric winds on the auroral red-line profile of atomic oxygen, *Planet. Space Sci.*, **19**, 1225–1228, 1971.

Hays, P. B., and R. G. Roble, Direct observations of thermospheric winds during geomagnetic storms, *J. Geophys. Res.*, **76**, 5316–5321, 1971.

Hays, P. B., A. F. Nagy, and R. G. Roble, Interferometric measurements of the 6300 Å Doppler temperature during a magnetic storm, *J. Geophys. Res.*, **74**, 4162–4168, 1969.

Hays, P. B., J. W. Meriwether, and R. G. Roble, Nighttime thermospheric winds at high latitudes, *J. Geophys. Res.*, **84**, 1905–1913, 1979.

Hays, P. B., T. L. Killeen, and B. C. Kennedy, The Fabry-Perot interferometer on Dynamics Explorer, *Space Sci. Instrum.*, **5**, 395–416, 1981.

Hays, P. B., T. L. Killeen, N. W. Spencer, L. E. Wharton, R. G. Roble, B. A. Emery, T. J. Fuller-Rowell, D. Rees, L. A. Frank, and J. D. Craven, Observations of the dynamics of the polar thermosphere, *J. Geophys. Res.*, **89**, 5597–5612, 1984.

Hedin, A. E., Neutral thermosphere composition and thermal structure, *Rev. Geophys. Space Phys.*, **17**, 477–484, 1979.

Hernandez, G., Analytical description of a Fabry-Perot spectrometer, *Appl. Opt.*, **5**, 1745–1748, 1966.

Hernandez, G., Lower-thermosphere temperatures determined from the line profiles of the OI 17924-K (5577 Å) emission in the night sky. I. Long-term behavior, *J. Geophys. Res.*, **81**, 5165–5172, 1976.

Hernandez, G, Direct measurements of nighttime thermospheric winds and temperatures. 3. Monthly variations during solar minimum, *J. Geophys. Res.*, **82**, 5505–5511, 1977.

Hernandez, G., Analytical description of a Fabry-Perot spectrometer. 4: Signal noise limitations in data retrieval; winds, temperature, and emission rate, *Appl. Opt.*, **17**, 2967–2972, 1978.

Hernandez, G., Vertical motions of the neutral thermosphere at midlatitude, *Geophys. Res. Lett.*, **9**, 555–557, 1982.

Hernandez, G., Solar, geomagnetic and long term effects on thermospheric neutral kinetic temperatures at midlatitude, *Adv. Space Res.*, **3**, 129–136, 1983.

Hernandez, G., Fabry-Perot Interferometers, pp. 9–54, *Cambridge University Press*, 1986.

Hernandez, G., and R. G. Roble, Direct measurement of nighttime thermospheric winds and temperatures. 1. Seasonal variations during geomagnetic quiet periods, *J. Geophys. Res.*, **81**, 2065–2074, 1976a.

Hernandez, G., and R. G. Roble, Direct measurements of nighttime thermospheric winds and temperatures. 2. Geomagnetic storms, *J. Geophys. Res.*, **81**, 5173–5181, 1976b.

Hernandez, G., and R. G. Roble, The geomagnetic quiet nighttime thermospheric wind pattern over Fritz Peak Observatory during solar cycle minimum and maximum, *J. Geophys. Res.*, **89**, 327–337, 1984a.

Hernandez, G., and R. G. Roble, Nighttime variation of thermospheric winds and temperatures over Fritz Peak Observatory during the geomagnetic storm of March 2, 1983, *J. Geophys. Res.*, **89**, 9049–9056, 1984b.

Hernandez, G. J., and J. P. Turtle, Nightglow 5577-Å [OI] line kinetic temperatures, *Planet. Space Sci.*, **13**, 901–904, 1965.

Hernandez, G., T. E. VanZandt, V. L. Peterson, and J. P. Turtle, Comparison of optical and incoherent scatter measurements of nighttime exospheric temperature at the magnetic equator, *J. Geophys. Res.*, **80**, 3271–3274, 1975.

Hernandez, G., R. G. Roble, E. C. Ridley, and J. H. Allen, Thermospheric response observed over Fritz Peak, Colorado, during two large geomagnetic storms near solar cycle maximum, *J. Geophys. Res.*, **87**, 9181–9192, 1982.

Hernandez, G., R. W. Smith, R. G. Roble, J. Gress, and K. C. Clark, Thermospheric dynamics at the South Pole, *Geophys. Res. Lett.*, **17**, 1255–1258, 1990.

Herrero, F. A., H. G. Mayr, I. Harris, F. Varosi, and J. W. Meriwether, Jr., Thermospheric gravity waves near the sources: comparison of variations in neutral temperature and vertical velocity at Sondre Stromfjord, *Geophys. Res. Lett.*, **11**, 939–942, 1984.

Hilliard, R. L., and G. G. Shepherd, Upper atmospheric temperatures from Doppler line widths, IV, A detailed study using the OI 5577Å auroral and nightglow emission, *Planet. Space Sci.*, **14**, 386–406, 1966.

Jacka, F., A. R. D. Bower, and P. A. Wilksch, Thermospheric temperatures and winds derived from OI λ 630 nm night airglow line profiles, *J. Atmos. Terr. Phys.*, **41**, 397–407, 1979.

Jahn, H., G. Fellberg, B. Gladitz, and M. Scheele, Maximum-likelihood optimization of a Fabry-Perot interferometer for thermospheric temperature and wind measurements, *J. Opt. Soc. Am.*, **72**, 386–391, 1982.

Kamiyama, H., S. Okano, T. Onuma, and T. Ichikawa, Measurement of the Doppler temperature of the oxygen green line observed at middle latitude, *Rep. Ionos. Space Res. Jap.*, **29**, 171–175, 1975.

Killeen, T. L., Energetics and dynamics of the Earth's thermosphere, *Rev. Geophys.*, **25**, 433–454, 1987.

Killeen, T. L., and P. B. Hays, Doppler line profile analysis for a multichannel Fabry-Perot interferometer, *Appl. Opt.*, **23**, 619–620, 1984.

Killeen, T. L., and R. G. Roble, An analysis of the high-latitude thermospheric wind pattern calculated by a thermospheric general circulation model. II. Neutral parcel transport, *J. Geophys. Res.*, **91**, 11291–11307, 1986.

Killeen, T. L., P. B. Hays, N. W. Spencer, and L. E. Wharton, Neutral winds in the polar thermosphere as measured from Dynamics Explorer, *Geophys. Res. Lett.*, **9**, 957–960, 1982.

Killeen, T. L., P. B. Hays, N. W. Spencer, and L. E. Wharton, Neutral Winds in the polar thermosphere as measured from Dynamics Explorer, *Adv. Space Res.*, **2**, 133–136, 1983.

Killeen, T. L., R. W. Smith, P. B. Hays, N. W. Spencer, L. E. Wharton, and F. G. McCormac, Neutral winds in the high latitude winter F-region: coordinated observations from ground and space, *Geophys. Res. Lett.*, **11**, 311–314, 1984.

Killeen, T. L., R. G. Roble, R. W. Smith, N. W. Spencer, J. W. Meriwether, Jr., D. Rees, G. Hernandez, P. B. Hays, L. L. Cogger, D. P. Sipler, M. A. Biondi, and C. A. Tepley, Mean neutral circulation in the winter polar F region, *J. Geophys. Res.*, **91**, 1633–1649, 1986.

Killeen, T. L., J. D. Craven, L. A. Frank, J. -J. Ponthieu, N. W. Spencer, R. A. Heelis, L. H. Brace, R. G. Roble, P. B. Hays, and G. R. Carignan, On the relationship between dynamics of the polar thermosphere and morphology of the aurora: Global-scale observations from Dynamics Explorers 1 and 2, *J. Geophys. Res.*, **93**, 2675–2692, 1988.

Kim, J. S., G. S. N. Murty, and S. Okano, Influence of the auroral electrojet and oval on mid-latitude thermospheric temperatures and meridional winds, *J. Geomag. Geoelectr.*, **42**, 597–606, 1990.

Kudo, K., Bunkou no kiso to houhou (Fundamentals and methods of spectroscopy) (in Japanese), pp. 465–470, *Ohm Publishing Co.*, Tokyo, 1985.

Larsen, M. F., I. S. Mikkelsen, J. W. Meriwether, R. Niciejewski, and K. Vickery, Simultaneous observations of neutral winds and electric fields at spaced locations in the dawn auroral oval, *J. Geophys. Res.*, **94**, 17235–43, 1989.

Lloyd, N., A. H. Manson, D. J. McEwen, and C. E. Meek, A comparison of middle atmospheric dynamics at Saskatoon (52°N, 107°W) as measured by a medium-frequency radar and a Fabry-Perot interferometer, *J. Geophys. Res.*, **95**, 7653–7660, 1990.

Manson, A. H., and C. E. Meek, Winds and tidal oscillations in the upper middle atmosphere at Saskatoon (52°N, 107°W, L=4.3) during the year June 1982–May 1983, *Planet. Space Sci.*, **32**, 1087–1099, 1984.

Manson, A. H., C. E. Meek, N. Lloyd, and D. J. McEwen, Dynamics of the lower thermosphere at Saskatoon (52°N, 107°W) during 1988/89: comparisons of measurements by a medium frequency radar and a Fabry-Perot interferometer, *Planet. Space Sci.*, **39**, 1511–1525, 1991.

McCormac, F. G., T. L. Killeen, E. Gombosi, P. B. Hays, and N. W. Spencer, Configuration of the high-latitude thermosphere neutral circulation for IMF By negative and positive, *Geophys. Res. Lett.*, **12**, 155–158, 1985.

Meriwether, J. W., Jr., J. W. Moody, M. A. Biondi, and R. G. Roble, Optical interferometric measurements of nighttime equatorial thermospheric winds at Arequipa, Peru, *J. Geophys. Res.*, **91**, 5557–5566, 1986.

Meriwether, J. W., T. L. Killeen, Jr., F. G. McCormac, A. G. Burns, and R. G. Roble, Thermospheric winds in the geomagnetic polar cap for solar minimum conditions, *J. Geophys. Res.*, **93**, 7478–7492, 1988.

Miller, N. J., H. G. Mayr, N. W. Spencer, L. H. Brace, and G. R. Carignan, Observations relating changes in thermospheric composition to depletions in topside ionization during the geomagnetic storm of September 1982, *J. Geophys. Res.*, **89**, 2389–2394, 1984.

Murty, G. S. N., and J. S. Kim, Geomagnetic quiet-time behavior of the thermospheric meridional winds and temperature at Albany, New York, *Planet. Space Sci.*, **36**, 197–203, 1988a.

Murty, G. S. N., and J. S. Kim, Thermospheric temperatures and meridional winds measured at Albany, New York during geomagnetically disturbed periods, *Planet. Space Sci.*, **36**, 677–685, 1988b.

Okano, S., and J. S. Kim, Photometric and interferometric observations of the SAR arc event of September 25/26, 1978, *J. Geophys. Res.*, **84**, 4441–4445, 1979.

Okano, S., and J. S. Kim, Thermospheric temperatures during geomagnetically disturbed periods, *J. Geomag. Geoelectr.*, **38**, 173–186, 1986a.

Okano, S., and J. S. Kim, Thermospheric temperatures during the July 5, 1978 storm: a possible existence of the nonthermal atomic oxygen, *J. Geomag. Geoelectr.*, **38**, 189–200, 1986b.

Okano, S., J. S. Kim, and T. Ichikawa, Measurements of thermospheric response to auroral activities, *Planet. Space Sci.*, **33**, 841–845, 1985.

Oliver, W. L., J. C. Foster, J. M. Holt, G. B. Loriot, V. B. Wickwar, J. D. Kelly, O. de la Beaujardiere, P. F. Bythrow, C. I. Meng, F. J. Rich, and R. E. Huffman, Initial Millstone Hill, Sondrestrom, and HILAT observations of thermospheric temperatures and frictional heating, *Geophys. Res. Lett.*, **11**, 911–914, 1984.

Ono, T., M. Ejiri, and T. Hirasawa, Monochromatic auroral images observed at Syowa Station, in Antarctica, *J. Geomag. Geoelectr.*, **39**, 65–95, 1987.

Ono, T., M. Ejiri, and T. Hirasawa, Observation of monochromatic auroral images and data processing, *The Antarctic Record*, **32**, 38–76, 1988.

Perreault, P., and S. -I. Akasofu, A study of geomagnetic storms, *Geophys. J. R. Ast. Soc.*, **54**, 547–573, 1978.

Price, G. D., and F. Jacka, The influence of geomagnetic activity on the upper mesosphere/lower thermosphere in the auroral zone. I. Vertical winds, *J. Atmos. Terr. Phys.*, **53**, 909–922, 1991.

Rees, D., P. A. Rounce, P. Charleton, T. J. Fuller-Rowell, I. McWhirter, and K. Smith, Thermospheric winds during the Energy Budget Campaign: ground-based Fabry-Perot observations supported by dynamical simulations with a three-dimensional, time-dependent thermospheric model, *J. Geophys.*, **50**, 202–211, 1982.

Rees, D., T. J. Fuller-Rowell, R. Gordon, T. L. Killeen, P. B. Hays, L. E. Wharton, and N. W. Spencer, A comparison of wind observations of the upper thermosphere from the Dynamics Explorer satellite with the predictions of a global time-dependent model, *Planet. Space Sci.*, **31**, 1299–1314, 1983.

Rees, D., A. H. Greenaway, R. Gordon, I. McWhirter, P. J. Charleton, and A. Steen, The Doppler Imaging System: initial observations of the auroral thermosphere, *Planet. Space Sci.*, **32**, 273–285, 1984a.

Rees, D., N. Lloyd, P. J. Charleton, and M. Carlson, Comparison of plasma flow and thermospheric circulation over northern Scandinavia using EISCAT and a Fabry-Perot interferometer, *J. Atmos. Terr. Phys.*, **46**, 545–564, 1984b.

Rees, D., R. W. Smith, P. J. Charleton, F. G. McCormac, N. Lloyd, and A. Steen, The generation of vertical thermospheric winds and gravity waves at auroral latitudes. I. Observations of vertical winds, *Planet. Space Sci.*, **32**, 667–684, 1984c.

Rees, D., R. Gordon, T. J. Fuller-Rowell, M. Smith, G. R. Carignan, T. L. Killeen, P. B. Hays, and N. W. Spencer, The composition, structure, temperature and dynamics of the upper thermosphere in the polar regions during October to December 1981, *Planet. Space Sci.*, **33**, 617–666, 1985.

Rees, D., A. Aruliah, T. J. Fuller-Rowell, V. B. Wickwar, and R. J. Sica, Winds in the upper mesosphere at mid-latitude: first results using an imaging Fabry-Perot interferometer, *Geophys. Res. Lett.*, **17**, 1259–1262, 1990.

Rees, D., S. Batten, A. L. Aruliah, T. J. Fuller-Rowell, A. D. Farmer, and K. S. C. Freeman, Long-lived polar thermospheric vortices: a combined radar and optical study, *J. Atmos. Terr. Phys.*, **53**, 493–514, 1991.

Rees, M. H., B. A. Emery, R. G. Roble, and K. Stamnes, Neutral and ion gas heating by auroral electron precipitation, *J. Geophys. Res.*, **88**, 6289–6300, 1983.

Roble, R. G., and B. A. Emery, On the global mean temperature of the thermosphere, *Planet. Space Sci.*, **31**, 597–614, 1983.

Roble, R. G., P. B. Hays, and A. F. Nagy, Calculated (OI) 6300 Å nightglow doppler temperatures for solar cycle minimum, *Planet. Space Sci.*, **16**, 1109–1113, 1968.

Roble, R. G., P. B. Hays, and A. F. Nagy, Photometric and interferometric observations of a mid-latitude stable auroral red arc, *Planet. Space Sci.*, **18**, 431–439, 1970.

Roble, R. G., R. E. Dickinson, and E. C. Ridley, Global circulation and temperature structure of thermosphere with high-latitude plasma convection, *J. Geophys. Res.*, **87**, 1599–1614, 1982.

Roble, R. G., R. E. Dickinson, E. C. Ridley, B. A. Emery, P. B. Hays, T. L. Killeen, and N. W. Spencer, The high latitude circulation and temperature structure of the thermosphere near solstice, *Planet. Space Sci.*, **31**, 1479–99, 1983.

Rohrbaugh, R. P., B. A. Tinsley, H. Rassoul, Y. Sahai, N. R. Teixeira, R. G. Tull, D. R. Doss, A. L. Cochran, W. D. Cochran, and E. S. Barker, Observations of optical emissions from precipitation of energetic neutral atoms and ions from the ring current, *J. Geophys. Res.*, **88**, 6317–6330, 1983.

Shiraki, H., CCD image sensor, *Ouyou Butsuri (Appl. Phys.) (in Japanese)*, **49**, 362–369, 1980.

Sica, R. J., Multi-instrument measurements of ionosphere-thermosphere coupling involving optical interferometry, *J. Geomag. Geoelectr.*, **43**, 467–478, 1991.

Sica, R. J., M. H. Rees, G. J. Romick, G. Hernandez, and R. G. Roble, Auroral zone thermospheric dynamics. 1. Averages, *J. Geophys. Res.*, **91**, 3231–3244, 1986a.

Sica, R. J., G. Gernandez, G. J. Romick, M. H. Rees, and R. G. Roble, Auroral zone thermospheric dynamics. 2. Individual nights, *J. Geophys. Res.*, **91**, 13593–13611, 1986b.

Sica, R. J., G. Hernandez, B. A. Emery, R. G. Roble, R. W. Smith, and M. H. Rees, The control of auroral zone dynamics and thermodynamics by the interplanetary magnetic field dawn-dusk (Y) component, *J. Geophys. Res.*, **94**, 11921–11932, 1989.

Sipler, D. P., and M. A. Biondi, Equatorial F-region neutral winds from nightglow OI 630.0 nm Doppler shifts, *Geophys. Res. Lett.*, **5**, 373–376, 1978.

Sipler, D. P., and M. A. Biondi, Midlatitude F region neutral winds and temperatures during the geomagnetic storm of March 26, 1976, *J. Geophys. Res.*, **84**, 37–40, 1979.

Sipler, D. P., B. B. Luokkala, and M. A. Biondi, Fabry-Perot determinations of midlatitude F-region neutral winds and temperatures from 1975 to 1979, *Planet. Space Sci.*, **30**, 1025–1032, 1982.

Sipler, D. P., M. A. Biondi, and R. G. Roble, F-region neutral winds and temperatures at equatorial latitudes: measured and predicted behaviour during geomagnetically quiet conditions, *Planet. Space Sci.*, **31**, 53–66, 1983.

Sipler, D. P., M. E. Hagan, M. E. Zipf, and M. A. Biondi, Combined optical and radar wind measurements in the F region over Millstone Hill, *J. Geophys. Res.*, **96**, 21255–21262, 1991.

Spencer, N. W., L. E. Wharton, H. B. Niemann, A. E. Hedin, G. R. Carignan, and J. C. Maurer, The Dynamics Explorer wind and temperature spectrometer, *Space Sci. Instrum.*, **5**, 417–428, 1981.

Spencer, N. W., L.E. Wharton, G. R. Carignan, and J. C. Maurer, Thermosphere zonal winds, vertical motions and temperature as measured from Dynamics Explorer, *Geophys. Res. Lett.*, **9**, 953–956, 1982.

Sridharan, R., S. Gurubaran, R. Raghavarao, and R. Suhasini, Co-ordinated thermospheric and F-region measurements from low latitudes, *J. Atmos. Terr. Phys.*, **53**, 515–519, 1991.

Stewart, R. D., R. W. Smith, D. Rees, J. R. Dudeney, and A. S. Rodger, First measurements of thermospheric winds in Antarctica by an optical ground-based method, *Nature*, **317**, 45–47, 1985.

Tohmatsu, T. and T. Ogawa, Compendium of aeronomy, pp. 49–104, Terra Scientific Publishing Company, Tokyo, 1990.

Truttse, Yu. L., and O. T. Yurchenko, Temperature of the upper atmosphere from the 6300 Å emission data, *Planet. Space Sci.*, **19**, 545–546, 1971.

Wallis, D. D., Geomagnetic influences on thermospheric winds observed in the auroral zone, *Ph.D thesis, Univ.of Alaska, College*, 1974.

Wharton, L. E., N. W. Spencer, and H. G. Mayr, The Earth's thermospheric superrotation from Dynamics Explorer 2, *Geophys. Res. Lett.*, **11**, 531–533, 1984.

White, M. H., D. R. Lampe, F. C. Blaha, and I. A. Mack, Characterization of surface channel CCD image arrays at low light levels, *IEEE J. Solid-State Circuits*, **SC-9**, 1–12, 1974.

Wickwar, V. B., J. W. Meriwether, Jr., P. B. Hays, and A. F. Nagy, The meridional thermospheric neutral wind measured by radar and optical techniques in the auroral region, *J. Geophys. Res.*, **89**, 10987–10998, 1984.

Winser, K. J., A. D. Farmer, D. Rees, and A. Aruliah, Ion-neutral dynamics in the high latitude ionosphere: first results from the INDI experiment, *J. Atmos. Terr. Phys.*, **50**, 369–377, 1988.

Yagi, T., and P. L. Dyson, Measurements of thermospheric temperatures at a mid-latitude station, *Planet. Space Sci.*, **33**, 203–206, 1985a.

Yagi, T., and P. L. Dyson, The response of the mid-latitude thermospheric wind to magnetic activity, *Planet. Space Sci.*, **33**, 461–467, 1985b.

Yagi, T., and P. L. Dyson, The influence of neutral temperatures and winds on the F-layer height, *J. Atmos. Terr. Phys.*, **47**, 575–579, 1985c.

Yagi, T., and P. L. Dyson, Observations of the mid-latitude neutral atmosphere and ionosphere during the storm of 5 March 1981, *J. Atmos. Terr. Phys.*, **47**, 1075–1080, 1985d.

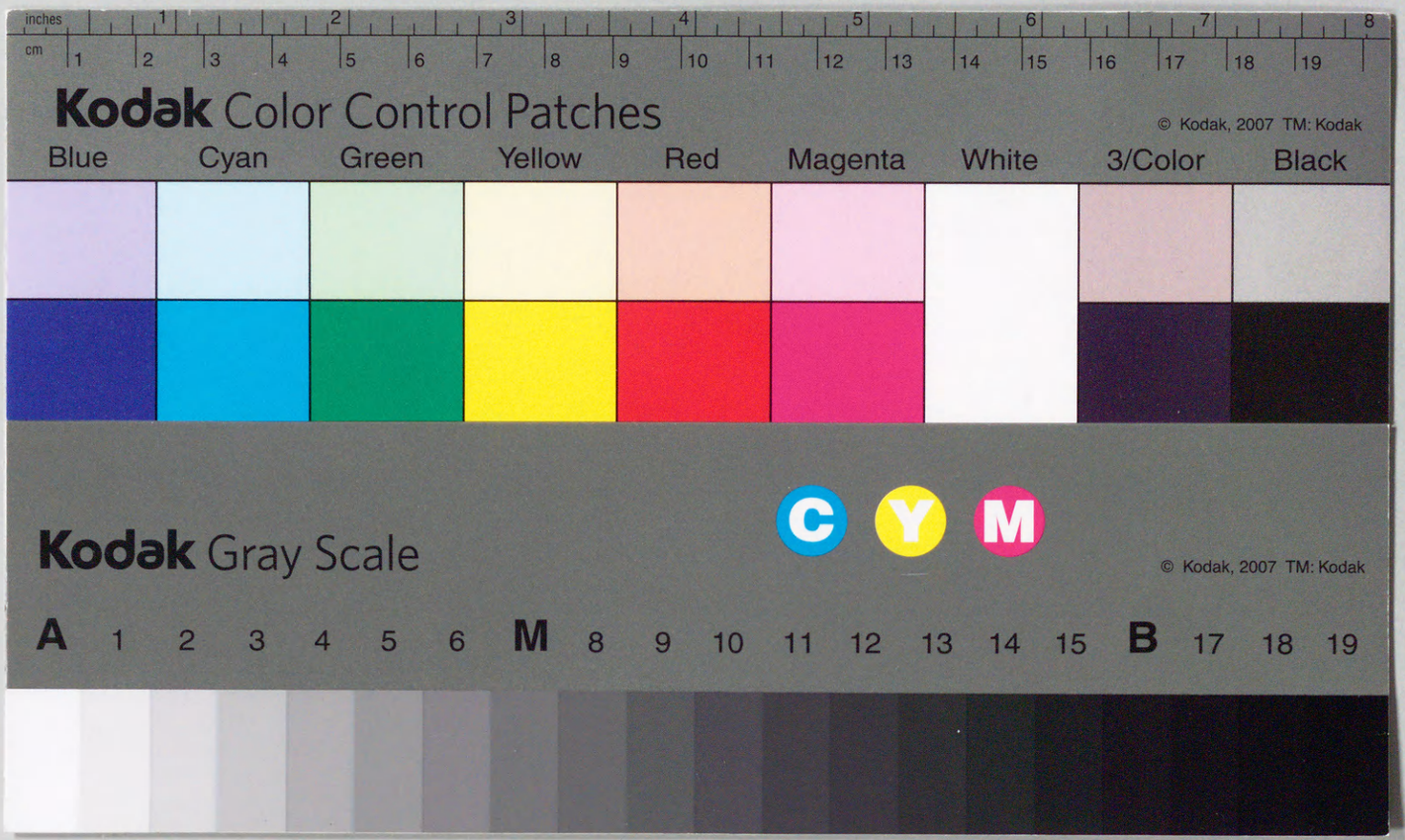
inches
cm
Kodak Color Control Patches
© Kodak, 2007 TM: Kodak
Blue
Cyan
Green
Yellow
Red
Magenta
White
3/Color
Black
Kodak Gray Scale
C
Y
M
© Kodak, 2007 TM: Kodak
A 1 2 3 4 5 6 M 8 9 10 11 12 13 14 15 B 17 18 19